Uneven temperatures in hot carrier solar cells : optical characterization and device simulation.

Thomas Vezin

To cite this version:

Thomas Vezin. Uneven temperatures in hot carrier solar cells : optical characterization and device simulation.. Physics [physics]. Institut Polytechnique de Paris, 2024. English. NNT : 2024IPPAX061 . tel-04861644

HAL Id: tel-04861644
https://theses.hal.science/tel-04861644v1

Submitted on 2 Jan 2025

INSTITUT
POLYTECHNIQUE
DE PARIS

NNT : 2024IPPAX061

Thèse de doctorat

Uneven temperatures in hot-carrier solar cells: optical characterization and device modelling

Thèse de doctorat de l'Institut Polytechnique de Paris
préparée à l'Institut Photovoltaïque d'Ile-de-France (IPVF)

École doctorale n°626 École doctorale de l'Institut Polytechnique de Paris (EDIPP)
Spécialité de doctorat : Physique

Thèse présentée et soutenue à Palaiseau, le 24/10/2024, par

THOMAS VEZIN

Composition du Jury :

Alistair Rowe Professeur associé, École polytechnique, Institut Polytechnique de Paris (PMC)	Président
Philippe Dollfus Directeur de recherche, Université Paris-Saclay (C2N)	Rapporteur
Maria Antonietta Loi Professeure, Université de Gröningen (Faculty of Science and Engineering)	Rapporteuse
Christophe Goupil Professeur, Université Paris-Cité (LIED)	Examinateur
Jean-François Guillemoles Directeur de recherche, Centre National de la Recherche Scientifique (UMR IPVF)	Directeur de thèse
Daniel Suchet Maître de conférences, École polytechnique, Institut Polytechnique de Paris (UMR IPVF)	Co-directeur de thèse

Remerciements

Merci à tou·te·s les membres de mon jury de thèse, et en particulier aux rapporteur·euse·s d'avoir pris le temps d'évaluer mon travail.

Merci également aux membres de mon comité de suivi individuel, Aloyse et Fabian, pour avoir consacré un peu de leur temps précieux à l'encadrement de ma thèse. C'était un plaisir de discuter avec vous et de vous présenter mes travaux en « avant-première ».

Je tenais aussi à remercier tout particulièrement Davide Boschetto, directeur de l'Ecole Doctorale de Physique, qui m'a sorti d'un sacré pétrin lorsque j'ai dû changer de thèse à l'été 2021.

Merci bien sûr à Jean-François. Ce n'était pas toujours évident de t'attraper, mais c'est probablement pour le mieux car je n'aurais pas forcément su quoi faire de toutes tes idées. Ce fut en tout cas un réel plaisir d'échanger avec toi, que ce soit sur le plan scientifique ou personnel. J'admire la sérénité avec laquelle tu parviens à infuser tes idéaux anarchistes dans la gestion de la vie sociale et scientifique du laboratoire.

Enfin, merci à Daniel. Tu as accompli ton rôle de directeur de thèse avec brio, et j'ai beaucoup appris à tes côtés. J'ai eu mes moments de doutes, peut être plus que de raison, mais tu as toujours su contrebalancer mon pessimisme aux moments opportuns. Merci d'avoir gardé le cap, j'essaierai de faire mien ton mantra « ne crions pas avant d'avoir mal » ! Et surtout, merci de m'avoir introduit à la recette du miso !

* * *

Merci à tou·te·s les collègues qui m'ont accompagné pendant tout ou partie de ces trois ans.

En tout premier, merci à toi Mahyar. C'est toi qui m'a tout appris, et cette thèse te doit beaucoup ! J'ai eu énormément de plaisir à te recroiser en conférence à Münster, et je te souhaite bonne chance pour ta carrière future. Merci également à Nathan et Shalu d'être venu·e·s grossir les rangs de l'équipe « porteurs chauds », et de m'avoir permis de transmettre à mon tour ce que j'avais reçu. Merci à Maxime et Lucile, qui ont aussi un peu fait partie de l'équipe à leur manière, et avec qui j'ai passé des moments inoubliables au Belambra Club. Merci enfin à Marie, avec qui je n'ai que de bons souvenirs – à Paris comme à Tokyo.

J'ai une pensée particulière pour les membres de l'équipe « carac » Daniel O., Baptiste, Julie, Géraud, Nao, Alexandra, Ange, et tous les autres. Heureusement que nous avions notre petit rendez-vous du lundi, et j'espère que vous continuerez à ranger la salle régulièrement malgré mon départ ! Merci également au bureau des gourmand·e·s (Cynthia, Aubin, Juliette, Meyssa, Diep) pour tous les gâteaux et la bonne ambiance.

Merci à Valérie, ma jeune retraitée préférée qui m'a si gentiment accueilli aux confins du monde pour une semaine de rédaction effrenée. C'est aussi grâce à toi que j'ai réussi à finir ma thèse dans les temps.

Merci à toute l'équipe d'encadrement des TPs d'optique, en particulier Ambroise et Léonard qui m'ont beaucoup appris sur les bases de l'optique et avec qui j'ai eu un plaisir non dissimulé à discuter science. Et surtout, surtout, un énorme merci à Yannis pour avoir coordonné tout ça, et pour m'avoir suivi et supporté toutes ces années. J'ai adoré travailler avec toi, et ce depuis ce fameux MODAL sur la supra des cuprates. Je te suis très reconnaissant d'avoir pris le temps de me conseiller sur mon orientation, pour mon stage de M1 ou pendant mon changement de thèse.

Merci à enfin à toute l'équipe de SolairePV, en particulier Stéphane, Amaury, Capucine, Martin, Maxime, et Tiphaine. Ce travail a vraiment été bouleversant pour moi, j'en avais besoin pour reconnecter ma recherche à des problématiques concrètes. Cela m'a permis de garder de la motivation dans les phases difficiles, et surtout cela m'a ouvert beaucoup de perspectives réjouissantes pour la suite.

>> Allez voir notre site web ! <<

Ce tableau des « collègues » ne serait pas complet si je n'avais pas un petit mot pour Guillaume. Cette thèse te doit beaucoup. Déjà parce que c'est grâce à toi que j'ai rencontré Daniel (petite pensée pour feu le « Club du KB »). Ensuite parce que cela fait près de dix ans que nous cheminons cote à cote depuis les bancs de l'X. Tu es un ami inestimable, et tu as aussi été un collègue formidable. J'admire ton énergie inépuisable dont je me suis beaucoup nourri. Nous avons pris des chemins différents, et il est désormais plus difficile de nous confondre l'un avec l'autre... Mais certains y parviennent toujours !

~~~~~~~~~~~~~~~~~~~~~~~~~~~~

Sur un plan plus personnel, je tiens absolument à remercier mes super colocs, qui m'ont apporté beaucoup de joies, quelques peines, et surtout du soutien durant la rédaction de mon manuscrit et la préparation de cette soutenance.

Merci Aram, j'ai adoré passer du temps à tes côtés, comme collègue mais aussi comme ami. Je suis désolé d'avoir quitté le LPICM aussi tôt, mais je suis très heureux de voir que tu as sû surmonter les obstacles et fini ta thèse, malgré un début vraiment pas évident.

Merci à tou·te·s mes ami·e·s. Je n'ai pas la place pour vous citer chacun·e d'entre vous, mais je ne vous oublie pas. Merci en particulier aux membres de la Sphinx, ça a été un honneur de m'engager à vos côtés. Et surtout un immense merci à Tout Pour Le Tout. Vous étiez la soupape dont j'avais besoin. On n'a jamais raté une occasion de se faire une bonne bouffe, de jouer de la musique et de parler à coeur ouvert, et on est pas prêts de s'arrêter !

Merci à ma famille, proche comme éloignée. J'ai toujours pu compter sur votre soutien en toute circonstance, et c'est aussi cette stabilité qui m'a donné la force de finir cette thèse.

Enfin, merci à Marion. Je n'ose dresser la liste de tout ce que tu m'as appris lors de ces quatre ans... Nous avons commencé à cheminer ensemble au début de nos thèses respectives, et je n'ai aucun doute que nous continuerons bien des années au delà. Merci du fond du coeur.
~~~~~~~~~~~~~~~~~~~~~~~~~~~~

Acronyms

BF Band Filling.

EQE External Quantum Efficiency.

GPL Generalized Planck Law.

HC Hot Carrier.

HCSC Hot-Carrier Solar Cell.

HDR High Dynamical Range.

HI Hyperspectral Imager.

PL Photoluminescence.

PLR Photoluminescence Ratio.

PLRBF Photoluminescence Ratio with Band Filling.

QFLS Quasi-Fermi-Level Splitting.

QW Quantum Well.

ROI Region of interest.

SNR Signal to Noise Ratio.

List of Figures

Contents

Chapter 1

Introduction

Table of contents

1.1 Introduction to photovoltaics

1.1.1 Why photovoltaics matter to humankind?

Humanity is currently facing an ecological crisis. This crisis appears in many forms: global warming, increased occurrence of extreme climate events [IPCC 2023], collapse of biodiversity, global pollution [Project 2023], etc.

One of the many causes of this crisis is the release of greenhouse gases in the atmosphere by human activities. Indeed, human activities nowadays heavily rely on fossil fuels to power engines, turbines, heating systems, etc. A possible technological way out of this addiction to fossil fuels is through *electrification*, as there exist low-carbon electricity production systems.

Photovoltaic (PV) systems are one of the low-carbon footprint electricity-producing systems, as shown in Figure 1.1. As their etymology suggests – *phōs* = light and *volt* =

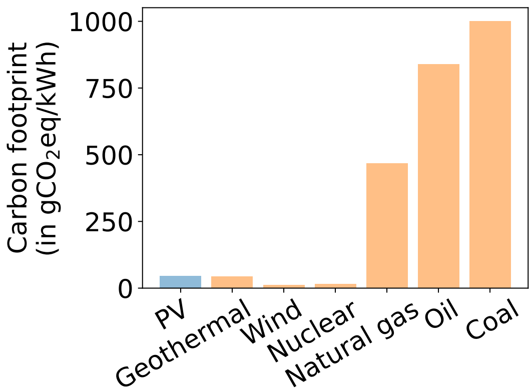

Figure 1.1: *Comparison of the carbon footprint (in* gCO_2eq/kWh*) of the most common electricity sources. Figure adapted from [Collin et al. 2023]. Sources [Pérez-Lopez et al. 2020], which reports numbers from the second IPCC report (2013).*

unit of the electromotive force –, photovoltaic systems allow the conversion of light into electrical power. It takes only about half an hour for the Sun to irradiate towards the Earth the energy consumed by humanity over an entire year. Photovoltaics allow us to take advantage of this enormous energy source.

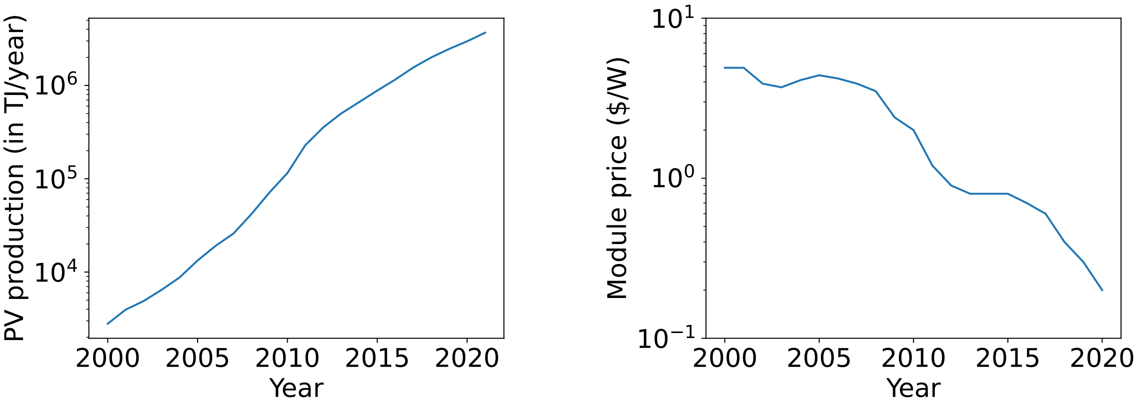

(a)

(b)

Figure 1.2: *(a) Evolution of the total electricity production by photovoltaic systems since 1990. (b) Evolution of the photovoltaic module prices since 1990. Sources: IEA Energy Statistics Data Browser.*

For this reason, photovoltaics has attracted growing attention in the past two decades. Indeed, as its production at industrial scale skyrocketed, its price decreased rapidly thanks to economies of scale and technological breakthroughs. Since 2000, electricity production from photovoltaics increased by a factor 1000, as shown in Figure 1.2a. In the meantime, the price of photovoltaic modules was divided by a factor 25 (Figure 1.2b).

Nowadays, photovoltaics is a mature industrial sector and represents a market of several hundred billion dollars per year. As shown in Figure 1.3a, an ever-increasing share of electricity production is provided by photovoltaics – and more generally from renewables. This good news must be put into perspective, as electricity represents only around 20 % of the total energy consumption on Earth. Therefore, as illustrated by Figure 1.3b, around 80 % of the energy used by humanity still comes from fossil fuels (coal, oil, gas). In addition, it appears that the total consumption of fossil fuels – and hence the total CO_2 emissions – has never been higher than today. This questions the very notion of *energy transition*: will we ever see a future where fossil fuels are completely replaced by renewable energies? Or will we keep adding new energy sources on top of the old ones? [Fressoz 2024]

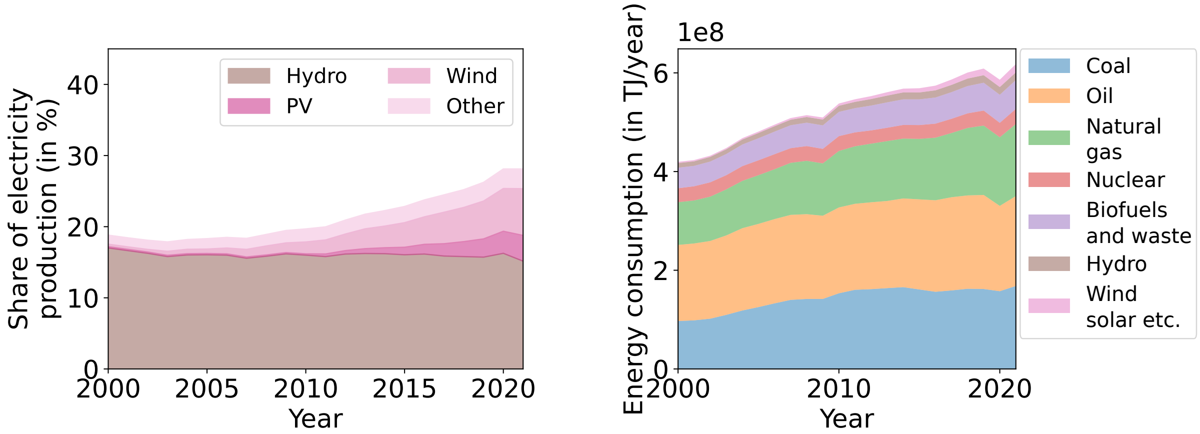

(a)

(b)

Figure 1.3: *(a) Share of the total electricity production of renewable energy sources. (b) Worldwide energy consumption by energy source, in* TJ/year*. Source: [IEA 2024].*

This question will not be answered in this manuscript. However, during my PhD at IPVF, I took part in an initiative called *SolairePV*[1], which aims at compiling data on photovoltaics and answering many questions from the general public. We eventually published this work under the form of 42 thematic factsheets which are freely accessible on our website [Collin *et al.* 2023].

In any case, photovoltaics is not just a potential solution to the ecological crisis; it's also a very interesting topic for scientific research. Photovoltaic systems sit at the crossroads of several scientific fields. First, these systems generate both continuous and intermittent currents, posing interesting questions for electrical engineering. Second, as energy-conversion systems, they are intrinsically linked to thermodynamics. Third, most photovoltaic systems use semiconductors and therefore are connected to condensed matter physics. Fourth, optics and photonics are involved in the optimization of light absorption in photovoltaic materials. Last, designing and building these systems involves materials science and chemistry.

1.1.2 Science of photovoltaics

The photovoltaic effect is the formation of an electrical bias at the edges of a device under illumination. In this section, we introduce several key notions to describe photovoltaic systems.

---

[1] This collective work (more than 20 collaborators) was recently awarded the "Prix Lumières Arnulf-Françon 2023" by the French Optical Society.

First of all, all photovoltaic systems require four ingredients [Suchet and Johnson 2023].

1. A material that converts the incoming light into excited electrons. This material is generally called the *absorber*.
2. The possibility to keep the electrons excited for a certain duration, called *lifetime*.
3. A mean to transport the excited electrons to the electrodes during their lifetime.
4. A built-in asymmetry that forces the electrons to exit the system from one of the electrodes and enter from the other.

Semiconductors offer practical solutions for all these requirements, and therefore most photovoltaic systems are built with semiconductors. In a schematic picture, semiconductors are composed of two *energy bands*: one low-energy valence band, which is almost completely filled by electrons, and one high-energy conduction band, which is almost completely empty. Those two bands are separated by an energy *bandgap*, denoted as E_g. Electrons may transition from one band to the other by gaining or loosing energy. One of the ways to do so is to absorb or emit photons of energy larger than the bandgap. This is depicted in Figure 1.4. Note that photons with energy below the bandgap will not interact with the semiconductor.

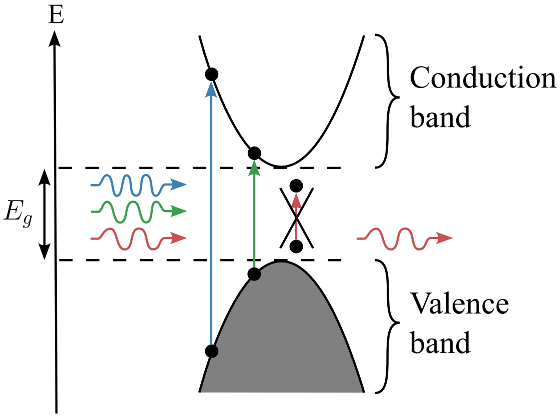

Figure 1.4: *Schematic representation of the interaction between photons and a semiconductor. The semiconductor valence band is filled with electrons, which may absorb blue and green photons to transition to the empty conduction band. However, red photons are not absorbed in this case, because their energy is lower than the semiconductor bandgap,* E_g.

When studying photovoltaic devices, one of the key figures of merit is the *energy-conversion efficiency*. It is defined as the total electrical power that the system can output divided by the total power that it receives from the Sun. A large part of the research on photovoltaic devices aims at increasing this efficiency, and has been successful in doing so, as exemplified by the famous NREL's Efficiency Chart.

1.1.3 Efficiency of photovoltaic devices

The race towards higher efficiencies is obviously driven by economical reasons. Installers care about how much energy they can produce per dollar invested. Therefore, the cost of energy producing units is expressed in \$/kWh. Today, the price of photovoltaic modules is only a small fraction (typically $20 - 40$ %) of the total price of a photovoltaic system. Consequently, reducing manufacturing costs of photovoltaic modules will not result in dramatic savings. The best way of increasing the cost-efficiency of photovoltaic systems is to increase their energy-conversion efficiency [Suchet and Johnson 2023] – assuming constant final price.

Another important consideration is that the Sun is a rather *diluted* resource, with an average irradiance of 1000 W.m^{-2} at the Earth's surface. Therefore, large surfaces of photovoltaic modules are required in order to produce substantial amounts of energy. For instance, with today's technology, its takes roughly a hundred times more surface to produce electricity from photovoltaic plants than from nuclear plants [Collin *et al.* 2023]. In that regard, higher efficiencies are crucial because they reduce the surface area needed to install a production unit of a given power capacity. This is particularly important in achieving the goal of zero net land artificialization, which France aims to reach by 2050 [Legifrance 2021].

Today, the record efficiency for a silicon solar cell – by far the dominant technology on the market – is above 26 % [Green *et al.* 2022]. These excellent performances are nearing the maximal theoretical efficiency of conventional solar cells, sometimes called *detailed balance limit*, which is around 30 %. In the following section, we recall the main lines of this derivation. Then, we discuss the possibility to overcome the detailed balance limit by changing some operating principles of solar cells.

Detailed balance limit The detailed balance limit was first introduced by Shockley and Queisser [Shockley and Queisser 1961]. They considered the operation of an ideal single-junction solar cell, which would absorb all photons above its bandgap. Every absorbed photon promotes one electron in the conduction band, as shown in Figure 1.4. As a consequence of Kirchhoff's law, materials that absorb light must emit light in return by allowing excited electrons in the conduction band to recombine and go back to the valence band. These radiative recombinations are unavoidable and Shockley and Queisser assumed that no other recombinations could occur. This is the so-called *radiative limit*. Finally, they assumed that the excess kinetic energy provided by high-energy photons (like the blue photon represented in Figure 1.4) would be lost to thermalization such that high-energy electrons would drop to the bottom of the conduction band before they can be extracted in the contacts.

The Shockley-Queisser model allows to understand why the notion of bandgap is so fundamental in photovoltaics. If the bandgap is too small ($E_g \to 0$), the system absorbs all incident photons, but looses it all to thermalization. In this case, the efficiency of the cell is zero. On the contrary, if the gap is too large ($E_g \to \infty$), then almost no photons are absorbed and the efficiency of the cell drops to zero again. In between those two extreme cases, there is an optimal value of the bandgap for which the efficiency of the cell is maximal.

Another key finding of Shockley and Queisser is that the voltage of the cell depends, among other factors, on the density of excited carriers. The higher the carrier density, the larger the voltage.

In the Shockley-Queisser model, the incoming Sun power splits into five different contributions, which depend on the bandgap of the solar cell. This is represented in Figure 1.5. This model predicts that the maximum efficiency of a solar cell is $\eta_{\text{Shockley-Queisser}} \simeq 30$ % for a bandgap $E_g \simeq 1.2$ eV. For a detailed discussion of the underlying assumptions and its impact on the operation of a solar cell, see for instance [Guillemoles *et al.* 2019, Vezin *et al.* 2024a].

It should be noted however that this detailed balance model does not represent the ultimate limit of efficiency that would be applicable to *any* photovoltaic technology. Indeed, it is deeply rooted in standard single-junction technology. For instance, absorption, radiative emission and thermalization properties are described in terms specific to semiconductors.

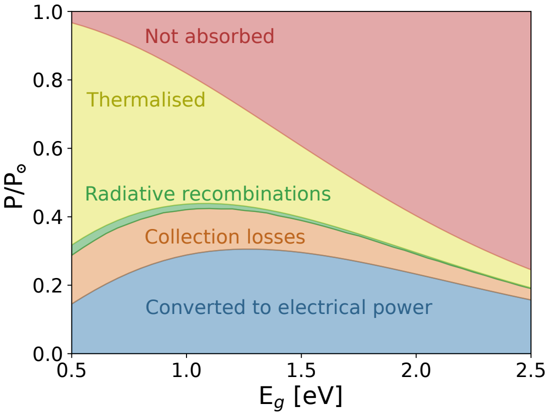

Figure 1.5: *Breakdown of the incoming Sun power between the five fundamental processes included in the Shockley-Queisser model [Shockley and Queisser 1961], as a function of the absorber bandgap. Adapted from [Vezin* et al. *2024a].*

Ultimate thermodynamical limit From an abstract thermodynamical perspective, a photovoltaic module can be thought of as a heat engine producing work by receiving heat from the Sun ($T_\odot = 5778$ K) and by releasing heat in the atmosphere ($T_{\text{amb}} = 293$ K). This heat engine will necessarily have an efficiency lower than Carnot efficiency $\eta_{\text{Carnot}} = 1 - T_{\text{amb}}/T_\odot \simeq 95$ %. However Carnot efficiency does not take into account the inevitable radiative losses due to Kirchhoff's law. A more advanced computation was proposed by [Landsberg and Tonge 1979], which led the following estimate for the ultimate limit of efficiency of a photovoltaic system (see [Vezin *et al.* 2024a]):

$$\eta_{\text{Lansberg}} = 1 - \frac{4}{3}\frac{T_{\text{amb}}}{T_\odot} + \frac{T_{\text{amb}}^4}{T_\odot^4} \simeq 93 \ \% \tag{1.1}$$

There is a huge gap between this ultimate limit and the detailed balance limit for standard single-junction solar cells. To bridge this gap and enhance the potential efficiency of photovoltaic systems, several concepts have been proposed. These are generally referred to as *third generation*, *advanced concepts* or *high-efficiency photovoltaics*.

1.1.4 High-efficiency photovoltaics

We presented the different concepts to outperform the Shockley-Queisser model in a book chapter to be published [Vezin *et al.* 2024a]. Here, we simply summarize its contents and introduce the notion of Hot-Carrier Solar Cell (HCSC) that will be discussed in this manuscript.

Concentration and multi-junctions First, it must be noticed that two approaches already allowed to break the 30 % limit predicted by Shockley and Queisser.

The first approach relies on *optical concentration* and consists of using a lens to concentrate sunlight onto a solar cell with a smaller surface area. This increases the carrier density in the cell, thereby enhancing its voltage and, consequently, its efficiency. However, due to the Sun being an extended light source, sunlight cannot be infinitely concentrated, and the maximum concentration factor is 46240 [Wurfel and Wurfel 2016]. Under this so-called *full concentration*, the detailed balance limit for the efficiency is around 40 % (see Figure 3.4). Using this concept, the National Research Energy Lab (NREL) managed to fabricate GaAs single-junction cells with 30.8 % efficiencies under 61 suns in 2022 [NREL 2024].

The second approach is called *multi-junctions* and consists in putting several cells of decreasing bandgaps in series. The first cell, with a high bandgap, converts efficiently high-energy photons and lets low-energy photons go through. These are then converted efficiently by the second cell, etc. With an infinite number of sub-cells, one can theoretically obtain a 87 % efficiency under full concentration [Green 2006], very close to the ultimate limit. But with only two cells, it is already possible to overcome the Shockley-Queisser limit. For instance, the best tandem cell to date was build by LONGi (China's biggest manufacturer of photovoltaic modules) and has an efficiency of 33.9 % [NREL 2024].

The combination of these two concepts allowed Fraunhofer ISE to build the all-time record cell: a quadruple junction with 47.6 % efficiency under a concentration factor of 665 [NREL 2024].

Advanced concepts As can be seen in Figure 1.5, the two main losses in a conventional solar cell are non-absorption of low-energy photons and thermalization of high-energy photons. Therefore the advanced concepts for high-efficiency photovoltaics tackle one or the other of these issues.

First, one may aim to avoid losing low-energy photons. To achieve this, an optical converter can be added to the cell, which absorbs two low-energy photons and emits a single high-energy photon that can be absorbed by the solar cell. This approach is called *up-conversion* [Trupke *et al.* 2002]. Similarly, it is possible to enable a two-photon transition *in the absorber* by creating a so-called *intermediate band* in the gap [Wolf 1960, Luque and Martí 1997]. In such an intermediate band absorber, a low-energy photon can excite an electron from the valence band to the intermediate band. This excited electron can then absorb a second low-energy photon, promoting it to the conduction band.

Second, one may aim to avoid thermalization of high-energy photons. An optical solution to this problem is to add to the cell an optical converter capable of absorbing one high-energy photon and emitting two low-energy photons closer to the bandgap of

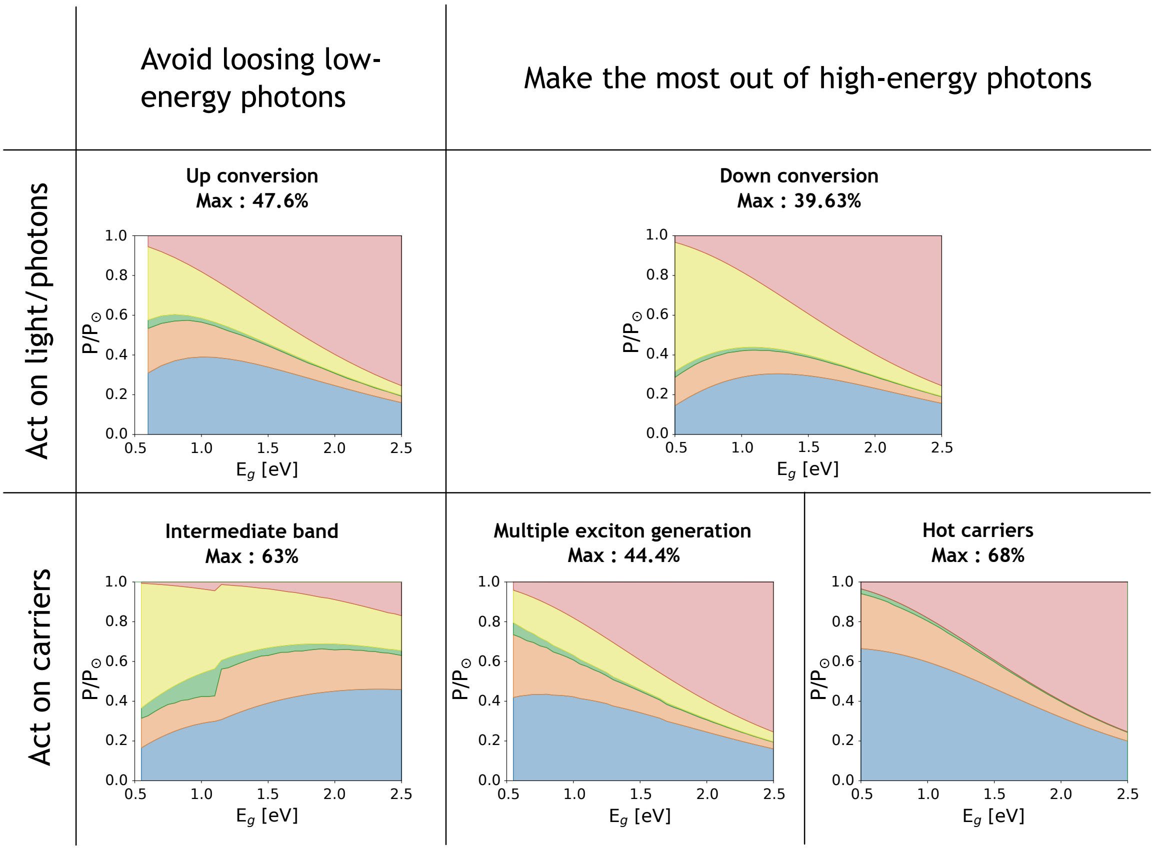

Figure 1.6: *Breakdown of the incoming Sun power (1 sun illumination) into the five fundamental processes for all advanced concepts for high-efficiency photovoltaics. Maximum efficiencies are reported in the titles. Colors are the same as in Figure 1.5. Adapted from [Vezin* et al. *2024a].*

the absorber. This proposition is symmetrical to up-conversion, and is called *down-conversion* [Trupke *et al.* 2002]. Similarly, it is possible to avoid high-energy electrons thermalization by using their excess energy to promote one or several additional electrons in the conduction band by *impact ionization* [Werner *et al.* 1994, Hanna and Nozik 2006]. This process is also called *multiple exciton generation*. Finally, if the thermalization processes are sufficiently inefficient in the absorber, the high-energy carriers may not have time to thermalize their excess energy before they are extracted in the contacts. This is the idea behind *Hot-Carrier Solar Cell (HCSC)*, which offer the highest theoretical efficiency: 68 % under one sun condition (see Figure 1.6) and up to 86 % under full concentration [Ross and Nozik 1982].

These advanced concepts are summarized in Figure 1.6, along with their theoretical optimal efficiency under one sun illumination. Note that none of the aforementioned advanced concepts has enabled the construction of a solar cell with an efficiency exceeding 30 % yet.

From now on we will focus on the notion of HCSC and its implications. We first define HCSCs and describe key characterization techniques and indicators in section 1.2. Then, we propose a historical overview of HCSCs from the 80s to today and show that these systems do not keep their promises yet in section 1.3. This calls for a more in-depth understanding of how HCSCs depart from their ideal behavior, and we will present our contribution to that understanding in section 1.4. Finally, we will close this chapter in section 1.5 by providing an outline of the entire manuscript.

1.2 Hot-carrier solar cells and their characterization

In this section, we first propose a definition of HCSCs. Then, we provide a detailed description of hot carriers. Finally, we examine standard characterization techniques and focus on one key parameter for studying thermalization in HCSCs: the thermalization coefficient.

1.2.1 Definitions

Hot-carrier solar cells In the Shockley-Queisser model, thermalization losses amount to roughly 30 % of the incoming Sun power (see Figure 1.5). HCSCs are solar cells in which these losses are reduced, and ideally negligible. In order to build a HCSC, two ingredients are necessary. First, one needs an absorber in which thermalization rate is low. In such a *hot-carrier absorber*, carriers do not fall at the band-edge and can be maintained in states of high energy, therefore forming hot-carrier distributions in the bands. Second, one needs *energy-selective contacts* to convert the excess heat of the carriers into a voltage boost as compared with regular solar cells. For perfectly selective contacts, the voltage of the HCSC writes [Ross and Nozik 1982]

$$e(V_{\text{HCSC}} - V_{\text{SC}}) = \frac{\Delta E_{\text{ext}} - \Delta\mu}{T}(T_c - T_L) \tag{1.2}$$

where

ΔE_{ext} = The extraction energy.
$\Delta\mu$ = The Quasi-Fermi-Level Splitting (QFLS) in the absorber.
T_c = The temperature of carriers.
T_L = The temperature of the lattice.

This equation resembles that of a thermoelectric device, for which the voltage is proportional to the difference in temperature across the device. In fact, HCSCs can be seen as the combination of a regular solar cell and of a thermoelectric device that converts the excess carrier temperature into an electrical voltage [Rodiere *et al.* 2015, Konovalov and Emelianov 2017].

Hot carriers To complement our definition of HCSCs, we need to provide some details on hot carriers. In general, the term “hot carrier” refers to carrier distributions out of thermal equilibrium with the surrounding lattice. Hot carriers have more kinetic energy than cold carriers, and this excess kinetic energy can be provided by a variety of phenomena, such as the interaction with an intense electric field, or the absorption of high-energy photons. Here, we provide a comprehensive picture of the microscopic mechanisms controlling hot-carrier distributions.

Because we are interested in hot carriers in the context of solar cells, we reproduce the description proposed in [Green 2003]. It focuses on the temporal evolution of a semiconductor subject to a short and intense laser excitation at high energy. This system is represented schematically in Figure 1.7.

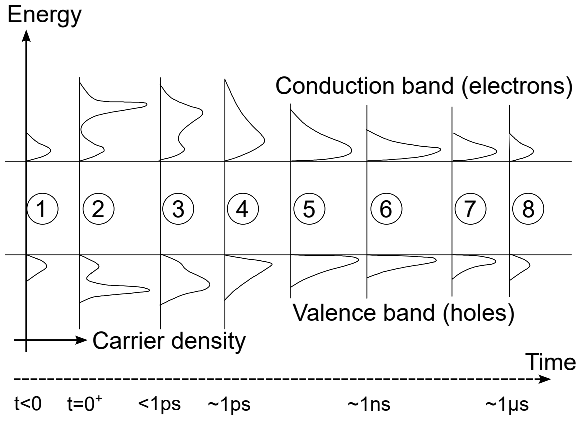

Figure 1.7: *Evolution of electron and hole distributions after a short, intense laser pulse at high energy. Adapted from [Green 2003].*

Before the laser pulse ①, the system is at ambient temperature and there is a small number of electrons (in the conduction band) and holes (in the valence band) because of thermal agitation. During the laser pulse ②, high-energy photons are absorbed, which generates high-energy electrons and holes in the bands. These populations do not follow a thermal distribution, and thus do not have a well defined temperature. Due to fast elastic carrier-carrier scattering, these non-equilibrium carriers quickly redistribute their energy ③, and reach a thermal distribution ④. Two types of elastic carrier-carrier scattering come into play, both mediated by Coulomb interaction:

- intraband interactions *i.e.* between carriers in the same band. These interactions allow the electrons (resp. holes) to reach a thermal distribution at temperature T_e (resp. T_h).
- interband interactions, *i.e.* between carriers in different bands. These interactions allow the electron-hole plasma to reach a single temperature T_c.

We call this phase the *equilibration* of carriers. It happens typically under 1 ps. After equilibration, carriers form thermal distributions at high temperature because they have simply redistributed among themselves the excess kinetic energy provided by the absorbed photons. This is what is called *hot carriers.*

After a few picoseconds, hot carriers start to interact with vibration modes of the lattice (so-called *phonons*) and begin to lose kinetic energy ⑤. This phase will be denoted as *thermalization*, and is illustrated in Figure 1.8. Carrier-phonon interactions are quite complex, as there exist many phonon types. In simple materials such as GaAs, there are four types: transverse acoustic (TA), longitudinal acoustic (LA), transverse optical (TO) and longitudinal optical (LO), which are presented schematically in Figure 1.8a. However, it was shown that the dominant thermalization process at room temperature in GaAs and other III-V semiconductors is carrier-LO phonon interaction, also called the *Fröhlich interaction* [Goebel and Hildebrand 1978, Shah 1981]. This can be partially understood by looking at the band structure of such materials, presented schematically in Figure 1.8b. During thermalization, carriers emit phonons and loose some of their kinetic energy. Because of energy and momentum conservation, carriers can only interact with zone-center phonons ($k \ll 2\pi/a$). Zone-center optical phonons have a significant energy

$E_{\mathrm{LO}} \simeq 36$ meV, and therefore are efficient at thermalizing carrier's excess energy. On the contrary, zone-center acoustic phonons have vanishing energies, and therefore contribute only weakly to thermalization.

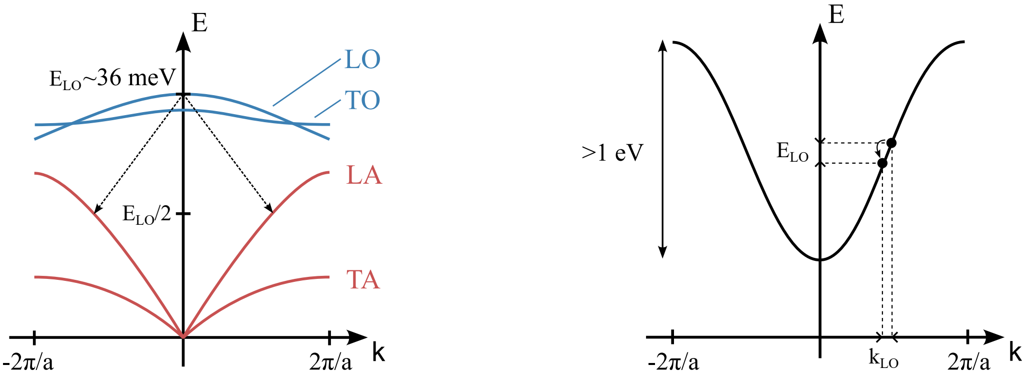

(a) (b)

Figure 1.8: *Schematic representation of (a) phonons and (b) electrons band structure in GaAs. Note that the scale for wavevectors is identical, while the scale for energies is not. In panel (a), dashed arrows indicate the Klemens mechanism, which is the decay of one LO phonon into two LA phonons of opposite momentum. a is the lattice constant.*

To cool down completely, hot carriers must emit a large number of zone-center optical phonons. However, they may also reabsorb part of these phonons – the reabsorption probability being proportional to the phonon density. LO phonon lifetime is controlled by their decay rate into acoustic phonons, a process called *Klemens relaxation*, represented with dashed arrows in Figure 1.8a. If Klemens relaxation is inefficient in comparison to the typical carrier-phonon interaction time, a large number of optical phonons may be created. This effect is called the *phonon bottleneck effect* and reduces the carrier thermalization rate as it increases the probability that phonons are reabsorbed by carriers.

Eventually, carriers reach a *thermal* equilibrium with the lattice at ambient temperature ⑥, typically within $0.1 - 10$ ns. Note that, at this stage, carrier populations in the semiconductor are still out of *chemical* equilibrium, because the carrier densities are still higher than what they would be in the dark. Finally, electrons and holes recombine together via radiative or non-radiative pathways ⑦, and go back to complete equilibrium ⑧ within a few microseconds.

Note that the timescales reported here are rough orders of magnitude, and are strongly dependent on the material and on the excitation regime (in particular carrier densities). In addition, although the different processes (equilibration, thermalization, recombination) are presented here sequentially, they may overlap in some cases. Yet this picture allows us to understand that hot carriers are not a rare phenomenon. In pulsed regime, hot carriers are generated after each high-energy laser pulse. Consequently, hot carriers can be detected "easily", provided that we can probe carrier distributions with a sufficiently short time resolution (typically < 1 ps) [Othonos 1998].

This brings us to the question of the detection and characterization of hot carriers.

1.2.2 Characterization and key indicators

Hot-carrier characterization techniques The first experimental signature of hot carriers was obtained by *carrier mobility measurements* [Shockley 1951]. However, such electrical detection does not allow to probe directly the carrier distribution inside the bands, and therefore does provide a direct proof of the presence of hot carriers [Bauer 1978].

Direct measurement of carrier distributions is made possible by various *spectroscopy* techniques, such as *transient absorption* or *photoluminescence* spectroscopy. These techniques measure the probability that a photon of a given energy is emitted or absorbed by the material. This probability depends on carrier distributions in the bands, and therefore it is possible to recover experimentally these distributions.

In the rest of this manuscript, we will focus on Photoluminescence (PL), and more specifically on continuous-wave PL, which is performed with continuous illumination and probes the system in steady-state. PL experiments consist in photogenerating electrons in the conduction band of a material, and recording the light reemitted as these electrons recombine. For a photon of energy E to be emitted, an electron-hole pair of the same energy must exist in the semiconductor. As carriers fill preferentially states up to few k_BT above the band-edge, emitted photons will have energies between E_g and E_g plus a few k_BT. This is the basic idea of hot-carrier spectroscopy: *hotter carriers will emit a spectrum with more significant high-energy tail.*

PL is a versatile technique for hot-carrier characterization. In particular, the excitation wavelength can be changed to adapt for different bandgaps and the power may be changed to probe different excitation regimes. In addition, PL is not only a way to probe hot-carrier distributions, but also to generate them [Shah and Leite 1969]. Finally, PL is a purely optical measurement such that it can be used on bare materials without contacts, which is particularly useful at early stages of the material development. In the context of solar cells, continuous-wave PL is particularly interesting because it probes the cell properties in conditions very similar to its actual operation.

However, simply detecting hot carriers with PL spectroscopy is not enough to characterize if a given material is a good hot-carrier absorber or not. Indeed, carrier temperature depends on the excitation regime, and in particular on the absorbed flux and power. This is why the notion of thermalization coefficient was proposed as the correct figure of merit to characterize hot-carrier absorbers.

A key indicator: the thermalization coefficient The thermalization coefficient, Q, characterizes the ability of an absorber to host a steady-state hot-carrier population *for a given power provided to the carriers.* When a material absorbs a certain radiation power I_{abs}, only a fraction of it is provided to the carriers as kinetic energy. This fraction depends on the bandgap of the material and on the average absorbed photon energy, $\langle E\rangle_{\text{abs}}$, and writes $I_{\text{th}} = (\langle E\rangle_{\text{abs}} - E_g)I_{\text{abs}}/\langle E\rangle_{\text{abs}}$ [Giteau *et al.* 2020]. In steady-state, all this power must be thermalized by the carriers, which eventually form a hot-carrier distribution at temperature $T_c > T_L$. Several different phenomenological definitions have been proposed for the thermalization coefficient (see for instance [Lyon 1986, Guillemoles *et al.* 2005, Le Bris *et al.* 2012] or [Giteau *et al.* 2020]). In this manuscript, we will retain the simplest form:

$$I_{\text{th}} = Q(T_c - T_L) \tag{1.3}$$

where Q is assumed to be constant.

Note that it is possible to establish an exact theoretical expression of the thermalized power from Fermi Golden Rule. This was done for instance in [Kumekov and Perel 1988, Tsai 2018] by assuming that thermalization was dominated by carrier-LO phonon interactions, and by taking into account the decay of LO phonons into acoustic phonons by Klemens mechanism. Such an approach leads to

$$I_{\text{th}} = \sum_{\boldsymbol{q}} E_{\boldsymbol{q}} \frac{N_{\boldsymbol{q}}(T_c) - N_{\boldsymbol{q}}(T_L)}{\tau_{\boldsymbol{q}}} \tag{1.4}$$

where

I_{th} = The power lost to thermalization by the carriers (in W.m^{-2}).
$E_{\boldsymbol{q}}$ = The energy of phonons with wavevector $\boldsymbol{q}$.
$N_{\boldsymbol{q}}(T) = (\exp(E_{\boldsymbol{q}}/(k_B T)) - 1)^{-1}$ is the population of mode $\boldsymbol{q}$ at thermal equilibrium at temperature T.
$\tau_{\boldsymbol{q}}$ = An interaction time which depends on the carrier-LO phonon interaction time, and on the decay rate of LO phonons into acoustic phonons.

For $T_L = 300$ K and carrier temperatures $T_c \leq 1000$ K, the term $N_{\boldsymbol{q}}(T_c) - N_{\boldsymbol{q}}(T_L)$ can be well approximated by its Taylor expansion of order 1, such that

$$I_{\text{th}} = \left[\sum_{\boldsymbol{q}} \frac{E_{\boldsymbol{q}}}{\tau_{\boldsymbol{q}}} \frac{\partial N_{\boldsymbol{q}}}{\partial T}(T_L) \right] (T_c - T_L) \tag{1.5}$$

It is tempting to identify the term in brackets with the thermalization coefficient defined earlier. However, this term is a complex function of the carrier and phonon distributions and, therefore, cannot be assumed to be constant.

1.3 State of the art of hot-carrier solar cells

In this section, we first provide a historical review of the concept of HCSC. Then, we describe the current state of research on this concept: promising materials have been investigated for the absorber and the energy-selective contacts, yet no convincing HCSC full device has been built.

1.3.1 History of the concept

Hot carriers The term *hot carrier* (or rather *hot electron*) was first introduced by Fröhlich in 1947 [Frohlich 1947]. At that time, Fröhlich was investigating dielectric discharge in insulators under large electric fields and proposed that electron temperature could be influenced by the applied electric field.

This concept was soon extended to semiconductors through the foundational work of Shockley [Shockley 1951]. Shockley, who was studying high-field transistors, observed that electron mobility was dependent on the electric field in such configurations. To explain this deviation from Ohm's Law, he introduced the idea that electron temperature could vary with the electric field. These considerations of mobility were central to the early years of hot-carrier studies, as exemplified by this early review [Koenig 1959].

After these founding years, the hot-carrier community grew bigger and started to tackle several different topics. The first one was the hunt for the *negative differential resistance* effect, which was effectively measured for the first time by Gunn in 1963 [Gunn 1963] and led to the development of the Gunn diode, a widely used electronic component. A second was the development of semiconductor lasers, which became effective in the late 60s [Holonyak 1997].

With the boom in electronics – particularly small-size and high-frequency transistors – understanding carrier dynamics in semiconductors became increasingly important. Carrier thermalization was indeed a limitation for transistor's operation frequency. This led to an abundant literature on carrier dynamics characterization using sub-picosecond spectroscopy techniques in the 1980s and 1990s. Most of this research focused on materials useful for electronic applications, such as silicon, germanium, GaAs and AlGaAs, and semiconductor lasers, such as InGaAsP alloys, which were used to emit light in the telecom band, especially at 1.3 and 1.55 µm [Othonos 1998]. This coincides with the time when Ross and Nozik proposed to take advantage of hot carriers in energy-conversion applications, and introduced the concept HCSC [Ross and Nozik 1982].

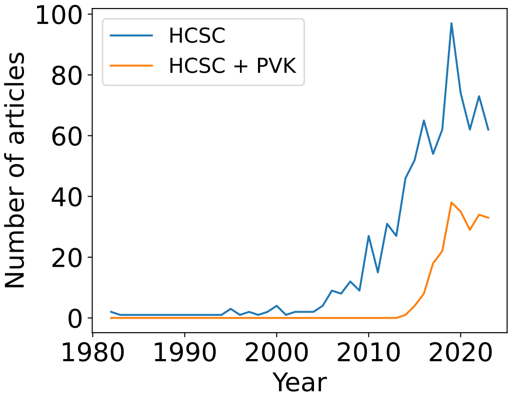

Figure 1.9: *Evolution of the number of publications mentioning "hot-carrier solar cell" in their abstract since the discovery of the concept (1982). Orange line indicates the number of articles mentioning also "perovskite". These results were obtained from a search in Web of Science database.*

Hot-carrier solar cells The concept of HCSCs was first described theoretically by analysing its energy-conversion efficiency [Ross and Nozik 1982]. Figure 1.9 shows the number of publications containing the words "hot-carrier solar cell" in their abstract since this original discovery.

In the 1980s and 1990s, a modest but steady number of articles were published each year. This is because most research efforts were focused on studying thermalization mechanisms in silicon, germanium, and III-V compounds rather than on constructing an actual HCSC. One of the most significant discoveries of this era was that III-V Quantum Wells (QWs) exhibit thermalization rates up to 100 times lower than their bulk counterparts [Pelouch *et al.* 1992, Rosenwaks *et al.* 1993]. During this period, Würfel proposed a completely different approach to describing HCSCs. While Ross and Nozik had extended the classical detailed balance model introduced by Shockley and Queisser in 1961, Würfel suggested examining a scenario with dominant impact ionization and Auger recombination processes [Wurfel 1997]. Surprisingly, he found that the limiting efficiency in this case (~ 85 % under full concentration) was very similar to the one predicted by the detailed balance model of Ross and Nozik (~ 86 % under full concentration).

The field started to expand after 2005 and the publication of the first book chapter on hot-carrier solar cells [Green 2003]. Some authors proposed to focus on phononic engineering to enhance the phonon bottleneck effect and thus reduce the thermalization rates in QWs [Guillemoles *et al.* 2005, Conibeer *et al.* 2008]. The notion of thermalization coefficient was proposed to characterize the ability of a given material to host hot-carrier effect in continuous regime [Guillemoles *et al.* 2005, Le Bris *et al.* 2012]. This period saw the publication of the first reviews on hot-carrier solar cells [König *et al.* 2010, Green *et al.* 2010].

In the early 2010s, the first experimental characterization of thermalization coefficients were performed, mostly in III-V materials [Le Bris *et al.* 2012, Hirst *et al.* 2014]. Simultaneously, several studies investigated the prerequisites in terms of material that would be necessary to build an actual HCSC [Takeda *et al.* 2010, Luque and Martí 2010, Feng *et al.* 2012, König *et al.* 2012], and the first experimental realization of a HCSC was reported [Dimmock *et al.* 2014]. Starting from 2014-2015, an increasing number of articles started to investigate perovskites for HCSCs, mostly with time-resolved techniques for the moment.

1.3.2 Components

Hot-carrier absorbers Hot carriers have been evidenced in various materials such as III-V materials [Shah and Leite 1969, Le Bris *et al.* 2012, Tedeschi *et al.* 2016], carbon nanotubes [Freitag *et al.* 2004], graphene [Gabor *et al.* 2011], MoS_2 [Nie *et al.* 2014], perovskites [Yang *et al.* 2016], silicon quantum dots [Zhang *et al.* 2016], etc. However, most of these investigations are performed with ultrafast spectroscopy techniques.

Most steady-state studies were performed on III-V materials, especially nanostructured ones [Conibeer *et al.* 2014]. A handful articles report steady-state hot-carrier characterization in perovskites [Fang *et al.* 2018, Papagiorgis *et al.* 2019, Lim *et al.* 2022, Sourabh *et al.* 2024], but the results are more difficult to interpret due to stability issues. Therefore we will focus our review on III-V materials.

III-V materials are good candidates for HCSC applications because of their stability and ability to absorb high excitation intensities without being damaged. In particular, different nanostructured III-V materials were tested for hot-carrier applications [Zhang *et al.* 2021], including QWs [Hirst *et al.* 2014, Rodiere *et al.* 2015, Whiteside *et al.* 2016, Esmaielpour *et al.* 2021a, Makhfudz *et al.* 2022], nanowires [Tedeschi *et al.* 2016, Limpert *et al.* 2017, Wang *et al.* 2021, Fast *et al.* 2021, Sandner *et al.* 2023] and quantum dots [Bremner *et al.* 2009, Harada *et al.* 2016, Behaghel *et al.* 2019]. Reported carrier temperature increase are typically $T - T_L \sim 100 - 200$ K at room temperature, although temperatures higher than 1000 K have been measured in InGaAsP QWs [Nguyen *et al.* 2018]. Most characterization of thermalization coefficients of III-V QWs yield estimates in the range $10 - 100$ $\mathrm{W.cm^{-2}.K^{-1}}$ [Le Bris *et al.* 2012, Esmaielpour *et al.* 2021b, Esmaielpour *et al.* 2021a], with an all-time low around 2 $\mathrm{W.cm^{-2}.K^{-1}}$ [Hirst *et al.* 2014]. These thermalization coefficients should be sufficiently low to build HCSCs exceeding the Shockley-Queisser limit, at least under full concentration [Le Bris *et al.*

2012].

The fact that nanostructures have such low thermalization coefficients seems to be linked to their phononic properties, although the exact mechanism remains elusive. Several authors reported that carrier-phonon interactions are reduced because confinement changes the phononic band structure and hence the carrier-phonon scattering rates [Riddoch and Ridley 1985, Sawaki 1986]. Other authors report that confinement may open phononic gaps which will reduce the LO phonons decay rates, and thus favor the appearance of a hot phonon bottleneck [Conibeer *et al.* 2008]. Finally, it was shown from numerical simulation that quantum confinement would lead to a reduction of carrier-phonon scattering rates even if confined phonons had the same band structure than in bulk [Makhfudz *et al.* 2022].

Energy-selective contacts In order to convert the temperature of hot carriers in the absorber into a voltage boost, it is necessary to extract the carriers via special contacts. Indeed, the carriers will necessarily thermalize quickly in the metallic electrodes. Therefore, HCSC contacts must ensure that the carriers convert their high temperature (kinetic energy) into potential energy before they reach the electrodes. In the ideal case, this process would happen without any heat losses, *i.e.* without entropy generation. This ideal case is called *isentropic* extraction [Wurfel 1997], and is analogous to Carnot cycles for ideal gases.

Systems having only one energy level were proposed to realize isentropic extraction [Wurfel 1997]. Indeed, in such single energy level systems, no scattering is possible and carrier thermalization is prohibited. Because such systems extract carriers at a given energy, they are usually called *energy-selective contacts*.

Resonant tunneling systems (either via a quantum well, quantum dots or defects states) were proposed as candidates for energy-selective contacts because of their peaked transmission function. For additional details on the architectures and materials used, refer for instance to the review proposed in [Gibelli 2016] (Section 4.E).

It has been pointed out that perfectly selective contacts may not have high enough electrical conductivity to allow a significant current to go through the device [Kirk and Fischetti 2012, Ferry *et al.* 2020]. However, several numerical simulations seem to disagree on that point. In particular, it was shown that extraction by a resonant tunnelling barrier made with a QW allowed to extract almost as much current as with a metallic contact [Cavassilas *et al.* 2022]. In addition, it was shown that the hypothesis of perfect selectivity is not essential and that semi-selective contacts would only lead to a ten-point reduction in efficiency [Le Bris and Guillemoles 2010].

In short, it seems that resonant tunneling systems and simple energy barriers are both suitable candidates for HCSCs energy-selective contacts.

1.3.3 Full devices

Although suitable candidate materials are known both for the hot-carrier absorber and the energy-selective contacts, very few attempts to build a full device are reported in literature. To the best of our knowledge, only four such attempts were reported, and are listed below by publication year:

- [Dimmock *et al.* 2014] designed a HCSC with a bulk GaAs absorber and a GaAs/AlAs double resonant tunneling barrier for the energy-selective contact. However, they reported "very small power conversion efficiency" and did not measure carrier temperature by continuous-wave PL spectroscopy.

- [Konovalov and Emelianov 2017] proposed a design with PbSe absorber and Zn-based semi-selective contacts. They measured an open-circuit voltage larger than the absorber bandgap under 500 suns illumination and attributed this effect to the presence of hot carriers, but they did not characterize carrier temperature with PL. Based on their reported JV characteristic, we estimated an efficiency of $\eta \simeq 0.07$ %.

- [Nguyen *et al.* 2018] proposed a design based on an InGaAsP/InGaAsP single QW absorber with InP barriers as semi-selective contacts. They reported hot-carrier temperatures as high as 1500 K and a device efficiency $\eta \simeq 11.6$ % at incident power equivalent to 50000 suns. To the best of our knowledge, this article is the only one that unambiguously demonstrate a voltage boost attributed to a hot-carrier effect.

- [Gong *et al.* 2024] reported a perovskite-based HCSC with phthalocyanines-based energy-selective contact for holes. They measured an efficiency of $\eta = 27.3$ % under 6 suns illumination. However, they did not measure carrier temperature by PL in steady-state, and even reported an *absence* of hot carriers in picosecond transient reflectivity measurements. Therefore the existence of hot carriers in their device remains elusive.

In conclusion, four HCSCs have been reported, and only one was unambiguously shown to host hot carriers [Nguyen *et al.* 2018]. This device still has underwhelming efficiency, well below the 30 % limit of Shockley-Queisser, and even further from the promises of HCSCs. Therefore it may be interesting to study how actual devices depart from the ideal assumptions that are usually made in HCSC models.

1.4 Towards non-ideal hot-carrier solar cells

In this section, we first review the non-idealities considered in literature. Then we introduce the original concept of *uneven temperatures*, which will be investigated throughout this manuscript.

1.4.1 Non-idealities already studied in literature

Several non-idealities have already been considered in HCSCs modeling.

First, a considerable amount of work regards non-ideal contacts. In particular, the fact that the contacts may not be perfectly energy-selective was investigated in [Le Bris and Guillemoles 2010]. The authors showed that semi-selective contacts would only lead to a ~ 10 points difference in final efficiency. Similarly, [Sharma *et al.* 2023] showed that a 45 % efficiency could be reached with semi-selective contacts and temperatures as low as 500 K in the absorber. [Marti *et al.* 2022] investigated thermoelectric properties of HCSC contacts and showed that perfectly selective contacts must have unrealistic thermoelectric properties to maintain extremely large efficiencies (above 80 %). Finally, some authors showed that the hypothesis of isentropic extraction implied vanishing power output, and proposed to study the impact of non-isentropic extraction on the HCSC performances [Limpert and Bremner 2015].

As far as the absorber is concerned, most of the work regards the modeling of finite thermalization rates via carrier-phonon interaction. Using a semi-phenomenological model for the thermalization rate, [Le Bris *et al.* 2012] showed that efficiencies higher than the Shockley-Queisser limit required $Q < 100$ W.cm^{-2}.K^{-1} under full concentration. [Tsai 2018] proposed a more rigorous derivation of the thermalized power from the Fermi Golden Rule, and integrated it numerically in the case of bulk GaAs absorbers. Some authors also studied the importance of carrier-carrier interactions to ensure fast equilibration of the system [Tsai 2019] and [Sharma 2023, chapter 4]. They concluded that Coulomb interaction was fast enough to ensure that carrier equilibration time was not a limiting parameter for HCSCs. Finally, it was shown that the role of Auger recombinations and impact ionization could not be neglected [Wurfel 1997], especially not in materials with bandgap smaller than 0.5 eV [Tsai 2019], although this does not seem to be detrimental to the operation of HCSCs.

1.4.2 Our original contribution: characterization and modelling of uneven temperatures in the absorber

An overlooked issue is that of transport of hot carriers *in* the absorber. As reminded in section 1.1.2, efficient transport is one of the keys to obtain high energy-conversion efficiencies. However, in hot-carrier absorbers, transport cannot be treated as in regular solar cells because of the presence of temperature gradients [Limpert *et al.* 2017]. Thermoelectric effects must be taken into account to describe hot-carrier transport. Surprisingly, this has never been addressed properly in the context of HCSCs.

In addition, HCSCs models usually assume that electrons and holes have the same temperature. As electrons and holes have very different effective masses in III-V materials (typically $m_h = 10\ m_e$), electrons receive about ten times more kinetic energy than holes when a photon is absorbed. Therefore, they may have significantly different temperatures. This had already been identified by Ross and Nozik in their founding paper, but they disregarded the effect:

> “Our formal model assumes that carriers in both bands are at the same T_H. As mentioned in the introduction, a real hot-carrier device is more likely to have one band – the one containing the majority carriers – fully thermalized, while the second band containing minority carriers is hot.” ([Ross and Nozik 1982])

In this manuscript, we will investigate both effects, and group them under the name *uneven temperatures*. They are represented schematically in Figure 1.10. We will be addressing the following questions:

- How can we characterize the existence of uneven temperatures?
- How do they affect the transport of carriers in HCSCs?
- In particular, how can the efficiency of HCSCs be affected by the presence of uneven temperatures?

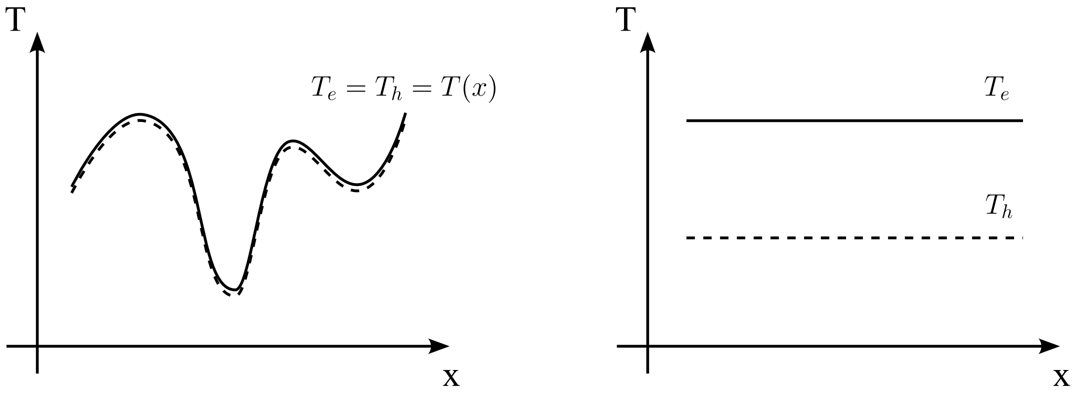

(a) (b)

Figure 1.10: *Schematic description of the situations of* uneven temperatures *studied in this manuscript. (a) Inhomogeneous temperatures in the absorber and (b) electrons and holes at different temperatures.*

1.5 Outline

We first introduce the methods used in this manuscript. We discuss the experimental methods in chapter 2, and emphasize on the determination of carrier temperature through continuous-wave PL spectroscopy. Then we discuss numerical methods in chapter 3 by defining the HCSC model that we will extend in this manuscript.

In chapter 4, we introduce the question of hot-carrier thermoelectric transport. This situation corresponds to Figure 1.10a, when temperature is not uniform in the absorber. We propose a theoretical description of this transport in the ambipolar regime, and report an experimental characterization of the transport coefficients using continuous-wave PL hyperspectral imaging.

The characterization of different temperatures for electrons and holes (see Figure 1.10b) is discussed in chapter 5. We show that continuous-wave PL spectroscopy allows to determine both temperatures simultaneously. We apply this method to PL measurements of an InGaAsP QW, and report hole temperatures close to ambient, while electrons reach temperatures as high as 1000 K.

The question of the impact of such uneven temperatures on the operation of HCSCs is addressed in chapter 6. We propose a development of the HCSC model to accommodate different temperatures for electrons and holes. We show that HCSCs are not only resilient to uneven temperatures, but also that having one carrier type hotter than the other is *beneficial* for the efficiency of the device. We report a potential increase in efficiency of ~ 2 points in the best case scenario.

We end this manuscript in chapter 7 with a short digression on the characterization of *cold* carriers. We investigate cooling properties of asymmetric double barrier heterostructures, and show their similarities with HCSCs selective extraction.

Chapter 2

Experimental toolbox: characterization of hot carriers by photoluminescence

As explained in the introduction, a Hot-Carrier Solar Cell (HCSC) is composed of an absorber and energy-selective contacts. In this manuscript, we will be focusing on the characterization and modelling of hot-carrier absorbers. The characterization of a hot-carrier absorber means the determination of its ability to host hot-carrier effect. In other words, we are interested in determining the carrier temperature reached in a given material. Since the temperature depends on excitation conditions, we will make sure to always report the temperature *for a given input (absorbed) power*.

Photoluminescence (PL) has proven to offer a powerful platform to characterize materials for solar cells in general, and hot-carrier absorbers in particular. Continuous-wave PL is particularly interesting in the context of photovoltaic absorbers, because it allows for the investigation of these systems properties in conditions close to their final purpose. In addition, it is a contactless measurement and therefore it can be used at early stages of the HCSC research, before the contacts are even created. Finally, PL is a versatile technique which allows to explore a vast combination of excitation wavelength and power.

In this chapter, we introduce the tools that will be used throughout this manuscript. First, we present the equation governing the emission of light by a semiconductor, the so-called Generalized Planck Law (GPL) (section 2.1). We emphasize the description of the absorptivity, which is at the core of hot-carrier characterization. Second, we describe the spectroscopy equipment, and in particular the hyperspectral imager that will be used in this work in section 2.2. We highlight few experimental developments conducted during this PhD. Third, we benchmark several methods commonly used to analyse carrier temperature from continuous-wave PL (section 2.3). Finally, we present in details the sample 5006 (InGaAsP single Quantum Well (QW)) which will be used for most PL experiments reported in this manuscript (section 2.4).

Table of contents

2.1 Theoretical description of photoluminescence

In this manuscript, we will often consider that electrons and holes follow distributions with different temperatures and chemical potentials. Therefore, in this section, we introduce the tools necessary to describe this case. We first present energy conventions adapted to a symmetrical treatment of electrons and holes. Then we introduce the parabolic band approximation that we will use in the entire manuscript. Third, following the main lines of [Wurfel 1982] and [Gibelli *et al.* 2016b], we derive the celebrated GPL in the two-temperature situation. Finally, we emphasize on the description of the absorptivity in III-V nanostructures.

2.1.1 Electrons, holes and energy conventions

PL involves states in both the conduction and the valence band. When a photon is absorbed, an electron in the valence band is promoted to the valence band. In this manuscript, we will describe the absence of electrons in the valence band as *holes*, as is usually done in semiconductors community. In this language, the absorption of a photon leads to the creation of an electron-hole pair of the same energy.

By definition, a hole has opposite charge ($+e$), momentum and energy to the corresponding electron in the valence band. As a consequence, hole electrochemical potential is the opposite of the electrochemical potential of electrons in the valence band, namely $\tilde{\mu}_h = -\tilde{\mu}_{e,V}$. This formalism can be understood graphically as a reversal of the energy axis when holes are considered, as presented in Figure 2.1. Using this reversed energy axis is not very common in semiconductors community, but it allows to express all holes properties with the usual tools of statistical physics, without having to introduce arbitrary signs in the equations. For instance, carrier distributions write

$$\begin{cases} f_e(E_e) = \left[\exp\left(\dfrac{E_e - \tilde{\mu}_e}{k_B T_e}\right) - 1\right]^{-1} \\ f_h(E_h) = \left[\exp\left(\dfrac{E_h - \tilde{\mu}_h}{k_B T_h}\right) - 1\right]^{-1} \end{cases} \tag{2.1}$$

where

k_B = Boltzmann constant ($k_B = 1.380 \times 10^{-23}$ J.K^{-1} $= 8.617 \times 10^{-5}$ eV.K^{-1})
T_i = The temperature of carrier i.
$\tilde{\mu}_i$ = The electrochemical potential of carrier i.

Because electrons and holes will be treated with equal importance in this manuscript, we chose to set the energy reference in the middle of the bandgap. This is represented schematically in Figure 2.1. We are fully aware that those notations are not the most common ones in semiconductors community, but they have been introduced before in the context of hot-carrier PL [Wurfel 1982, Gibelli *et al.* 2016a].

Note that we write $\tilde{\mu}_i$ the electrochemical potential of carrier i and μ_i its chemical potential. Under an electrical potential V, we have that $\tilde{\mu}_i = \mu_i + q_i V$ with our conventions. By convention, we write $e \simeq 1.609 \times 10^{-19}$ C the elementary charge, and $q_i = \pm e$ the algebraic charge of carrier i, which is negative for electrons and positive for holes.

We will also denote by latin letter E_i the total (kinetic and potential) energy of carrier i, and by greek letter ϵ_i its kinetic energy only (particularly in chapter 4). With our notations, $E_i = \epsilon_i + E_g/2$ for both carriers. Note that the letter E without any subscript is used to denote the energy of a photon. Finally, we denote vectors in bold.

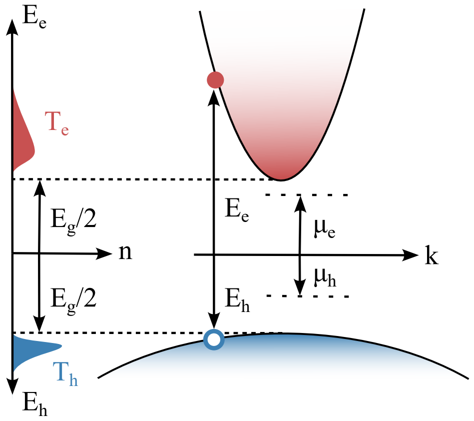

Figure 2.1: *Schematic representation of the energy conventions used in this manuscript. We represent the case of a semiconductor with parabolic bands under illumination. The band shown in red is called* conduction band, *while the band shown in blue is called* valence band. *Color gradients represent the occupation of each band. Carrier densities are represented on the vertical left axis. We represent here a case where holes are colder than electrons on purpose, as it will be discussed in chapter 5 and chapter 6. By convention, the energy axis is reversed of holes. This means that positive quantities for electrons are denoted by upwards arrows, while they are denoted by downwards arrows for holes.*

2.1.2 Parabolic band approximation

All systems studied in this manuscript are direct bandgap semiconductors studied at temperatures close to room temperature ($T < 1000$ K). Therefore, it is reasonable to use the *parabolic band approximation* to describe their properties. In this approximation, we assume that the dispersion relation in each band is given by the following parabolic relation, which is illustrated in Figure 2.1

$$E_i(\boldsymbol{k}_i) = \frac{E_g}{2} + \frac{\hbar^2 \boldsymbol{k}_i^2}{2m_i} \tag{2.2}$$

where

E_g = The bandgap of the absorber, such that $E_g/2$ is the band-edge for band i (see Figure 2.1.
$\boldsymbol{k}_i$ = The wavevector considered.
$m_i = \hbar^2 \left(\frac{\partial^2 E_i}{\partial k_i^2}\right)^{-1}$ the so-called effective mass of band i, which is assumed to be uniform in reciprocal space.

For such a system, energy and momentum conservation impose that when a photon of energy E is absorbed, it provides an energy E_e to the electrons and E_h to the holes,

where

$$\begin{cases} E_e = \dfrac{E_g}{2} + (1-\xi)(E - E_g) \\ E_h = \dfrac{E_g}{2} + \xi(E - E_g) \end{cases} \tag{2.3}$$

with $\xi = \dfrac{m_e}{m_e + m_h}$ is the *effective mass mismatch.*

Note how electrons and holes do not get the same fraction of the incident photon energy when they have different effective masses. This will be commented further in chapter 5 and chapter 6.

2.1.3 Generalized Planck Law of Photoluminescence

The theory of luminescence relates the properties of the radiation emitted by carriers recombination to the properties of the electronic distributions. In return, this theory provides a straightforward means to evaluate the electronic distributions by analyzing the radiation properties. To describe PL quantitatively, we need to study the different types of light-matter interactions. In this manuscript, we study only direct bandgap semiconductors, in which there are three fundamental light-matter interactions, illustrated in Figure 2.2:

1. Absorption: a photon of energy E is absorbed by the semiconductor. For this process to happen, an electron of the valence band is promoted in the conduction band (*i.e.* an electron-hole pair is created).

2. Stimulated emission: an incident photon of energy E provokes the recombination of an electron-hole pair, which duplicates the incident photon (same energy, same direction, same phase).

3. Spontaneous emission: an electron-hole pair recombines by emitting a photon in a random direction.

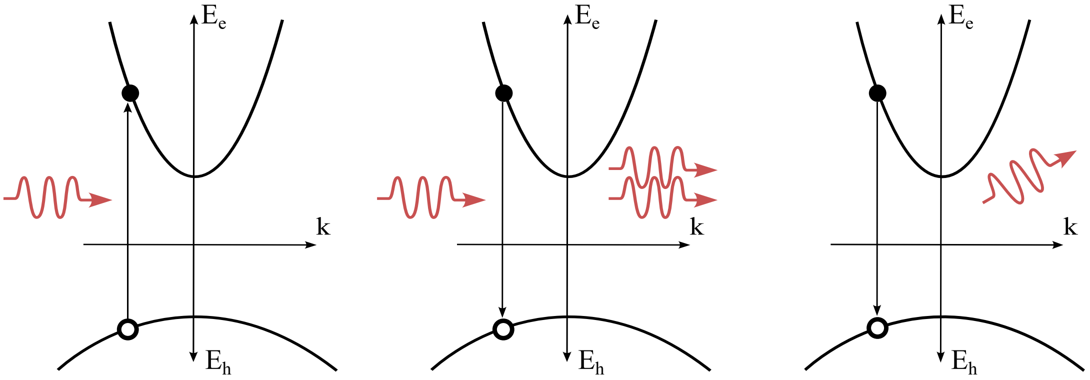

$R_\uparrow \propto n_\gamma(1-f_e)(1-f_h)$ $R_\downarrow \propto n_\gamma f_e f_h$ $R_{\text{sp}} \propto \rho_\gamma f_e f_h$

Figure 2.2: *Schematic representation of the three fundamental light-matter interactions. From left to right: absorption, stimulated emission and spontaneous emission. The transition probabilities are reported in italic.*

The term *photoluminescence* refers to the spontaneous emission of photons by a system excited by light. Therefore in the following we will focus on describing a composite system made of a semiconductor in interaction with surrounding photons.

Emission of light in an elementary volume of semiconductor Let us first describe the emission and absorption rates in an elementary volume of semiconductor dV. We make use of Fermi Golden Rule to describe the rates of the three different processes [van Roosbroeck and Shockley 1954, Lasher and Stern 1964, Wurfel 1982]. These rates are expressed here as a number of photons of a given energy E emitted per second and per unit volume, *i.e.* in s^{-1}.m^{-3}.J^{-1}.

$$R_{\uparrow}(E) = \frac{2\pi}{\hbar} n_{\gamma}(E) \left(\frac{L^3}{8\pi^3}\right)^2 \int d^3k_e d^3k_h \left|M_{eh}(\boldsymbol{k}_e, \boldsymbol{k}_h)\right|^2 \delta(E_e+E_h-E)(1-f_e(\boldsymbol{k}_e))(1-f_h(\boldsymbol{k}_h)) \tag{2.4}$$

$$R_{\downarrow}(E) = \frac{2\pi}{\hbar} n_{\gamma}(E) \left(\frac{L^3}{8\pi^3}\right)^2 \int d^3k_e d^3k_h \left|M_{eh}(\boldsymbol{k}_e, \boldsymbol{k}_h)\right|^2 \delta(E_e+E_h-E) f_e(\boldsymbol{k}_e) f_h(\boldsymbol{k}_h) \tag{2.5}$$

$$R_{\text{sp}}(E) = \frac{2\pi}{\hbar} \rho_{\gamma}(E) \left(\frac{L^3}{8\pi^3}\right)^2 \int d^3k_e d^3k_h \left|M_{eh}(\boldsymbol{k}_e, \boldsymbol{k}_h)\right|^2 \delta(E_e+E_h-E) f_e(\boldsymbol{k}_e) f_h(\boldsymbol{k}_h) \tag{2.6}$$

where

n_{γ} = The spectral density of photons at energy E (in m^{-3}.J^{-1}).
ρ_{γ} = $\frac{8\pi E^2}{h^3}(\frac{n_{\text{op}}}{c})^3$ the photon density of states (in m^{-3}.J^{-1}), which depends on the optical index n_{op}.
f_i = The occupation function of particle i as described in Equation (2.1).
E_i = The energy of particle i involved in the transition (see Equation (2.3)).
M_{eh} = $\langle \boldsymbol{k}_e | H | \boldsymbol{k}_h \rangle$ the matrix element coupling the state $\boldsymbol{k}_e$ (in the conduction band) and the state $\boldsymbol{k}_h$ (in the valence band).

We will not attempt to solve explicitly these equations. Instead, we will link these equations to the absorption coefficient $\alpha(E)$ of the system, which is much simpler to handle. The absorption coefficient translates the fact that photons have a certain probability of being absorbed when they travel through the volume dV of material. By definition,

$$\begin{aligned} R_{\downarrow} - R_{\uparrow} &= \alpha(E)\phi_{\gamma}(E) && (2.7) \\ &= \frac{2\pi}{\hbar} n_{\gamma}(E) \left(\frac{L^3}{8\pi^3}\right)^2 \int d^3k_e d^3k_h \left|M_{eh}\right|^2 \delta(E_e+E_h-E)(1-f_e-f_h) && (2.8) \end{aligned}$$

where $\phi_{\gamma} = cn_{\gamma}/n_{\text{op}}$ is the photon flux reaching volume dV, in s^{-1}.m^{-2}.J^{-1} (c is the speed of light in vacuum).

Note how the spontaneous emission rate resembles this expression.

$$R_{\text{sp}}(E) = \frac{2\pi}{\hbar} n_{\gamma}(E) \left(\frac{L^3}{8\pi^3}\right)^2 \int d^3k_e d^3k_h \left|M_{eh}\right|^2 \delta(E_e+E_h-E)(1-f_e-f_h) \times \frac{f_e f_h}{1-f_e-f_h} \tag{2.9}$$

The only difference is a term $f_e f_h/(1 - f_e - f_h)$ in the integral. When electrons and holes follow thermal distribution (possibly at different temperatures), this term writes

$$\frac{f_e f_h}{1 - f_e - f_h} = \frac{1}{\exp\left(\frac{E_e - \tilde{\mu}_e}{k_B T_e} + \frac{E_h - \tilde{\mu}_h}{k_B T_h}\right) - 1} \tag{2.10}$$

and therefore it depends only on the energy of the electrons and holes participating in the optical transition. Under the assumption of parabolic and isotropic bands, momentum conservation imposes that all electron (resp. holes) states participating in a transition at a given energy E have the same energy, $E_e(E)$ (resp. $E_h(E)$, see Figure 2.1). Therefore, this factor does not really depend on $\boldsymbol{k}_e$ and $\boldsymbol{k}_h$ and can be taken out of the integral. We thereby recover the Van Roosbroeck-Shockley equation, which links the spontaneous emission rate to the absorption coefficient (see Statement 2.1).

Statement 2.1. (Lasher-Stern equation)
Assuming (i) parabolic and isotropic bands for electrons and holes and (ii) thermal distribution of electrons and holes, the emission of light of an elementary volume of semiconductor is given by the Van Roosbroeck-Shockley, or Lasher-Stern equation [van Roosbroeck and Shockley 1954, Lasher and Stern 1964].

$$R_{\mathrm{sp}}(E) = \frac{8\pi E^2 n_{\mathrm{op}}^2}{h^3 c^2} \alpha(E) \frac{f_e f_h}{1 - f_h - f_e} \tag{2.11}$$

where R_{sp} is expressed $\mathrm{s}^{-1}.\mathrm{m}^{-3}.\mathrm{J}^{-1}$. Note that we never had to specify explicitly the matrix elements. Note also that α depends on carrier distributions inside the bands through *carrier-induced* effects such as Band Filling (BF) or bandgap renormalization [Bennett *et al.* 1990].

Toolbox 2.1. (Absorption coefficient for parabolic bands)
Let us compute an expression for the absorption coefficient. The absorption coefficient is defined by Equation (2.7), which can be rewritten as

$$\begin{aligned}\alpha(E) &= \frac{n_{\mathrm{op}}}{n_\gamma c}\left(R_\uparrow - R_\downarrow\right) \\ &= \frac{2\pi n_{\mathrm{op}}}{\hbar c}\left(\frac{L^3}{8\pi^3}\right)^2 \int d^3k_e d^3k_h \left|M_{eh}(\boldsymbol{k}_e, \boldsymbol{k}_h)\right|^2 \delta(E_e + E_h - E)(1 - f_e - f_h)\end{aligned} \tag{2.12}$$

This expression can be computed explicitly by assuming that (i) the matrix element simply imposes momentum conservation ($\boldsymbol{k}_e = \boldsymbol{k}_h$) and is otherwise the same for all states contributing to the transition at energy E ($M_{eh}(\boldsymbol{k}_e, \boldsymbol{k}_h) = M_{eh}(E)\delta(\boldsymbol{k}_e - \boldsymbol{k}_h)$) and (ii) assuming parabolic bands. In this case, the term $1 - f_e - f_h$ can be taken out of the integral, and we find

$$\alpha(E) \propto M_{eh}(E)(1 - f_e - f_h)(E - E_g)^{D/2-1} \tag{2.13}$$

where

$M_{eh}(E)$ = A matrix element that we will typically consider as a constant fitting parameter.
$1 - f_e - f_h$ = Represents the fact that states with non-negligible occupation function are less likely to absorb photons. This term is called Band Filling (BF) and will be instrumental in chapter 5.
D = the dimensionality of the absorber.

This formula means in particular that, for QWs as the one that will be studied in this manuscript (see section 2.4), the absorption coefficient should resemble a step-like function (one plateau per energy level in the QW).

Emission of light in a thick semiconductor The derivation above allowed us to compute the spontaneous emission rate of an elementary volume of material. To describe real systems, we need to integrate the relation above over a finite thickness d.

Photon conservation imposes that the photon flux follows

$$\boldsymbol{\nabla}.\boldsymbol{\phi}_\gamma(z) = \frac{\partial \phi_\gamma}{\partial z}(z) = R_{\text{sp}}(z) + R_\uparrow(z) - R_\downarrow(z) = R_{\text{sp}}(z) + \alpha(z) \times \phi_\gamma(z) \tag{2.14}$$

where ϕ_γ is expressed in $\text{s}^{-1}.\text{m}^{-2}.\text{J}^{-1}$.

Assuming that the material and the carrier densities are homogeneous, the absorption coefficient, the distribution functions and hence the spontaneous emission rate do not depend on z. Then we can integrate this equation and we obtain

$$\phi_\gamma(d^-) = (1 - \exp(-\alpha d))\,\frac{R_{\text{sp}}}{\alpha} = A(E)\frac{8\pi E^2 n_{\text{op}}^2}{h^3c^2}\frac{f_e f_h}{1 - f_e - f_h} \tag{2.15}$$

where we introduced $A(E) = 1 - \exp(-\alpha d)$ the *internal absorptivity* of the system.

Emission of light out of the semiconductor The previous expression was obtained *in* the semiconductor, right below the surface. But what we can really observe is the photon flux coming *out* of the system, which forms the PL signal. To compute this flux, we need to take into account the (energy-dependent) transmission $T(E)$ across the semiconductor-air interface and Snell-Descartes law of refraction. Let us consider the flux of photons j_γ (in $\text{s}^{-1}.\text{J}^{-1}$) coming from an elementary surface dS, in a direction Ω forming an angle θ with the normal to dS. Since the spontaneous emission is isotropic, we have that

$$j_\gamma(\Omega, E) = \frac{1}{4\pi}\phi_\gamma(d^+)\cos\theta dSd\Omega dE = \frac{T(E)}{4\pi}\phi_\gamma(d^-)\cos\theta' dSd\Omega' dE \tag{2.16}$$

And finally, writing the conservation of *etendue* at the interface ($\cos\theta d\Omega dS = n_{\text{op}}^2\cos\theta' d\Omega' dS$, see Figure 2.3), and replacing $\phi_\gamma(d^-)$ by its expression (Equation (2.15)), we find that

$$j_\gamma(\Omega, E) = T(E)A(E)\frac{2E^2}{h^3c^2}\frac{f_e f_h}{1 - f_e - f_h}\cos\theta dSd\Omega dE \tag{2.17}$$

where we introduced $T(E)$ the transmissivity of the interface, often written in terms of reflectivity $T(E) = 1 - R(E)$ or in terms of *external absorptivity* (*i.e.* the absorptivity as seen from the ambient air) $\mathcal{A}(E) = T(E)A(E)$.

This equation can be rewritten in terms of PL intensity

$$\phi_{\mathrm{PL}}(\Omega, E) \equiv \frac{j_\gamma(\Omega, E)}{\cos\theta dS d\Omega dE} = \frac{2E^2}{h^3c^2}\mathcal{A}(E)\frac{f_e f_h}{1 - f_e - f_h} \tag{2.18}$$

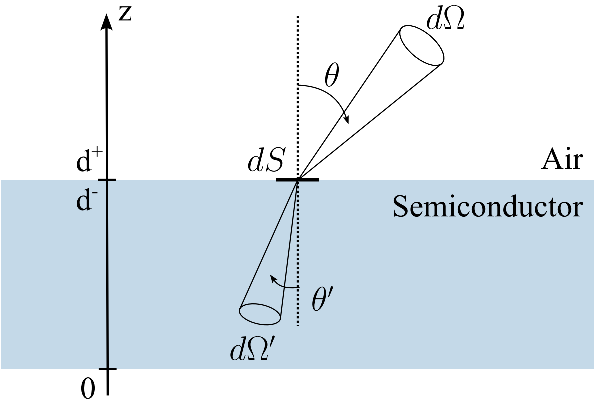

Figure 2.3: *Etendue conservation at a planar interface.*

Equation (2.18) is the main equation for PL emission that we will be using in this manuscript. As compared with Lasher-Stern equation (see Equation (2.11)), this one does not depend on the optical index of the material. Let us recall that it is derived assuming parabolic bands, thermal distribution of electrons and holes and homogeneous material. By taking additional assumptions on the temperature of electrons and holes, one may recover the isothermal GPL (see Statement 2.2), or its two-temperature variation that we will discuss further in chapter 6 and chapter 5.

Statement 2.2. (One-temperature Generalized Planck Law)
The emission of light by a layer of a homogeneous material is given by the Generalized Planck Law (GPL) [Wurfel 1982]. It derives directly from Equation (2.18) by assuming that electrons and holes have the same temperature T, which may however be different from the lattice temperature.

$$\phi_{\mathrm{PL}}(E) = \frac{2E^2}{h^3c^2}\mathcal{A}(E)\frac{1}{\exp\left(\dfrac{E - \Delta\mu}{k_B T}\right) - 1} \tag{2.19}$$

where

ϕ_{PL} = The photon flux emitted per unit of surface, energy and solid angle, expressed in $\mathrm{s}^{-1}.\mathrm{m}^{-2}.\mathrm{sr}^{-1}.\mathrm{J}^{-1}$

$\mathcal{A}$ = $(1 - R)A$ is the external absorptivity of the sample

$\Delta\mu = \tilde{\mu}_e + \tilde{\mu}_h = \mu_e + \mu_h$ is the QFLS, *i.e.* the difference between the chemical potential of electrons in the conduction and the valence band.

The GPL can be decomposed in two terms: the external absorptivity $\mathcal{A}(E)$ and a black-body like contribution characterized by a temperature and a QFLS.

The internal absorptivity depends on the optical indices of the material. As we will see in the following section, it is a tricky quantity that is difficult to quantify precisely. it is generally approximated with semi-phenomenological model

2.1.4 Detailed description of the absorptivity

In this section, we propose to discuss several properties of the absorptivity that are relevant for hot-carrier absorbers, and in particular III-V nanostructures. First, we discuss microscopical effects on the absorption coefficient. Then, we describe how the absorptivity can be computed from the absorption coefficient in complex materials. Finally, we propose two experimental methods to determine the absorptivity of a given sample.

Toolbox 2.2. (Notations for the absorptivity)
In this chapter, we use several quantities related to the absorptivity. Here is a comprehensive list of our notations and definitions.

$\alpha(E)$ = Absorption coefficient, in m^{-1}. The probability that a photon of energy E is absorbed between z and $z + dz$ is given by $\alpha(E)dz$. For an absorbing material, $\alpha(E) > 0$. However, in emitting materials such as highly excited semiconductors (in a strong regime of BF), it is possible that $\alpha(E) < 0$.

$A(E)$ = *Internal* absorptivity of a thick sample (dimensionless). It corresponds to the probability that a photon is absorbed as it passes through the whole sample. A is obtained by integrating α over the trajectory of a photon. By definition, $0 \leq A(E) \leq 1$.

$R(E)$ = Reflectivity of a sample. It corresponds to the probability that a photon coming from the material is reflected at the interface with the exterior. Symmetrically, it also corresponds to the probability that an external photon is reflected at the interface with the semiconductor. By definition, $0 \leq R(E) \leq 1$.

$\mathcal{A}(E) = (1 - R(E))A(E)$ is the *external* absorptivity of the sample. It corresponds to the probability that an external photon is absorbed in the material.

Absorption coefficient We have presented a model for ideal absorption coefficient in Toolbox 2.1. This crude model is usually not precise enough to reproduce real absorption coefficients. In particular it is common to observe the following effects in hot-carrier absorbers and in experimental conditions relevant for hot-carrier generation:

1. **Sub-bandgap absorption and broadening.** In real systems, the absorption coefficient does not abruptly drop to 0 below the bandgap. A smoother decrease is usually observed, sometimes referred to as *Urbach tail*. This sub-bandgap absorption can be explained by various phenomena: disorder at the interatomic level [Sritrakool *et al.* 1986], heavy doping [Kane 1963], photon-assisted tunneling (Franz-Keldysh

effect) [Fox 2010], etc. A comprehensive phenomenological expression to reproduce a vast class of sub-bandgap phenomena was proposed by [Katahara and Hillhouse 2014] and relies on the convolution of an ideal absorption coefficient by a smoothing function. Similarly, all transitions that should be abrupt in theory are in practice smoothed by temperature and/or phonon effects (e.g. different energy levels in a QW).

2. **Excitons.** In QWs, exciton absorption can be non-negligible even at room temperature [Chemla 1985]. Excitons are quasiparticles coming from the electrostatic interaction between electrons and holes. Because of the attractive interaction by Coulomb potential, bound states with energy lower than the bandgap ($E_{x,n} = E_g - R_y/n^2$ with R_y the Rydberg energy) are created and may contribute to the absorption coefficient [Chuang 2012]. Exciton absorption may be described as additional gaussian peaks centered around the exciton energies $E_{x,n}$. Because Coulomb potential will also affect the free carrier wavefunctions, free carrier absorption in the presence of excitons will be modified by the so-called *Sommerfeld enhancement factor* (see section 2.4.3).

3. **Lattice heating.** To generate hot carriers, we need intense optical excitation. At these high excitation powers, it is common to heat not only the carriers but also the lattice. In most III-V samples, lattice heating translates into a bandgap decrease (so-called *red-shift*) [Varshni 1967]. The fact that the bandgap depends on lattice temperature allows us to monitor the lattice temperature when we conduct hot-carrier experiments. See section 2.3.6 for details.

4. **Bandgap renormalization.** One last important effect at large carrier concentrations is bandgap renormalization (or bandgap shrinkage). When electrons or holes become degenerate and the occupation of the energy levels close to the bottom of the bands is non negligible, Coulomb repulsion between carriers produces a decrease of the effective band edge energy. In GaAs, this effect results in a decrease of the effective bandgap $\Delta E_g \sim 10-40$ meV at carrier concentrations $n \sim 10^{17}-10^{19}$ cm^{-3} [Bennett *et al.* 1990].

Note that this list is by no means exhaustive. Additional effects, such as free carrier absorption or the inclusion of light and heavy hole bands, could be discussed depending on the material, the experimental conditions, etc.

Absorptivity To study PL emission, one needs to determine the absorptivity of a sample, and not only its absorption coefficient. For a thick layer of homogeneous material and assuming that the absorptivity is constant in the layer, these two quantities are linked by Beer-Lambert law

$$A(E) = 1 - \exp(-\alpha d) \tag{2.20}$$

However, when studying materials composed of several layers such as QWs, Beer-Lambert law is not sufficient. Different solutions exist to treat the emission of a multilayer.

1. **Single-pass reabsorption model.** In this approach, internal reflections are completely neglected, and we take into account only the reabsorption of emitted light as it propagates through the successive layers. This can be justified in stacks composed of alloys with similar compositions, for which the optical indices varies only

weakly from layer to layer. This case is illustrated in Figure 2.4 and in [Nguyen *et al.* 2018]. In this manuscript, we will exclusively use this approach because it provides a convenient analytical form for the absorptivity of the stack as a function of the absorptivity of each layer. See Equation (2.29).

2. **Transfer matrix method (TMM).** This second approach includes reflections at each interface, but is valid only for stacks with planar interfaces. If the optical indices of all materials are known, one can solve Maxwell continuity equations and compute the electric field at every position in the stack. This method allows to simulate optical resonances in the stack, which can be very important in nanostructured III-V materials [Limpert *et al.* 2017]. However, finding the optical indices of each layer can prove difficult for non-standard materials. In addition, carrier-induced effects such as band-filling, bandgap renormalization, etc are often not implemented in TMM codes. For this reason, TMM was not used in this manuscript, although it could be very relevant to study QW stacks.

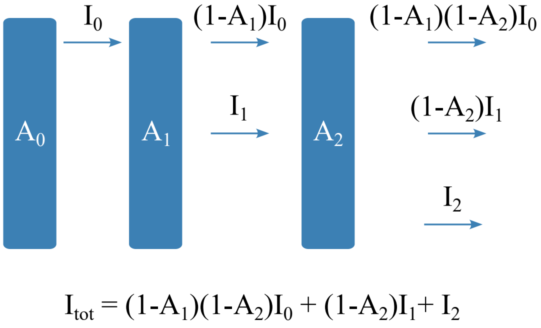

Figure 2.4: *Illustration of the single-pass reabsorption model in the case of a trilayer.*

Measurement The standard technique to measure the *internal* absorptivity of a given sample is *reflection/transmission spectroscopy.* It consist in illuminating a sample with a white lamp of known spectrum, and measuring the reflection and transmission probabilities at all photon energies. From there, one can compute the absorptivity as

$$A(E) = 1 - R(E) - T(E) \tag{2.21}$$

Note that in this formula, T is the transmissivity of the sample but R is the reflectivity of the interface.

In photovoltaic community, it is common to measure the *external* absorptivity through External Quantum Efficiency (EQE) measurement, also called Photocurrent Spectroscopy. EQE is a photo-electrical measurement which requires that the sample has electrical contacts. It consists in collecting the charges photogenerated with a monochromatic light of varying photon energy. The EQE spectrum represents the ratio between the number of collected charges and the number of photons sent on the sample. Therefore,

$$EQE(E) = \mathcal{A}(E)P_C(E) = (1 - R(E))A(E)P_C(E) \tag{2.22}$$

where P_C is the collection probability, *i.e.* the probability that a photogenerated electron-hole pair is collected in the contacts. For optimized photovoltaic devices, we assume that $P_C = 1$, such that the EQE spectrum is equal to the external absorptivity spectrum.

2.2 Spectroscopy equipments and hyperspectral imager

The main experimental platform used to measure PL spectra in this manuscript is a Hyperspectral Imager (HI). It is a special kind of spectrometer capable of *imaging* the surface of the sample with a spectral resolution. In short, it measures images of the sample surface at different wavelengths. A schematic representation of the HI is provided on Figure 2.5a. An example of HI data (called a PL cube) is shown on Figure 2.5b.

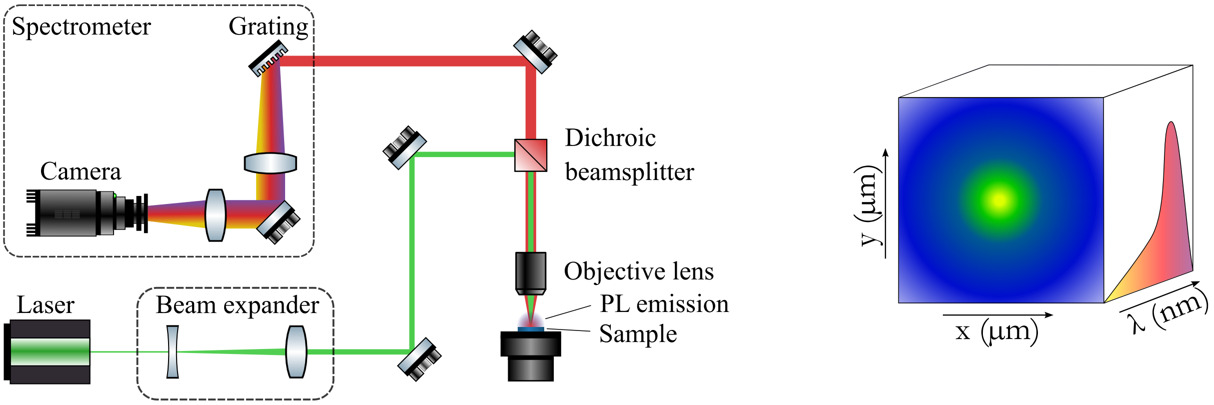

(a) (b)

Figure 2.5: *(a) Schematic representation of the HI used to generate the PL measurements in this manuscript. (b) Typical output of the HI, called a "cube" since it contains two dimensions of spatial information and one dimension of spectral information.*

Spatial resolution is interesting for hot-carrier characterization because it allows to select spatial regions that are more likely to exhibit strong hot-carrier properties. For instance, in point illumination, spectra emitted at the center of the laser excitation receive more energy than those at the edge of the laser spot, and therefore they will be hotter. In addition, HI acquisitions allow to measure carrier diffusion and characterize hot-carrier transport properties, as will be shown in chapter 4.

The HI used in this manuscript is a NIR HI produced by PhotonEtc. It is equiped with an InGaAs camera (NIRvana 640, produced by PrincetonInstruments) with a measurement range 900 − 1600 nm. We used this HI with a ×50 apochromatic objective lens produced by Mitutoyo. The laser source is a 980 nm monomode laser produced by Aerodiode with nominal power 700 mW. We replaced the dichroic beamsplitter of Figure 2.5a by the combination of a BSW26R 50:50 beamsplitter and a FELH1050 long-pass filter, both from Thorlabs. This setup has a spectral resolution of 2 nm. In combination with the objective lens described above, its spatial resolution (sparrow criterion) imposed by diffraction is 1.7 µm.

The InGaAs camera presented here is characterized by a gaussian dark noise with offset of $\sim 10^4$ counts and standard deviation $\sigma \sim 10^2$ counts (see Figure 2.6). Its dynamical range is $2^{16} = 65536$ counts. Therefore, the maximum Signal to Noise Ratio (SNR) of this camera is $(2^{16} - 10^4)/10^2 \simeq 550$.

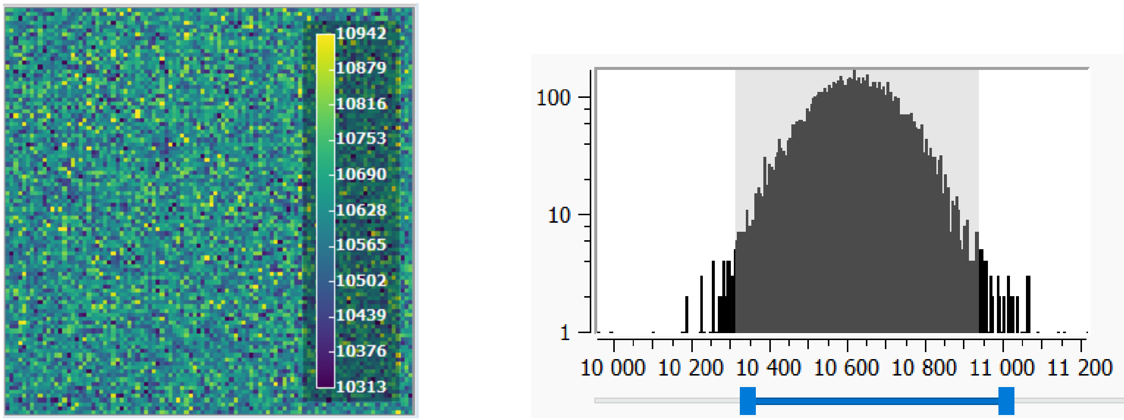

(a)

(b)

Figure 2.6: *(a) Example of a dark acquisition with the NIR HI. Scale is in counts. (b) Histogram of this image.*

During this PhD, we conducted several improvements of the HI setups, which are reported in the sections below. In addition, I wrote a user manual for IPVF HIs that is now used to train new users.

2.2.1 Control of the excitation size

In order to study carrier diffusion with our HI, we tried to reduce the size of the laser spot as much as possible. First, we used an achromatic objective lens (Mitutoyo APO NIR x50 0.41 NA) to avoid chromatic aberration and make sure that PL emission and laser excitation were focused into the same focal plane. Then, we used a beam expander composed of two converging lenses to control the size, divergence and shape of this laser beam. Finally, we acquired a new 980 nm monomode laser (Aerodiode CCSI, 700 mW), which can be focused to a smaller spot size as compared with multimode lasers. We managed to obtain a Gaussian profile of radius 1.6 µm at 2σ (see Figure 2.7a). Achieving such a small laser spot, we could measure a sizeable difference between the laser spot size and the PL spot size, as reported in Figure 2.7c. This indicates that we are in a regime where carrier diffusion is measurable.

2.2.2 High Dynamical Range method

As shown in Figure 2.6, the infrared camera used in our experiments has a rather low SNR due to large dark noise. Therefore we developed a High Dynamical Range (HDR) method to increase the SNR. HDR is very common in photography, and consists of acquiring several images at different exposure times. These images are then stitched together to keep only the correctly exposed parts of each one. This algorithm is embedded in most modern cameras.

The HDR method for hyperspectral cubes relies on the same principle. We first acquire an initial cube by choosing an exposure time that does not saturate the sensor. Then, we acquire several successive cubes by doubling the exposure time each time. This reveals

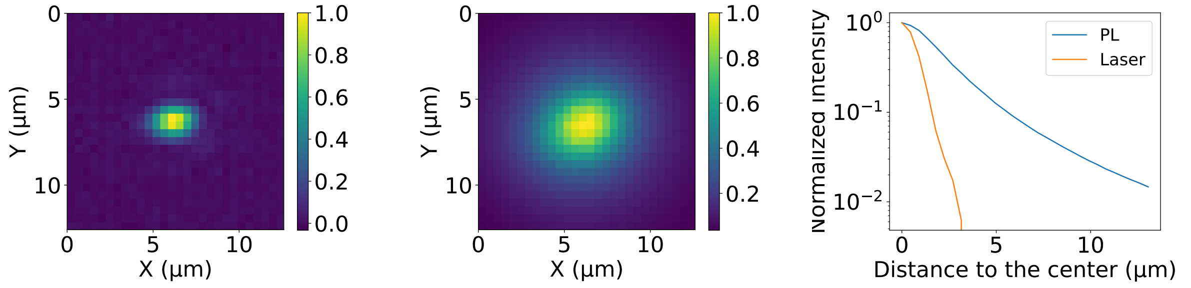

(a) (b) (c)

Figure 2.7: *Characterization of the illumination profiles obtained in point illumination configuration. (a) Laser, (b) integrated PL, (c) comparison between laser and PL profiles.*

underexposed parts of the initial cube. Once all cubes are acquired, we merge them by keeping only "correctly exposed" points of each acquisition. The result of such a procedure significantly increases signal over noise ratio, as can be seen on Figure 2.8.

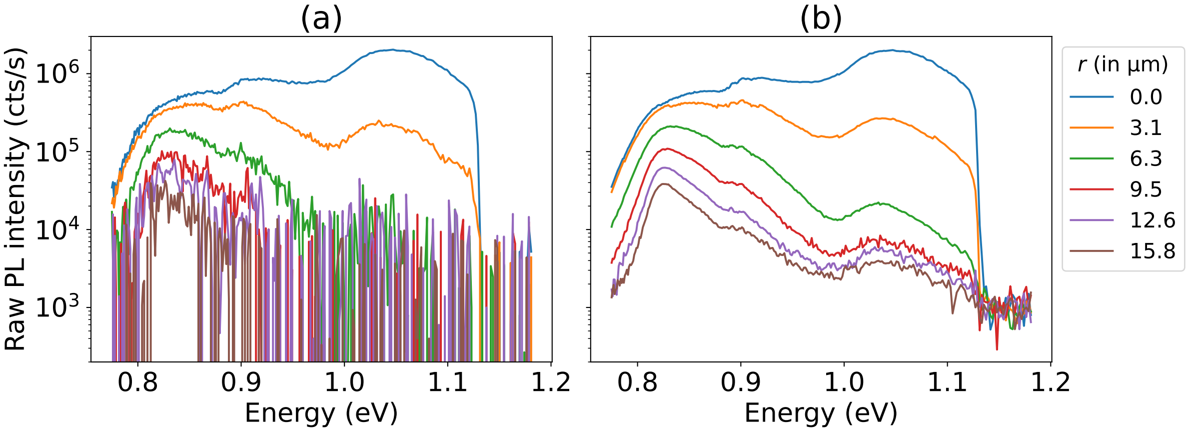

Figure 2.8: *Raw PL spectra acquired in point illumination at different distances from the laser spot. (a) Without and (b) with HDR technique.*

2.2.3 Absolute calibration

Calibration is a way to extract *configuration-invariant* photoluminescence spectra from configuration-dependent acquisitions. After proper calibration, the spectrum should no longer depend on the specific configuration (filters, exposure time, camera, optics, etc.) in which it was measured. One of the strength of IPVF HIs at IPVF is that they can easily be *absolutely calibrated*. This means that we can access the absolute value of the PL spectra, in $s^{-1}.m^{-2}.sr^{-1}.J^{-1}$, rather than the "arbitrary units" usually employed in the literature. This is particularly useful to measure precisely the QFLS (and/or the carrier density).

Some details of the calibration procedure and of this code are presented in Appendix D. Part of the experimental effort of this PhD was spent in improving this calibration procedure. First, we proposed to replace the old procedure with a new one, with fewer steps, for which we submitted a *"Déclaration d'Invention"*. Second, I developed a user-friendly calibration code that is now used by all HI users.

2.3 Carrier temperature measurement from photoluminescence spectra

Several methods are known and used in the literature to extract carrier temperature from a PL spectrum [Esmaielpour *et al.* 2022]. Choosing one or the other relies on a tradeoff between complexity and accuracy. Usually, we first run a quick analysis using either high-energy linear fit (section 2.3.1) or Photoluminescence Ratio (PLR) (section 2.3.2). Then, if the results look promising, we move to Photoluminescence Ratio with Band Filling (PLRBF) (section 2.3.3) or full fit (section 2.3.4).

2.3.1 High-Energy Linear Fit

High-energy linear fit is the historical method to determine carrier temperature. It was first proposed in [Shah and Leite 1969] to study photo-induced hot-carrier effect in a GaAs sample placed in a helium bath at 2 K.

This method relies on the assumption that the absorptivity saturates at high energy: $\mathcal{A}(E) = \mathcal{A}_0$ for E sufficiently large. In this range, and provided that $E \gg \Delta\mu$, the GPL (Equation (2.19)) can be rewritten as

$$\ln\left(\frac{h^3c^2 I_{PL}(E)}{2E^2}\right) = -\frac{E}{k_BT} + \frac{\Delta\mu}{k_BT} + \ln(\mathcal{A}_0) \tag{2.23}$$

In this case, the PL spectrum has an exponential behavior, whose slope is controlled by the carrier temperature T (see Figure 2.9a). This equation can be fitted by ordinary least square to obtain the temperature. Note that it is technically possible to measure also the QFLS $\Delta\mu$, provided that the calibration is absolute and that $\mathcal{A}_0$ is known.

Advantages

- With this method, temperature is measured independently from the QFLS. Therefore, absolute calibration is not mandatory. Only the relative calibration is necessary to estimate the temperature.
- For conventional photovoltaic absorbers, which are optimized to have large absorption coefficients, this method is usually accurate since $\mathcal{A} \gtrsim 0.95$ will have little to no variations for $E > E_g$.
- This method runs very quickly with ordinary least squares, and can be applied to a large number of PL spectra. For instance, it could be run on a HI cube containing 1000 × 1000 spectra in a fraction of a second.

Limitations

- Typical hot-carrier absorbers are low-dimensional III-V materials, which tend to have low absorptivity. In this case, the assumption of constant absorptivity is rarely met. For instance, the absorptivity of a QW is expected to be a step-like function with several plateaus, such that it may be tricky to find a region of constant absorptivity.
- In addition, due to their low density of states, such low-dimensional materials will exhibit saturation effects such as BF. This effect changes the slope of the spectrum, and can be mistaken as a temperature increase if we use high-energy linear fit. Similarly, at the high excitation rates necessary to produce hot carriers, the assumption that we can find a window where $E \gg \Delta\mu$ may not hold. See for instance the results in chapter 4 and chapter 5.
- At high energy, the PL signal is usually weak and the SNR is low. This changes the observed slope, and may result in an overestimate of the temperature. See for instance the slope for $E > 1.05$ eV in Figure 2.8b.

2.3.2 Photoluminescence Ratio

PLR is another simple fitting method which relies on a completely different assumption than high-energy linear fit. For this method, we acquire several PL spectra at increasing excitation powers ($I_{PL}^{(1)}, ..., I_{PL}^{(N)}$) and assume that the absorptivity of the sample does not depend on the excitation power.

In this case, the ratio between $I_{PL}^{(i)}$ and $I_{PL}^{(1)}$ has a simple expression. For $E \gg \Delta\mu$,

$$\begin{aligned}\ln\left(\frac{I_{PL}^{(i)}}{I_{PL}^{(1)}}(E)\right) &= \frac{\dfrac{2E^2}{h^3c^2}\mathcal{A}^{(i)}(E)\exp\left(-\dfrac{E-\Delta\mu^{(i)}}{k_BT^{(i)}}\right)}{\dfrac{2E^2}{h^3c^2}\mathcal{A}^{(1)}(E)\exp\left(-\dfrac{E-\Delta\mu^{(1)}}{k_BT^{(1)}}\right)} \\ &= -\frac{E}{k_B}\times\left(\frac{1}{T^{(i)}}-\frac{1}{T^{(1)}}\right)+\frac{\Delta\mu^{(i)}}{k_BT^{(i)}}-\frac{\Delta\mu^{(1)}}{k_BT^{(1)}} \qquad (2.24)\end{aligned}$$

In this case, the PLR has an exponential behavior, whose slope is controlled by the difference between the carrier temperature $T^{(i)}$ and the reference temperature $T^{(1)}$. Therefore, if the reference spectrum was recorded at sufficiently low excitation power, then $T^{(1)}$ is equal to the lattice temperature T_L and it is possible to measure the temperature of all the spectra.

This equation can be fitted by ordinary least square method to obtain the temperature. It is also possible to measure the QFLS $\Delta\mu^{(i)}$, provided that the reference QFLS is known.

Advantages

- This method relies on a less restrictive assumption than high-energy linear fit.
- PLR allows to determine carrier temperature independently from QFLS and therefore absolute calibration is not necessary. In fact, if temperature is the only variable of interest, then it is not necessary to calibrate the spectrometer at all, as the division by a reference spectrum of known temperature acts as some sort of calibration.

- Similarly to high-energy linear fit, this method requires little computational power and can be applied to millions of spectra in a fraction of a second.

Limitations

- The assumption that the absorptivity is independent of the excitation power can be disrupted by many so-called *power-dependent effects*, among which: lattice heating, BF, bandgap renormalization, etc (see section 2.1.4).
- Similarly to high-energy linear fit, the assumption that $E \gg \Delta\mu$ may not hold at high excitation powers.

2.3.3 Photoluminescence Ratio with Band Filling

PLRBF is an attempt to push the limits of validity of PLR. Since we usually need high excitation powers to generate hot carriers, we often probe regimes where BF cannot be neglected anymore. The effect of BF is to reduce the absorption coefficient close to the gap, which disrupts the assumptions of both high-energy linear fit and PLR. As shown in Figure 5.1b, the effect of BF becomes significant when $\Delta\mu \gtrsim E_g - 5k_BT$.

BF can be described as a modulation of the absorption coefficient $\alpha(E,T,\Delta\mu) = \alpha_0(E) \times BF(E,T,\Delta\mu)$ (see Equation (2.7), [Bennett *et al.* 1990]). We do not know the shape of α_0 *a priori*, but this problem disappears under the assumption that the absorptivity is low. In the low absorptivity regime, $A(E,T,\Delta\mu) = 1 - \exp(-\alpha(E)d) \simeq \alpha(E,T,\Delta\mu)d$. Therefore,

$$\begin{aligned}\frac{I_{PL}^{(i)}}{I_{PL}^{(1)}}(E) &= \frac{A_{ext}^{(i)}}{A_{ext}^{(1)}} \times \frac{\left[\exp\dfrac{E-\Delta\mu^{(i)}}{k_BT^{(i)}} - 1\right]^{-1}}{\left[\exp\dfrac{E-\Delta\mu^{(1)}}{k_BT^{(1)}} - 1\right]^{-1}} \\ &= \frac{BF(E,T^{(i)},\Delta\mu^{(i)})}{BF(E,T^{(1)},\Delta\mu^{(1)})} \times \frac{\left[\exp\dfrac{E-\Delta\mu^{(i)}}{k_BT^{(i)}} - 1\right]^{-1}}{\left[\exp\dfrac{E-\Delta\mu^{(1)}}{k_BT^{(1)}} - 1\right]^{-1}}\end{aligned} \tag{2.25}$$

Advantages

- Because this method takes into account the effect of BF, it allows to determine the temperature of degenerate systems.

Limitations

- This method assumes that the only power-dependent effect is BF. Thus it does not allow to describe other common effects such as lattice heating, bandgap renormalization, etc.
- Since Equation (2.25) is not linear, this method does not allow to estimate the temperature independently from the QFLS. This has two implications. (i) If the

reference QFLS is unknown, the system is overparametrized and it will be difficult to measure the temperature with a good accuracy. Therefore, knowning the reference QFLS is recommended, which requires absolute calibration, as well as an estimate of α_0. (ii) Because convergence towards the global minimum is not ensured in solving non-linear systems, it is safer to rely on a global search algorithm such as *differential evolution* [Storn 1997]. However, this is much more computationally intensive than the two previous methods, and therefore it is difficult to treat large datasets with this technique.

2.3.4 Full fit

Full fit refers to techniques where the absorptivity is modeled in the entire range of PL emission. With full fit, we try to reproduce the entire PL spectrum, and not only a restricted energy interval.

There are many different ways of performing a full fit, which are based on different ways of estimating or modelling the absorptivity.

1. The absorptivity can be simply *measured* (see section 2.1.4). In this case it will be used as an input in the GPL and the temperature will be deduced solely from the blackbody-like contribution. Such an approach is valid only if there are no power-dependent effects affecting the absorptivity.

2. Alternatively, it can be possible to *compute* the absorptivity. This can be done from scratch with a quantum mechanical model such as k.p theory [Tomic *et al.* 2003]. Or, if the optical indices of the materials are known, it is possible to apply a transfer matrix method to compute the absorptivity [Heavens 1960]. Depending on the kind of model used, including power-dependent effects will be more or less easy.

3. The approach that we will develop in this manuscript consists in building a *phenomenological model* that includes all the effects necessary to explain the PL spectra shape and its variation with excitation power. Elements that one can include in such a model have already been discussed in section 2.1.4. We will present a concrete example in section 2.4.3.

From now on in this manuscript, the term *full fit* will refer to the last approach.

Advantages

- Full fit analysis allows to describe any power-dependent phenomenon. Therefore this technique is applicable to any type of sample provided that we can build an appropriate absorptivity model.

- Full fit is particularly well suited to describe nanostructures, where power-dependent effects such as BF and linewidth broadening are common.

Limitations

- Full fit models usually rely on a large number of parameters. For instance, the model for the InGaAsP QW presented in this chapter has 16 parameters. This raises a concern of *overfitting*: how can we ensure that the fit converges towards physically-meaningful parameters? A possible solution is to determine as many parameters as possible from complementary measurements. In this chapter, we will present how 6 of the 16 parameters can be estimated from EQE measurement in section 2.4.4.

- To optimize such a large number of parameters in a non-linear model, using a global-search algorithm is mandatory. This means that the computation time of full fit will be significant, typically several minutes per spectrum. Therefore this technique is restricted to data sets containing several hundred spectra at most. In this PhD work, we used the `differential_evolution` algorithm from Python's `scipy.optimize` module (documentation). Differential evolution is a flexible yet robust global-search algorithm with few easy-to-understand parameters to fine-tune [Storn 1997].

2.3.5 Comparison of the four fitting methods

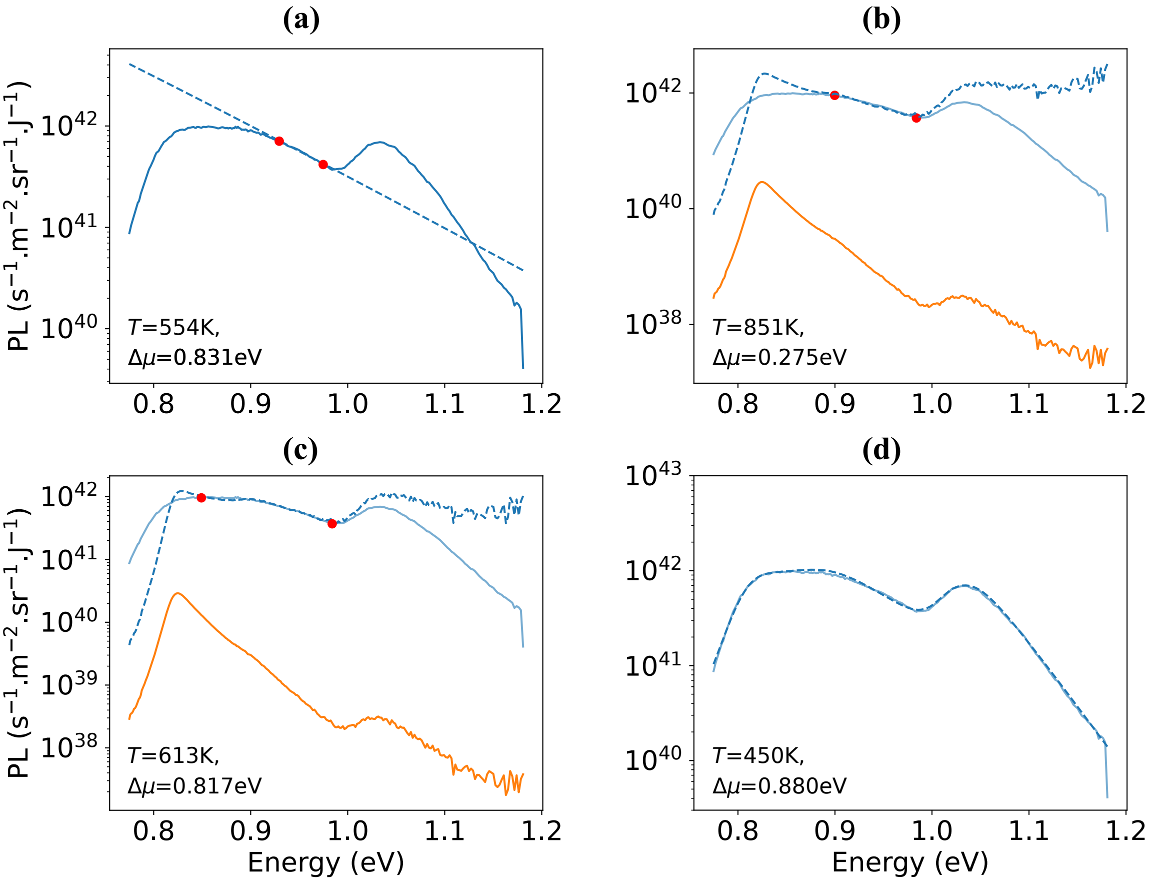

Figure 2.9: *Different fitting techniques applied on the same PL spectrum from sample 5006 (InGaAsP QW). (a) High-Energy Linear Fit, (b) Photoluminescence Ratio (PLR), (c) Photoluminescence Ratio with Band Filling (PLRBF), (d) Full Fit. Red dots indicate the fit boundaries. Note that for the PLR (resp. PLRBF) method, the dashed spectrum is obtained by multiplying the fitted model for the PL ratio – given by* Equation (2.24) *(resp.* Equation (2.25)*) – by the reference spectrum (in orange).*

Figure 2.9 presents a comparison of the four fitting methods described above for a given

PL spectrum of the InGaAsP QW that will be presented in next section (section 2.4). High-energy linear fit is presented in Figure 2.9a. Because the QW spectrum exhibits an elbow around 0.9 eV, finding a range of energies at which the spectrum has a mono-exponential shape is difficult. Therefore the temperature extracted from this method is ambiguous and depends strongly on the choice of fitting interval, which is not very satisfying.

The elbow at 0.9 eV is due to the presence of a secondary optical transition, which is not a power-dependent effect. Therefore PLR can be used to estimate the temperature despite this elbow. The result of this analysis is reported in Figure 2.9b. As compared with the high-energy linear fit, the fitting interval is now extended, and the estimated temperature is lower. However, the fitted spectrum (in dashed lines) does not coincide with the measurement at low energies $E < 0.9$ eV, outside the fitting boundaries. This is because of the presence of a strong BF effect, which reduces the absorption close to the QFLS. PLR method predicts that $\Delta\mu \sim 0.817$ eV. This means that the BF effect is noticeable at least until $0.95 - 1$ eV, and therefore the assumption to apply PLR method is not valid.

It is thus necessary to include some BF in the analysis of this spectrum, which can be done thanks to the PLRBF method. This is reported in Figure 2.9c. This time, the fit is satisfying almost over the entire range of QW emission. Notice how the carrier temperature is lower than the one obtained by PLR method, thanks to proper inclusion of the BF effect. However, the low-energy part is still poorly reproduced, because of the combination of two effects: (i) exciton screening, which reduces the amplitude of the peak at 0.82 eV [Chemla 1985] and (ii) spectral linewidth broadening, which increases sub-bandgap absorption [Esmaielpour *et al.* 2017].

Only a full fit allows to account for these two effects. We were able to establish a full fit model to describe this sample PL emission (see section 2.4.3) and the resulting fit on this spectra is shown on Figure 2.9d. As full fit is our most advanced method, we consider its result as the ground truth for the determination of the temperature and of the QFLS. Interestingly, we see that PLRBF method underestimates carrier temperature in this case. This is because PLRBF is very sensitive to the choice of fitting energy range. In this case, the fitting energy range was too large, such that spectral linewidth broadening was mistaken for BF, which led to an overestimate of the QFLS and an underestimate of the temperature.

Result 2.1. (Full fit is mandatory to study QW PL spectra)
This section shows that QW are complex optical systems which cannot be approximated by simple fitting methods, because

1. they have step-like absorptivity which cannot be approximated by a constant ;
2. they have low density-of-states and therefore are subject to BF at the high excitation rates necessary to produce hot carriers ;
3. they host many power-dependent effects, including exciton screening and spectral linewidth broadening.

As a consequence, the only method that leads to reliable temperature estimates in the general case is full fitting the PL spectra. Other methods may also be valid in some specific configurations, but their validity needs to be assessed on a case-by-case basis.

2.3.6 Are we heating the lattice?

To characterize the hot-carrier effect, it is necessary to measure both lattice and carrier temperature. Indeed, what matters is the difference in temperature between the carriers and the lattice. If the carriers are hot, but the lattice is equally hot, there is no hot-carrier effect.

Varshni law Carrier and lattice temperatures affect the high-energy tail of the PL spectrum the same way. However, lattice temperature also changes the bandgap of the material, while carrier temperature does not. This change of bandgap is mainly due to lattice dilatation (change of lattice constant) and change in electron-lattice interaction strength [Varshni 1967]. This effect was summarized in the following phenomenological equation:

$$E_g(T) = E_g(T = 0\ \mathrm{K}) - \frac{\alpha T^2}{\beta + T} \tag{2.26}$$

where α and β are material-dependent parameters. A comprehensive review of Varshni parameters in most common III-V alloys can be found in [Vurgaftman *et al.* 2001].

This change in bandgap will result in a shift in PL peak energy. In III-V compounds, $\alpha > 0$ such that the bandgap (and hence the PL peak energy) decreases with increasing lattice temperatures. This effect is often called *red shift*. One can thus hope to determine the lattice temperature from the *PL peak shift*, while the carrier temperature can be assessed from the high-energy slope of the spectrum.

In general, the precise link between the bandgap of a material and its PL peak position is not straightforward. A usual derivation assuming $\alpha \propto \sqrt{E - E_g}$, the PL peak position can be computed at $E_{\mathrm{peak}} = E_g + k_B T_c/2$. But we have already pointed out that real PL data could not be explained by this idealized absorption coefficient (see section 2.1.4). In real materials, spectral broadening needs to be taken into account (see for instance [Katahara and Hillhouse 2014]). In this realistic configuration, the PL peak position cannot be expressed analytically as a function of the bandgap and the temperature, but could be assessed numerically.

Yet, we are interested in lattice temperatures slightly higher than ambiant $T_L \gtrsim T_{\mathrm{amb}} = 300$ K. In this range, Varhsni law is well approximated by a linear dependency in most III-V materials, as $\beta \lesssim 300$ K [Vurgaftman *et al.* 2001]. Therefore, even if we cannot relate the bandgap to the PL peak, their *variation* with respect to room temperature should be the same.

The precision of this method is limited first by the wavelength resolution of our PL measurement setup. For our NIR HI setup, it is typically 2 nm, which translates into an energy resolution around 2 meV for measurement wavelengths around 1000 nm. This leads to a theoretical limit in the lattice temperature measurement of GaAs of 4 K (Figure 2.10c). However, in more complicated cases with strong hot-carrier effect, BF contribution or spectral bandwidth broadening, lattice temperature assessment will be much less precise than this theoretical limit, and the precision should be assessed carefully.

Calibration by temperature-dependent photoluminescence For some materials, Varshni parameters may not be available. In particular, the development of efficient HCSCs may require the development of new materials (III-V QW for instance) of unknown Varshni parameters. For these materials, we propose here a methodology based on PL measurements to *calibrate* the PL peak shift with lattice temperature for any sample.

This method relies on a measurement of PL spectra at different lattice temperatures in the range of interest. (i) Place the sample in a cryostat or on a heat plate. (ii) Measure the temperature-dependent PL with temperature steps of 10 K. Make sure to wait sufficiently long at each temperature to ensure that the sample is thermalized before starting the PL measurement. (iii) Measure the PL peak shift at each temperature.

After performing this calibration step, one should be able to retrieve the lattice temperature of a given sample simply by looking at the position of the PL peak.

To prove the feasability of the methodology described above, we measured PL spectra of a GaAs sample for increasing temperatures in the range $293 - 423$ K. The results of this experiment are summarized in Figure 2.10. Is shown on Figure 2.10b, the PL peak energy is not equal to the bandgap (computed from Varshni law). However, the PL peak *shift* is equal to the bandgap *shift* predicted by Varshni law, as shown on Figure 2.10c. This corroborates the validity of our method.

Note that, the difference between the PL peak energy and the bandgap is around 5 meV, which is not equal to $k_B T/2$. This illustrates the difficulty to relate the position of the PL peak to the bandgap. Note also that in this specific case, we find that that PL peak shift is linear in the lattice temperature. However the methodology presented here allows to estimate lattice temperature from PL peak shift even if the relation between them is not linear.

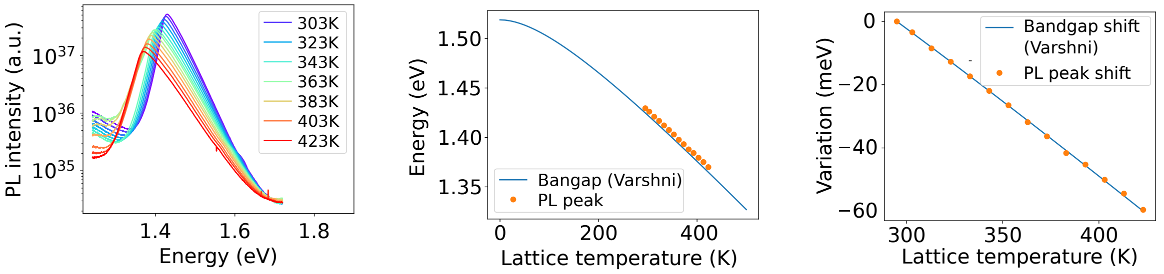

(a) (b) (c)

Figure 2.10: *Determination of lattice temperature from PL peak position and comparison with theoretical prediction using Varshni law. (a) Temperature dependent PL spectra obtained for a GaAs sample. (b) Theoretical GaAs bandgap (*$\alpha = 0.54$ meV.K^{-1} *and* $\beta = 204$ K*) and experimentally measured PL peak position dependency on lattice temperature. (c) Theoretical bandgap variation and experimentally measured PL peak shift with increasing lattice temperature.*

2.4 Presentation of the InGaAsP sample used in this work

Most of the experiments presented in this manuscript were performed on the same InGaAsP/InGaAsP single QW called *sample 5006* in the text. It was provided by FOTON Institute and has already proven excellent hot-carrier capabilities [Nguyen *et al.* 2018].

2.4.1 Composition

This InGaAsP/InGaAsP single QW has a p-i-n structure, and its composition is given in Table 2.1. An example of band structure computed under illumination is shown in Figure 2.11. This sample was processed in mesas to divided into several cells of varying size. Each cell is contacted with gold electrodes on both sides. The presence of electrical contacts allows optoelectronic characterization such as EQE measurements (see section 2.1.4).

Composition	**Doping**	**Thickness**	**Role**
InGaAs	p^{++}	170 nm	Contact layer
$\mathrm{In_{.8}Ga_{.2}As_{.435}P_{.565}}$	p^{+}	50 nm	
InP	p^{+}	50 nm	Cladding
$\mathrm{In_{.8}Ga_{.2}As_{.435}P_{.565}}$	i	120 nm	Barrier
$\mathrm{In_{.78}Ga_{.22}As_{.81}P_{.19}}$	i	7.4 nm	Quantum well
$\mathrm{In_{.8}Ga_{.2}As_{.435}P_{.565}}$	i	130 nm	Barrier
InP	n^{+}	40 µm	Substrate / Cladding

Table 2.1: *Composition of sample 5006, the InGaAsP single QW studied in this manuscript. Adapted from [Nguyen* et al. *2018].*

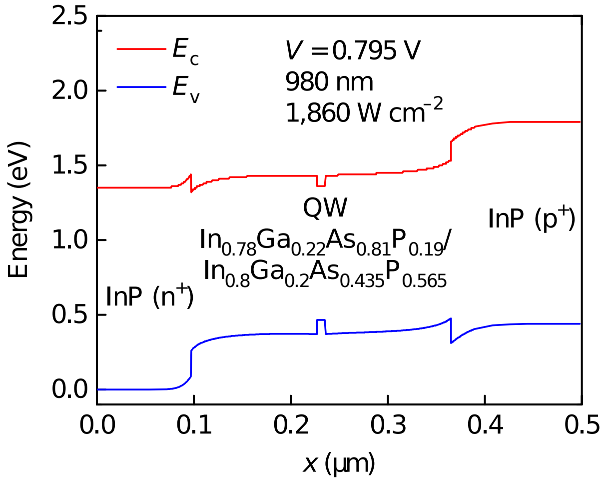

Figure 2.11: *Band diagram of sample 5006 at open-circuit condition, with an optical excitation at* 980 nm *and* 1890 W.cm^{-2}. *Reproduced from [Nguyen* et al. *2018].*

2.4.2 Absorptivity measurement

We measured the absorptivity of this sample at room temperature by EQE measurement (see section 2.1.4). This experiment was conducted with a ThermoFisher FTIR-FTPS. It is reported in Figure 2.12a.

The absorption in the region $0.8 \leq E \leq 1$ eV is representative of the QW, with one excitonic peak ($E_x \simeq 0.82$ eV) and two optical transitions ($E_1 \simeq 0.82$ eV, $E_2 \simeq 0.9$ eV). The absorption above $E_b \simeq 1.05$ eV is due to the barriers and exhibits a typical increase in $\sqrt{E - E_b}$ in the range $1.05 - 1.15$ eV, as expected for bulk absorptivity (see section 2.1.4).

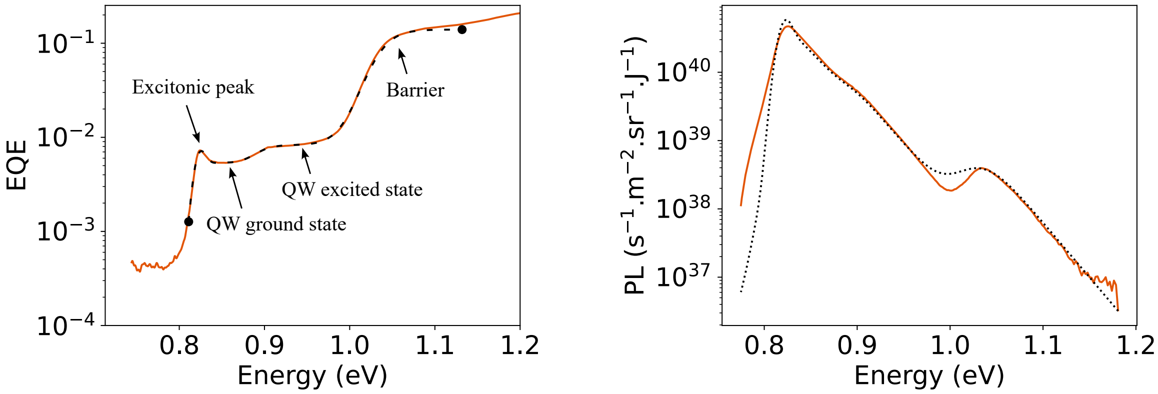

(a) (b)

Figure 2.12: *Absorptivity and low-intensity PL spectrum of sample 5006. (a) Absorptivity measured by EQE. Dashed line represents a full fit commented in section 2.4.4. (b) Low intensity PL spectrum. Dotted line is obtained by multiplying the EQE spectrum by a blackbody-like contribution with* $T = 300$ K *and* $\Delta\mu = 0.7$ eV*. Small deviations can be explained by power-dependent phenomena such as exciton screening of spectral linewidth broadening.*

2.4.3 Full fit model

We present here the model that was designed to fit PL emission of sample 5006. See section 4.3.2 and section 5.5.1 for experimental results. As seen on Figure 2.12b, PL spectra of this sample include contributions from the QW and from the barriers.

QW absorption coefficient As shown in section 2.1.4, QW emission can be modeled by a step-like function. In this specific case, two optical transitions must be included $E_1 \simeq 0.82$ eV and $E_2 \simeq 0.89$ eV. In addition, excitons must be taken into account (see

Figure 2.12a). This results in the following model for QW absorption coefficient:

$$\begin{aligned}\alpha_{w0}(E) &= a_x \exp\left(-\frac{(E-E_x)^2}{2\Gamma_x^2}\right)\\ &+a_1\frac{1}{1+\exp\left(-\frac{E-E_1}{\Gamma_1}\right)}\times\frac{2}{1+\exp\left(-2\pi\sqrt{\frac{R_y}{|E-E_1|}}\right)}\\ &+a_2\frac{1}{1+\exp\left(-\frac{E-E_2}{\Gamma_2}\right)}\end{aligned} \tag{2.27}$$

where we took into account the Sommerfeld enhancement factor in the first level only [Nguyen *et al.* 2018].

Barrier absorption coefficient For the barrier, we should in theory use a model compatible with bulk emission, with an absorption coefficient $\alpha_{b0} \propto \sqrt{E-E_b}$. However, since we are not interested in estimating precisely the temperature of carriers in the barrier, we use a simpler step-like function instead:

$$\alpha_{b0}(E) = a_b\frac{1}{1+\exp\left(-\frac{E-E_b}{\Gamma_b}\right)}$$

Band filling BF contribution is included both for the QW and the barriers, such that the internal absorptivity A_i of each layer ($i = w$ or b) writes

$$A_i(E) = 1-\exp(-\alpha_{i0}(E)d_i \times BF(E,T_i,\Delta\mu_i))) \tag{2.28}$$

Emission of the multilayer Finally, we model the whole stack with a single-pass reabsorption model (see section 2.1.4), which yields

$$I_{PL}(E) = \frac{2(1-R)E^2}{h^3c^2}\left\{A_w(1-A_b)\frac{1}{1+\exp\left(\frac{E-\Delta\mu_w}{k_BT_w}\right)}\right.\\ \left.+\left[A_b(1-A_w)(1-A_b)+A_b\right]\frac{1}{1+\exp\left(\frac{E-\Delta\mu_b}{k_BT_b}\right)}\right\} \tag{2.29}$$

2.4.4 Strategy to avoid overfitting

Our full fit model requires to estimate 16 different parameters for each PL spectrum. Four are related to the carrier distribution: in the well (T_w, $\Delta\mu_w$) and in the barrier (T_b, $\Delta\mu_b$). Twelve are related to the material (a_x, E_x, Γ_x, a_1, E_1, Γ_1, a_2, E_2, Γ_2, a_b, E_b, Γ_b). Several of these parameters are redundant. For instance, increasing $\Delta\mu$ and a_1 has almost the same effect on the modelled PL spectrum. Therefore, it is not possible to determine all 16 parameters exclusively from PL spectra. To avoid this overfitting, we determine as many parameters as possible from an absorptivity (EQE) measurement.

Some of the PL model parameters depend on excitation conditions. For instance, spectral linewidths Γ_i are subject to linewidth broadening, a power-dependent effect [Esmaielpour *et al.* 2017]. Similarly, bandgap renormalization may induce a power-dependent decrease of the bandgap E_1, and thus of the exciton energy $E_x = E_1 - R_y$ [Bennett *et al.* 1990]. The exciton absorption amplitude a_x is subject to screening by the photogenerated free carriers [Chemla 1985]. Finally, carrier distributions will obviously depend on excitation power. These parameters (a_x, E_x, Γ_x, Γ_1, Γ_2, Γ_b, T_w, $\Delta\mu_w$, T_b and $\Delta\mu_b$) must be fitted independently for every PL spectrum.

In contrast, the six remaining parameters (a_1, R_y, a_2, E_2, a_b and E_b) can be considered independent of the excitation conditions. They may therefore be estimated from an absorptivity measurement, and in particular by fitting the EQE spectrum reported in Figure 2.12a. EQE being performed in low excitation condition, we fitted the absorptivity model derived from Equation (2.29), assuming that $T_w = T_b = 293\ K$ and $\Delta\mu_w = \Delta\mu_b \ll E_x$. Table 2.2 reports the fitted value of those six *material* parameters, which were used to model all PL spectra.

Parameter	a_1	R_y	a_2	E_2	a_b	E_b
Value	5.4 10^5	0.005	7.4 10^5	0.890	8.5 10^5	1.035
Unit	m^{-1}	eV	m^{-1}	eV	m^{-1}	eV

Table 2.2: *Optical parameters of sample 5006 determined by EQE measurement. These values were used to fit all PL spectra emitted by this sample throughout this manuscript.*

Note that Rydberg was set to 5 meV because over-parametrization prevented us from measuring it from the EQE spectrum. In the following, we will keep this value constant. Fortunately, this parameter has little to no impact on the estimates of carrier temperature.

Chapter 3

Theoretical toolbox: model for hot-carrier solar cells

As stated in the general introduction, we will study non-ideal Hot-Carrier Solar Cells (HCSCs) by modeling their operation. In this chapter, we present the main elements of a classical detailed balance model for HCSCs. This model is directly inspired from the seminal work of Ross and Nozik [Ross and Nozik 1982], although we add a phenomenological coefficient to represent finite thermalization rates. We will eventually extend this model in chapter 6 to include the effect of uneven temperatures.

Here, we first recall how to model the main elements of a HCSC in section 3.1. Second, we define the balance equations that allow to compute the thermodynamical state of a HCSC at a given operation point in section 3.2. Third, we provide the expression of the voltage of a HCSC depending on its thermodynamical state in section 3.3. Fourth, we detail how our model can be utilized to compute the efficiency of a given HCSC. Finally, we prove that our model allows to reproduce accurately the historical results of Shockley-Queisser and Ross-Nozik.

Table of contents

3.1 Description of hot-carrier solar cells constituting elements

In this section, we *recall* the main elements that are required to simulate a HCSC in the particle-conservation model, namely *sunlight*, a *hot-carrier absorber* and *energy-selective contacts*. These elements are summarized in Figure 3.1. The model described in this section is inspired by [Le Bris and Guillemoles 2010], but we simplified the description of thermalization and of selective extraction.

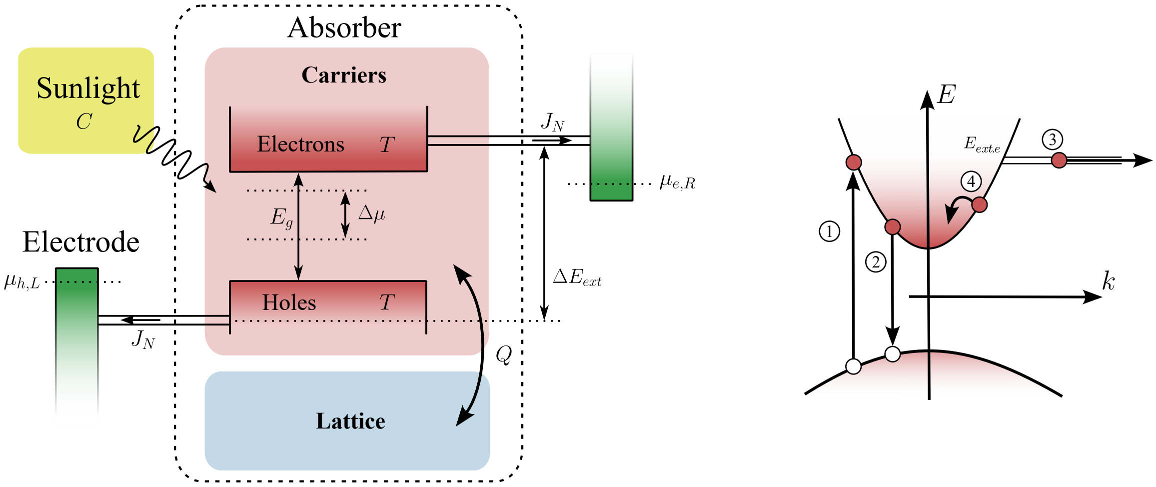

(a) (b)

Figure 3.1: *Schematic representation of a HCSC. (a) Representation of all subsystems (sunlight, absorber and energy-selective contacts) along with their parameters in the model. (b) Representation of the microscopical processes included in the model for electrons and holes. Blue indicates a cold system, while red indicates a hot system.*

3.1.1 Sunlight and concentration factor

To simulate real life devices, we model HCSCs with Sun as a light source. We approximate sunlight by a blackbody radiation of temperature $T_\odot = 5778$ K. On earth, the sun is seen with a solid angle $\Omega_\odot = 4\pi \sin^2(\theta_\odot/2) = 6.794 \times 10^{-5}$ str. This means that incoming photons from the sun form a cone of half angle $\theta_\odot = 4.650 \times 10^{-3}$ rad (see Figure 3.2).

Because HCSCs typically require large excitation powers, we assume that the system is equipped with a concentration system. Under concentration, the HCSC sees the sun with an effective angle $\theta'_\odot$. We parametrize the concentration with the *concentration factor* C. Under concentration, the solar cell sees the sun with an effective half-angle $\theta'_\odot \geq \theta_\odot$, and receives a solar flux increased by a factor C with respect to 1 sun condition (see Figure 3.2). Because of *etendue* conservation, the concentration factor writes $C = (\pi \sin^2 \theta'_\odot)/(\pi \sin^2 \theta_\odot)$. When the sun covers the entire half space above the cell, $\theta'_\odot = \pi/2$ and we obtain the maximum concentration factor $C_{\max} = 1/\sin^2(\theta_\odot) \simeq 46240$.

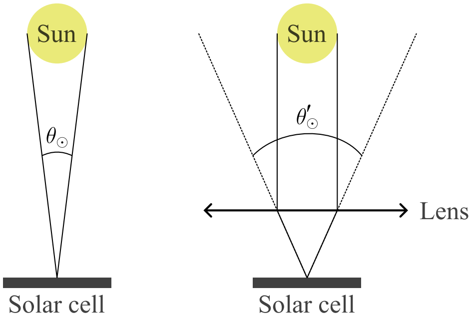

Figure 3.2: *Schematic representation of a solar cell receiving solar flux (left) without concentration and (right) with concentration.*

Statement 3.1. (Incoming solar flux under concentration)
For a given concentration factor C, the solar flux incident on the HCSC is given by the following blackbody radiation [Le Bris 2011]

$$\phi_\odot(C,E) = \pi \sin^2(\theta_\odot)\, C \frac{2}{h^3c^2} E^2 \left(\exp\left(\frac{E}{k_B T_\odot}\right) - 1\right)^{-1} \tag{3.1}$$

where $\phi_\odot$ is expressed in s^{-1}.m^{-2}.J^{-1}.

3.1.2 Absorber

The absorber of a HCSC absorbs photons and generates charge carriers. In this HCSC model, we assume that electrons and holes share the same temperature. They may exchange energy with their surroundings through four different processes, described schematically in Figure 3.1b.

1. Photons absorption. When a photon of energy E is absorbed, it promotes an electron-hole pair at the same energy. The absorption is characterized by an absorbed flux Φ_{abs} (in s^{-1}.m^{-2})

$$\Phi_{\text{abs}} = \int_{E_g}^{\infty} \phi_\odot(C,E)\, dE \tag{3.2}$$

and an absorber power P_{abs} (in W.m^{-2})

$$P_{\text{abs}} = \int_{E_g}^{\infty} E\, \phi_\odot(C,E)\, dE \tag{3.3}$$

Those two quantities depend on the *absorber bandgap* E_g, but also on the concentration factor C.

2. Radiative recombinations (photons emission). As a consequence of reciprocity, if the absorber is able to absorb light, it must be able to emit light as well. In the so-called *radiative limit*, we assume that all recombinations are radiative. During a radiative recombination, an electron-hole pair of energy E' recombines to generate a photon of same energy. The rate at which photons are emitted is given by the Generalized Planck Law (GPL) introduced in Statement 2.2. It depends on carrier distributions inside the bands through the carrier temperature T and Quasi-Fermi-Level Splitting (QFLS) $\Delta\mu$. We assume that the absorber has an ideal step-like absorptivity $A(E) = \Theta(E - E_g)$, where Θ is the usual Heaviside function, such that The emission of photons is characterized by an emitted flux Φ_{rad} (in $\text{s}^{-1}.\text{m}^{-2}$)

   $$\Phi_{\text{rad}} = \int_{E_g}^{\infty} \frac{2E^2}{h^3c^2} \left(\exp\left(\frac{E - \Delta\mu}{k_B T} \right) - 1 \right)^{-1} dE \tag{3.4}$$

   and power P_{rad} (in $\text{W}.\text{m}^{-2}$),

   $$P_{\text{rad}} = \int_{E_g}^{\infty} \frac{2E^3}{h^3c^2} \left(\exp\left(\frac{E - \Delta\mu}{k_B T} \right) - 1 \right)^{-1} dE \tag{3.5}$$

   which both depend on the bandgap E_g, and on carrier distributions through T and $\Delta\mu$.

3. Extraction of electrons and holes. To produce electrical work, electrons and holes must be extracted out of the absorber. We consider that extraction is a property of the contacts, and it will therefore be described in the following section.

4. Thermalization of carriers. As discussed in the general introduction, thermalization by carrier-LO phonon interaction is difficult to simulate. In this work, we describe thermalization by a purely phenomenological equation [Giteau *et al.* 2020].

   $$P_{\text{th}} = Q(T - T_L) \tag{3.6}$$

   where P_{th} is the power lost to thermalization, in $\text{W}.\text{m}^{-2}$ and Q is called the *thermalization coefficient* of the absorber and is usually expressed in $\text{W}.\text{cm}^{-2}.\text{K}^{-1}$.

Statement 3.2. (Parametrization of the absorber)
The absorber of the HCSC is described by four variables. The absorption properties are governed by the bandgap E_g. Thermalization of carriers is described through a phenomenological thermalization coefficient Q. Finally, carrier distributions are parametrized by their *effective* temperature T and QFLS $\Delta\mu$.

3.1.3 Energy-selective contacts

In the modeling of the contacts, we follow the approach of Ross and Nozik [Ross and Nozik 1982, Wurfel 1997]. We assume that the contacts are perfectly selective and that they have infinite electrical conductivity. Therefore, the contacts do not limit the current flowing through the device, J_N, which can take *a priori* any value. These energy-selective contacts are characterized only by the extraction energy ΔE_{ext} (see Figure 3.1a), because the power extracted out of the absorber via the contacts writes

$$P_{\text{ext}} = eJ_N \Delta E_{\text{ext}} \tag{3.7}$$

Statement 3.3. (Parametrization of the energy-selective contacts)
The energy-selective contacts are parametrized by one single variable: the difference between the extraction energy of electrons and holes, ΔE_{ext}.

3.2 Balance equations

In the particle conservation model, the thermodynamical state of the system (*i.e.* the carrier distribution parameters T and $\Delta\mu$) are established based on balance equations. We first describe the particle balance in section 3.2.1, then the power balance in section 3.2.2.

3.2.1 Particle balance

The number of carriers in the absorber is changed by the following three processes: photon absorption, radiative recombinations and carrier extraction. In steady state, the number of carriers stays constant, such that

$$\Phi_{\text{abs}}(C, E_g) - \Phi_{\text{rad}}(E_g, T, \Delta\mu) - J_N = 0 \tag{3.8}$$

where

Φ_{abs} = The total solar flux absorbed by the system (in $s^{-1}.m^{-2}$, see Equation (3.2)).
Φ_{rad} = The photon flux emitted by the system (in $s^{-1}.m^{-2}$, see Equation (3.4)).
J_N = The particle current running through the cell (in $s^{-1}.m^{-2}$). By convention, the particle current is considered positive when electrons flow from the left to the right (i.e. are extracted from the absorber). Since we use generator conventions for the electrical current, such a positive particle current is associated with positive electrical current.

3.2.2 Power balance

The energy contained in the HCSC is changed by the same three processes involved in particle balance. In addition, one must take thermalization into account. In steady-state, the HCSC is in such a state that

$$P_{\text{abs}}(C, E_g) - P_{\text{rad}}(E_g, T, \Delta\mu) - P_{\text{th}}(Q, T) - P_{\text{ext}}(J_N, \Delta E_{\text{ext}}) = 0 \tag{3.9}$$

where

P_{abs} = The power absorbed from sunlight (in W.m^{-2}, see Equation (3.3)).
P_{rad} = The power emitted by the HCSC (in W.m^{-2}, see Equation (3.5)).
P_{th} = The thermalized power (in W.m^{-2}, see Equation (3.6)).
P_{ext} = The power lost by the absorber due to the extraction of electron-hole pairs (in W.m^{-2}, see Equation (3.7)). Note that this is not the electrical power output, as part of this power cannot be converted to electrical work, and is lost as heat.

We restrict ourselves to the Boltzmann approximation in the absorber ($\Delta\mu \ll E_g$). In this case, the emitted flux and power can be integrated explicitly and expressed analytically as a function of E_g, T and $\Delta\mu$. This allows to considerably speed up the computations.

Note however that the Boltzmann approximation cannot be used to describe the *absorbed* flux and power. This is because we want to simulate devices with vanishing bandgaps $E_g \to 0$ eV. The Boltzmann approximation would hold here only if $E_g \gg k_B T_\odot \simeq 0.5$ eV. Fortunately, this does not increase dramatically the computation time as the absorbed flux and power depend only on E_g and C and can be computed once and for all for a given choice of HCSC structure.

3.3 Voltage of the hot-carrier solar cell

The voltage of the HCSC is, by definition, the amount of electrical work that one can get by extracting an electron at one side and reinjecting it in the other side. As such, the electrical power output of the HCSC, P_{elec}, writes

$$P_{\text{elec}} = eJ_N \times V \tag{3.10}$$

where $eJ_N = J_e$ is the electrical current, in A.m^{-2} and V is the voltage in V. This equation can be expressed equivalently as $P_{\text{elec}} = J_N \times eV$, where J_N is the particle current in s^{-1}.m^{-2} and eV is the work obtained per carrier, in J.

The voltage of the cell depends on the thermodynamical state of the absorber. It can be computed by an entropy balance between the absorber and the contacts [Wurfel 1997, Limpert and Bremner 2015]. Details of this computation will be provided in section 6.2.2 in the two-temperature case. Here, we simply recall the classical result obtained in the particle conservation model with perfectly selective energy contacts and isentropic extraction.

Statement 3.4. (Voltage of the HCSC)
For a HCSC with perfectly selective contacts and isentropic extraction, the work obtained per carrier is [Ross and Nozik 1982]

$$eV = \Delta\mu \frac{T_L}{T} + \Delta E_{\text{ext}} \left(1 - \frac{T_L}{T}\right) \tag{3.11}$$

3.4 Operation of the hot-carrier solar cell

We are interested in finding the maximum power point of the simulated HCSCs, *i.e.* the operation point of the cell which produces the highest electrical power (Equation (3.10)). This can be done by simulating the JV characteristic of the cell: we compute the voltage V for every possible current J_N with the procedure described in Statement 3.5. From there, we can compute the electrical power delivered at every operation point and identify the maximum power point.

Statement 3.5. (Physical engine underlying the HCSC particle conservation model)
The operation of a HCSC in the particle conservation model is defined by a set of two equations: the particle balance (Equation (3.8)) and the power balance (Equation (3.9)). For a choice of concentration factor and bandgap, these equations depend only on 3 variables: two describing the distribution of carriers in the bands (T, $\Delta\mu$), and one being the current flowing through the device, J_N.

We can therefore simulate the operation of the device at any given current J_N by solving the following system:

$$\begin{cases} 0 = \Phi_{\text{abs}} - \Phi_{\text{rad}}(T, \Delta\mu) - J_N \\ 0 = P_{\text{abs}} - P_{\text{rad}}(T, \Delta\mu) - Q(T - T_L) - J_N \Delta E_{\text{ext}} \end{cases} \tag{3.12}$$

Once T and $\Delta\mu$ are known from solving this system, it is possible to compute the voltage of the cell from Equation (3.11).

To provide an example of such a simulation, we computed the operation of three different cells with same bandgap $E_g = 1$ eV but different extraction energies. The result is respresented on Figure 3.3. We represent the JV characteristic, but also the temperatures as a function of the current, the chemical potentials, and we represent the particle and power balances in a graphical way.

As can be seen on Figure 3.3b, the temperatures in the absorber depend strongly on the operation point (current) and on the extraction energy ΔE_{ext}. If the extraction energy ΔE_{ext} is larger than the average absorbed energy ($\langle E_{\text{abs}} \rangle \simeq 1.87$ eV in this case), then the extraction will tend to decrease the average energy of the remaining carriers, hence decrease the temperature. This process is called *evaporative* or *thermionic cooling* [Mahan 1994, Suchet *et al.* 2017] and will be discussed in chapter 7. On the opposite, if $\Delta E_{\text{ext}} < \langle E_{\text{abs}} \rangle$, then extraction will tend to increase the temperature. This case may be called symmetrically *thermionic heating*. In this configuration, carrier temperature may exceed that of the Sun. This is not a contradiction because the HCSC is not a closed system in interaction with the sun only.

In the best case scenario, the current that can be extracted out of the HCSC is limited the finite absorbed flux: $J_N \leq J_{\text{abs}} = e\Phi_{\text{abs}} \simeq 600$ A.m^{-2} in this case. However, for large extraction energies ΔE_{ext}, it is not always to find physical solutions for the system. Indeed, the radiated flux and power are linked by a simple relation in the Boltzmann approximation: $P_{\text{rad}} = (E_g + k_B T) \times J_{\text{rad}}$. Using this relation, it is possible to rewrite the power balance equation as

$$P_{\text{rad}} = P_{\text{abs}} - J_N \Delta E_{\text{ext}} - Q(T - T_L) = (E_g + k_B T) J_{\text{rad}} \tag{3.13}$$

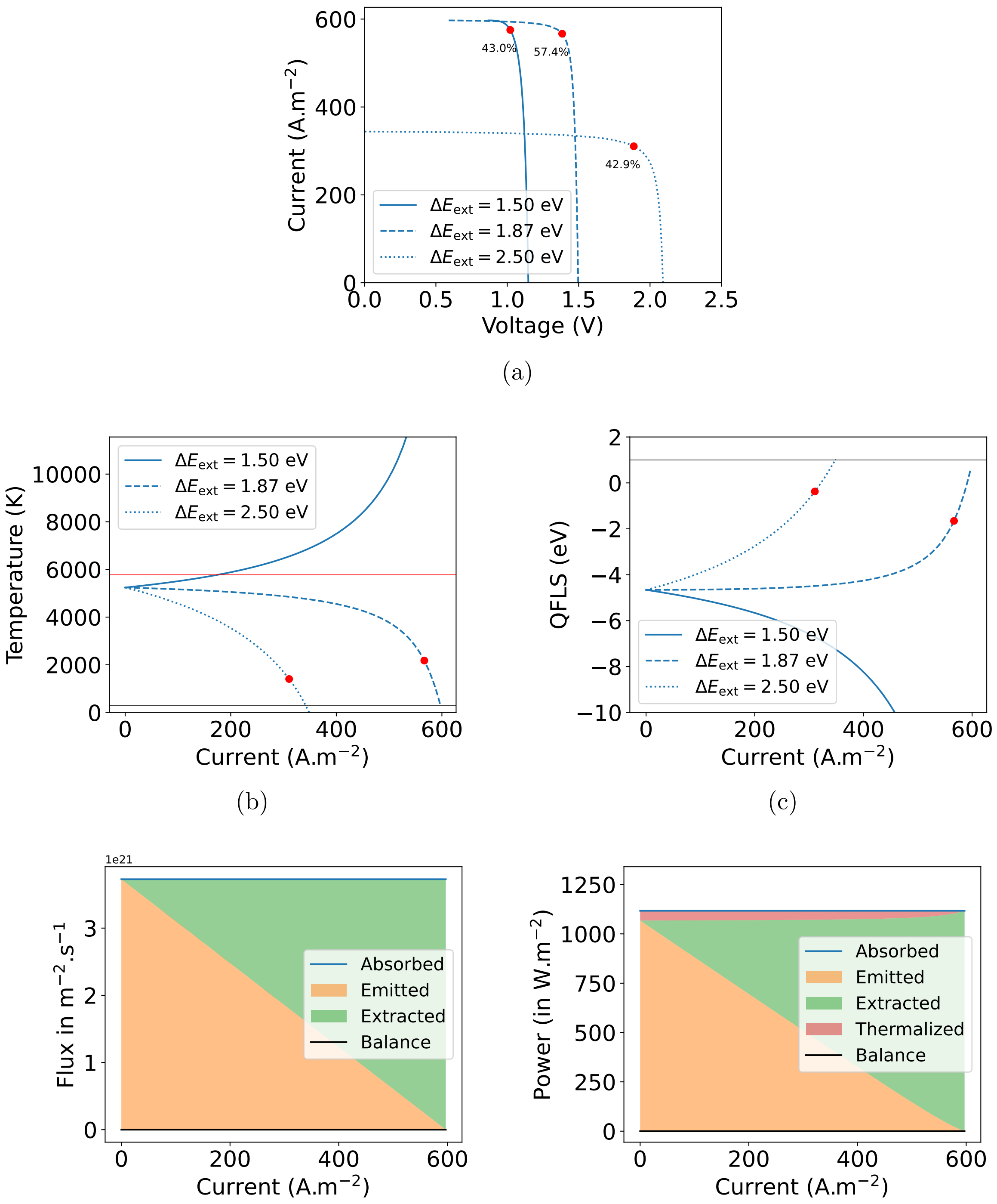

(a)

(b)

(c)

(d)

(e)

Figure 3.3: *Representation of the operation of a HCSC under one sun illumination for different extraction energies* ΔE_{ext}*. (a) JV characteristics and efficiency at maximum power point, (b) Temperature. Black line indicates lattice temperature while red line indicates sun temperature. (c) QFLS. Black line indicates the bandgap. (d) Particle balance. (e) Power balance. Red dots indicate the maximum power point of the system. These cells were simulated with the following parameters:* $E_g = 1$ eV, $Q = 10^{-6}$ W.cm^{-2}.K^{-1}*. Note that the particle and power balance are represented only in the case* $\Delta E_{\text{ext}} = \langle E_{\text{abs}} \rangle \simeq 1.87$ eV.

As $T \geq 0$, we find that

$$\begin{cases} P_{\text{rad}} \leq P_{\text{abs}} - J_N \Delta E_{\text{ext}} + QT_L \\ P_{\text{rad}} \geq E_g J_{\text{rad}} = E_g (J_{\text{abs}} - J_N) \end{cases} \tag{3.14}$$

where the first (resp. second) equation comes from the middle (resp. right) term of Equation (3.13). These two constraint may be incompatible for specific values of ΔE_{ext} and J_N. More precisely, the system will have no physical solution if and only if

$$\begin{cases} \Delta E_{\text{ext}} > \Delta E_{\text{crit}} \\ J_N > J_{\text{crit}} \end{cases} \quad \text{with} \quad \begin{cases} \Delta E_{\text{crit}} = E_g + \dfrac{P_{\text{abs}} - E_g J_{\text{abs}} + QT_L}{J_{\text{abs}}} \\ J_{\text{crit}} = \dfrac{P_{\text{abs}} - E_g J_{\text{abs}} + QT_L}{\Delta E_{\text{ext}} - E_g} \end{cases} \tag{3.15}$$

For instance, with $E_g = 1$ eV, $C = 1$, $\Delta E_{\text{ext}} = 2.5$ eV and $Q = 1 \times 10^{-6}$ W.cm^{-2}.K^{-1}, this formula yields $J_{\text{crit}} \simeq 370$ A.m^{-2}, as exemplified in Figure 3.3b. Larger extraction currents lead to unphysical solutions with negative temperatures.

This critical behavior is also present in the ideal model of Ross and Nozik ($Q = 0$), and was predicted and criticized by Würfel in his seminal paper [Wurfel *et al.* 2005]. To circumvent it, Würfel proposed another approach to model HCSCs, which relies on dominant Auger recombinations such that the carrier QFLS is always zero. However, we usually measure non-vanishing QFLSs when probing hot-carrier absorbers with continuous-wave Photoluminescence (PL) spectroscopy, so our samples cannot be modeled by Würfel's approach.

3.5 Limiting cases

In this section, we prove that our HCSC model is able to reproduce classical results from the literature. When reproducing previous computations, we must keep in mind that we cannot expect to recover the exact same value for the optimal efficiency or optimal cell design (bandgap, extraction energy). Indeed, these values depend on simulation choices such as the model for the solar flux, which may vary slightly from author to author.

3.5.1 The ideal thermalized solar cell (Shockley-Queisser)

The most famous solar cell model is Shockley-Queisser model for a fully thermalized, single-junction solar cell [Shockley and Queisser 1961]. In this model, electrons and holes are supposed to be at lattice temperature due to infinitely fast thermalization. We should therefore recover this model by simulating a HCSC with $Q \to +\infty$.

Figure 3.4 represents the efficiency of a solar cell with high thermalization coefficient ($Q = 10^2$ W.cm^{-2}.K^{-1}) depending on its bandgap and on the concentration factor C. We recover the classical result that, under one sun illumination, the optimal efficiency of a monojunction solar cell is $\eta_{\text{SQ}} \simeq 30$ %, obtained at a bandgap $E_g \simeq 1.26$ eV. Similarly, at full concentration, we recover $\eta_{\text{SQ}} \simeq 40$ % for a slightly lower bandgap of $E_g = 0.98$ eV.

Note that the operation of such a thermalized solar cell does not depend on the extraction energy ΔE_{ext}. This can be seen on the expression of the voltage. In the case where $T \simeq T_L$, Equation (3.11) becomes

$$eV = \Delta\mu \tag{3.16}$$

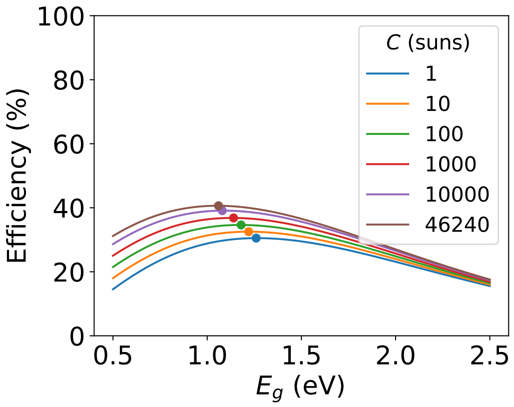

Figure 3.4: *Efficiency of a thermalized solar cell ($Q = 10^3$ W.cm^{-2}.K^{-1}) as a function of its bandgap E_g for different concentration factors C. Dots indicate the maximum efficiency reached at each concentration factor.*

Another way to understand this it to look at the power balance in the case of arbitrarily large thermalization coefficient. In this case, the lattice is considered an infinitely large heat reservoir, in strong thermal coupling with carriers. Therefore, even if carriers were to be extracted at "unrealistic" energies $\Delta E_{\text{ext}} \gg \langle E_{\text{abs}} \rangle$, the lattice would provide enough thermal energy to compensate the extreme extraction power. This is represented in Figure 3.5 for an unrealistic thermalized solar cell with $E_g = 1$ eV and $\Delta E_{\text{ext}} = 3$ eV. It appears that, at large extracted currents $J_N > 250$ A.m^{-2}, carriers temperature drops below lattice temperature (see Figure 3.5a), and therefore carriers *receive* heat from the lattice (shown in dark red color in Figure 3.5b). Note that this extra energy cannot be converted into work and will be lost as heat in the contacts.

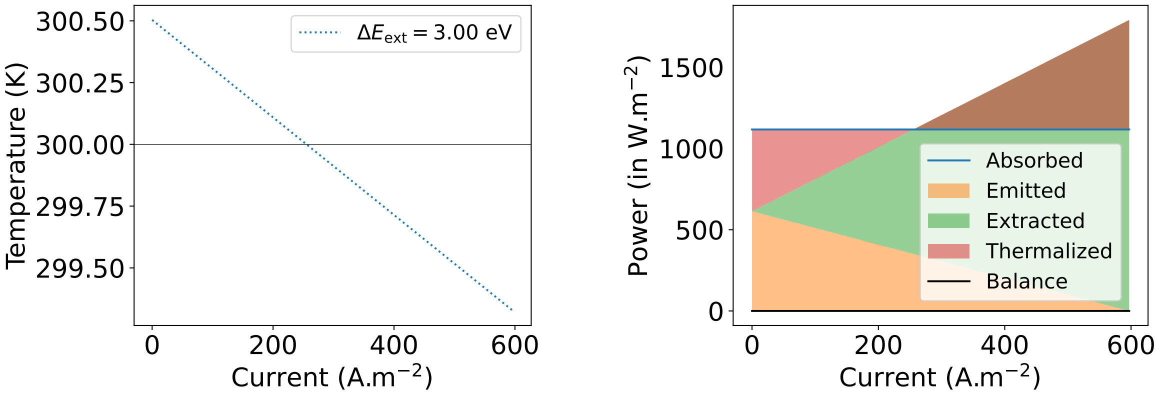

(a) (b)

Figure 3.5: *Operation of a thermalized solar cell with unrealistically high extraction energy $\Delta E_{\text{ext}} = 3$ eV ($E_g = 1$ eV and $Q = 10^3$ W.m^{-2}.K^{-1}). (a) Carrier temperature, (b) representation of the power balance. Note how carriers receive heat from the lattice at large extraction currents to compensate for the large extraction energy (in dark red).*

Note also that this phenomenon occurs because we assumed infinite conductivity of the electrical contacts. A more physically consistent description of the current is provided in [Le Bris and Guillemoles 2010, Equation (2)] in a Landauer-like approach. In this case, the current is imposed by the difference in carrier distribution at both ends of the energy-selective contact and by its transmission function. Consequently, if the extraction energy is extremely large, the current becomes negligible because there are no carriers to extract at such high energies.

3.5.2 The ideal hot-carrier solar cell (Ross-Nozik)

Another celebrated solar cell model is the one provided by Ross and Nozik [Ross and Nozik 1982] for ideal HCSC, which assumes that there is no thermalization at all. We can recover it by using a HCSC with $Q \to 0$.

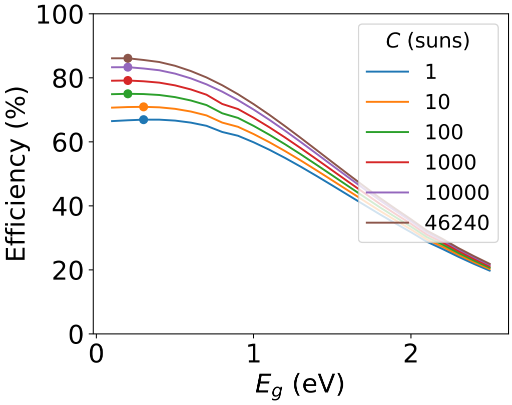

Figure 3.6: *Efficiency of an ideal HCSC ($Q = 10^{-8}$ W.cm^{-2}.K^{-1}) as a function of its bandgap for different concentration factors C.*

As for the Shockley-Queisser model, we computed the efficiency of an ideal HCSC (with $Q = 10^{-8}$ W.cm^{-2}.K^{-1}) for varying absorber bandgap and concentration factor C. The result is represented on Figure 3.6. We again recover the classical results that, under one sun illumination, the optimal efficiency of an ideal HCSC is $\eta_{\mathrm{RN}} \simeq 67$ %, for vanishing bandgap $E_g \to 0$ eV. Similarly, at full concentration, we also recover $\eta_{\mathrm{RN}} \simeq 86$ % for a vanishing bandgap.

In this case, the extraction energy ΔE_{ext} has a tremendous impact on the cell efficiency (see Equation (3.11)). The efficiency reported on Figure 3.6 was therefore computed by optimizing the extraction energy at every step.

To visualize the impact of the extraction energy on the ideal HCSC efficiency, we computed the efficiency while varying bandgap and extraction energy at the same time. The result is presented in Figure 3.7. It shows that, in order to maintain an efficiency larger than 60 % in 1 sun conditions or larger than 70 % under full concentration, the bandgap must be smaller than 0.75 eV and the extraction energy must be carefully selected, approximately in the range $1.4 - 2$ eV. Note that the optimal extraction energy depends on the bandgap, but apparently not on the concentration factor.

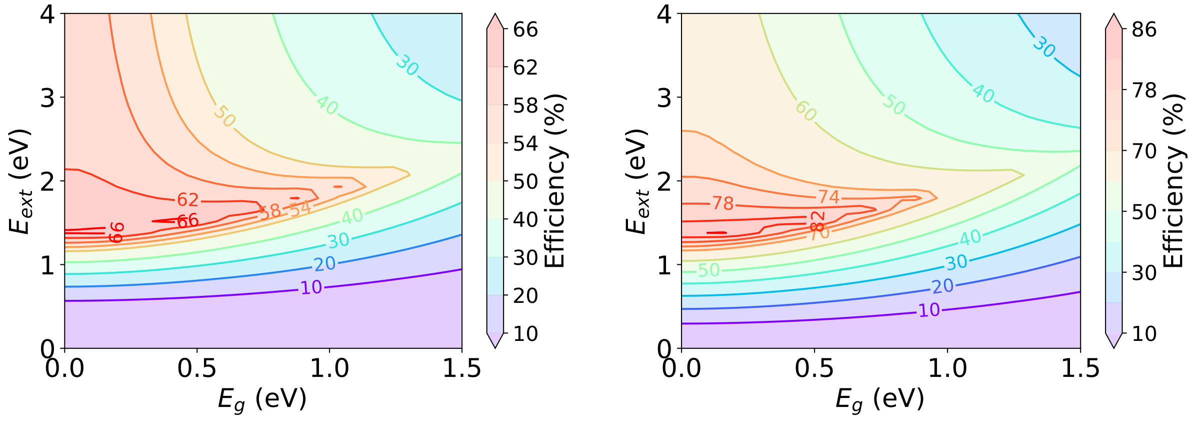

(a)

(b)

Figure 3.7: *Efficiency of an ideal HCSC as a function of its bandgap and its extraction energy (a) under one sun illumination and (b) under full concentration.*

3.5.3 From Ross-Nozik to Shockley-Queisser

Finally, we study the transition from ideal to thermalized HCSC by increasing the thermalization coefficient. We display this computation for a non-ideal HCSC of bandgap $E_g = 0.1$ eV in Figure 3.8. Few instabilities appear at highest concentration factors, but they are not meaningful.

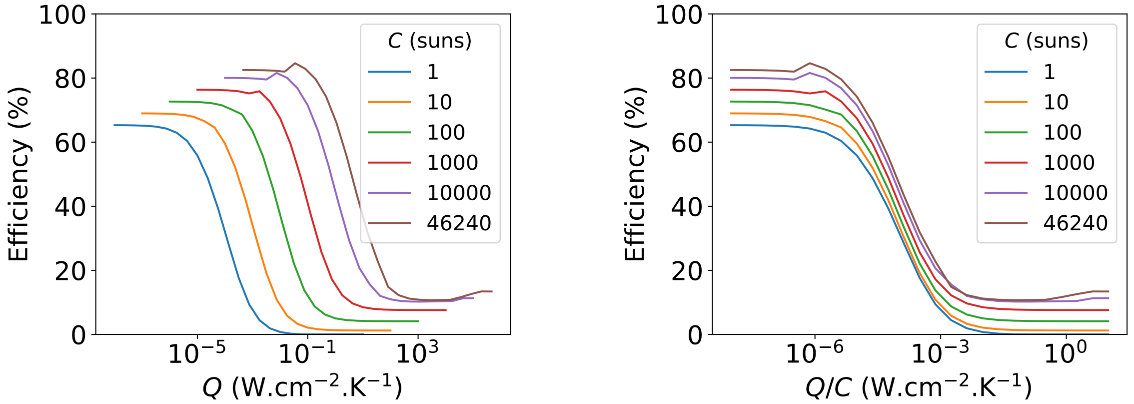

(a)

(b)

Figure 3.8: *Effect of the thermalization coefficient on the efficiency of a non-ideal hot-carrier solar cell for different concentration factors C. (a) Efficiency as a function of Q and (b) as a function of Q/C. Computations are done assuming $E_g = 0.1$ eV. Oscillations at highest concentration factors are numerical instabilities.*

First, this study confirms the intuition that the efficiency of a HCSC decreases when thermalization becomes more effective (Figure 3.8a). In addition, increasing the concentration increases the efficiency of HCSCs regardless of their thermalization coefficient. This is a well known effect of concentration: increasing the concentration increases the absorbed density of photons, but not their mean energy. Therefore, the QFLS in the

E_g	0.1	0.5	1	1.5	2	3
Q/C	1.3×10^{-2}	9×10^{-3}	5×10^{-3}	2.8×10^{-3}	1.4×10^{-3}	3.3×10^{-4}

Table 3.1: *Estimation of the maximum thermalization coefficient that allows to surpass Shockley-Queisser limit (Equation (3.20)), as a function of the absorber bandgap. The bandgap is expressed in* eV *while the thermalization coefficient is expressed in* W.cm^{-2}.K^{-1}.

absorber increases, but not the temperature. This results in a voltage boost (see Equation (3.11)) and consequently an increase of the efficiency.

Yet, the thermalization coefficient alone is not sufficient to compare the performances of a given absorber. For instance, with $Q = 10^{-1}$ W.cm^{-2}.K^{-1}, the HCSC would have vanishing efficiency under one sun condition, but close to ideal behavior under full concentration. Therefore, the relevant parameter to compare a HCSC to Shockley-Queisser and Ross-Nozik limiting cases is Q/C, as reported in Figure 3.8b. The range over which the efficiency drops from maximum (Ross-Nozik) to minimum (Shockley-Queisser) is the same at all concentration factors and corresponds roughly to $10^{-6} < Q/C < 10^{-2}$ (in W.cm^{-2}.K^{-1}).

This threshold for Q/C actually depends on the bandgap of the absorber. In fact, a HCSC will have increased efficiency with respect to Shockley-Queisser model if and only if carriers are sufficiently hot with respect to the lattice. Looking at the power balance equation at open-circuit voltage,

$$\begin{aligned} Q(T - T_L) &= P_{\text{abs}}(C, E_g) - P_{\text{rad}}(C, E_g, T, \Delta\mu) && (3.17)\\ &= C P_{\text{abs}}(C = 1, E_g) - C P_{\text{rad}}(C = 1, E_g, T, \Delta\mu) && (3.18)\\ &= C[P_{\text{abs}}(C = 1, E_g) - \underbrace{\langle E \rangle_{\text{rad}}}_{=E_g + k_B T} (J_{\text{abs}}(C = 1, E_g) - \underbrace{J_N}_{=0})] && (3.19) \end{aligned}$$

Such that, eventually, $T - T_L \geq 10$ K at open-circuit voltage if and only if

$$\begin{aligned} \frac{Q}{C} &\leq \frac{1}{10} (P_{\text{abs}}(C = 1, E_g) - (E_g + k_B T_L) J_{\text{abs}}(C = 1, E_g)) && (3.20)\\ &\leq \frac{J_{\text{abs}}(C = 1, E_g)}{10} (\langle E \rangle_{\text{abs}} - E_g - k_B T_L) && (3.21) \end{aligned}$$

This constraint is illustrated for different values of the bandgap in Table 3.1.

Result 3.1. (Relevant parameter to compare HCSCs)
The temperature reached in the absorber of a given HCSC depends not only on the thermalization coefficient Q, but also on the concentration factor C and the bandgap of the cell. To surpass Shockley-Queisser efficiency, the ratio Q/C must be lower than a threshold defined in Equation (3.20), which depends on the bandgap. For reasonable bandgaps $E_g \leq 1$ eV, the threshold lies in between 10^{-2} and 5×10^{-3} W.cm^{-2}.K^{-1}.

At realistic concentration factors $C < 10^3$, this means that hot-carrier absorbers must have a thermalization factor below $5 - 10$ W.cm^{-2}.K^{-1} to increase the performances of HCSCs. Most thermalization coefficients measured in III-V Quantum Wells

(QWs) have slightly larger thermalization coefficients $Q \sim 10 - 100$ W.cm^{-2}.K^{-1} (see section 1.3.2). This emphasizes the importance of continuing to search for materials with even lower thermalization coefficients.

Note that a similar conclusion was reached in [Giteau *et al.* 2019], where the authors studied the influence of light trapping on the performances of HCSCs. They showed that the relevant parameter to compare HCSCs with different light path enhancement factors F was Q/F. Therefore, it is likely that the correct parameter to study the thermalization rate of a HCSC with light trapping *and* concentration will be Q/FC.

Finally, in Figure 3.9, we represent the efficiency of an optimal HCSC as a function of its bandgap, for different thermalization coefficients. This figure illustrates how the non-ideal HCSC model allows us to go continuously from Ross-Nozik model ($Q \to 0$, shown in black) to Shockley-Queisser ($Q \to +\infty$, shown in red). This figure reproduces the results of [Le Bris *et al.* 2012, Figure 7].

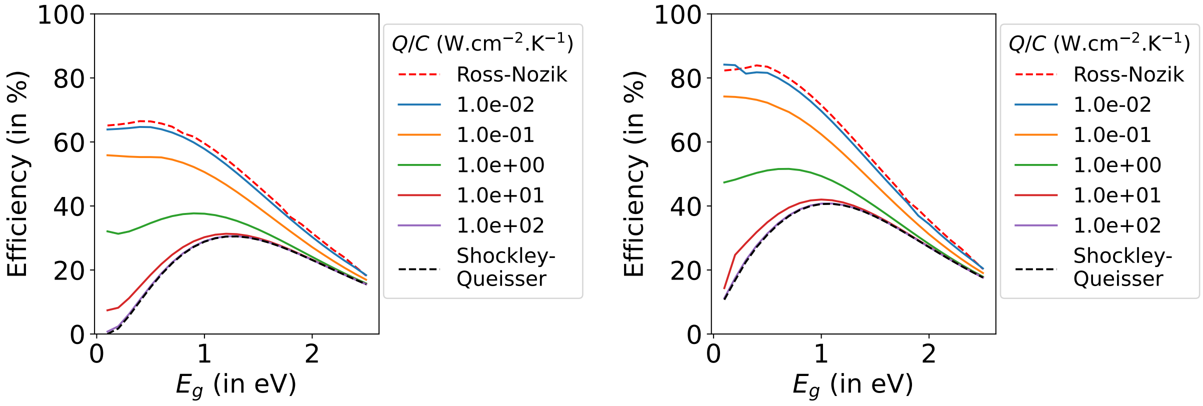

(a)

(b)

Figure 3.9: *Effect of the bandgap on the Efficiency of a non-ideal HCSC, for different thermalization coefficients Q. (a) With one sun illumination, (b) under full concentration. The extraction energy* ΔE_{ext} *is optimized at every point of the computation.*

3.6 Conclusion

In this chapter, we presented a model of HCSC based on detailed balance equations in the radiative limit. We showed that our model was able to reproduce both Shockley-Queisser and Ross-Nozik historical results, as well as all intermediate cases. We showed that the relevant parameter to compare thermalization in HCSCs was the ratio between the thermalization coefficient Q and the concentration factor C. In particular, the transition from a fully thermalized solar cell to an ideal HCSC occurs for $10^{-6} \lesssim Q/C \lesssim 10^{-2}$ W.cm^{-2}.K^{-1}. This HCSC model will be extended in chapter 6 to the case of two-temperature HCSCs, where electrons and holes are not necessarily at the same temperature.

Chapter 4

Inhomogeneous temperatures: thermoelectric transport of hot carriers

In conventional solar cells, understanding carrier transport has been a key to increase performances. Optimizing transport properties was a main driver of research on silicon solar cells architectures. This research can be summarized in three points

1. achieving higher lifetimes and mobilities through the control of crystal purity and interface passivation ;
2. ensuring better collection at the semiconductor-metal interface, which led to the development of highly doped contacts ;
3. optimizing the geometrical design of the top grid to ensure good charge collection while minimizing self-shading.

In Hot-Carrier Solar Cells (HCSCs), these considerations of mobility, lifetime and interfaces are still very important. However, additional complexity comes from the fact that carriers must be taken out of a *hot* absorber to a *cold* contact. This means that carrier diffusion is not only ruled by carrier concentration gradients and electric fields, but also by heat gradients. Such coupled transport is not usual in photovoltaics, but comes naturally in thermoelectricity. Therefore, in this chapter, we attempt to describe the transport of hot carriers in a formalism inspired by thermoelectricity.

Several authors already attempted to describe the extraction of carriers from a HCSC in terms of thermoelectricity, both from the experimental and theoretical perspective. For instance, [Limpert *et al.* 2015] analysed the voltage of a HCSC and distinguished the contribution of the photovoltaic and thermoelectric effects. Similarly, [Konovalov and Emelianov 2017] proposed a purely thermoelectric description of HCSCs with vanishing bandgaps and semi-selective contacts. Finally, [Marti *et al.* 2022] discussed heat losses during carrier extraction, showing that energy-selective contacts of a HCSC should have unrealistically large thermoelectric figure of merit ($ZT \geq 8$) to maintain efficiencies higher than 80 %. From the experimental perspective, it was shown that the equilibrium between a hot Quantum Well (QW) absorber and a cold barrier could be described by a pseudo Seebeck coefficient [Rodiere *et al.* 2015]. Some authors also discussed the similarities between hot-carrier extraction and photothermoelectric effect [Limpert *et al.* 2017].

However, an overlooked problem is the transport *within* the absorber. Many candidates for hot-carrier absorber are based on III-V nanostructures. In such systems, internal reflexions are to be expected, leading to inhomogeneous light absorption, hence inhomogeneous temperatures [Limpert *et al.* 2017]. This was investigated experimentally by means of hyperspectral Photoluminescence (PL) measurements in point illumination, in the limiting case of vanishing currents and negligible carrier recombinations [Gibelli *et al.* 2016c]. Some authors proposed a more advanced transport model of hot excitons and trions, which includes radiative and non radiative recombinations [Park *et al.* 2021]. However, a comprehensive model of thermoelectric transport for hot carriers in the context of HCSC has not yet been established.

This is because this system explores unusual conditions for thermoelectricity. First, many thermoelectric investigations focus on determining material properties. In contrast, in HCSCs, relevant thermoelectric properties are those of photogenerated populations which depend on excitation condition, as in photo-Seebeck [Okazaki *et al.* 2012] and photo-thermoelectric experiments [Gabor *et al.* 2011]. Second, the intense optical excitation necessary for hot-carrier generation results in high carrier densities and strong electrostatic coupling between electrons and holes, leading to ambipolar diffusion [Ruzicka *et al.* 2010b]. Finally, we consider a situation with strongly inhomogeneous illumination, which cannot be described with a constant chemical potential, as typically assumed in most ambipolar derivations [Price 1955, Gurevich *et al.* 1995, Goldsmid 2016].

This chapter presents a novel framework for describing thermoelectric ambipolar transport of hot carriers in the absorber, valid even in the degenerate case. In section 4.2, we show that this framework resembles the usual thermoelectric transport equation, provided we use effective ambipolar transport coefficients. Then in section 4.3, we propose an experimental setup which aims at generating this thermoelectric transport and probing it with purely optical methods. By using point-like excitation and hyperspectral imaging, we map carrier densities and temperatures with micrometric resolution. Finally, in section 4.4, we show that the ambipolar transport coefficients, and in particular Seebeck coefficient, can be directly measured from this optical experiment. This chapter is adapted from [Vezin *et al.* 2024b].

Table of contents

4.1 Highlights

Theoretical Highlight 4.1. (Ambipolar transport of hot carriers)

It is possible to describe the thermoelectric transport of hot carriers in the ambipolar approximation. We prove that the particle current writes

$$\boldsymbol{J}_N = -\frac{\sigma_{\text{amb,i}}}{e^2}\boldsymbol{\nabla}\mu_i - \frac{\sigma_{\text{amb,i}}S_{\text{amb,i}}}{q_i}\boldsymbol{\nabla}T$$

where $\sigma_{\text{amb,i}}$ and $S_{\text{amb,i}}$ are effective ambipolar transport coefficients defined in Equation (4.29).

This equation allows the theoretical description of hot-carrier transport when either illumination or temperature or both are inhomogeneous. It is valid even in the degenerate case.

Experimental Highlight 4.1. (Mapping carrier distributions)

Using a hyperspectral imager, it is possible to map optically the carrier temperature, chemical potential and density [Rodière 2014, Chapter 3].

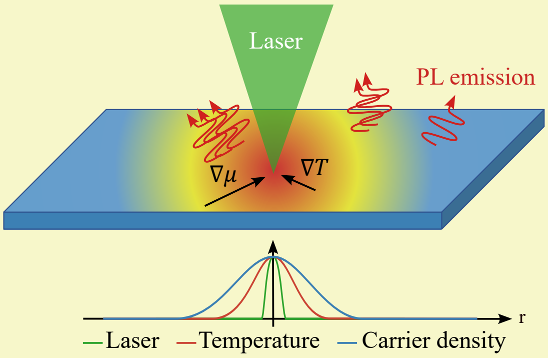

Experimental Highlight 4.2. (Optical determination of ambipolar Seebeck coefficient)

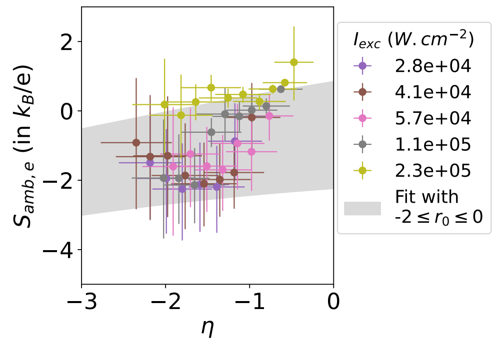

This experiment allows us to measure the ambipolar transport coefficients, and in particular Seebeck coefficient (see Figure). Assuming (i) constant mobility and (ii) slowly varying Seebeck coefficient, one can show that

$$S_{\text{amb,e}} \simeq -\frac{-\dfrac{C}{\gamma_e}n^3 + \dfrac{1+g_1}{q_e^2}\boldsymbol{\nabla}\left(n.\boldsymbol{\nabla}\mu_e\right)}{\dfrac{1}{q_e}\boldsymbol{\nabla}\left(n.\boldsymbol{\nabla}T\right)}$$

4.2 Thermoelectric transport of hot carriers

In this section, we recall the usual description of thermoelectric transport based on Boltzmann transport equation [Pottier 2007]. First, we introduce the general framework of our study: continuity equation for particle conservation, and the linear regime for the currents, in section 4.2.1. Then we introduce Boltzmann transport equation in the relaxation time approximation, which allows to derive expressions of transport coefficients in section 4.2.2. Finally, we discuss the *ambipolar* transport relevant for HCSCs in section 4.2.3, and point out the differences with textbook treatments of ambipolar thermoelectric transport.

4.2.1 Particle conservation and linear regime

We introduce here the general framework in which we study carrier transport. In the field of semiconductors, transport is often studied with drift-diffusion, which is a classical description. This approach relies on the description of particle conservation through a continuity equation (see Statement 4.1).

Statement 4.1. (Carrier conservation and continuity equation)
The continuity equation describing carrier conservation writes

$$\partial_t n_i = G_i - R_i - \boldsymbol{\nabla}.\boldsymbol{J}_{N,i} \tag{4.1}$$

where

i = Denotes either electrons (e) or holes (h)
n_i = Concentration of carrier i (in m^{-3})
G_i = Generation rate of carrier i (in $\mathrm{m}^{-3}.\mathrm{s}^{-1}$). In our case study, we only consider photogeneration, but in the general case, other processes such as impact ionization may contribute.
R_i = Recombination rate of carrier i (in $\mathrm{m}^{-3}.\mathrm{s}^{-1}$). Recombination can be attributed to several process, such as Shockley-Read-Hall recombinations, radiative recombinations or Auger recombinations (see Toolbox 4.1).
$\boldsymbol{J}_{N,i}$ = Particle current (in $\mathrm{m}^{-2}.\mathrm{s}^{-1}$)

In this section, we describe the diffusion of a given carrier type of charge $q = \pm e$ without specifying it. Therefore we do not repeat the index i everywhere, but note that equations presented below apply either on electrons or holes. We recall that the conventions used in this chapter were introduced in section 2.1.1.

In the standard (isothermal) drift-diffusion approach, the particle current has two contributions:

1. the *drift* of charge carrier due to the presence of an electric field (Ohm's law) $J_{\mathrm{N,drift}} = \frac{\sigma}{q}\boldsymbol{E}$;

	σ	$\bar{\mu}$	D
Electrical conductivity	σ	$qn\bar{\mu}$	$\dfrac{q^2nD}{k_BT}$
Electrical mobility	$\dfrac{\sigma}{qn}$	$\bar{\mu}$	$\dfrac{qD}{k_BT}$
Diffusion coefficient	$\dfrac{k_BT\sigma}{q^2n}$	$\dfrac{\bar{\mu}k_BT}{q}$	D

Table 4.1: *Relations between the electrical conductivity σ, the mobility $\bar{\mu}$ and the diffusion coefficient D.*

2. and the *diffusion* of carriers due to an inhomogeneous concentration (Fick's law) $J_{\text{N,diff}} = -D\boldsymbol{\nabla} n = -\frac{nD}{k_BT}\boldsymbol{\nabla}\mu$.

Drift and diffusion are actually two sides of the same coin. Thanks to Einstein relation ($\sigma = \frac{q^2nD}{k_BT}$), they can be merged by introducing the *electrochemical potential* $\tilde{\mu} = \mu + qV$. In that case, the total *drift-diffusion* current writes

$$J_N = \frac{\sigma}{q}\boldsymbol{\nabla}\tilde{\mu} \tag{4.2}$$

In the isothermal case, it is possible to parametrize the problem either by the electrical conductivity σ, by the electrical mobility $\bar{\mu}$ or by the diffusion coefficient D. The equivalence between these descriptions is highlighted in Table 4.1.

To account for hot-carrier transport, we need to extend drift-diffusion to the non-isothermal regime (*i.e.* when there is a temperature gradient). In this case, it is not sufficient to describe only the *particle* flux, as there is also a *heat* flux in the system. Following Onsager matrix formalism, particle and heat fluxes are coupled (see Statement 4.2). In this context, it is customary to parametrize the particle flux by the electrical conductivity and Seebeck coefficient [Gurevich *et al.* 1995, Pottier 2007, Goldsmid 2016] (see Equation (4.6)).

Statement 4.2. (Onsager matrix formalism and transport coefficients) Onsager matrix formalism is a general framework to study coupled fluxes. It relates fluxes (of particle, energy, etc) to gradients of their conjugate thermodynamical potential (electrochemical potential, temperature, etc).

Several equivalent descriptions exist in the case of thermoelectric transport, depending on the variables that are most convenient to describe the system. The first description expresses the particle current $\boldsymbol{J}_N$ and energy current $\boldsymbol{J}_E$ [Pottier 2007]

$$\begin{pmatrix} \boldsymbol{J}_N \\ \boldsymbol{J}_E \end{pmatrix} = \begin{pmatrix} L_{NN} & L_{NE} \\ L_{EN} & L_{NN} \end{pmatrix} \begin{pmatrix} -\boldsymbol{\nabla}\dfrac{\tilde{\mu}}{T} \\ \boldsymbol{\nabla}\dfrac{1}{T} \end{pmatrix} \tag{4.3}$$

In thermodynamics, it is often useful to introduce the heat flux $\boldsymbol{J}_Q^* = \boldsymbol{J}_E - \tilde{\mu}\boldsymbol{J}_N$. In this case,

$$\begin{pmatrix} \boldsymbol{J}_N \\ \boldsymbol{J}_Q^* \end{pmatrix} = \begin{pmatrix} L_{11} & L_{12} \\ L_{21} & L_{22} \end{pmatrix} \begin{pmatrix} -\dfrac{1}{T}\boldsymbol{\nabla}\tilde{\mu} \\ \boldsymbol{\nabla}\dfrac{1}{T} \end{pmatrix} \tag{4.4}$$

Finally, in semiconductor physics, the most familiar form involves transport coefficients and gradients of electrochemical potential and temperature [Wachutka 1990, Gurevich *et al.* 1995]

$$\begin{pmatrix} \boldsymbol{J}_N \\ \boldsymbol{J}_Q^* \end{pmatrix} = \begin{pmatrix} -\dfrac{\sigma}{q^2} & -\dfrac{\sigma S}{q} \\ -\dfrac{\sigma S T}{q} & -\kappa - \sigma S^2 T \end{pmatrix} \begin{pmatrix} \boldsymbol{\nabla}\tilde{\mu} \\ \boldsymbol{\nabla} T \end{pmatrix} \tag{4.5}$$

where σ is the electrical conductivity, S is the Seebeck coefficient and κ is the thermal conductivity. The equivalence between transport coefficients (σ, S, κ) and Onsager matrix elements $\{L_{ij}\}$ is given in Table 4.2.

In particular, the particle current writes

$$\boldsymbol{J}_N = -\frac{\sigma}{q^2}\boldsymbol{\nabla}\tilde{\mu} - \frac{\sigma S}{q}\boldsymbol{\nabla} T \tag{4.6}$$

Electrical conductivity	σ_i	$\dfrac{q_i^2}{T} L_{11}$	$\dfrac{q_i^2}{T} L_{NN}$
Thermal conductivity	κ_i	$\dfrac{1}{T^2}\dfrac{L_{11}L_{22} - L_{12}^2}{L_{11}}$	$\dfrac{1}{T^2}\dfrac{L_{EE}L_{NN} - L_{NE}^2}{L_{NN}}$
Seebeck coefficient	S_i	$\dfrac{1}{q_i T}\dfrac{L_{12}}{L_{11}}$	$\dfrac{1}{q_i T}\left(\dfrac{L_{NE}}{L_{NN}} - \tilde{\mu}_i\right)$

Table 4.2: *Expression of transport coefficients in terms of two families of Onsager matrix elements.*

4.2.2 Thermoelectric transport

4.2.2.1 General theory

We call *thermoelectric transport* the situation where a particle flux is induced by the conjugate action of an electrochemical potential difference and a temperature difference. In this section, we recall some standard results from linear transport theory [Pottier 2007] which will be useful to our work.

Statement 4.3. (Boltzmann transport equation)
Boltzmann transport equation is an approximate description of the evolution of a many-body system using a single-particle distribution function $f(\boldsymbol{r}, \boldsymbol{k})$. It is a classical equation that was introduced originally to study the out-of-equilibrium dynamics of dilute gases. It writes [Pottier 2007]:

$$\frac{\partial f}{\partial t} + \boldsymbol{v}(\boldsymbol{k}).\boldsymbol{\nabla}_{\boldsymbol{r}} f + \frac{\boldsymbol{F}}{\hbar}.\boldsymbol{\nabla}_{\boldsymbol{k}} f = \left(\frac{\partial f}{\partial t}\right)_{\text{coll}} \tag{4.7}$$

where

$\boldsymbol{r}$ = The position in real space.
$\boldsymbol{k}$ = The wavevector in reciprocal space.
$\boldsymbol{v}$ = The velocity, which depends the band structure of the material.
$\boldsymbol{F}$ = The external force applied on the particles at position $\boldsymbol{r}$ and wavevector $\boldsymbol{k}$.
$\left(\frac{\partial f}{\partial t}\right)_{\text{coll}}$ = The variation of f induced by collisions.

Statement 4.4. (Relaxation Time Approximation)
The relaxation time approximation relies on the fact that collisions tend to draw the distribution function towards its equilibrium value $f^{(0)}$ with an effective relaxation time $\tau(\boldsymbol{k})$. In other words,

$$\left(\frac{\partial f}{\partial t}\right)_{\text{coll}} = -\frac{f - f^{(0)}}{\tau(\boldsymbol{k})} \tag{4.8}$$

The equilibrium distribution is often assumed to be thermal. Therefore, for a gas of fermions, $f^{(0)}(E, \boldsymbol{r}) = \left[\exp\left(\frac{E - \tilde{\mu}(\boldsymbol{r})}{k_B T(\boldsymbol{r})}\right) - 1\right]^{-1}$. The local electrochemical potential $\tilde{\mu}(\boldsymbol{r})$ and temperature $T(\boldsymbol{r})$ are imposed by boundary conditions (illumination, recombinations, etc).

From now on, we consider the configuration where the carrier density $n(\boldsymbol{r})$ and temperature $T(\boldsymbol{r})$ are not constant, and particles may be subject to an electric field $\boldsymbol{E}(\boldsymbol{r}) = -\boldsymbol{\nabla} V$. In the following, we will use the shortcut $\boldsymbol{\nabla} = \boldsymbol{\nabla}_{\boldsymbol{r}}$ and focus on the particle current.

$$\boldsymbol{J}_N = \frac{2}{(2\pi)^3} \int f \boldsymbol{v} d^3 k \tag{4.9}$$

By using the first-order development $f = f^{(0)} + f^{(1)}$, with $f^{(1)} \ll f^{(0)}$, we find that, in steady-state,

$$f^{(1)}(\boldsymbol{r}, \boldsymbol{k}) = -\tau(\boldsymbol{k}) \boldsymbol{v}(\boldsymbol{k}). \left(\boldsymbol{\nabla}\tilde{\mu} + \frac{\epsilon(\boldsymbol{k}) - (\mu - E_g/2)}{T} \boldsymbol{\nabla} T\right) \left(-\frac{\partial f^{(0)}}{\partial \epsilon}\right) \tag{4.10}$$

This expression allows us to compute explicitly the current, as $\boldsymbol{J}_N = 2/(2\pi)^3 \int f^{(1)} \boldsymbol{v} d^3k$ due to $f^{(0)}$ (resp. $\boldsymbol{v}$) being even (resp. odd) in $\boldsymbol{k}$. We find that $\boldsymbol{J}_N$ can be written as

$$\boldsymbol{J}_N = -\frac{L_{11}}{T}\boldsymbol{\nabla}\tilde{\mu} - \frac{L_{12}}{T^2}\boldsymbol{\nabla}T \tag{4.11}$$

with

$$\begin{cases} L_{11} = & \dfrac{T}{3}\displaystyle\int_0^{\infty} v^2\rho(\epsilon)\tau(\epsilon)\left(-\frac{\partial f^{(0)}}{\partial \epsilon}\right) d\epsilon \\ L_{12} = & \dfrac{T}{3}\displaystyle\int_0^{\infty} \left(\epsilon - (\mu - \frac{E_g}{2})\right) v^2\rho(\epsilon)\tau(\epsilon)\left(-\frac{\partial f^{(0)}}{\partial \epsilon}\right) d\epsilon \end{cases} \tag{4.12}$$

This allows us to compute explicitly the electrical conductivity and Seebeck coefficient (see Statement 4.5).

Statement 4.5. (Mott relations)
Boltzmann transport equation can be rewritten in terms of the usual linear current relations. This requires the relaxation time approximation, as well as a first order development. In this framework, transport coefficients can be expressed explicitly as [Pottier 2007, Goldsmid 2016]

$$\begin{cases} \sigma = & \dfrac{q^2}{3}\displaystyle\int_0^{\infty} v^2\rho(\epsilon)\tau(\epsilon)\left(-\frac{\partial f^{(0)}}{\partial \epsilon}\right) d\epsilon \\ S = & -\dfrac{1}{qT}\dfrac{\displaystyle\int_0^{\infty} \left(\epsilon - (\mu - \frac{E_g}{2})\right) v^2\rho(\epsilon)\tau(\epsilon)\left(-\frac{\partial f^{(0)}}{\partial \epsilon}\right) d\epsilon}{\displaystyle\int_0^{\infty} v^2\rho(\epsilon)\tau(\epsilon)\left(-\frac{\partial f^{(0)}}{\partial \epsilon}\right) d\epsilon} \end{cases} \tag{4.13}$$

where ρ is the carrier density of states (note that $\rho_e \neq \rho_h$ in general).

This forms the general framework in which we study thermoelectric transport of carriers. To use these formula and compute the theoretical value of transport parameters, few quantities need to be specified:

1. The group velocity v. It depends on the material but can be computed for any known band structure, as $v = \dfrac{1}{\hbar}\dfrac{\partial E}{\partial k}$.
2. same goes for the density of state $\rho(\epsilon)$.
3. $\partial f^{(0)}/\partial \epsilon$ depends only on the local carrier distribution through T and μ, but can be computed provided we know these quantities (for instance from PL measurements, see section 4.3).
4. τ is a phenomenological relaxation time. In this chapter, we will use a standard parametrization $\tau(\epsilon) = A_0\epsilon^{r_0}$, where A_0 and r_0 are free parameters[1] [Pottier

---

[1] This form comes naturally by computing the collision integral in the case where electrons are scattered

2007, Goldsmid 2016]. Note that since τ appears both on the numerator and denominator of S, the Seebeck coefficient is independent of A_0. However, the electrical conductivity (and mobility) is proportional to A_0. We assume that $r_{0,e} = r_{0,h} = r_0$, but allow relaxation times of electrons and holes to differ via A_0 (*i.e.* we allow $A_{0,e} \neq A_{0,h}$).

4.2.2.2 Transport coefficients of a QW in the parabolic band approximation

In the parabolic band approximation, these transport coefficients can be expressed as a function of the effective mass m. We discuss here the case of a QW, for which $\rho = m/(2\pi\hbar^2)$, which will prove useful in section 4.4.

In the Boltzmann approximation, Equation (4.13) can be integrated explicitly, and we obtain

$$\begin{cases} \sigma = \dfrac{q^2}{12\pi}(k_B T)^{r_0+1} A_0 \Gamma(r_0+2) \exp\left(\dfrac{\mu - E_g/2}{k_B T}\right) \\ S = -\dfrac{k_B}{q}\left(\dfrac{\mu - E_g/2}{k_B T} - (r_0+2)\right) \end{cases} \tag{4.14}$$

In this case, the carrier density writes $n = \frac{m}{2\pi\hbar^2} k_B T \exp\left(\frac{\mu - E_g/2}{k_B T}\right)$. Consequently, we can express the carrier mobility $\bar{\mu}$ as

$$\bar{\mu} = \frac{\sigma}{qn} = \frac{q\hbar^2}{6}(k_B T)^{r_0}\Gamma(r_0+2)\frac{A_0}{m} \tag{4.15}$$

When the system is degenerate, it is no longer possible to give an analytical expression for σ, n and S. However, the case of very degenerate systems (or metals) with $\mu \geq E_g/2 + 4k_B T$ can be treated approximately, as shown in [Goldsmid 2016]. We obtain

$$\begin{cases} \sigma = \dfrac{8q^2}{3\sqrt{2}}\left(\dfrac{2}{h^2}\right)^{3/2} A_0(\mu - E_g/2)^{r_0+1} \\ S = \dfrac{q}{e}\dfrac{\pi^2}{3}\dfrac{k_B}{e}(r_0+2)\dfrac{k_B T}{\mu - E_g/2} \end{cases} \tag{4.16}$$

and in particular, $S \xrightarrow[\mu \to \infty]{} 0$.

4.2.3 Ambipolar thermoelectric transport

Now that we have recalled the equations governing the thermoelectric transport of independendant carriers, we can focus on the specific case of semiconductors. In semiconductors, carrier diffusion is *bipolar*, as two carrier types (electrons and holes) must be considered.

Since holes and electrons are charged particles, they interact through the Coulomb potential. Two usual limiting cases are considered in the literature: (i) the *bipolar* case, in which the Coulomb interaction is neglected such that electrons and holes can be described

---

by ionized impurities ($r_0 = 3/2$) or neutral impurities ($r_0 = -1/2$) [Pottier 2007, Chapter 8.A]. The generalization of this form with an arbitrary exponent does not seem to rely on physical grounds. However, it allows to compute the electrical conductivity of a degenerate semiconductor easily as a function of r_0 [Pottier 2007, Eq. (5.10)].

independantly and (ii) the *ambipolar* case, in which the Coulomb interaction is intense, so that carriers must be transported at the same rate.

Systems relevant for HCSC applications are semiconductors subject to intense photogeneration so as to create the hot carriers. These excitation rates generate high carrier densities, which will interact strongly via Coulomb interaction. Therefore, they must be described in the ambipolar approximation (see Statement 4.6).

Statement 4.6. (Ambipolar transport and electroneutrality)

The transport of charges in a hot-carrier absorber must be described in the ambipolar approximation. Therefore, the electron and hole particle fluxes are equal everywhere, and there is no net charge current

$$\boldsymbol{J}_{N,e}(\boldsymbol{r}) = \boldsymbol{J}_{N,h}(\boldsymbol{r}) \Leftrightarrow \boldsymbol{J}_e + \boldsymbol{J}_h = \boldsymbol{0} \tag{4.17}$$

An important consequence of ambipolar transport is that local electroneutrality must hold. Indeed, (i) electron and hole generation and recombination rates are equal ($G_e = G_h$ and $R_e = R_h$) and (ii) the photogenerated population are much larger than doping. Thus, if the carriers are confined in the absorber, we must have

$$n_e(\boldsymbol{r}) = n_h(\boldsymbol{r}) \tag{4.18}$$

In the following, we first recall the standard treatment of ambipolar thermoelectric transport that can be found in most textbooks [Goldsmid 2016]. Then, we present the derivation adapted to the situation of HCSCs and discuss the differences with the textbook treatment.

4.2.3.1 Textbook derivation

The textbook treatment of ambipolar transport in thermoelectric semiconducting systems is done in the absence of illumination. In the dark, the electrochemical potential of electrons and holes is the same, *i.e.* the Quasi-Fermi-Level Splitting (QFLS) is negligible. In other words, with our conventions (see section 2.1.1), $\boldsymbol{\nabla}\tilde{\mu}_e = -\boldsymbol{\nabla}\tilde{\mu}_h \equiv \boldsymbol{\nabla}\tilde{\mu}$. In this case, using Equation (4.6), the total electrical current writes

$$\boldsymbol{J}_e + \boldsymbol{J}_h = (\sigma_e + \sigma_h)\boldsymbol{\nabla}\tilde{\mu} - (\sigma_e S_e + \sigma_h S_h)\boldsymbol{\nabla}T = \boldsymbol{0} \tag{4.19}$$

where the last equality reflects the ambipolar assumption.

Therefore this system is described with an ambipolar Seebeck coefficient that can be written as a weighted average of the electron and hole Seebeck coefficients [Goldsmid 2016]

$$S_{\text{amb}} = \frac{|\boldsymbol{\nabla}\tilde{\mu}|}{|\boldsymbol{\nabla}T|} = \frac{\sigma_e S_e + \sigma_h S_h}{\sigma_e + \sigma_h} \tag{4.20}$$

In principle, this derivation is done in the dark, in the absence of a QFLS and electrical conductivities and Seebeck coefficients depend only on the doping of the material and on the lattice temperature. However, the condition $\boldsymbol{\nabla}\tilde{\mu}_e = -\boldsymbol{\nabla}\tilde{\mu}_h$ holds true in the case of a homogeneous illumination with constant QFLS across the device. Therefore, Equation (4.20) is still valid under homogeneous illumination. In this case, sometimes called *photo-Seebeck* effect [Okazaki *et al.* 2012], the Seebeck coefficients will depend not only on the material, but also on the illumination conditions through the carrier distributions.

This fundamental remark is illustrated in Figure 4.1a, which shows the variation of S_e, S_h and S_{amb} with the reduced QFLS $\eta = \dfrac{\Delta\mu - E_g}{k_B T}$. Note that in this representation, we assume electroneutrality to compute μ_e and μ_h from $\Delta\mu$ and $T = 300$ K.

By definition, $S_e < 0$, $S_h > 0$, and $\sigma_{e,h} > 0$. Therefore, the ambipolar Seebeck coefficient S_{amb} must lie in between Seebeck coefficients of electrons and holes. The weights in the average of S_{amb} depend on the ratio between the electrical conductivities σ_e/σ_h. As was already discussed in previous section, σ_i is proportional to the relaxation time of carrier i ($\sigma_i \propto A_{0,i}$). Therefore, S_{amb} depends on the ratio of electron and holes relaxation times $A_{0,e}/A_{0,h}$. Therefore we represent several values of this ratio in Figure 4.1a. Strictly speaking, S_{amb} depends also on the scaling of the relaxation time, r_0. However, this variation is much weaker than the one with the relaxation time ratio, and is not represented here.

The expression of the ambipolar Seebeck coefficient can be simplified in the non degenerate regime Equation (4.14). In this case, $S_i = -\dfrac{k_B}{q_i}\left(\dfrac{\mu_i - E_g/2}{k_B T} - (r_0 + 2)\right)$ is linear in μ_i and hence in $\Delta\mu$ using electroneutrality. Also because of electroneutrality, Equation (4.20) can be expressed as a function of the carrier mobilities $\bar{\mu}_i \propto A_{0,i}/m_i$, and therefore

$$S_{\mathrm{amb}} = \frac{\dfrac{A_{0,e}}{m_e} S_e + \dfrac{A_{0,h}}{m_h} S_h}{\dfrac{A_{0,e}}{m_e} + \dfrac{A_{0,h}}{m_h}} \tag{4.21}$$

Therefore, the non-degenerate ambipolar Seebeck coefficient is a linear function of the QFLS, and its slope is controlled by the ratio $(m_e A_h)/(m_h A_e)$.

4.2.3.2 Derivation for an inhomogeneous illumination

We present here our original contribution. We imagine a case where illumination is not homogeneous. An extreme example is a PL experiment with point illumination, as depicted in Figure 4.3.

Because the illumination is not homogeneous, the QFLS is not constant and therefore the electrochemical potentials of electrons and holes are not parallel one to the other. In this case, the particle currents write

$$\boldsymbol{J}_{N,i} = -\frac{\sigma_i}{q_i}\boldsymbol{E} - \frac{\sigma_i}{q_i^2}\boldsymbol{\nabla}\mu_i - \frac{\sigma_i S_i}{q_i}\boldsymbol{\nabla} T \tag{4.22}$$

To investigate this system, we first relate the gradient of chemical potential of electrons and holes by using electroneutrality. Because HCSCs operate at large excitation powers, we keep the general form of electroneutrality and do not make use of Boltzmann approximation (see Appendix B for details).

$$\boldsymbol{\nabla}\mu_h = g_1(\mu_e, \mu_h, T)\boldsymbol{\nabla}\mu_e + g_2(\mu_e, \mu_h, T)\boldsymbol{\nabla} T \tag{4.23}$$

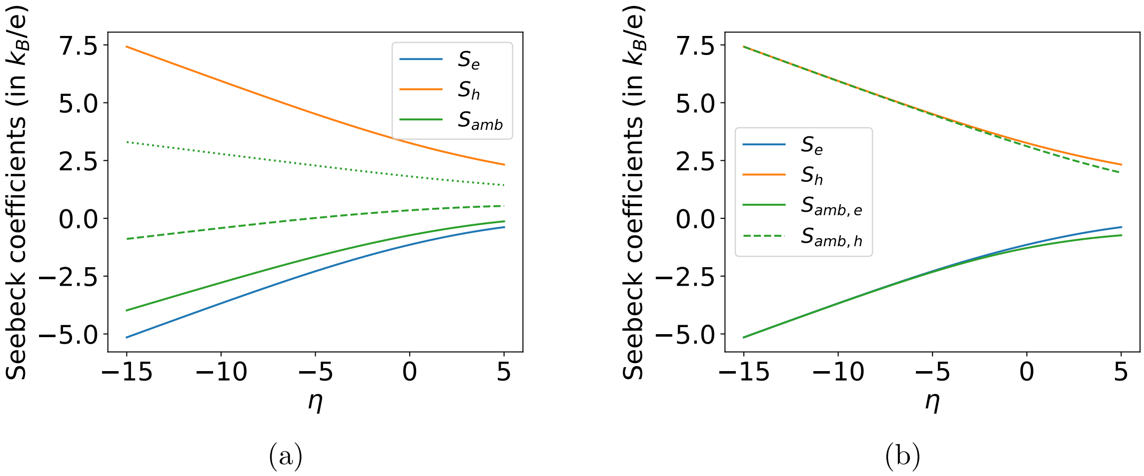

(a) (b)

Figure 4.1: *Ambipolar Seebeck coefficients computed from Boltzmann transport equation in the relaxation time approximation (Equation (4.13)) assuming (a) standard homogeneous illumination or (b) inhomogeneous illumination as developed in this chapter. In panel (a), we report three different values of the hole relaxation time:* $A_{0,h} = A_{0,e}$ *(plain),* $A_{0,h} = 5\,A_{0,e}$ *(dashed) and* $A_{0,h} = 20\,A_{0,e}$ *(dotted). The derivation is done using the parameters of sample 5006 (see section 2.4), with* $T = 300$ K *and* $r_{0,e} = r_{0,h} = -1$.

where

$$g_1(\mu_e,\mu_h,T) = \frac{m_e}{m_h}\frac{\displaystyle\int_0^\infty \frac{\partial h}{\partial \mu}(x,\mu_e,T)dx}{\displaystyle\int_0^\infty \frac{\partial h}{\partial \mu}(x,\mu_h,T)dx} \tag{4.24}$$

$$g_2(\mu_e,\mu_h,T) = \frac{\displaystyle\frac{m_e}{m_h}\int_0^\infty \frac{\partial h}{\partial T}(x,\mu_e,T)dx - \int_0^\infty \frac{\partial h}{\partial T}(x,\mu_h,T)dx}{\displaystyle\int_0^\infty \frac{\partial h}{\partial \mu}(x,\mu_h,T)dx} \tag{4.25}$$

$$h(x,\mu,T) = \frac{1}{1+\exp\left(x+\dfrac{E_g/2-\mu}{k_BT}\right)} \tag{4.26}$$

The functions g_1 and g_2 have complex expressions, but they can be evaluated numerically provided that carrier distributions (*i.e.* parameters μ_e, μ_h and T) are known. Figure 4.2 presents the variations of g_1 and g_2 with the reduced QFLS η. Note that in the non-degenerate regime, $g_1 = 1$ and $g_2 = -k_B\ln(m_h/m_e)$, such that we recover the standard electroneutrality relation $\mu_h = \mu_e - k_BT\ln(m_h/m_e)$ [Wurfel and Wurfel 2016].

Using this simplification, we evaluate the electrostatic field necessary to ensure that transport is ambipolar (*i.e.* without net transport of charges). A similar derivation was proposed by [Price 1955] in the homogeneous case, and we extend it here to our inhomogeneous situation. We obtain

$$\boldsymbol{E} = \frac{1}{e}\frac{g_1\sigma_h-\sigma_e}{\sigma_e+\sigma_h}\boldsymbol{\nabla}\mu_e + \left(\frac{\sigma_eS_e+\sigma_hS_h}{\sigma_e+\sigma_h}+\frac{\sigma_h}{\sigma_e+\sigma_h}\frac{g_2}{e}\right)\boldsymbol{\nabla}T \tag{4.27}$$

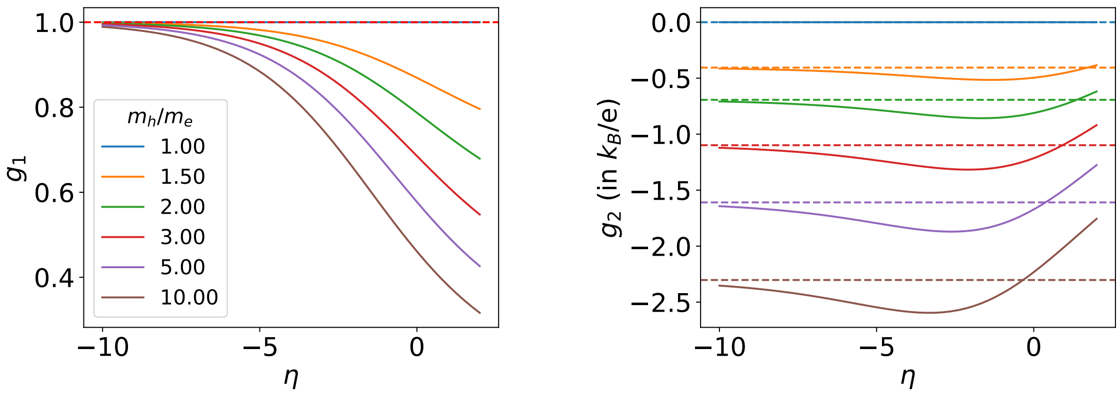

(a) (b)

Figure 4.2: *Representation of the functions involved in the electroneutrality relation (see Equation (4.23)). (a)* g_1 *and (b)* g_2*, displayed as a function of the reduced QFLS, assuming* $T = 300$ K*. Different ratios of effective mass* m_h/m_e *are represented. Dashed lines indicate the asymptotes for a non-degenerate system.*

Note that we could obtain a similar expression with $\boldsymbol{\nabla}\mu_h$. However, since transport is ambipolar, it is strictly equivalent to consider electrons or holes.

Result 4.1. (Ambipolar transport coefficients)
Injecting the expression of the electric field in Equation (4.6), we find that the ambipolar hot-carrier current can be written without the explicit electric field [Vezin *et al.* 2024b]. This requires to introduce ambipolar electrical conductivities $\sigma_{\text{amb,i}}$ and Seebeck coefficients $S_{\text{amb,i}}$

$$\boldsymbol{J}_N = \boldsymbol{J}_{N,e} = \boldsymbol{J}_{N,h} = -\frac{\sigma_{\text{amb,i}}}{e^2}\boldsymbol{\nabla}\mu_i - \frac{\sigma_{\text{amb,i}}S_{\text{amb,i}}}{q_i}\boldsymbol{\nabla}T \tag{4.28}$$

where

$$\begin{cases} \sigma_{\text{amb,e}} = \dfrac{\sigma_e\sigma_h}{\sigma_e+\sigma_h}(1+g_1), \quad \sigma_{\text{amb,h}} = \dfrac{\sigma_e\sigma_h}{\sigma_e+\sigma_h}(1+1/g_1) \\ S_{\text{amb,e}} = \dfrac{e(S_e-S_h)-g_2}{e(1+g_1)}, \quad S_{\text{amb,h}} = \dfrac{e(S_h-S_e)-g_2/g_1}{e(1+1/g_1)} \end{cases} \tag{4.29}$$

This is the main result of this theoretical investigation. It shows that in the context of HCSCs, a full description of the ambipolar transport of electrons and holes resembles the usual thermoelectric equations with effective ambipolar coefficients. This derivation was done in the context of HCSCs, but could also be useful to study photothermoelectric experiments, and particularly those of the carrier-gradient type [Limpert *et al.* 2017].

Note that in our case, contrary to the textbook treatment of *homogeneous* thermoelectric transport (see section 4.2.3.1), it is not possible to attribute a single effective electrical conductivity nor Seebeck coefficient to electrons and holes. This is a consequence of electroneutrality. In the homogeneous treatment, we assumed that $\boldsymbol{\nabla}\mu_e = -\boldsymbol{\nabla}\mu_h$. In the inhomogeneous case developed here, electroneutrality imposes a completely different relation $\boldsymbol{\nabla}\mu_e = \boldsymbol{\nabla}\mu_h + k_B \ln(m_h/m_e)\boldsymbol{\nabla}T$ (presented here in the non degenerate case).

Figure 4.1b represents the Seebeck coefficient of electrons and holes computed from Equation (4.13) with $r_0 = 1$, as well as the corresponding ambipolar Seebeck coefficient in the inhomogeneous case. Note how this situation differs from the homogeneous derivation displayed in Figure 4.1a. First, inhomogeneous ambipolar Seebeck coefficients no longer depend on the electrical conductivities. Therefore they not depend on the pre-factors of the relaxation time $A_{0,e}$ and $A_{0,h}$. Second, in the non-degenerate case ($\eta \ll -1$),

$$S_{\mathrm{amb,i}} = \frac{k_B}{2e}\left[\mathrm{sign}(-q_i)(\eta - 2(r_0+2)) + \ln\left(\frac{m_h}{m_e}\right)\right] \tag{4.30}$$

Consequently, the inhomogeneous ambipolar Seebeck coefficients exhibit a universal slope $\pm k_B/(2e)$ as a function of η.

We now understand how to describe theoretically the transport of hot carriers in inhomogeneous illumination conditions. In the following, we will use this theory to measure hot-carrier diffusion with a hyperspectral PL experiment performed with a point illumination. We first report the experiment design in section 4.3, and explain how to analyse the data to map carrier distributions. Then, we discuss how to derive transport coefficients from this experiment in section 4.4. In particular, we determine the ambipolar Seebeck coefficient and validate the theory presented above.

4.3 Imaging carrier distributions with photoluminescence

In this section, we propose a PL experiment to image hot-carrier transport in a QW absorber. This data will be used to validate the ambipolar transport formalism established in the previous section (see section 4.4).

Imaging broadband PL has been used to measure isothermal diffusion [Paget *et al.* 2012]. The addition of spectral resolution makes it possible to map simultaneously carrier density and temperature [Rodière 2014]. Such a hyperspectral technique was used to probe hot-carrier transport before [Gibelli *et al.* 2016c], but only with a rudimentary transport model.

4.3.1 Description of the experiment

Using our absolutely calibrated hyperspectral imager described in section 2.2, we record spatially resolved PL spectra. Therefore, with one single acquisition, we can map the temperature and QFLS in a hot-carrier absorber [Esmaielpour *et al.* 2020]. A schematic of this experiment is provided in Figure 4.3.

Point illumination In order to see carrier diffusion, we need to use a laser illumination as small as possible (so-called *point illumination*). Indeed, if the laser sport size is much smaller than the carrier diffusion length, there will be a sizeable difference between the PL spot size and the laser spot size. This configuration is represented in Figure 4.3.

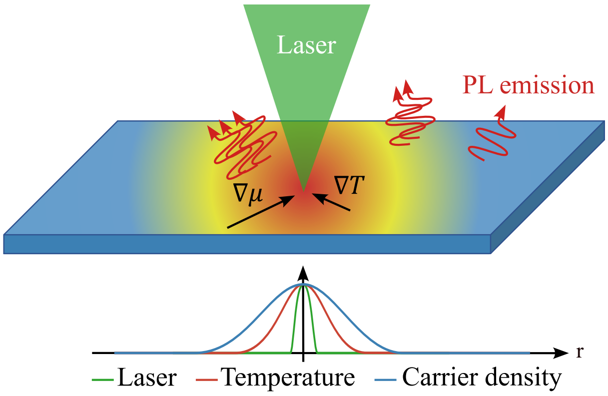

Figure 4.3: *Schematic representation of the hyperspectral PL experiment allowing to measure hot-carrier transport. We use a point illumination to photogenerate hot carriers at the center of the sample. In this configuration, carriers move due to a concentration gradient ($\boldsymbol{\nabla}\mu$) and a temperature gradient ($\boldsymbol{\nabla}T$). We collect spatially and spectrally resolved PL to probe the carrier distribution at different distances from the center.*

Therefore, we upgraded our experimental setup to achieve a laser spot as small and circular as possible. The details of this configuration are provided in section 2.2.1.

Spectrometer and sample We investigate the sample described in section 2.4, which is an InGaAsP/InGaAsP single QW which exhibits strong hot-carrier effect. We studied this material using a NIR hyperspectral imager equipped with a NIRvana 640 (InGaAs camera). This setup has a spectral resolution of 2 nm. In combination with the objective lens described above, this system has a spatial resolution (sparrow criterion) of 1.7 µm imposed by diffraction. However, the resolution of the camera is below this limit, as the pixel are $\sim$ 450 nm in size.

Experiment plan and data analysis To probe several different excitation regimes and to characterize the hot-carrier effect in this sample, we used 9 excitation intensities ranging from 6.3×10^3 to 2.3×10^5 W.cm^{-2} (*i.e.* several 10^4 to few 10^6 suns). For each excitation intensity, we measured a hyperspectral cube of size $\sim 30 \times 30$ µm, and spectral range $1050 - 1600$ nm (2 nm resolution).

Since the InGaAs camera has low Signal to Noise Ratio (SNR) (see section 2.2.3), we used the High Dynamical Range (HDR) method described in section 2.2.2. Every acquisition was repeated 5 times with exposure times ranging from 1 to 50. This allowed us to push the SNR close to 10^{-5}, which allowed us to resolve proper PL spectra up to $\sim$ 10 µm (see Figure 4.4b).

By ensuring that the laser beam was circular even after being focused, we could take advantage of the invariance by rotation of the system to integrate radially the PL spectra. This allowed to increase the SNR even further, and to reduce the diffusion problem to only one dimension, which is much simpler.

Thanks to all these steps, we were able to analyse spectra ranging from 0 to 13 µm, *i.e.* 30 spectra per excitation intensity. Our dataset is therefore composed of 270 PL spectra. Few spectra are represented in Figure 4.4.

Figure 4.4a represents spectra at the center of the PL spot for a selected set of excitation intensities. Figure 4.4b represents spectra at 5 different radii of the PL spot for a given excitation intensity $I_{\text{exc}} = 4.1 \times 10^4$ W.cm^{-2}. The peak around 0.82 eV is attributed to the emission of the QW, while the peak at 1.05 eV is consistent with emission from the barrier [Nguyen *et al.* 2018]. The elbow visible around 0.89 eV is attributed to the emission of an excited state of the QW.

The shape of QW emission spectrum depends strongly on the excitation intensity, which is indicative of a stronger hot-carrier effect and/or band filling effect at high laser intensities. Similarly, the shape of QW emission spectrum depends on the distance to the laser, which is indicative of a stronger hot-carrier effect and/or band filling effect in the center.

These spectra were analysed using a full fit technique, whose details can be found in section 2.3.4.

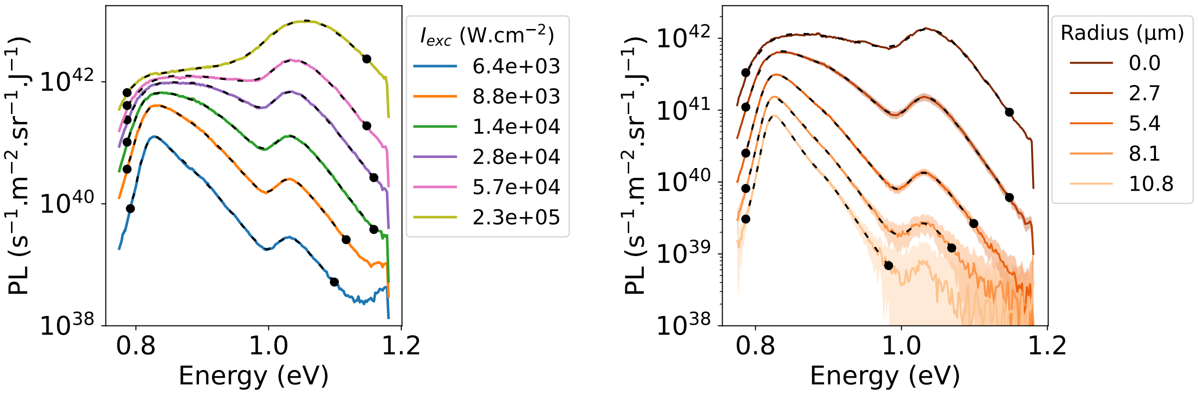

(a)

(b)

Figure 4.4: *PL spectra of sample 5006. (a) Spectra at the center of the laser spot for different excitation intensities. Not all excitation intensities are represented for clarity. (b) Angularly integrated spectra for increasing radii at a single excitation intensity* $I_{exc} = 4.1 \times 10^4$ *W.cm*$^{-2}$. *Pale envelope represents the dispersion of the spectra aggregated during angular integration. Dashed lines represent the result of a full fit.*

4.3.2 Carrier distribution profiles

4.3.2.1 Results and discussion

From the measurement of $T(r)$ and $\Delta\mu(r)$, and owing to local electroneutrality, we deduce the local carrier density $n(r) = n_e = n_h$ and the corresponding chemical potentials $\mu_e(r)$ and $\mu_h(r)$. These measurements are all reported in Figure 4.5. Note that we do not make assumptions on the degeneracy of the system in this case. Hence we compute the carrier density and the chemical potentials of electrons and holes with the full Fermi-Dirac distributions.

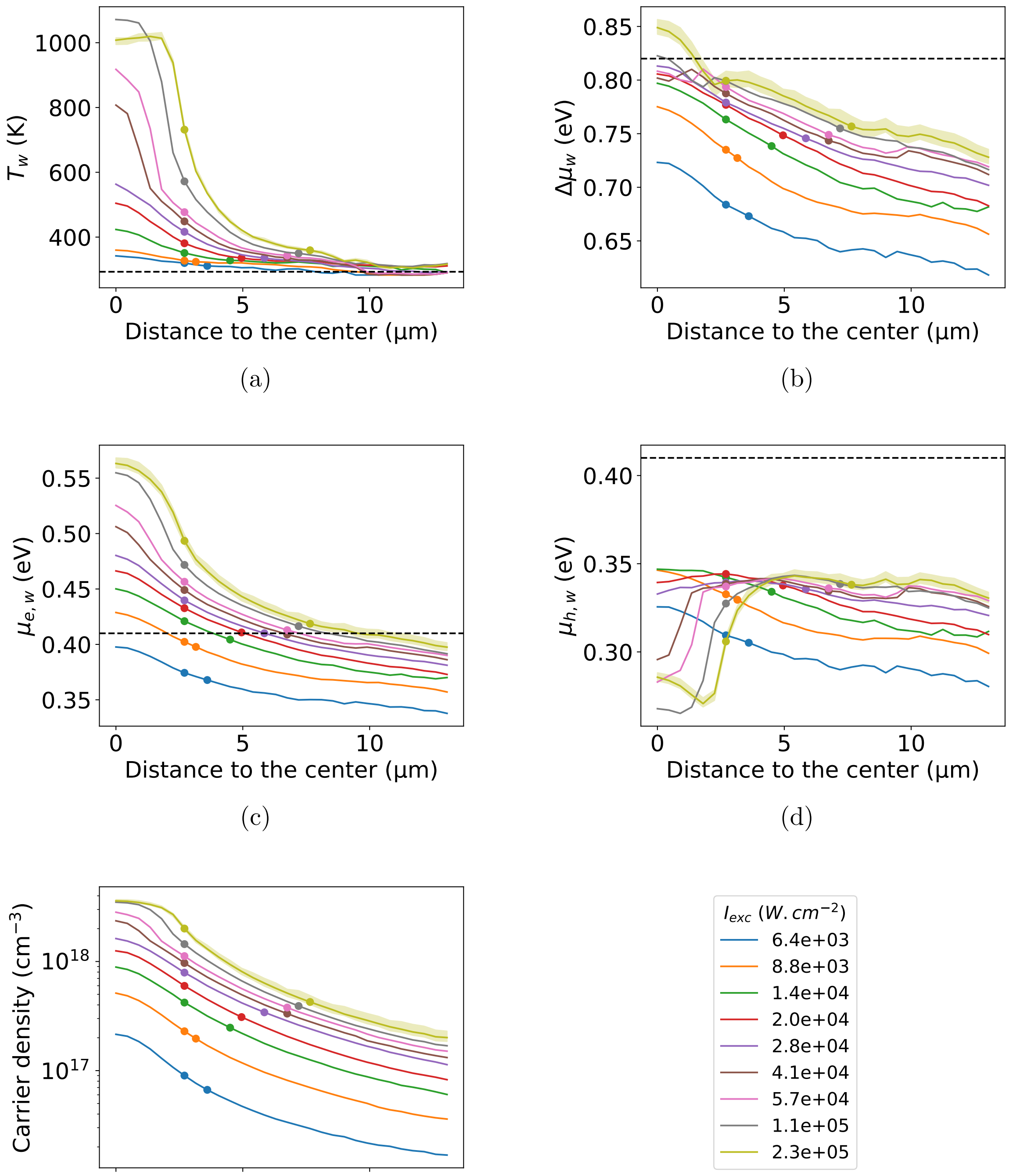

(a)

(b)

(c)

(d)

(e)

(f)

Figure 4.5: *Spatial variations of (a) carrier temperature, (b) QFLS, (c) electrons chemical potential, (d) holes chemical potential, (e) carrier concentration for increasing excitation intensities* I_{exc}. *Legend is shown in (f). Colored dots represent the boundaries of region II defined in section 4.4.3 for all excitation intensities. Dashed lines indicate room temperature* $T_{\text{amb}} = 293$ *K in (a), QW bandgap* ($E_g = 0.82$ eV) *in (b), position of the conduction band* ($E_C = 0.41$ eV) *in (c) and position of the valence band* ($E_V = 0.41$ eV) *in (d). Pale green region indicates the estimated errorbars for the highest excitation intensity. Similar errorbars are expected at all intensities but are not represented to enhance readability.*

Figure 4.5a shows the spatial profiles of carrier temperature for increasing laser intensities. Temperature is shown to increase with increasing excitation intensity, as we expect from a hot-carrier absorber – except for a few incoherent spectra at highest intensity and close to the center. In this range of power, carrier temperature reach more than 1000 K. It is also shown to decrease as we look further and further away from the center.

Result 4.2. (Hot-carrier diffusion length)
At distances larger than 10 µm, carriers are thermalized with the lattice at room temperature regardless of the excitation intensity [Vezin *et al.* 2024b]. At high excitation intensities, carrier temperature remains above room temperature for typically $6-8$ µm, much larger than the laser radius. Therefore we report hot-carrier diffusion length in the order of few µm, several times the value previously reported in monolayers ($\sim$ 500 nm) [Ruzicka *et al.* 2010a, Yuan *et al.* 2017], in perovskites thin films ($\sim$ 230 nm) [Guo *et al.* 2017] and in nanowires ($\sim$ 300 nm) [Fast *et al.* 2022].

The QFLS profiles for increasing excitation intensity are presented in Figure 4.5b. Unsurprisingly, the QFLS increase with increasing power, and decreases with increasing distance to the generation region. However, few points at largest injection are incoherent because of noise introduced by our HDR method.

Electron (resp. hole) chemical potential are presented in Figure 4.5c (resp. Figure 4.5d). At high excitation intensities, the electrons form a completely degenerate electron gas as their chemical potential is well above the conduction band ($E_C \simeq 0.41$ eV). However, the hole distribution remains non degenerate due to the discrepancy in effective masses. Note that despite the visible drop of μ_h close to the center and at high intensity, carrier density is decreasing with increasing distance to the center (see Figure 4.5e). This is simply because the drop of μ_h is compensated by a large increase of carrier temperature in this region.

Finally, spatial profiles of carrier density are presented in Figure 4.5e. Carrier density is increasing with increasing excitation intensity, as absorbing more photons will promote more carriers in the bands. Additionnally, carrier density decreases with increasing distance to the center. This is expected from a point illumination experiment, as carriers are photogenerated at the center, and then diffuse to further distances while recombining. Note that if the thermoelectric transport is strong enough, it is possible in principle to observe a carrier density smaller at the center than at the edge [Park *et al.* 2021]. In the experiment reported here, such an extreme effect did not occur.

4.3.2.2 Uncertainties

We distinguish two types of uncertainty, represented schematically on Figure 4.6. The first one consists of *position-dependent* uncertainties. For instance, noise in the PL spectra and partial overfitting introduce a random uncertainty of approximately $1-2$ % over the determination of carrier temperature and QFLS. The uncertainty on temperature was estimated based on the region $r > 10$ µm, where carriers are thermalized at ambient temperature. Since PL signal is roughly proportional to $\exp((\Delta\mu - E_g)/(k_B T))$, carrier temperature and QFLS are anti-correlated by the fitting procedure. Therefore, random noise on the carrier temperature translates into a random noise on the QFLS.

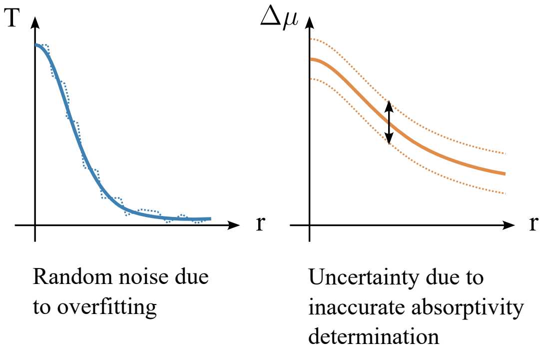

Figure 4.6: *Schematic representation of the two uncertainty sources affecting the determination of transport coefficients.*

The second consist of *global* uncertainties, which affect all measurements similarly, irrespective of the position and excitation intensity. These uncertainties are less crucial, since they will not be magnified by the computation of gradients. The uncertainty on the determination of the absorption coefficient (see section 2.1.4) leads to an estimated ± 20 meV uncertainty in the QFLS.

4.4 Measuring transport coefficients

To measure the transport coefficients from our PL experiment, we distinguish three different regimes from which we extract different information (see Fig. 4.7).

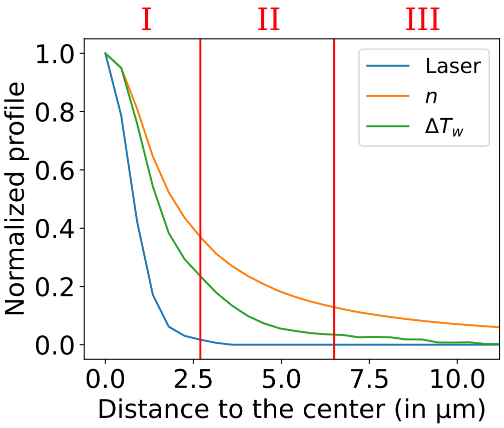

Figure 4.7: *Normalized spatial profiles of laser, carrier concentration and carrier temperature, measured at high excitation intensity* $I_{exc} = 5.7 \times 10^4$ $W.cm^{-2}$. *Vertical lines highlight three regimes: (III) isothermal diffusion, where electrical conductivity may be measured, (II) thermoelectric diffusion, where Seebeck coefficient may be measured, (I) region dominated by generation and not used in this study.*

In the central region (I), the generation term in the continuity equation (Equation (4.1)) is significant and carrier density is highest. We estimate that this region spans until the laser intensity reaches 5 % of its maximal intensity, namely $r = 2.7$ µm. Because of difficulties to model the generation rate with precision in such a complex structure, we discard this region from our analysis.

Far from the center (III) (typically 3.6 − 7.7 µm), carriers have relaxed towards the lattice temperature, and the concentration profile is determined by isothermal diffusion. In this isothermal region, it is possible to measure both the recombination rate (section 4.4.1) and electrical conductivity up to a multiplicative constant (section 4.4.2). Note that the begining of this isothermal region depends greatly on excitation power, as hotter carriers tend to diffuse further (see Figure 4.5a).

In between these regions (II), carriers experience a significant temperature gradient and their transport is induced not only by the charge concentration gradient, but also by thermoelectric effects, which grants access to Seebeck coefficient.

The boundaries of these regions are represented for every excitation intensity in Fig. 4.5.

4.4.1 Recombination

Toolbox 4.1. (Standard recombination rates)
There are three main recombination routes for carriers in semiconductors.

The first one is the celebrated *Shockley-Read-Hall recombination*, which describes trap-assisted recombinations. This kind of recombination is described by [Shockley and Read 1952]

$$R_{\mathrm{SRH}} = \frac{n_e n_h - \bar{n}_i^2}{\tau_e n_h + \tau_h n_e} \simeq \frac{n}{\tau_e + \tau_h} \tag{4.31}$$

where

$\bar{n}_i$ = Intrinsic carrier density ($\bar{n}_i \propto \exp(-E_g/k_B T)$)
τ_i = Recombination time of carrier i

The simplification is obtained because, in our case, $n_e = n_h = n \gg n_i$. It explains why SRH recombination is sometimes called *monomolecular* recombination.

The second recombination rate is the *radiative recombination*, which describes the emission of a photon by a electron-hole pair. A precise description of this recombination rate is provided by the Generalized Planck Law (GPL) (see Equation (2.19)). However, this form is not practical as it depends on a large number of parameters. In Boltzmann regime, the GPL reduces to

$$R_{\mathrm{rad}} = \int_{\theta=0}^{\pi} \left[\int_{E=0}^{\infty} I_{\mathrm{PL}}(E) dE \right] 2\pi \cos\theta d\theta \simeq B n_e n_h = B n^2 \tag{4.32}$$

Hence it is sometimes called *quadratic* or *bimolecular recombination.*

The third and last recombination rate is *Auger recombination*, which describes the recombination of a electron-hole pair to promote an electron high in the conduction band. It is of course possible to promote a light hole in the valence band instead of an electron. However, the promotion of a heavy hole is forbidden by momentum conservation. The description of Auger process can become very complex, especially when several conduction/valence bands are taken into account [Agrawal and Dutta 1993]. We stick here to a simple description with only one band

$$R_{\text{Auger}} \simeq C_e n_e^2 n_h + C_h n_e n_h^2 = C n^3 \tag{4.33}$$

To distinguish whether recombinations are mostly monomolecular, bimolecular or trimolecular, we turn to the region III, far from the center, where diffusion is isothermal ($\boldsymbol{\nabla} T = \mathbf{0}$) and photogeneration is negligible.

In this region, carrier conservation (Equation (4.1)) writes

$$R = \boldsymbol{\nabla}.\left(\frac{\sigma_{\text{amb,e}}}{e^2}\boldsymbol{\nabla}\mu_e\right) \tag{4.34}$$

Using the relation $\sigma_i = q_i \bar{\mu}_i n_i$ and Equation (4.29), the ambipolar electrical conductivity can be written in terms of carrier mobilities $\bar{\mu}_i$ as

$$\sigma_{\text{amb,e}} = (1+g_1)\frac{2(-\bar{\mu}_e)\bar{\mu}_h}{\bar{\mu}_h - \bar{\mu}_e} en \equiv (1+g_1)\gamma_e n \tag{4.35}$$

Assuming that γ_e is slowly with the carrier densities (in comparison to n), the dominant term in the conservation equation is

$$R \simeq \frac{\gamma_e}{e^2}\boldsymbol{\nabla}.\left((1+g_1)n\boldsymbol{\nabla}\mu_e\right) \tag{4.36}$$

Since we measured the spatial profiles of n, μ_e and μ_h (see Figure 4.5), we can compute the right hand side of this equation. This term can then be compared to typical scalings of the recombination rate (see Toolbox 4.1), as presented on Figure 4.8.

Result 4.3. (Dominant Auger recombinations)
Figure 4.8 indicates that *Auger recombinations* are dominant in our system. This is actually consistent with the high carrier densities measured in our PL experiment, as $n \sim 10^{17} - 10^{18}$ cm^{-3} (see Figure 4.5e).

4.4.2 Electrical conductivity

Once radiative recombinations are determined, electrical conductivity can be measured. Indeed, since Auger recombinations dominate, Equation (4.36) becomes

$$C n^3 = \frac{\gamma_e}{e^2}\boldsymbol{\nabla}.\left((1+g_1)n\boldsymbol{\nabla}\mu_e\right) \tag{4.37}$$

Therefore if we know the value of C, we can determine γ_e. For our specific quaternary QW, it is difficult to find tables of the Auger recombination rate. It would be possible to

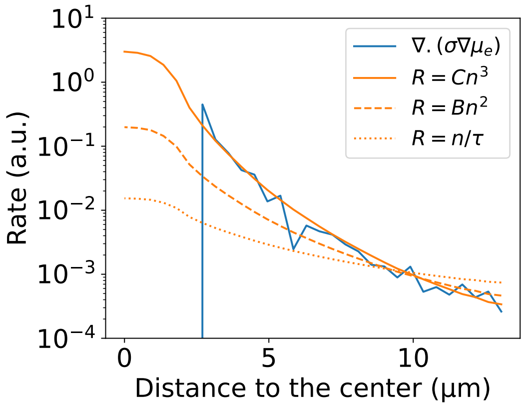

Figure 4.8: *Diffusion rate and recombination rate in the isothermal regime (Equation (4.34)), assuming various dominant recombinations mechanisms (monomolecular, bimolecular or Auger). Far from the center, carrier conservation imposes that blue and orange lines should collapse one to another. Profiles are established based on a high intensity acquisition* $I_{exc} = 1.1 \times 10^5$. *W.cm*$^{-2}$*).*

compute the value of C [Agrawal and Dutta 1993], but this is beyond the scope of this manuscript. Therefore we will restrict ourselves to the determination of the ratio C/γ_e, which means that we will only know the conductivity up to a multiplicative constant.

Figure 4.9 presents the determination of C/γ_e. As is visible on this figure, the experimental noise means that there is an uncertainty of ± $15 - 20$ % over the determination of C/γ_e.

We find that the ratio C/γ_e decreases with increasing excitation intensity, and has typical order of magnitude $10^{-22} - 10^{-20}$ $\mathrm{m^4.V.s^{-1}.A^{-1}}$. This is consistent with typical values of the Auger coefficient in InGaAsP quantum wells $C \sim 10^{-27}$ $\mathrm{cm^6.s^{-1}}$ [Smith *et al.* 1985] and mobility $\bar{\mu}_e \sim 10^{3-4}$ $\mathrm{cm^2.(Vs)^{-1}}$ [Agrawal and Dutta 1993].

4.4.3 Seebeck coefficient

4.4.3.1 Computation and uncertainties

The ambipolar Seebeck coefficient can be computed from the analysis of region II. This time, the temperature gradient is no longer negligible. We assume that the variations of $S_{\mathrm{amb,e}}$ are sufficiently small, such that the contribution of $\boldsymbol{\nabla} S_{\mathrm{amb,e}}$ to transport is negligible. Under this assumption, Equation (4.1) can be rewritten to express the ambipolar Seebeck coefficient from measured quantities as:

$$S_{\mathrm{amb,e}} \simeq -\frac{-\dfrac{C}{\gamma_e}n^3 + \dfrac{1}{e^2}\boldsymbol{\nabla}.\left((1+g_1)n\boldsymbol{\nabla}\mu_e\right)}{\dfrac{1}{q_e}\boldsymbol{\nabla}.\left((1+g_1)n\boldsymbol{\nabla}T\right)} \tag{4.38}$$

where the quantity C/γ_e has been estimated as presented in section 4.4.2. To compute uncertainty on this ambipolar Seebeck coefficient, we consider the following error sources: (i) random noise on the temperature profiles and random shift of the QFLS profiles as explained in section 4.3.2 (ii) uncertainty on the estimate of C/γ_e as explained in

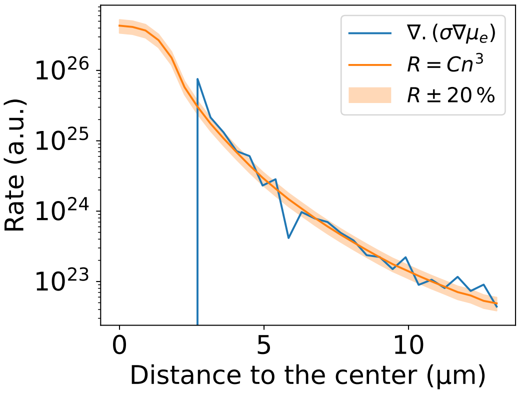

Figure 4.9: *Diffusion rate and Auger recombination rate determined from PL measurement. The parameter C/γ_e is obtained by balancing the right and left hand side of Equation (4.36) at large distances ($r > 8$ µm). This example is obtained with high excitation intensity $I_{exc} = 1.1 \times 10^5$ W.cm^{-2}. Orange line represents the best fit for $r > 8$ µm, while pale yellow region indicates the ± 20 % uncertainty.*

section 4.4.1. Instead of computing a cumbersome error propagation, we simulate noisy profiles of T, μ_e and n, and compute the ambipolar Seebeck coefficient on these profiles. By taking the standard deviation of $S_{\text{amb,e}}$ over several realizations, we obtain the errobars shown in Figure 4.10.

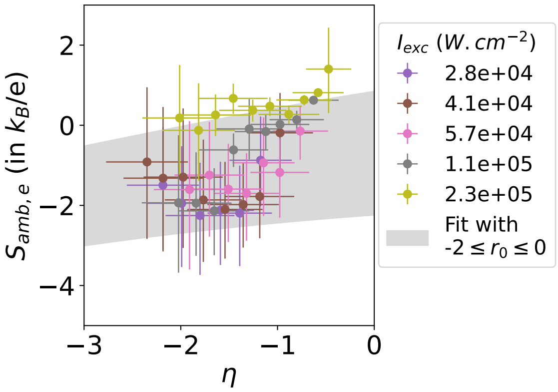

Figure 4.10: *Ambipolar Seebeck coefficient $S_{\text{amb,e}}$ determined from PL measurements (from Equation (4.38)), plotted versus the corresponding reduced QFLS η. Grey region indicates the values modelled from Boltzmann transport equation (see Equation (4.13)) with $-2 \leq r_0 \leq 0$.*

4.4.3.2 Results

Experimental determination of the ambipolar Seebeck coefficient at all the relevant excitation conditions is presented in Figure 4.10 and plotted versus the reduced QFLS η. Points with uncertainty larger than $4k_B/e$ are discarded. Note that the four lowest excitation intensity files exhibit a rather small temperature gradient. Therefore, after adding noise to the temperature profiles, the uncertainties over the determination of $S_{\mathrm{amb,e}}$ became very high. This explains why those four files are not shown on the figure. This fact also explains why we explore such a small region for η. Symmetrically, the points at highest excitation intensity (shown in grey and green) have much larger temperature gradient, hence lower errorbars than the others.

The ambipolar Seebeck coefficient takes values between -3 and 1 k_B/e, which is the typical order of magnitude of Seebeck coefficients in QWs [Hicks *et al.* 1996]. Such a large value is surprising however for an *ambipolar* Seebeck coefficient. That is because the usual derivation of ambipolar Seebeck coefficient is done in *dark conditions* and leads to $S_{\mathrm{amb}} = (\sigma_e S_e + \sigma_h S_h)/(\sigma_e + \sigma_h)$ [Goldsmid 2016]. In such case, the Seebeck coefficients of electrons and holes compensate each other. However, this chapter treats the case of *strong photogeneration*, and therefore our ambipolar Seebeck coefficient is different in nature. In our case, Seebeck coefficients of electrons and holes *add up*, as reported in Equation (4.29). Therefore, we expect that our ambipolar Seebeck coefficient should be of the same order of magnitude than the one of electrons and holes.

4.4.3.3 Quantitative discussion

For a more quantitative discussion, we make use of Boltzmann transport equation in the relaxation time approximation, which has been presented in section 4.2.2. In the approach described in Equation (4.13), the ambipolar Seebeck coefficient $S_{\mathrm{amb,e}}$ is parametrized by one single free parameter r_0.

Because of the dispersion on our data points, it is not possible to determine the exact value of r_0. However, our experimentally determined values are consistent with $-2 \leq r_0 \leq 0$ (see Figure 4.10).

The comparison of our results with Boltzmann transport equation also allows us to study the asymptotic behavior of the ambipolar Seebeck coefficient. In the non-degenerate regime ($\eta \ll -1$), the ambipolar Seebeck coefficient is given by Equation (4.30), and therefore should vary linearly with the reduced QFLS, with a universal slope $k_B/2e$. This means in particular that the ambipolar Seebeck coefficient should be larger at lower η, hence for lower excitation intensity, as is the case with photo-Seebeck [Okazaki *et al.* 2012]. However, if the excitation is not high enough, carriers will stay cold and out optical method will not permit to measure the Seebeck coefficient, as was already discussed previously.

Result 4.4. (Validation of our hot-carrier ambipolar transport theory) Using the theory of hot-carrier ambipolar transport developed in section 4.2, we were able to measure the ambipolar Seebeck coefficient of sample 5006 from a purely optical method [Vezin *et al.* 2024b]. We report values between -3 and 1 k_B/e, consistent with the relaxation time approximation with a scaling $-2 \leq r_0 \leq 0$.

4.5 Conclusion

This chapter lays the theoretical framework necessary to study thermoelectric and ambipolar transport of photogenerated hot carriers. Starting from Boltzmann equation in the relaxation time approximation, we described this hot-carrier transport with effective ambipolar transport coefficients valid even in the degenerate regime. Then we proposed a purely optical method to image hot-carrier transport. It consists of measuring PL with an absolutely calibrated hyperspectral imager in point illumination configuration. We showed that we could determine the recombination rate, electrical conductivity and the ambipolar Seebeck coefficient in sample 5006, which is an InGaAsP/InGaAsP single QW. Results were qualitatively consistent with numerical estimates obtained from Boltzmann transport equation in the relaxation time approximation.

This study opens new perspectives to understand the properties of non-ideal HCSCs, where transport phenomena may limit device efficiency. Specifically, it enables the description of inhomogeneous HCSCs, where carrier transport is influenced by inhomogeneous hot-carrier distributions. This question will be considered in chapter 6.

Perspectives

- In order to determine experimentally the value of the electrical conductivity and Seebeck coefficient, it is necessary to assume that carrier mobility is constant. However, this assumption does not hold when carrier temperature changes, nor when the system becomes degenerate. Therefore, it would be interesting to lift this assumption. This could be achieved for instance by computing the mobility scaling law with respect to temperature, as is proposed in [Höpfel *et al.* 1986].

- Another interesting development to this study would be the inclusion of diffusion effects in the definition of the thermalization coefficient. In the presence of diffusion, some of the energy is taken away from the generation spot instead of being thermalized. This reduces the apparent temperature at the generation spot, and hence leads to an overestimation of the thermalization coefficient. A similar effect has been investigated in the context of carrier lifetime measurement. When the laser spot size is smaller than carrier diffusion length, diffusion lowers the steady-state carrier density at the laser spot, leading to an underestimation of the carrier lifetime [Vidon 2022, Chapter 3]. Theoretically, it should be possible to distinguish the contributions of diffusion and thermalization in the energy conservation equation, and therefore propose a definition of the thermalization coefficient independent of diffusion effects. Experimentally, we could study the evolution of the thermalization coefficient with laser spot sizes ranging from a fraction of the hot-carrier diffusion length to several times this value.

- Finally, it would be interesting to simulate the establishment of a chemical potential and temperature gradient for a known illumination profile. This would pave the way towards the description of realistic HCSCs with inhomogeneous carrier concentration and temperature in the absorber. The equations necessary to solve this problem are well known [Wachutka 1990], but solving them numerically is a technical challenge.

Chapter 5

Distinct temperatures: discriminating electrons from holes temperatures

In III-V materials, electrons and holes generally do not have the same effective mass. Therefore they are likely to have different temperatures. Indeed, the energy of absorbed and emitted photons is unevenly distributed among them. Similarly, the fact that they have different dispersion relations imply that their coupling with phonons – and hence their thermalization rates – will be different. By contrast, carrier-carrier interactions such as Coulomb interaction and Auger recombinations tend to equate the carrier temperatures. The temperatures reached in steady-state will result from a trade-off between all these contributions.

As a consequence, many investigations in III-V materials in the 80s - 90s reported different temperatures for electrons and holes. The coexistence of two temperatures was first predicted in GaAs by numerical simulations [Asche and Sarbei 1984]. They showed that, in the transient regime, electrons should equilibrate at a *higher* temperature than holes for a few picoseconds, due to weak electron-hole interaction. Many subsequent models, known as *two-temperature models*, introduced different temperatures for electrons and holes. These models aimed to incorporate a growing number of effects, such as various carrier-carrier interactions, carrier degeneracy, and quantum confinement [Leo and Collet 1991, Taylor *et al.* 1992, Hayes and Phillips 1994]. Some of them even account for non-thermal distributions [Osman and Ferry 1987, Ferry *et al.* 1988].

Simultaneously, several experiments investigated two-temperature effects. First, continuous wave Photoluminescence (PL) was used to show that the *effective* temperature of the electron-hole plasma depends on the majority carrier type in GaAs/AlGaAs heterostructures [Shah *et al.* 1985]. Then, the combination of continuous-wave PL and electrical mobility measurements allowed to distinguish the temperature of electrons and holes for the first time [Höpfel *et al.* 1986, Pan *et al.* 1986]. However, this technique had limitations. It was applicable only to highly doped samples or weak photogeneration regimes. Additionally, it required the sample to have electrical contacts. After these pioneering works in steady-state by Shah *et al.*, electron and hole temperatures were exclusively studied with time-resolved methods, including ultrafast time-resolved photoluminescence [Polland *et al.* 1987, Snoke *et al.* 1992, Chébira *et al.* 1992, Zhou *et al.* 1992, Gong *et al.* 1993] and transient absorptivity spectroscopy [Bradley *et al.* 1989, Alexandrou *et al.* 1995, Langot *et al.* 1996]. In most cases, these authors reported that electrons were hotter than holes.

The challenge of spectroscopy-based two-temperature measurements lies in the fact that that spectroscopy techniques are simultaneously sensitive to electron and hole distributions. To disentangle the contribution from each carrier, the authors usually rely on identifying spectral regions where variations of the signal come dominantly from one carrier type. This typically requires heavily doped samples, as in the case of band-edge PL [Chébira *et al.* 1992, Zhou *et al.* 1992], band-edge absorption [Langot *et al.* 1996] or electron-acceptor PL measurements [Snoke *et al.* 1992]. Another possibility is to probe transitions including high-energy hole states, for instance conduction band - spin-orbit split-off valence band transitions [Alexandrou *et al.* 1995].

Therefore, the only methods reported in literature to determine electron and hole temperatures in steady-state require that the sample has electrical contacts. In this chapter, we propose the first experimental method to determine simultaneously electron and hole temperatures purely from continuous-wave PL measurements.

We first recall the expression of PL emission in a two-temperature model [Gibelli *et al.* 2016b] in section 5.2. By analysing this emission law, we highlight the fact that two-temperature determination is made possible by the presence of Band Filling (BF) in section 5.3. Our technique is thus restricted to regimes of strong excitation, where BF is significant, *i.e.* when electrons and holes are *close enough* to being degenerate (see section 5.3.2 for a detailed discussion). After introducing some methodological details in section 5.4, we apply this two-temperature measurement technique to PL spectra acquired from an InGaAsP/InGaAsP single Quantum Well (QW). We report electron temperatures of $\sim$ 1000 K at largest excitation intensity, while holes remain close to room temperature (see section 5.5.1).

This chapter is adapted from [Vezin *et al.* 2024c].

Table of contents

5.1 Highlights

Theoretical Highlight 5.1. (Proof of concept)
It is theoretically possible to determine electron and hole individual temperatures from continuous-wave PL spectroscopy. This technique relies on the measurement of band filling and therefore requires a good knowledge of the absorptivity. In addition, it can be used only if the system is sufficiently close to degeneracy, when the Quasi-Fermi-Level Splitting (QFLS) is few k_BT below the gap. Since hot-carrier absorbers are characterized at large excitation intensities, this limitation should not be very restrictive.

Experimental Highlight 5.1. (Experimental evidence)
Our technique was used on PL spectra from sample 5006 (InGaAsP QW). We showed that electrons could become as hot as 1000 K, while holes remained much colder, close to lattice temperature.

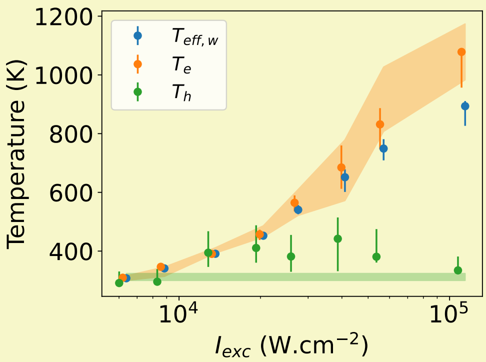

Experimental Highlight 5.2. (Signature of electron-hole interactions)
The increase of hole temperatures, though small, is too large to be explained only by photon absorption. This is the demonstration that holes must receive energy from the electrons, by Coulomb interaction, Auger recombinations or by LO phonon-mediated interactions.

5.2 Two-temperature Generalized Planck Law

Light emission by a semiconductor is generally described by the Generalized Planck Law (GPL) [Wurfel 1982], which considers that electrons and holes are at thermal equilibrium. In chapter 2, we have shown that this law could be generalized to distinct temperature for electrons and holes, under the assumption of parabolic bands (see Equation (2.18)). In this section, we simply recall the expression of this two-temperature GPL.

Statement 5.1. (Two-temperature Generalized Planck Law)
If electrons and holes can be described by Fermi-Dirac distributions of temperature T_i and chemical potential μ_i, then the photon flux emitted by the system is described by the two-temperature GPL [Gibelli *et al.* 2016b]

$$I_{\mathrm{PL}}(E) = \frac{2\pi}{h^3c^2}A(E)\frac{E^2}{\exp\left(\dfrac{E-\Delta\mu_{\mathrm{eff}}}{k_BT_{\mathrm{eff}}}\right)-1} \tag{5.1}$$

where h is Planck constant, c is the speed of light in vacuum, k_B is Boltzmann constant. E is the energy of the emitted photon, $A(E)$ is the absorptivity of the system, and T_{eff} (resp. $\Delta\mu_{\mathrm{eff}}$) is the effective temperature (resp. QFLS) of the system.

The effective temperature and QFLS are defined as [Pan *et al.* 1986, Gibelli *et al.* 2016b]

$$\begin{cases} \dfrac{1}{T_{\mathrm{eff}}} = \dfrac{1-\xi}{T_e} + \dfrac{\xi}{T_h} \\ \dfrac{\Delta\mu_{\mathrm{eff}}}{k_BT_{\mathrm{eff}}} = \dfrac{\mu_e}{k_BT_e} + \dfrac{\mu_h}{k_BT_h} - \dfrac{E_g}{k_B}\left(\dfrac{1}{2}-\xi\right)\left(\dfrac{1}{T_h}-\dfrac{1}{T_e}\right) \end{cases} \tag{5.2}$$

where $\xi = m_e/(m_e+m_h)$ is called the *effective mass mismatch* and E_g is the bandgap of the absorber.

This shows that the PL spectrum of a system composed of two thermal distribution of electrons and holes at different temperatures can be described by a single effective temperature and a single effective QFLS. Thus, distinguishing T_e and T_h solely from this formula is impossible, as was pointed out by many authors [Höpfel *et al.* 1986, Chébira *et al.* 1992]. The key to simultaneously determining T_e and T_h is a proper description of the absorptivity's dependence on carrier distributions. This dependence is captured through the BF term, which will be discussed in the following section.

Toolbox 5.1. (Conversion table)
In this chapter and in the following, we will often go back and forth between the carrier distribution parameters (T_e, μ_e, T_h, μ_h) and effective parameters that are easier to describe light emission (T_{eff}, $\Delta\mu_{\mathrm{eff}}$, r). We provide here a conversion table valid in the Boltzmann approximation and assuming electroneutrality (see Appendix B).

$$\left\{\begin{aligned}
\frac{1}{T_{\text{eff}}} &= \frac{1-\xi}{T_e} + \frac{\xi}{T_h} \\
\frac{\Delta\mu_{\text{eff}}}{k_B T_{\text{eff}}} &= \frac{\mu_e}{k_B T_e} + \frac{\mu_h}{k_B T_h} - \frac{E_g}{k_B}\left(\frac{1}{2}-\xi\right)\left(\frac{1}{T_h}-\frac{1}{T_e}\right) \\
r &= \frac{T_e}{T_h} \\
T_e &= T_{\text{eff}}(1-\xi+r\xi) \\
T_h &= T_{\text{eff}}\left(\frac{1-\xi}{r}+\xi\right) \\
\mu_e &= \frac{1}{2}(1-\xi+r\xi)\Delta\mu_{\text{eff}} - \frac{D}{4}(1-\xi+r\xi)k_B T_{\text{eff}}\ln\left(\frac{r\xi}{1-\xi}\right) - \frac{E_g}{2}\xi(r-1) \\
\mu_h &= \frac{1}{2}\left(\frac{1-\xi}{r}+\xi\right)\Delta\mu_{\text{eff}} + \frac{D}{4}\left(\frac{1-\xi}{r}+\xi\right)k_B T_{\text{eff}}\ln\left(\frac{r\xi}{1-\xi}\right) + \frac{E_g}{2}(1-\xi)\frac{r-1}{r}
\end{aligned}\right. \tag{5.3}$$

where D is the dimensionality of the system ($D = 2$ for QWs and $D = 3$ for bulk absorbers). In the case of a degenerate system, all equations still hold except the last two, which no longer have analytical expressions.

5.3 Band filling allows for the simultaneous determination of electron and hole temperatures

In this section, we present how it is theoretically possible to determine simultaneously electron and hole distributions from a single PL spectrum. At the high excitation rates necessary to produce hot-carriers, the absorptivity $A(E)$ of the system depends on carrier populations through population-dependent effects such as BF, bandgap renormalization [Bennett *et al.* 1990], exciton screening [Chemla 1985] or spectral linewidth broadening [Esmaielpour *et al.* 2022]. Some of these population-dependent effects carry additional information on the carrier populations.

In particular, we present how BF allows to distinguish electron and hole temperature from PL spectra (see section 5.3.1). Then, we determine a quantitative threshold for the QFLS, above which two-temperature determination is possible (see section 5.3.2).

5.3.1 Two-temperature band-filling effect

As was already discussed in section 2.1, BF is a population-dependent effect representing the change in absorption coefficient $\alpha(E)$ due to the non-negligible occupation of electron and hole levels close to their respective chemical potential. In general, BF writes [Bennett *et al.* 1990]

$$\alpha(E) = \alpha_0(E) \times (1 - f_h(E_h) - f_e(E_e)) \tag{5.4}$$

where α (resp. α_0) is the absorption coefficient of the system in the presence (resp. absence) of BF, while E_e (resp. E_h) is the energy of the electron (resp. hole) involved in the absorption of a photon of energy E (see Figure 2.1).

Statement 5.2. (Band-filling in the two-temperature model)
We assume that (i) electrons and holes follow thermal distributions and (ii) the bands are parabolic so that the energy E of an incoming photon is shared between electrons and holes as $E_e = E_g/2 + (1-\xi)(E-E_g)$ and $E_h = E_g/2 + \xi(E-E_g)$. Under these conditions, the BF contribution writes

$$1 - f_h(E_h) - f_e(E_e) = \sinh\left(\frac{E-\Delta\mu_{\text{eff}}}{2k_BT_{\text{eff}}}\right) \Big/ \left[\cosh\left(\frac{E-\Delta\mu_{\text{eff}}}{2k_BT_{\text{eff}}}\right) + \cosh\left(\frac{1}{2}\left[\frac{E}{k_B}\left(\frac{1-\xi}{T_e} - \frac{\xi}{T_h}\right) - \frac{\mu_e}{k_BT_e} + \frac{\mu_h}{k_BT_h} - \frac{E_g}{k_B}\left(\frac{1}{2}-\xi\right)\left(\frac{1}{T_e}+\frac{1}{T_h}\right)\right]\right)\right] \tag{5.5}$$

As can be seen in Equation (5.5), the BF contribution cannot be expressed only in terms of effective temperature and QFLS. Therefore, thanks to this term, the two-temperature GPL depends individually on T_e and T_h through the BF contribution to the absorptivity $A(E)$ [Vezin *et al.* 2024c].

The magnitude of BF effect depends on carrier populations: if the chemical potential of carriers is too low, carrier population will be small and BF effect will be negligible. Therefore we are interested in establishing the regime in which this effect is sufficient to distinguish electron and hole temperatures. This will be the topic of the following section.

5.3.2 Conditions to distinguish electron and hole temperature

5.3.2.1 Qualitative analysis

To illustrate the role of BF and of the independent temperatures of electrons and holes, we simulate PL spectra of the InGaAsP QW described in section 2.3.4 and in section 4.3. In principle, four carrier distribution parameters (T_e, T_h, μ_e and μ_h) are necessary to simulate a two-temperature spectrum. However, electroneutrality provides a relation between these four parameters, such that only three are independent (see Appendix B). In this section, we choose to use the effective temperature T_{eff}, the reduced QFLS $\eta = \dfrac{\Delta\mu_{\text{eff}} - E_g}{k_BT_{\text{eff}}}$ and the temperature mismatch $r = T_e/T_h$. The correspondence between T_e, T_h, μ_e, μ_h and T_{eff}, $\Delta\mu_{\text{eff}}$, r has been presented in Toolbox 5.1.

First, to visualize the effect of BF, we simulated PL spectra using different values of the reduced QFLS and of the temperature mismatch. The result can be seen on Figure 5.1a. When the reduced QFLS is sufficient ($\eta \geq -4$ for instance), the spectra exhibit a clear dependence on r, which is visible in the low-energy part of the PL spectrum, close to the PL peak. On the contrary, when the reduced QFLS is too low ($\eta = -8$ for instance), spectra with different temperature mismatch r can hardly be distinguished.

This is simply because the system is not degenerate in this case, making BF negligible. To illustrate this, we represent the BF contribution for the same conditions as the PL spectra in Figure 5.1b. By definition, $1 - f_e - f_h = 1$ when the carrier population in the bands is negligible. Therefore, BF contribution can be considered negligible when

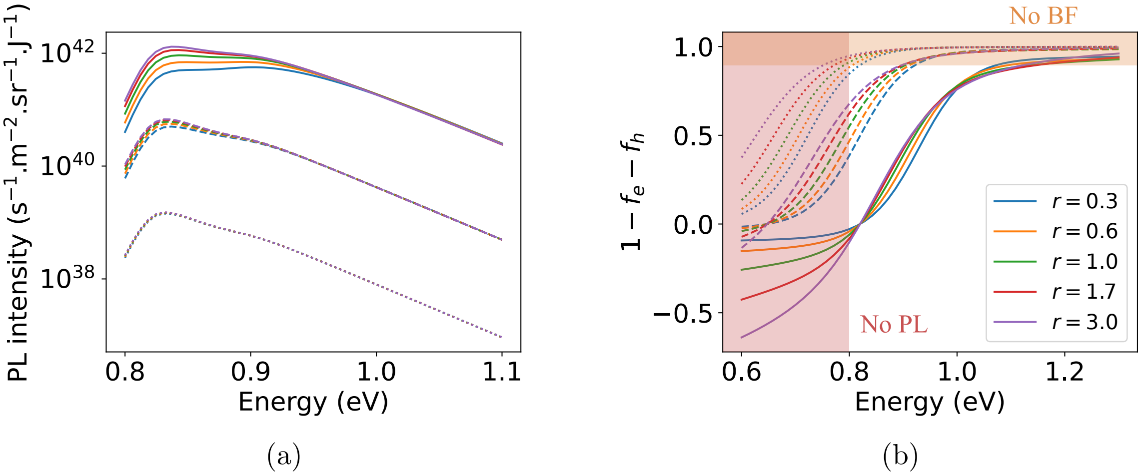

Figure 5.1: *Visualization of the effect of BF on PL spectra. (a) Simulated PL spectra of an InGaAsP QW for different reduced QFLS ($\eta = -8$ (dotted), -4 (dashed) and 0 (plain)) and different temperature mismatch $r = T_e/T_h$, at same $T_{\text{eff}} = 500$ K. (b) Simulated BF in the same conditions. Note that the energy scale (x axis) is slightly larger than in panel (a).*

$1 - f_e - f_h > 0.9$. This condition is represented in a pale orange color in Figure 5.1b. BF contribution is always significant for energies $E \leq \Delta\mu + 6k_BT$, but PL signal drops rapidly below the bandgap. Therefore, when $\Delta\mu \leq E_g - 6k_BT$, there is no significant contribution of BF to the PL signal.

5.3.2.2 Quantitative analysis

We now want to establish a quantitative threshold for η above which two-temperature measurement is possible. To do so, we compare the impact of r on the spectrum with typical measurement noise. Our Hyperspectral Imager (HI) setup has a typical additive gaussian noise $\sigma = 0.25$ % (see section 2.2). Therefore, a gaussian noise of mean 0 and standard deviation $\sigma \times \max(I_{\text{PL}})$ is added to all the PL spectra simulated in this section.

We first computed a collection of spectra at different values of η with a nominal value $r_{\text{nom}} = 1.8$. For every η, we computed the *objective function* (defined in section 5.4.2 and in particular Equation (5.8)) between this nominal spectrum and a set of simulated spectra with different temperature mismatch $0.25 < r < 4$. This objective function, normalized to the minimum achievable value due to the presence of noise, is represented in Figure 5.2.

When $\eta \leq -8$, the objective function between spectra with $1 \leq r \leq 4$ is less than the variations induced by noise, and they cannot be distinguished. On the contrary, for $\eta \geq -4$, it becomes possible to distinguish spectra with $r = r_{\text{nom}} \pm 10$ % (red dashed lines). This confirms our intuition that η must be “large enough” to ensure that we can distinguish two spectra with different temperature mismatch r. However, the precise value of the threshold depends on many arbitrary choices such as the desired precision on r, the shape of the spectrum, the choice of objective function, the Signal to Noise Ratio (SNR), etc. Therefore it may vary from $\eta \geq -7$ to $\eta \geq -3$. We write this condition as $\eta \gtrsim -5$ (see the glossary for a definition of the different symbols used).

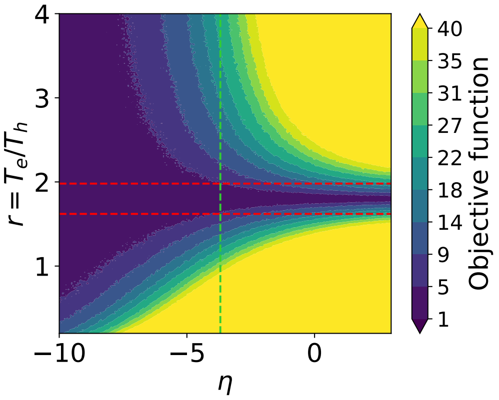

Figure 5.2: *Objective function computed between a reference spectrum with* $T_{\text{eff}} = 500$ K *and* $r = 1.8$ *(*$T_e = 540$ K *and* $T_h = 300$ K*) and spectra of varying r (y axis), as a function of the reduced QFLS (x axis). Red dashed lines highlight the region* $r = r_{\text{nom}} \pm 10$ %. *Green dashed line indicate the threshold above which two-temperature determination is possible.*

Result 5.1. (Condition to distinguish electron and hole temperature) Electron and hole temperatures may be distinguished from assessing the BF contribution to PL spectra if, and only if, the QFLS is larger than than a few $k_B T$ below the gap. Determining the temperature mismatch with a 10 % precision typically requires $\Delta\mu_{\text{eff}} \gtrsim E_g - 5k_B T_{\text{eff}}$. This detection threshold depends on the required precision, on the SNR, on the spectrum shape, etc. Note that this condition is necessary but not sufficient. It is derived under the assumption of perfectly known absorptivity, which may not hold in real experiments. This will be further discussed in section 5.5.

5.4 Experimental two-temperature determination in sample 5006 – Methodological details

In the previous section, we studied *theoretically* how two-temperature determination was possible from assessing the BF contribution to PL spectra. We worked with simulated spectra to prove the feasibility of the method in a somewhat idealized where the absorptivity was perfectly known.

In this section, we provide methodological details to make this two-temperature determination possible on *experimental* data. We first describe the sample and the spectrometer used in section 5.4.1. Then, we explain how we designed a composite objective function that allows to in section 5.4.2. Finally, we discuss how to assess the uncertainties associated with such a complex two-temperature determination method in section 5.4.3. Results will be presented in section 5.5.1 and discussed in section 5.5.2.

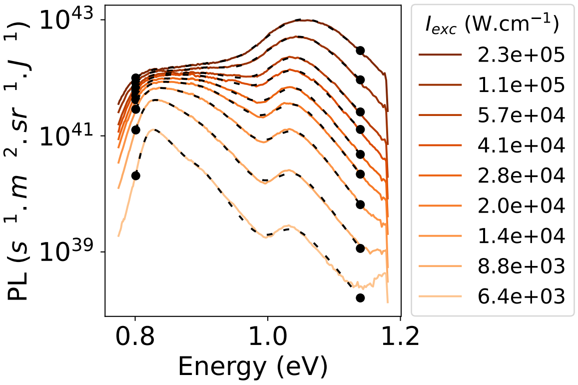

Figure 5.3: *PL spectra of sample 5006, acquired at increasing excitation intensity. Dashed lines represent the result of a two-temperature full fit.*

5.4.1 Sample and experimental conditions

We applied our two-temperature determination technique on PL spectra from sample 5006 (InGaAsP/InGaAsP single QW described in section 2.4). For this study, we used the same PL spectra as in section 4.3. But this time, we used only the most intense spectrum obtained at the center of the illumination spot.

These spectra are shown on Figure 5.3. QW emission can be seen around $E_g = 0.82$ eV, with a secondary optical transition visible around $E_2 = 0.89$ eV. The barrier emission can be seen above 1.05 eV. A clear change in slope at high energy in QW emission is indicative of hot-carrier and BF effect, as will be explained below. Features related to two-temperature effect are not immediately visible, but will be discussed in section 5.5.

In terms of fitting, we again used the full fit approach described in section 2.4.3. As discussed in section 2.4.4, we use an External Quantum Efficiency (EQE) measurement to fit 6 material parameters and reduce the risk of overfitting. This time we described the BF term of the barrier with the two-temperature model presented in section 5.3.1. Since there are no hot carriers in the barrier, we kept a one-temperature model for the BF in the barrier. The introduction of the two-temperature BF term means that there are 2 additional parameters to our model (T_e, T_h, μ_e and μ_h instead of simply T_{eff} and $\Delta\mu_{\text{eff}}$). However, thanks to electroneutrality, only one of them is independent (see Appendix B).

5.4.2 Choice of objective function to minimize

5.4.2.1 Objective functions definition

In spectroscopy in general, and in hot-carrier community in particular, it is customary to fit PL spectra with a logarithmic scale. Indeed, a change in carrier temperature results in a change of the high-energy slope, which can be easily identified in logarithmic scale (see section 2.3.1). Additionally, PL spectra span over several orders of magnitude, such that a linear scale would not be sensitive to spectral regions of low intensity, in particular the high-energy part. Therefore, the usual objective function used to fit 1-temperature models is defined as

$$[d_{\log}(I_{\mathrm{PL}}, I_{\mathrm{PL}}^{\mathrm{exp}})]^2 = \sum_{E_{\mathrm{LB}} \leq E_i \leq E_{\mathrm{UB}}} \frac{\left(\log I_{\mathrm{PL}}(E_i) - \log I_{\mathrm{PL}}^{\mathrm{exp}}(E_i)\right)^2}{N \langle \log I_{\mathrm{PL}}^{\mathrm{exp}} \rangle^2} \tag{5.6}$$

where

I_{PL} = The modeled spectrum.
$I_{\mathrm{PL}}^{\mathrm{exp}}$ = The measured spectrum that we aim to reproduce with the model.
E_{LB} = The lower bound of the energy interval over which the fit is performed.
E_{UB} = The upper bound of the energy interval over which the fit is performed.
N = The number of points measured in the spectrum.
$\langle \cdot \rangle$ = The average over the measurement points.

Note that the normalization by $N\langle \log I_{\mathrm{PL}}^{\mathrm{exp}} \rangle^2$ is not necessary, but it makes it easier to compare different objective functions.

For the 2-temperature fit, the low-energy part of the PL spectrum becomes very important. Indeed, it is the region in which one can observe the effect of BF and hence of the temperature mismatch between electrons and holes. A linear objective function would be more sensitive to small discrepancies of the temperature mismatch:

$$[d_{\mathrm{lin}}(I_{\mathrm{PL}}, I_{\mathrm{PL}}^{\mathrm{exp}})]^2 = \sum_{E_{\mathrm{LB}} \leq E_i \leq E_{\mathrm{UB}}} \frac{\left(I_{\mathrm{PL}}(E_i) - I_{\mathrm{PL}}^{\mathrm{exp}}(E_i)\right)^2}{N \langle I_{\mathrm{PL}}^{\mathrm{exp}} \rangle^2} \tag{5.7}$$

To combine the advantages of those two objective functions, we designed a composite objective function consisting of a logarithmic scale at high energy and a linear scale at low energy. The separation between those two regions is controlled by a hyperparameter E_0, while the relative weights are controlled by another hyperparameter λ:

$$\begin{aligned}[d(I_{\mathrm{PL}}, I_{\mathrm{PL}}^{\mathrm{exp}})]^2 = \frac{1}{1+\lambda^2} \Bigg[& \sum_{E_{\mathrm{LB}} \leq E_i \leq E_0} \frac{\left(I_{\mathrm{PL}}(E_i) - I_{\mathrm{PL}}^{\mathrm{exp}}(E_i)\right)^2}{N_{\leq} \langle I_{\mathrm{PL}}^{\mathrm{exp}} \rangle_{\leq}^2} \\ & + \lambda^2 \sum_{E_0 < E_i \leq E_{\mathrm{UB}}} \frac{\left(\log I_{\mathrm{PL}}(E_i) - \log I_{\mathrm{PL}}^{\mathrm{exp}}(E_i)\right)^2}{N_{>} \langle \log I_{\mathrm{PL}}^{\mathrm{exp}} \rangle_{>}^2} \Bigg]\end{aligned} \tag{5.8}$$

where

$N_{\leq}$ = The number of measurements points at energy lower than E_0.
$N_{>}$ = The number of measurements points at energy greater than E_0.
$\langle \cdot \rangle_{\leq}$ = The average over the subset of points at energy lower than E_0.
$\langle \cdot \rangle_{>}$ = The average over the subset of points at energy greater than E_0.

5.4.2.2 Performance comparison

To make a choice between the different available objective functions, we need to compare their performances on experimental PL spectra. Since we do not know the expected value of the parameters (and in particular of the temperatures) for each spectrum, we chose to rely on a dispersion indicator. For each spectrum, we compute the standard

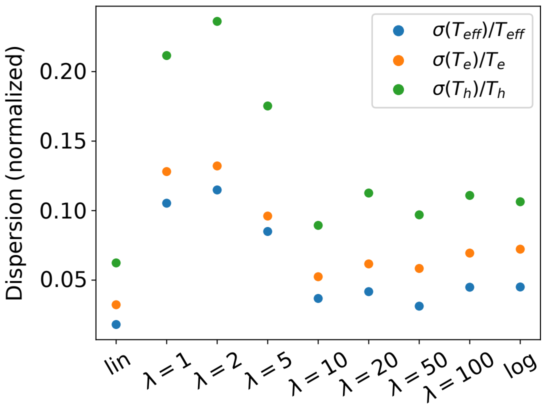

Figure 5.4: *Dispersion over the estimated carrier temperature obtained with each objective function.*

deviation over the estimated temperatures (in %) obtained by varying the energy lower bounds from 0.77 eV to 0.83 eV. Then, we average these standard deviations over all PL spectra to obtain our final dispersion indicator.

In this study, we set $E_0 = 0.90$ eV, in the middle of the QW emission, and $E_{\text{UB}} = 1.14$ eV. However, the hyperparameter λ varies from 1 to 100. We also tried the pure linear and pure logarithmic objective function over the entire range $[E_{\text{LB}}, E_{\text{UB}}]$ for the sake of comparison.

The comparison of the dispersion obtained with these different objective functions is presented on Figure 5.4. It appears that the objective function with lowest dispersion is the pure linear one. However, in our investigations on other samples, we noticed that this linear objective function would systematically overestimate the carrier temperature because it is not sensitive enough to the high-energy part of the PL spectra. The next best objective function is the composite objective function with $\lambda = 10$. Therefore we used this composite objective function to fit the PL spectra presented in section 5.4.2.

Note that the mean dispersion over the estimated temperature is typically $5 - 10$ % with this objective function. Note also that the dispersion over hole temperature is systematically the largest, more than twice the dispersion over T_{eff}. This is linked to the large effective mass imbalance in this material ($\xi \simeq 0.09$). This imbalance means that the relative weight of hole temperature in the effective temperature is much smaller than the weight of electron temperature (see Equation (5.2)). Therefore, the fit will be less sensitive to the value of T_h than T_e.

Result 5.2. (Optimal objective function for the two-temperature determination)
Precise two-temperature determination requires the fitting of two distinct energy ranges: (i) the high-energy side to ensure that we can determine the effective temperature, and (ii) the low-energy side so that we are sensitive to individual temperatures. This leads us to propose a composite objective function to compare spectra, which is logarithmic in the high-energy range and linear in the low-energy range (see Equation (5.8)).

5.4.3 Uncertainties

The 11 parameters of our two-temperature full fit model cannot be determined independently, as the fitting procedure induces a correlation between their values. This is a well-known *overfitting* issue. To assess the magnitude of the overfitting error, it is possible to perform a *sensitivity analysis*. It consists in repeating each fit several times by changing some conditions around a *reference* situation. For each repetition, we compare the fit goodness (i.e. the value of the objective function evaluated between the modeled and the measured spectrum) to the reference fit goodness. We consider the new fit *acceptable* if its fit goodness is not higher than 3 % above the reference one. The resulting uncertainty on the parameter values is taken as the difference between the maximum and minimum value obtained in all the *acceptable* repetitions.

Note that the acceptability threshold (3 % in our case) is arbitrary. However, we observed that the objective function between an experimental PL spectrum and its best fit varies of several tens of percent from one spectrum to the other. Therefore, any variation below a few percents is not significant.

Reference case. The reference situation was obtained by setting the energy range for the fit to $E_{\text{LB}} = 0.80$ eV and $E_{\text{UB}} = 1.14$ eV. We also set the hyperparameter $\lambda = 10$ (see section 5.4.2). All 11 fitting parameters were completely free, although we forced the exciton absorption peak A_x to decrease with increasing excitation intensity to account for exciton screening [Chemla 1985]. Similarly, we imposed that the bandgap of the material would decrease to mimic bandgap renormalization [Bennett *et al.* 1990]. Finally, we imposed that spectral linewidths Γs would increase with increasing excitation intensity [Esmaielpour *et al.* 2022]. The resulting full fit is shown in Figure 5.3.

Influence of the fitting interval. Then, we studied the influence of the energy range by changing E_{LB} in the range 0.80 ± 0.3 eV. We did not change E_{UB} as the high-energy region, and in particular barrier emission has no impact on the determination of electron and hole temperatures in the QW.

Influence of exciton screening. Finally, we changed manually the magnitude of the exciton absorption peak A_x by ±30 % around the value obtained in the reference situation. Indeed, exciton screening is a power-dependent effect that changes the absorptivity in the low-energy part of the PL spectrum, precisely where the two-temperature determination is possible. Therefore the relative contribution of exciton screening and two-temperature effect are difficult to disentangle and this leads to increased uncertainty on the temperature determination.

Note that to make a complete sensitivity analysis, we should have included also:

1. the influence of the linewidth broadenings Γ_x and Γ_1, as well as of the exciton energy level E_x. Indeed, these three parameters also have an influence over the shape of the low-energy part of the spectra.

2. the cross-sensitivity of tested parameters, instead of looking at the influence of one single parameter.

However, the two-temperature full fit analysis performed here is very demanding in computational power. Such a complete sensitivity analysis would require to fit thousands of spectra, which is not reasonable on a laptop.

5.5 Experimental two-temperature determination in sample 5006 – Results and discussion

5.5.1 Results

In Figure 5.5, we report the results of the 2-temperature full fits as a function of the excitation intensity I_{exc}.

Carrier temperatures in the QW are displayed in Figure 5.5a. As intensity increases, the effective temperature increases from ambient to about 900 K. Similarly, electron temperature increases from ambient temperature to about 1000 K. However, hole temperature exhibits no clear trend and stays below 500 K at all intensities.

For low excitation powers $I_{\text{exc}} \leq 2 \times 10^4$ W.cm^{-2}, electron and hole temperatures are not distinguishable from the effective temperature due to large uncertainties. However, for larger excitation powers $I_{\text{exc}} > 2 \times 10^4$ W.cm^{-2}, holes are found to be significantly colder than electrons.

Result 5.3. (Two-temperature determination)
We report the first purely optical simultaneous determination of electron and hole temperatures in steady state. We showed that electrons reach temperatures above 1000 K at largest excitation intensities, while holes remain below $\sim$ 500 K [Vezin *et al.* 2024c]. This suggests that holes remain cold while electrons become hot, as was previously reported by many authors in transient regime [Asche and Sarbei 1984, Bradley *et al.* 1989] and fewer in steady-state [Pan *et al.* 1986, Whiteside *et al.* 2019].

QFLS and carrier chemical potentials are represented in Figure 5.5b. At low intensity $I_{\text{exc}} \leq 3 \times 10^4$ W.cm^{-2}, the QFLS and both chemical potentials increase for increasing intensity. However, at larger intensity, the QFLS and the electron chemical potential decrease. This decrease is associated with a large increase of both T_{eff} and T_e, such that carrier density is still increasing (see Figure 5.5e). Note that the measurement of these chemical potentials offers another proof that $T_e > T_h$. Indeed, at high intensity, it appears clearly that $\Delta\mu_{\text{eff}} < \mu_e + \mu_h$. Because of electroneutrality and Equation (5.2), this is equivalent to $T_e > T_h$.

The inset of Figure 5.5b represents the value of the reduced QFLS η. Note that $\eta \geq -3$ for all measured intensities. Therefore, as stated in section 5.3.2, we are in the regime in which two-temperature determination is possible *a priori*. However, as the uncertainty over T_e and T_h is around $100 - 200$ K, it is not possible to distinguish them until T_{eff} surpasses 500 K. This happens only for intensities $I_{\text{exc}} > 2 \times 10^4$ W.cm^{-2}. Such a large uncertainty over T_e and T_h is caused by the many power-dependent effects affecting the absorptivity. These effects prevent us from knowing the exact shape of the absorptivity.

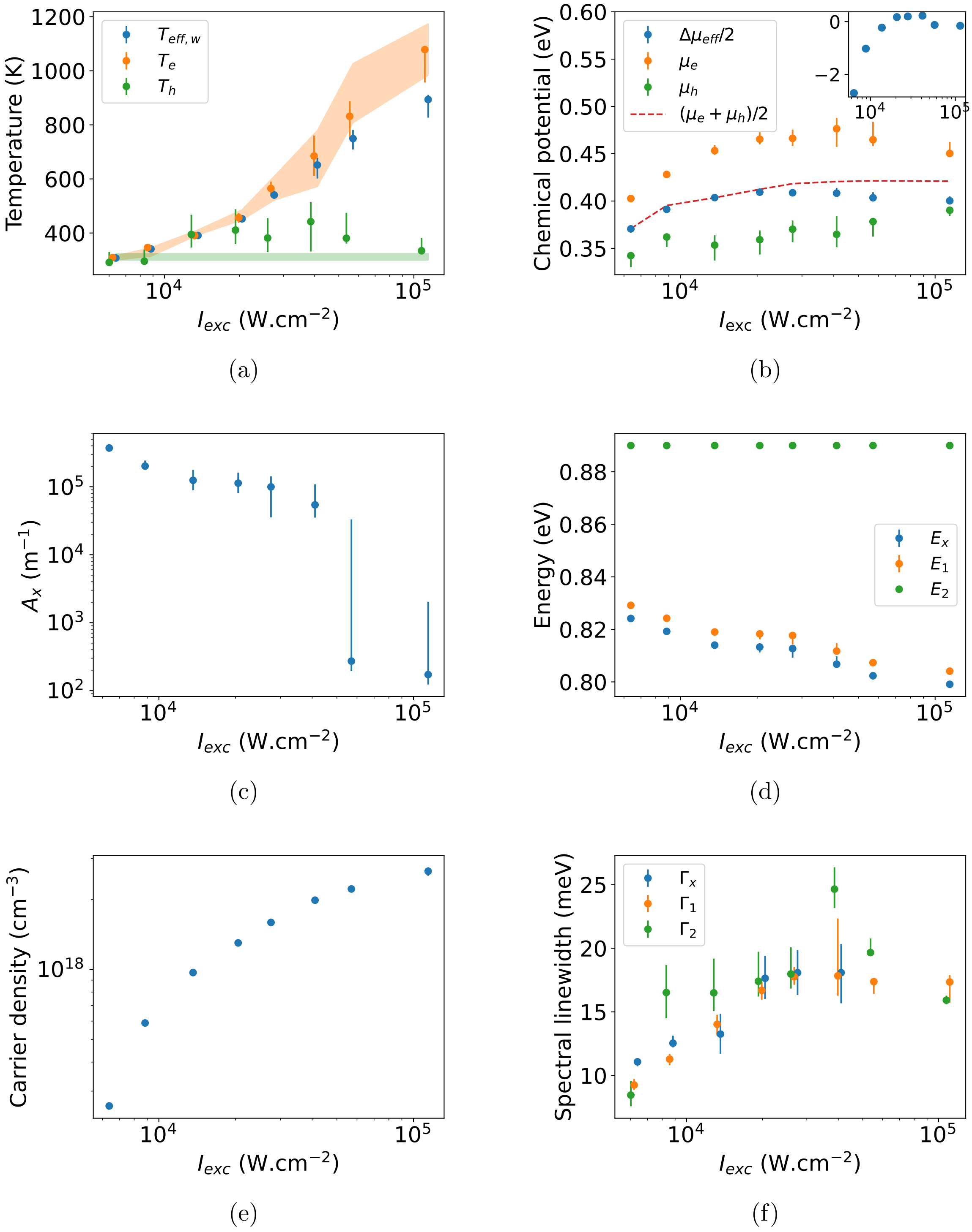

(a) (b) (c) (d) (e) (f)

Figure 5.5: *Parameters obtained from the two-temperature full fit at all excitation intensities. (a) Temperatures. Pale regions indicate the boundaries as described in section 5.5.2.1. (b) QFLS and carrier chemical potentials. Inset represents the reduced QFLS η. (c) Amplitude of the exciton absorption A_x. (d) Energy transitions in the QW. (e) Carrier density in the QW. (f) Spectral linewidths of the QW.*

Therefore, two-temperature determination would be more precise on samples with more stable absorptivity.

We report the estimated value of the exciton absorption peak amplitude in Figure 5.5c. The amplitude of the exciton peak decreases with increasing excitation intensity, which is an indication of exciton absorption screening [Chemla 1985]. The large error bars covering several orders of magnitude at highest intensity are due to the fact that the exciton contribution to the PL spectra is negligible at such high intensity. In fact, as soon as $A_x < 5 \times 10^4$ m^{-1}, the exciton peak contribution becomes negligible as compared with the contribution of the first level of the QW and the fitting algorithm cannot distinguish values lower than this threshold.

We also report the value of the QW energy levels in Figure 5.5d. This figure is mostly governed by constraints given to the fitting routine. Indeed, we imposed that E_2 would be constant and equal to 0.89 eV, that Rydberg energy $R_y = E_1 - E_x$ would also be constant and equal to 5 meV and that E_x could only decrease to mimic band-gap renormalization. We measure $\Delta E_x \simeq 25$ meV between highest and lowest excitation intensities. This is the typical order of magnitude expected in GaAs at such a carrier density $n \sim 10^{18}$ cm^{-3} [Bennett *et al.* 1990].

Finally, the QW spectral linewidths are presented in Figure 5.5f. All linewidths tend to increase with increasing excitation intensity because more phonons are emitted at high excitation [Esmaielpour *et al.* 2022]. Note that we do not report the two last points for Γ_x. Indeed, as explained above, the exciton absorption peak is negligible in this regime, such that the linewidth of excitonic peak cannot be measured.

5.5.2 Discussion

5.5.2.1 Energy exchanges

Insight about energy exchanges in this system can be obtained by looking at physical boundaries for carrier temperatures. First, since electrons and holes gain energy from the incoming light, their temperatures must be greater than lattice temperature T_L. Second, if electrons and holes do not exchange energy, their mean energy (hence temperature) is limited by the fact that the absorbed photons have a finite mean energy [Gibelli *et al.* 2016b]. Finally, electron and hole temperatures are linked to the effective temperature by a hyperbolic relation (Equation (5.2)). For a given value of T_{eff}, the upper bound on T_h imposes a lower bound on T_e and reciprocally. Therefore, three different constraints apply on the carrier temperatures:

$$\begin{cases} T_L \leq T_e \leq (1-\xi)\, T_{\max} \\ T_L \leq T_h \leq \xi T_{\max} \\ \dfrac{1}{T_{\text{eff}}} = \dfrac{1-\xi}{T_e} + \dfrac{\xi}{T_h} \end{cases} \tag{5.9}$$

where $T_{\max} = 2\left(\langle E_{\text{abs}}\rangle - E_g\right)/3k_B$ and $\langle E_{\text{abs}}\rangle = E_{\text{las}} = 1.265$ eV is the average energy of absorbed photons. This set of equations is depicted schematically in Figure 5.6.

We computed these boundaries for all fitted values of T_{eff}, and reported the result in pale colors in Figure 5.5a. Note that the boundaries derived for electron and hole temperatures depend strongly on the effective mass mismatch ξ. In this InGaAsP QW,

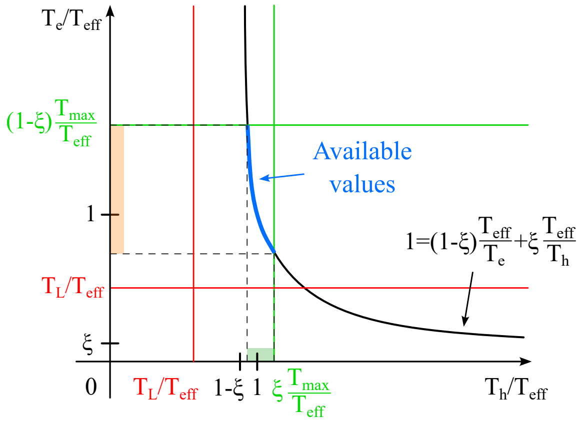

Figure 5.6: *Schematic representation of physical constraints on T_e and T_h for a given value of $T_{\text{eff}} \simeq 2T_L$ and $\xi \simeq 0.09$. Red (resp. green) lines show the lower (resp. upper) bound for electron and hole temperatures given by Equation (5.9). Pale colors indicate the accessible temperature range, as shown in Figure 5.5a.*

the extreme mass mismatch $\xi \simeq 0.09$ implies a very restrictive constraint on T_e and T_h, as shown in Figure 5.7c.

The fitted value of electron temperature (orange points) is always comprised in the physically available range (light orange region). However, hole temperature is almost systematically above the boundaries (light green region). This means that electron-hole interactions cannot be completely neglected. In fact, holes capture a fraction of the electron energy (through Coulomb scattering or Auger recombination for instance), and can therefore reach higher temperatures than what would be allowed purely from photon absorption, as described in [Bradley *et al.* 1989, Leo and Collet 1991].

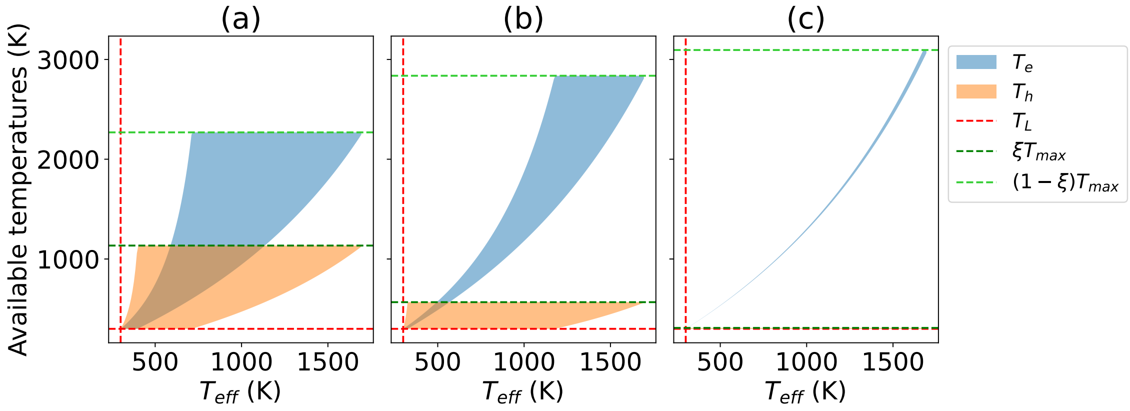

Figure 5.7: *Restricted boundaries for electron and hole temperatures as a function of the effective temperature T_{eff}, assuming no electron-hole interaction, for different values of the mass mismatch: (a) $\xi = 0.33$, (b) $\xi = 0.17$, (c) $\xi = 0.09$. For this plot, $E_g = 0.82\ eV$ and $E_{\text{las}} = 1.265\ eV$. In panel (c), hole temperature is comprised between 300 and 310 K, and is therefore not distinguishable from lattice temperature.*

Result 5.4. (Energy redistribution between electrons and holes)
We showed that holes are hotter than what would be allowed purely by photon absorption. This means that they have exchanged some energy with electrons, through Coulomb interaction for instance [Vezin *et al.* 2024c]. Such an energy redistribution has been described theoretically [Leo and Collet 1991] and experimentally [Bradley *et al.* 1989] in time-resolved PL experiments. However, it had never been evidenced with PL in steady-state before.

5.5.2.2 Carrier thermalization in the two-temperature model

As discussed in the general introduction, carrier thermalization is often described by a thermalization coefficient Q, such that the temperature elevation is roughly proportional to the thermalized power I_{th} (see Equation (1.3)). The generalization of this property to systems with two temperatures is not straightforward, as will be shown in this section.

We follow the detailed balance derivation proposed by several authors [Kumekov and Perel 1988, Tsai 2018], which allows to derive an exact expression of the thermalization rates based on Fermi Golden Rule. Taking into account the emission and absorption of LO phonons by both carrier types, as well as the decay of LO phonons into acoustic phonons, we show that the steady-state phonon population writes

$$N_{\boldsymbol{q}} = \frac{\dfrac{N_{\boldsymbol{q}}(T_e)}{\tau_{\boldsymbol{q}}^e} + \dfrac{N_{\boldsymbol{q}}(T_h)}{\tau_{\boldsymbol{q}}^h} + \dfrac{N_{\boldsymbol{q}}(T_L)}{\tau_{\boldsymbol{q}}^{\text{LO}}}}{\dfrac{1}{\tau_{\boldsymbol{q}}^e} + \dfrac{1}{\tau_{\boldsymbol{q}}^h} + \dfrac{1}{\tau_{\boldsymbol{q}}^{\text{LO}}}} \tag{5.10}$$

where

$N_{\boldsymbol{q}}(T) = \left[\exp\left(\dfrac{E_{\boldsymbol{q}}}{k_B T}\right) - 1\right]^{-1}$ = is the equilibrium phonon population at temperature T.
$\tau_{\boldsymbol{q}}^i$ = The interaction time of LO phonons with carrier i.
$\tau_{\boldsymbol{q}}^{\text{LO}}$ = The decay time of LO phonons into acoustic phonons by Klemens mechanism.

Therefore, following Equation (1.4) the energy loss rate of electrons in steady state writes

$$\left(\frac{dE}{dt}\right)_e = \sum_{\boldsymbol{q}} \frac{E_{\boldsymbol{q}}}{\tau_{\boldsymbol{q}}^e} \frac{\dfrac{N_{\boldsymbol{q}}(T_e) - N_{\boldsymbol{q}}(T_h)}{\tau_{\boldsymbol{q}}^h} + \dfrac{N_{\boldsymbol{q}}(T_e) - N_{\boldsymbol{q}}(T_L)}{\tau_{\boldsymbol{q}}^{\text{LO}}}}{\dfrac{1}{\tau_{\boldsymbol{q}}^e} + \dfrac{1}{\tau_{\boldsymbol{q}}^h} + \dfrac{1}{\tau_{\boldsymbol{q}}^{\text{LO}}}} \tag{5.11}$$

and using the familiar linear expansion for $N_{\boldsymbol{q}}(T_i) - N_{\boldsymbol{q}}(T_j)$ [Giteau *et al.* 2020], we show that

$$\left(\frac{dE}{dt}\right)_e = \sum_{\boldsymbol{q}} \frac{E_{\boldsymbol{q}}}{\tau^e_{\boldsymbol{q}}} \left[\frac{1}{1+\frac{\tau^e_{\boldsymbol{q}}}{\tau^h_{\boldsymbol{q}}}+\frac{\tau^e_{\boldsymbol{q}}}{\tau^{\mathrm{LO}}_{\boldsymbol{q}}}} \frac{E_{\boldsymbol{q}}}{k_B T_h^2}(T_e - T_h) \frac{\exp\left(\frac{E_{\boldsymbol{q}}}{k_B T_h}\right)}{\left(\exp\left(\frac{E_{\boldsymbol{q}}}{k_B T_h}\right)-1\right)^2} \right. \\ \left. + \frac{1}{1+\frac{\tau^{\mathrm{LO}}_{\boldsymbol{q}}}{\tau^e_{\boldsymbol{q}}}+\frac{\tau^{\mathrm{LO}}_{\boldsymbol{q}}}{\tau^h_{\boldsymbol{q}}}} \frac{E_{\boldsymbol{q}}}{k_B T_L^2}(T_e - T_L) \frac{\exp\left(\frac{E_{\boldsymbol{q}}}{k_B T_L}\right)}{\left(\exp\left(\frac{E_{\boldsymbol{q}}}{k_B T_L}\right)-1\right)^2} \right] \tag{5.12}$$

This can be put under the form

$$\left(\frac{dE}{dt}\right)_e = Q_{eh}(T_e - T_h) + Q_{eL}(T_e - T_L) \tag{5.13}$$

where Q_{eh} and Q_{eL} are complex functions of the carrier distributions (μ_e, μ_h, T_e, T_h), and LO phonon dispersion relation. Note that Q_{eh} and Q_{eL} have the dimension of thermalization coefficients, and can be expressed in W.cm^{-2}.K^{-1}.

This equation is fundamental, because it states that the thermalization rate of electrons depends not only on the difference of temperature between electrons and the lattice, but also on the difference of temperature between electrons and holes. The latter is a term of electron-hole interaction mediated by LO phonons. It can be understood with the following picture. When electrons are hotter than holes, they emit more LO phonons. Holes may reabsorb part of these LO phonons emitted by electrons. Consequently, electrons lose energy to holes through LO phonons.

Result 5.5. (Energy redistribution mediated by LO phonons)
In the two-temperature model, carrier energy loss rates can be written as a term of relaxation towards lattice temperature plus a term of relaxation towards the other carrier temperature. This carrier-carrier interaction mediated by LO phonons may be instrumental to understand carrier thermalization in the two-temperature model. In particular, it might explain the energy redistribution observed in the previous section.

5.6 Conclusion

In this chapter, we proposed the first purely optical method to determine simultaneously electron and hole temperatures from photoluminescence in steady-state. This technique relies on the measurement of BF effect. Therefore, it applies only to systems close enough to degeneracy (typically $\Delta\mu_{\mathrm{eff}} \gtrsim E_g - 5k_BT_{\mathrm{eff}}$). This condition is not expected to be restrictive for most hot-carrier absorber which are submitted to intense photogeneration. In addition, the determination of electron and hole temperatures requires a good knowledge of the absorptivity of the system, otherwise the contribution of BF may not distinguishable.

We successfully applied this technique on sample 5006 (InGaAsP/InGaAsP single quantum well) at room temperature. We report electron temperatures around 1000 K at largest excitation intensity, while holes remain much colder, close to the lattice temperature. The small increase in hole temperature was shown to be too large to be explained by photon absorption. Therefore, we evidenced energy redistribution between electrons and holes. We suggested that phonon-mediated electron-hole interactions could potentially explain this effect. However, further in-depth investigation of two-temperature thermalization is required.

As will be discussed in the following chapter, proper two-temperature characterization of hot-carrier absorbers may help increase slightly the performances of Hot-Carrier Solar Cells (HCSCs).

Perspectives

- Reduce the uncertainty over the determination of carrier temperatures. This requires to study a sample with more stable absorptivity.
- Investigate in greater details the two-temperature thermalization model. Can it explain the carrier temperature dependence with excitation power? To this extent, studying PL spectra acquired with more homogeneous laser spot would be convenient to reduce energy diffusion effects.
- The possibility to distinguish electron and hole temperatures opens interesting perspectives with respect to hot-carrier transport. Indeed, the study proposed in chapter 4 assumed that electrons and holes had the same temperature. However, a more general theoretical framework with unequal temperatures would be rather straightforward, especially if holes are assumed to stay at lattice temperature. The biggest difficulty is on the experimental side, as uncertainty over electron and hole temperatures is still too large to allow us to measure reliable gradients.

Chapter 6

Operation, design and resilience of a two-temperature hot-carrier solar cell

In the previous two chapters, we have shown that temperatures in the absorber of a Hot-Carrier Solar Cell (HCSC) could be uneven. In chapter 4, we generated and studied a temperature gradient in a hot-carrier absorber. In chapter 5, we investigated the case of different temperatures for electrons and holes. In fact, both effects imply that the temperature of electrons extracted at one end of the device and of holes extracted at the other end will be different (see Figure 6.1). In this chapter, we investigate the effect of such uneven temperatures on the operation and design of HCSCs, and in particular on their efficiency.

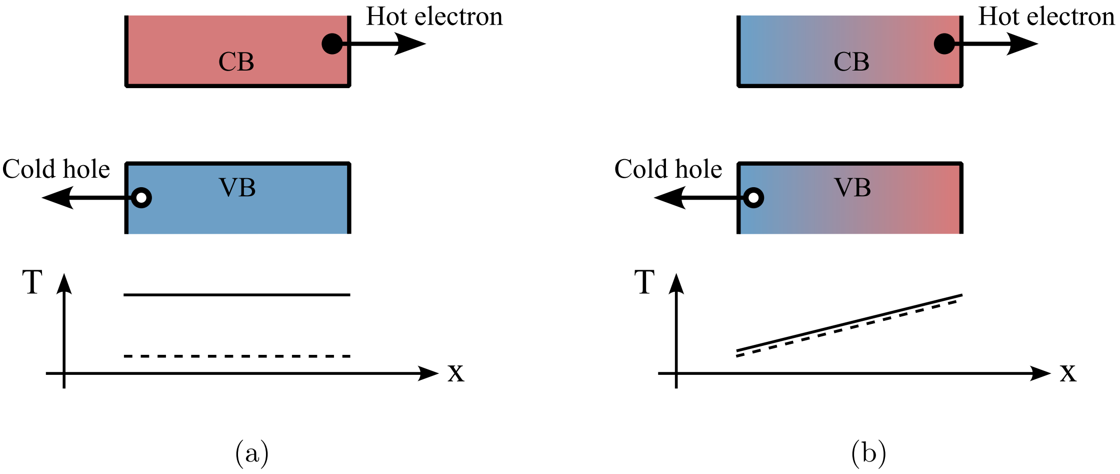

(a) (b)

Figure 6.1: *Similarities between (a) a HCSC with different temperature for electrons and holes and (b) a HCSC with a gradient of temperature. CB (resp. VB) stands for conduction (resp. valence) band.*

To do so, we investigate primarily the situation depicted in Figure 6.1a, where electrons and holes have different but homogeneous temperature. We first propose an extension of the model presented in chapter 3, that accounts for different homogeneous temperatures for electrons and holes. This model differs from previous isothermal approaches [Ross and Nozik 1982, Wurfel 1997, Le Bris and Guillemoles 2010, Limpert *et al.* 2015] by the fact that we explicitly distinguish electrons and holes, which are assumed to form thermal distributions with different temperatures. It is largely inspired by [Gibelli *et al.* 2019], but we simplified many elements of the model to be able to obtain more explicit results. In particular,

1. we consider the energy-selective contacts as ideal because we want to focus on the effect of the two temperatures and we do not try to be as realistic as possible. This simplification notably allows us to establish an expression for the voltage of the cell.

2. we do not include electron-hole interactions.

In this chapter, we focus on computing the energy-conversion efficiency of the system in various conditions. In particular, we will study the notion of *resilience* to two-temperature effects: is it important to consider two-temperature effects when designing a HCSC? How do two-temperature HCSCs behave when they are used in non-optimal configurations?

In this chapter, we first describe the two-temperature model in section 6.2. We then use this model to compute the operation of an example two-temperature HCSC in section 6.3. Then, we discuss specifically the impact of the two-temperature effect on the performances of HCSCs in section 6.4 and show that the two-temperature effect actually increases the efficiency of such devices by about 2 percentage points at best. We further analyze the sensitivity of HCSCs with respect to the position of their extraction levels. While in one-temperature HCSCs, only the difference between electron and hole extraction energy is significant, in two-temperature HCSCs, the precise position of these levels is crucial for maintaining high efficiencies.

Results from this chapter are currently being reviewed in *EPJ Photovoltaics*.

Table of contents

6.1 Highlights

Theoretical Highlight 6.1. (Two-temperature HCSC model)
We describe the equations that allow to model a two-temperature HCSC. This model is a generalization of the one proposed in chapter 3, where we distinguish electrons from holes in the power balance.

Numerical Highlight 6.1. (Impact of the two-temperature effect on the efficiency of HCSCs)
Two-temperature HCSCs exhibit higher efficiencies – 2 percentage points at best – as compared with their one-temperature counterparts. However, this effect vanishes for ideal HCSCs with vanishing thermalization coefficients. Therefore, the optimal efficiency of two-temperature HCSCs is the same as one-temperature ones, about 86 % under full concentration.

Numerical Highlight 6.2. (Resilience of two-temperature HCSCs)
HCSCs are resilient to two-temperature effects, in the sense that HCSCs designed based on incorrect knowledge of the individual temperatures of electrons and holes would have, at worse, and efficiency reduced by about 2 percentage points. However, two-temperature HCSCs are sensitive to the position of each energy-selective contact, and not only on their difference, as is the case for one-temperature HCSCs.

6.2 Two-temperature hot-carrier solar cell modelling

In this section, we present the two-temperature HCSC model, which is represented schematically in Figure 6.2. We first describe the balance equations governing such a system. Then we provide a complete derivation of the voltage of the two-temperature HCSC in the case of isentropic extraction. Finally, we show that the two-temperature model can simulate any one-temperature HCSC, provided that the correct parameters are used.

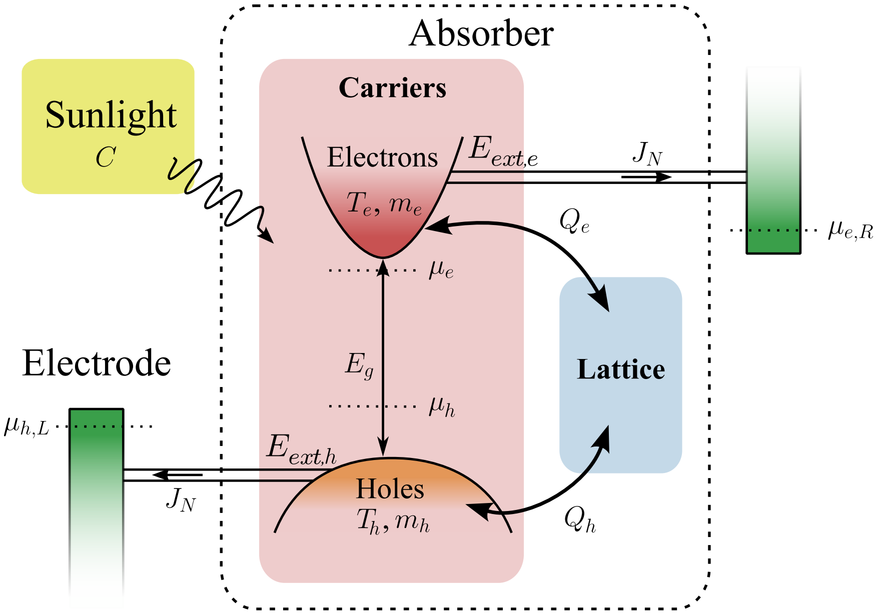

Figure 6.2: *Schematic representation of a two-temperature HCSC. All parameters are represented explicitly. Colors are representative of the expected temperature of each subsystem (blue for cold, red for hot).*

6.2.1 Balance equations in the two-temperature model

Just like for the one-temperature HCSC model presented in chapter 3, we consider a system illuminated by the sun (with concentration factor C). The absorber is a semiconductor of bandgap E_g, described within the Boltzmann approximation, in which carriers may (1) absorb photons, (2) emit photons by radiative recombination, (3) be extracted isentropically by perfectly selective contacts and (4) thermalize with the lattice. However, this time, we distinguish the effect of these 4 processes on electrons and holes. Electrons and holes distributions are still thermal distribution, but may have different temperature T_e and T_h, and different chemical potentials μ_e and μ_h.

6.2.1.1 Particle balance

All the processes changing the number of particles in the two-temperature HCSC are symmetrical for electrons and holes. Therefore, the particle balance writes the same for the two subsystems. In steady state, the number of electrons should stay constant, such that

$$\Phi_{\text{abs}} - \Phi_{\text{rad}} - J_N = 0 \tag{6.1}$$

where

$\Phi_{\text{abs}} = \int_{E_g}^{\infty} \phi_{\odot}(E)\, dE$ is the total solar flux absorbed by the system (in $\text{s}^{-1}.\text{m}^{-2}$). It depends on the bandgap of the absorber E_g and on the concentration factor C.

$\Phi_{\text{rad}} = \int_{E_g}^{\infty} \frac{2\pi}{h^3c^2} E^2 \left(\exp \frac{E-\Delta\mu_{\text{eff}}}{k_B T_{\text{eff}}} - 1\right)^{-1} dE$ the photon flux emitted by the system (in $\text{s}^{-1}.\text{m}^{-2}$), described by the two-temperature GPL (see Equation (2.18)). It depends on the bandgap of the material E_g, but also on the effective temperature T_{eff} and QFLS $\Delta\mu_{\text{eff}}$ (see Equation (5.2)).

J_N = the particle current running through the cell (in $\text{s}^{-1}.\text{m}^{-2}$).

The particle balance of the two-temperature HCSC relies on the same 4 variables than the one of the one-temperature HCSC, namely: the concentration factor C, the bandgap of the absorber E_g, the effective temperature T_{eff} and the effective QFLS $\Delta\mu_{\text{eff}}$.

6.2.1.2 Power balance

In the two-temperature HCSC, it is necessary to write one power balance for electrons and one for holes. Indeed, as was highlighted in chapter 5, none of the processes that change electrons or holes energy are symmetrical for the two carrier types. In steady-state,

$$P_{\text{abs,i}} - P_{\text{rad,i}} - P_{\text{th,i}} - P_{\text{ext,i}} = 0 \tag{6.2}$$

where

i = Denotes either electrons (e) or holes (h).

$P_{\text{abs,i}} = \int_{E_g}^{\infty} E_i(E)\phi_{\odot}(E)\, dE$ is the power absorbed by carrier type i (in $\text{W}.\text{m}^{-2}$). It depends only on the bandgap E_g, on the concentration factor C and on the effective mass mismatch ξ through the term $E_i(E)$ (see Equation (2.3)).

$P_{\text{rad,i}} = \int_{E_g}^{\infty} E_i(E)\phi_{\text{rad}}(E)\, dE$ is the power emitted by the subsystem composed of carriers i (in $\text{W}.\text{m}^{-2}$). It depends on the bandgap of the material E_g, on the effective temperature T_{eff} and QFLS $\Delta\mu_{\text{eff}}$ through the term $\phi_{\text{rad}}(E)$, but also on the effective mass mismatch ξ through the term $E_i(E)$.

$P_{\text{th,i}} = Q_i(T_i - T_L)$ is the power thermalized by carriers i (in $\text{W}.\text{m}^{-2}$). A priori, electrons and holes have different thermalization coefficients.

$P_{\text{ext,i}} = J_N E_{\text{ext,i}}$ is the power lost by carriers i due to the extraction (in $\text{W}.\text{m}^{-2}$). $E_{\text{ext,i}}$ is the extraction energy of carrier i. A priori, electrons and holes have different extraction energies, as represented in Figure 6.2.

It appears that the description of the power balance in the two-temperature HCSC is more complex than for the one-temperature HCSC. This time, it is necessary to distinguish thermalization coefficients and extraction energies of electrons and holes. In addition, it is necessary to introduce the effective mass mismatch ξ. However, the only term that depends on T_e and T_h individually in these equations is the thermalized power. All other terms depend only on the effective temperature.

Within the effective mass approximation, electrons and holes participating in absorbing a photon of energy E all have the same energy, given by Equation (2.3). Using this relation, the absorbed and emitted powers can be put under the following simple form:

$$P_{\mathrm{abs,e}} = (1-\xi)P_{\mathrm{abs}} - \left(\frac{1}{2} - \xi\right) E_g \Phi_{\mathrm{abs}} \tag{6.3}$$

$$P_{\mathrm{abs,h}} = \xi P_{\mathrm{abs}} + \left(\frac{1}{2} - \xi\right) E_g \Phi_{\mathrm{abs}} \tag{6.4}$$

And emitted fluxes $P_{\mathrm{rad,i}}$ have similar expressions (simply replace "abs" by "rad" in the formula).

It may appear surprising that the power radiated by electrons (resp. holes) depends only on the effective temperature T_{eff}, and not directly on electron (resp. hole) temperature T_e (resp. T_h). However, that is simply a consequence of the fact that we assumed perfect absorptivity $A(E) = \Theta(E - E_g)$ in the two-temperature GPL (see Equation (5.1)).

6.2.2 Voltage of two-temperature hot-carrier solar cells

To compute the voltage of a two-temperature HCSC, we assume that electrons and holes are described by thermal distributions, characterized by T_e, μ_e, T_h and μ_h. These four variables form the *thermodynamical state* of the absorber. By convention, electrons are extracted at the right contact (at room temperature and with a chemical potential $\mu_{\mathrm{e,R}}$), and holes are extracted in the left contact (with chemical potential $\mu_{\mathrm{h,L}}$). Note that the latter process is equivalent to reinjecting electrons in the absorber from the left contact, with a chemical potential $\mu_{\mathrm{e,L}} = -\mu_{\mathrm{h,L}}$.

The voltage of an electrical device V is linked to the work that one can extract from an electron circulating across the system. By definition, this is linked to the chemical potential of the electrodes as

$$eV = \frac{P_{\mathrm{elec}}}{J_N} = \mu_{\mathrm{e,R}} + \mu_{\mathrm{h,L}} \tag{6.5}$$

By writing the thermodynamical equilibrium of the two-temperature HCSC, it is possible to compute $\mu_{\mathrm{e,R}}$ and $\mu_{\mathrm{h,L}}$ as a function of the thermodynamical state in the absorber. We write the variation of energy in the absorber, dU_e^{abs}, and in the contact dU_e^{con} at the right side of the system, where an electron is removed from the absorber and injected in the contact. By definition,

$$\begin{cases} dU_e^{\mathrm{abs}} = -E_{\mathrm{ext,e}} = -\mu_e + T_e dS_e^{\mathrm{abs}} \\ dU_e^{\mathrm{con}} = +E_{\mathrm{ext,e}} = +\mu_{\mathrm{e,R}} + T_L dS_e^{\mathrm{con}} \end{cases} \tag{6.6}$$

where

$E_{\mathrm{ext,e}}$ = The extraction energy of electrons at the right contact.
μ_e = The chemical potential of electrons in the absorber.
T_e = The temperature of electrons in the absorber.
T_L = The temperature of carriers in the contact. In this chapter, we assume that $T_L = 300$ K.
dS_e^{abs} = The variation of entropy in the absorber at the right contact.
dS_e^{con} = The variation of entropy in the right contact.

Similarly, at the left contact, where an electron is injected from the contact to the absorber (*i.e.* a hole is injected from the the absorber valence band to the contact valence band), one gets

$$\begin{cases} dU_h^{\text{abs}} = -E_{\text{ext,h}} = -\mu_h + T_h dS_h^{\text{abs}} \\ dU_h^{\text{con}} = +E_{\text{ext,h}} = +\mu_{\text{h,L}} + T_L dS_h^{\text{con}} \end{cases} \tag{6.7}$$

where the signs of $E_{\text{ext,h}}$, μ_h and $\mu_{\text{h,L}}$ have been changed because we describe electrons in the valence band as holes with opposite energy and chemical potential (see section 2.1.1).

Since the exchange of particles is supposed to be isentropic, no entropy is created in the system, such that

$$dS^{\text{abs}} + dS^{\text{con}} = 0 \quad \Leftrightarrow \quad dS_e^{\text{abs}} + dS_h^{\text{abs}} = -dS_e^{\text{con}} - dS_h^{\text{con}} \tag{6.8}$$

By injecting Equation (6.6) and Equation (6.7), we obtain

$$\frac{\mu_e - E_{\text{ext,e}}}{T_e} + \frac{\mu_h - E_{\text{ext,h}}}{T_h} = -\frac{E_{\text{ext,e}} - \mu_{e,R} + E_{\text{ext,h}} - \mu_{h,L}}{T_L} \tag{6.9}$$

$$i.e. \quad eV = E_{\text{ext,e}}\left(1 - \frac{T_L}{T_e}\right) + \mu_e \frac{T_L}{T_e} + E_{\text{ext,h}}\left(1 - \frac{T_L}{T_h}\right) + \mu_h \frac{T_L}{T_h} \tag{6.10}$$

Result 6.1. (Voltage of a two-temperature hot-carrier solar cell)
The voltage of a two-temperature HCSC is given by

$$eV = E_{\text{ext,e}}\left(1 - \frac{T_L}{T_e}\right) + \mu_e \frac{T_L}{T_e} + E_{\text{ext,h}}\left(1 - \frac{T_L}{T_h}\right) + \mu_h \frac{T_L}{T_h} \tag{6.11}$$

In general, this equation involves the chemical potentials and extraction energies of electrons and holes independently. In the special case where $T_e = T_h = T_{\text{eff}}$, we recover the usual voltage of a one-temperature HCSC, which only depends on the total extraction energy $\Delta E_{\text{ext}} = E_{\text{ext,e}} + E_{\text{ext,h}}$ and on the QFLS $\Delta\mu_{\text{eff}} = \mu_e + \mu_h$

$$eV = \Delta E_{\text{ext}}\left(1 - \frac{T_L}{T_{\text{eff}}}\right) + \Delta\mu_{\text{eff}} \frac{T_L}{T_{\text{eff}}}$$

6.2.3 Retrieving one-temperature hot-carrier solar cells

Our two-temperature model allows to simulate any one-temperature HCSCs. Indeed, by carefully selecting the two-temperature model parameters, we can ensure that electron and hole temperatures are equal at all operation points (*i.e.* at all J_N). At open-circuit voltage ($J_N = 0$), one finds that $T_e = T_h$ if and only if

$$\begin{cases} Q_e = (1-\xi)Q \\ Q_h = \xi Q \end{cases} \tag{6.12}$$

where Q is a free parameter that can take any positive value. And then to have $T_e = T_h$ for any arbitrary value of the current, we find that:

$$\begin{cases} E_{\text{ext,e}} = \dfrac{E_g}{2} + (1-\xi)(\Delta E_{\text{ext}} - E_g) \\ E_{\text{ext,h}} = \dfrac{E_g}{2} + \xi(\Delta E_{\text{ext}} - E_g) \end{cases} \tag{6.13}$$

where ΔE_{ext} is another free parameter.

This shows that it is possible to build a HCSC which will have $T_e = T_h$ at all operating points, no matter how strong the mass mismatch is. In this configuration, the two-temperature HCSC becomes strictly equivalent to the one-temperature model defined in chapter 3. In particular, in this configuration, the cell is parametrized by a single effective thermalization coefficient Q and a single extraction energy ΔE_{ext}.

Note that the parametrization of this particular two-temperature HCSC depends on the mass mismatch ξ, but it can be shown that its operation does not. In particular, the effective temperature, the voltage, the efficiency, etc. will not depend on ξ but only on the value of Q and ΔE_{ext}.

6.3 Operation of two-temperature hot-carrier solar cells

Now that we have defined the equations ruling two-temperature HCSCs, we are interested in finding their maximum power point. This can be done by simulating the JV characteristic of the cell, similarly to what was presented for one-temperature HCSCs in chapter 3. For all possible values of the current J_N, we compute the voltage with the procedure described in Result 6.2. From there, we can identify the operation point that maximizes the electrical power output of the HCSC: $P_{\text{elec}} = eJ_NV$.

Result 6.2. (Physical engine underlying our two-temperature HCSC model) A two-temperature HCSC is defined by a set of seven "material" parameters: C, E_g, ξ, $E_{\text{ext,e}}$, $E_{\text{ext,h}}$, Q_e and Q_h. The internal state of the HCSC is defined by four thermodynamical variables describing the carrier distributions (T_e, μ_e, T_h and μ_h).

For a given extraction current J_N, the thermodynamical state of the absorber may be determined by solving a system of four equations:

1. The particle balance

$$0 = \Phi_{\text{abs}} - \Phi_{\text{rad}}(T_{\text{eff}}, \Delta\mu_{\text{eff}}) - J_N \tag{6.14}$$

2. Two power balance equations (one for electrons and one for holes)

$$\begin{cases} 0 = P_{\text{abs,e}} - P_{\text{rad,e}}(T_{\text{eff}}, \Delta\mu_{\text{eff}}) - Q_e(T_e - T_L) - J_N E_{\text{ext,e}} \\ 0 = P_{\text{abs,h}} - P_{\text{rad,h}}(T_{\text{eff}}, \Delta\mu_{\text{eff}}) - Q_h(T_h(T_{\text{eff}}, T_e) - T_L) - J_N E_{\text{ext,h}} \end{cases} \tag{6.15}$$

where the relation $T_h(T_{\text{eff}}, T_e)$ is given by the definition of the effective temperature. Note that these three first equation depends only on three variables: T_{eff}, T_e

and $\Delta\mu_{\text{eff}}$ (see Toolbox 5.1 for a conversion table), so we can already determine three of the four variables with this set of equations.

3. Finally, we close the system with electroneutrality relation. As we assumed that the carrier distributions could be described by the Boltzmann approximation, electroneutrality writes (see Appendix B):

$$\frac{\mu_e}{T_e} = \frac{\mu_h}{T_h} + \frac{3}{2}k_B \ln\left(\frac{m_h T_h}{m_e T_e}\right) + \frac{E_g}{2}\left(\frac{1}{T_e} - \frac{1}{T_h}\right) \tag{6.16}$$

Once T_e, μ_e, T_h and μ_h are known from solving this system for a specific value of the current J_N, the voltage of the cell is given by Equation (6.11):

$$eV = E_{\text{ext,e}}\left(1 - \frac{T_L}{T_e}\right) + \mu_e\frac{T_L}{T_e} + E_{\text{ext,h}}\left(1 - \frac{T_L}{T_h}\right) + \mu_h\frac{T_L}{T_e}$$

We provide an example of cell simulation in Figure 6.3. We represent the JV characteristic, but also electron and hole temperatures as a function of the extraction current, the chemical potentials, and we represent the particle and power balances in a graphical way.

We purposely represent a case with high electron extraction energy and low hole extraction energy, such that electron temperature decreases with increasing extraction current, while hole temperature increases. At open-circuit voltage, electron temperature is higher than that of holes due to the fact that electrons have lower effective mass and that thermalization coefficients are equal. However, as the current increases, hole temperature becomes larger than electron temperature, and can even become hotter than the Sun. As was already explained in section 3.4, this is not contradictory.

Also as in section 3.4, we observe that the system does not always have physical solutions, especially at large current and extraction energies. For two-temperature HC-SCs, there are two constraints as both electron and hole temperatures must be positive. The condition obtained in the one-temperature case (Equation (3.15)) can be extended straightforwardly, and we get that the system admits no physical solution if and only if

$$\begin{cases} E_{\text{ext,e}} > E_{\text{crit,e}} \text{ or } E_{\text{ext,h}} > E_{\text{crit,h}} \\ J_N > \min(J_{\text{crit,e}}, J_{\text{crit,h}}) \end{cases} \quad \text{with} \quad \begin{cases} E_{\text{crit,e}} = \dfrac{E_g}{2} + \dfrac{P_{\text{abs,e}} - (E_g/2)J_{\text{abs}} + Q_e T_L}{J_{\text{abs}}} \\ E_{\text{crit,h}} = \dfrac{E_g}{2} + \dfrac{P_{\text{abs,h}} - (E_g/2)J_{\text{abs}} + Q_h T_L}{J_{\text{abs}}} \\ J_{\text{crit,e}} = \dfrac{P_{\text{abs,e}} - (E_g/2)J_{\text{abs}} + Q_e T_L}{E_{\text{ext,e}} - E_g/2} \\ J_{\text{crit,h}} = \dfrac{P_{\text{abs,h}} - (E_g/2)J_{\text{abs}} + Q_h T_L}{E_{\text{ext,h}} - E_g/2} \end{cases} \tag{6.17}$$

In Figure 6.3, we represent a case where $E_{\text{ext,e}} > E_{\text{crit,e}}$. Therefore, the extracted current is limited by $J_{\text{crit,e}} \simeq 440$ A.m^{-2} rather than by $J_{\text{abs}} \simeq 600$ A.m^{-2}, and for $J_N \to J_{\text{crit,e}}$, we notice that $T_e \to 0$ K.

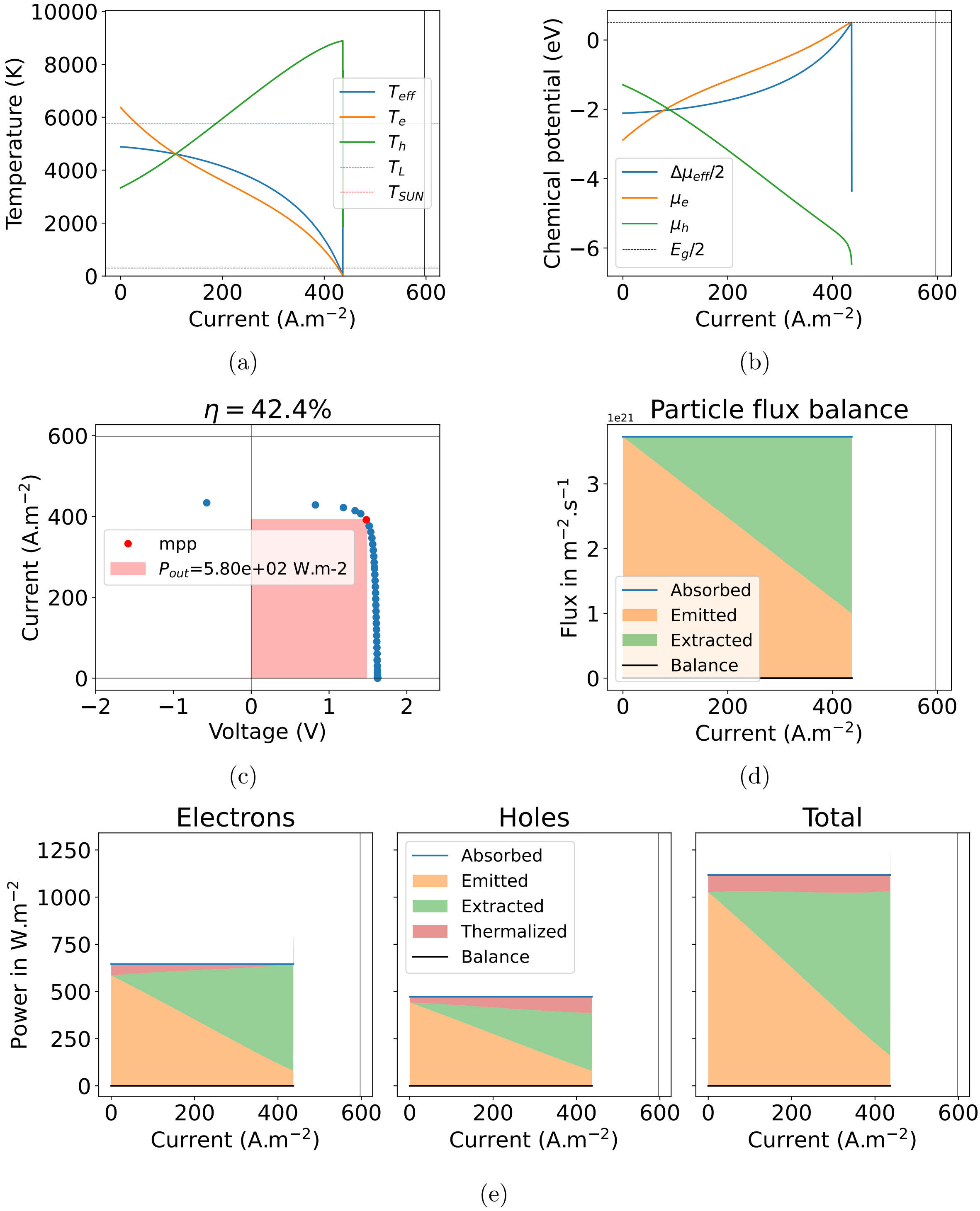

(a)

(b)

(c)

(d)

(e)

Figure 6.3: *Representation of the operation of a two-temperature HCSC under one sun illumination: (a) temperatures, (b) QFLS, (c) JV characteristics, (d) particle balance, (e) power balance. Plain black line indicates the absorbed current* $J_{\mathrm{abs}} = e\Phi_{\mathrm{abs}} \simeq 600\ \mathrm{A.m^{-2}}$. *This cell was simulated with the following parameters:* $E_g = 1$ eV, $\xi = 1/3$, $Q_e = Q_h = 1 \times 10^{-6}\ \mathrm{W.cm^{-2}.K^{-1}}$, $E_{\mathrm{ext,e}} = 1.3$ eV, $E_{\mathrm{ext,h}} = 0.7$ eV.

6.4 Impact of the two-temperature effect on the operation of hot-carrier solar cells

In this section, we propose to evaluate the impact of two-temperatures on the operation of HCSCs. To do so, we need a reference one-temperature HCSC as point of comparison. There exist many different ways of defining the reference HCSC. For instance, it could be a cell with same effective temperature or same total thermalized power, and these definitions are not equivalent. Therefore, we start by describing how we define the designs to compare in section 6.4.1. Second, we compute the efficiency of a HCSC with and without two-temperature effects in section 6.4.2, and show that the two-temperature HCSC is always more efficient than the one-temperature one (at fixed T_{eff}). Finally, we study the sensitivity of two-temperature HCSCs to their design in section 6.4.3. We show that the position of each energy-selective contact matters when designing the two-temperature, but that it is not mandatory to assess precisely the temperature mismatch in the absorber to design efficient HCSCs.

6.4.1 One and two-temperature designs

We imagine that we want to build a HCSC with a given material as absorber. In this configuration, all properties of the absorber (bandgap E_g, effective mass mismatch ξ, thermalization coefficients Q_e and Q_h) are imposed by the choice of material. Therefore, we call *design* of the HCSC the choice of position for its energy-selective contacts. To find the optimal design of this HCSC, we test all possible combinations of $E_{\text{ext,e}}$ and $E_{\text{ext,h}}$ until we find the combination with highest efficiency. The HCSC optimal design depends on the temperature of carriers in the absorber, and therefore on the thermalization coefficients Q_e and Q_h.

However, in general, thermalization coefficients cannot be found in tables, and we must measure them, for instance with continuous-wave Photoluminescence (PL) spectroscopy. Indeed, PL experiments are conducted at open-circuit ($J_N = 0$), and it is generally possible to know the absorbed flux and power. From there, measuring electron and hole temperatures with PL spectroscopy (see chapter 5) is equivalent to measuring the thermalization rates, because all other parameters in the balance equations governing the system are known (see Result 6.2).

When using two-temperature analysis on PL spectra, it is possible to measure the true thermalization coefficients, that we write Q_e^{2T} and Q_h^{2T}. The optimal design obtained for this set of thermalization coefficients is called *2T design*, and the resulting efficiency of the HCSC is called *2T efficiency*, written as η^{2T}.

However, standard PL analysis does not provide that much information on the sample, as represented in Figure 6.4. It only grants access to the effective temperature T_{eff}. With such knowledge, it is not possible to recover the true values of Q_e and Q_h. Instead, we would obtain the values Q_e^{1T} and Q_h^{1T} such that $T_e = T_h = T_{\text{eff}}$ at open-circuit, as shown in Figure 6.4b. Based on these “incorrect” values of the thermalization coefficients, we can compute what we call here the *1T design* (see Figure 6.4c), which is the optimal design of a cell assuming that $Q_e = Q_e^{1T}$ and $Q_h = Q_h^{1T}$. The efficiency of the device composed of the *real* absorber equipped with contacts placed following the 1T design is called *1T efficiency*, η^{1T}.

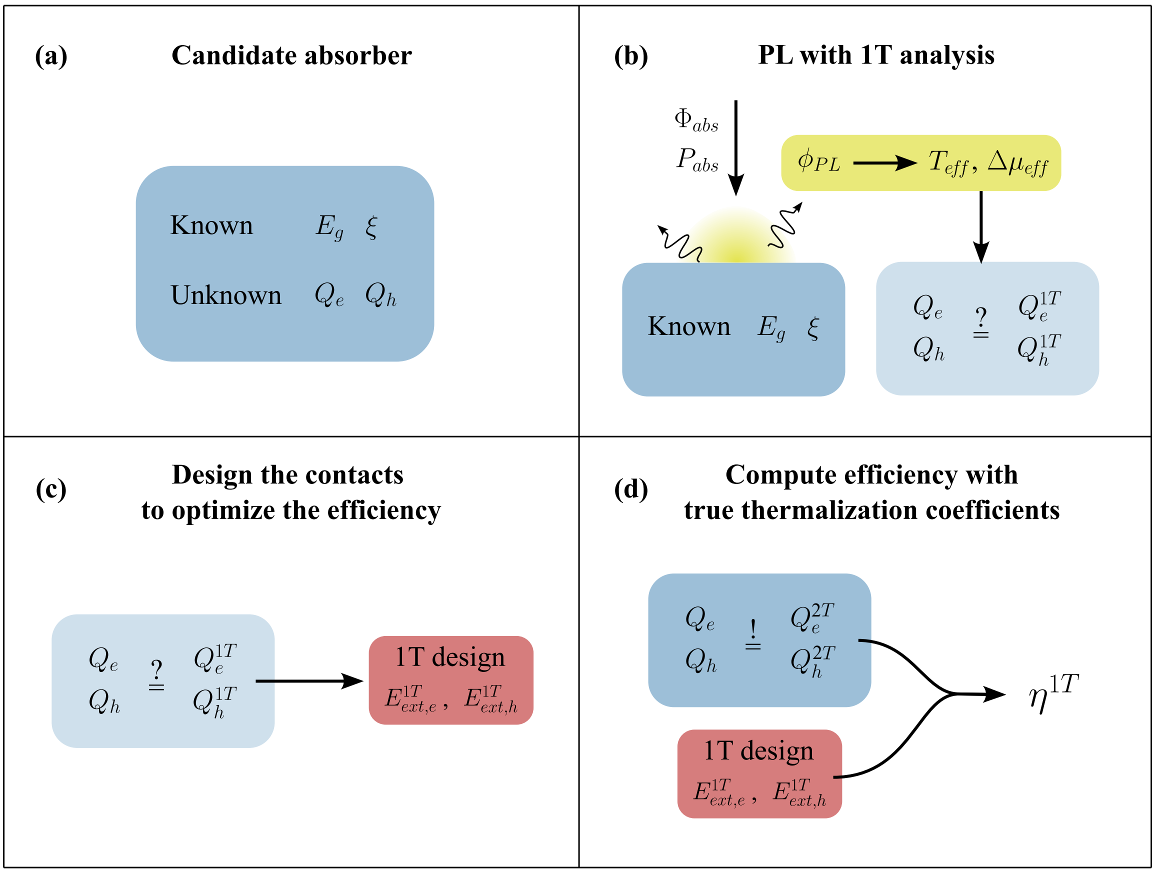

Figure 6.4: *Steps to design a HCSC from one temperature PL analysis. (a) Representation of the absorber with unknown thermalization coefficients. (b) From a one-temperature PL analysis, we determine the thermalization coefficients such that* $T_e = T_h = T_{\text{eff}}$ *in the absorber. (c) Using the thermalization coefficients determined in (b), we deduce the optimal position of the extraction energies (1T design). (d) Finally, we compute the 1T efficiency of the device by using its true thermalization coefficients, obtained from a two-temperature PL analysis.*

6.4.2 Sensitivity of hot-carrier solar cells to the two-temperature effect

In this section, we assume that a certain absorber has been characterized by PL under 1 sun conditions, and that its effective temperature at open-circuit T_{eff} is known. We are interested in comparing the 1T and 2T designs for different values of the temperature mismatch $r = T_e/T_h$ at open-circuit. We will first report the efficiencies, then the position of the extraction energies, and finally we will study the variations of electrical figures of merit with r.

6.4.2.1 Efficiency

Figure 6.5 presents the efficiencies of the two designs computed with $E_g = 1$ eV and $T_{\text{eff}} = 2000$ K under one sun illumination. This situation corresponds to $Q \simeq 2 \times 10^{-5}$ W.cm^{-2}.K^{-1}.

Notice how the 2T efficiency is always higher than the 1T efficiency. This is expec-

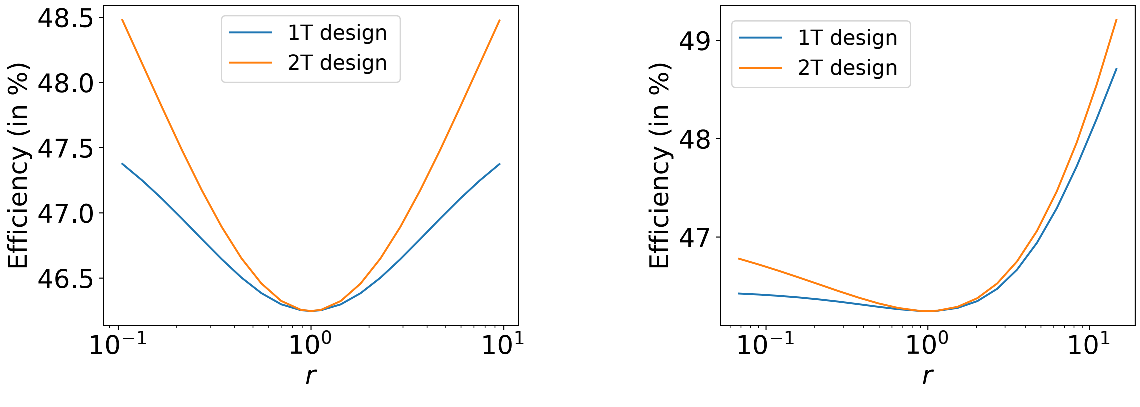

(a) (b)

Figure 6.5: *Comparison of the efficiencies of HCSCs based on the 1T and 2T designs as a function of the temperature mismatch r for an effective mass mismatch (a)* $\xi = 1/2$ *and (b)* $\xi = 1/11$. *Computations are performed assuming an effective temperature* $T_{\text{eff}} = 2000$ K *at open-circuit and a bandgap* $E_g = 1$ eV.

ted, as both efficiencies are computed by simulating a HCSC with the same absorber, but different contacts. As the 1T design is computed assuming incorrect values of the thermalization coefficients, it is necessarily less efficient than the 2T design, which is the optimum computed with correct thermalization coefficients.

More surprisingly, the 1T efficiency is always *higher* when $r \neq 1$ than when $r = 1$. This means that the two-temperature effect is beneficial even for HCSCs which have been designed disregarding this effect.

However, the two-temperature effect disappears both for the 1T and 2T designs when $Q_{e,h} \to 0$ and $Q_{e,h} \to \infty$. This can be understood as follows:

- When $Q_{e,h} \to 0$, thermalization losses become negligible. But in this case, the only term allowing to distinguish T_e and T_h in the equations disappear (see Result 6.2). Therefore the operation of the two-temperature HCSC no longer depends on the value of r.

- When $Q_{e,h} \to \infty$, the fast thermalization ensures that $T_e \simeq T_h \simeq 300$ K, such that there cannot be two temperatures in the absorber.

Therefore, the two-temperature effect does not change the efficiency of ideal HCSC, nor of ideal thermalized solar cells.

In the symmetrical case ($\xi = 1/2$, see Figure 6.5a), it does not matter which carrier is hotter than the other. However, when effective masses are not the same (see Figure 6.5b), this is no longer the case. It appears that the HCSC is more efficient when the hottest carriers are the lighter ones. In the case presented here, electrons are the lightest carriers so this corresponds to $r > 1$.

Result 6.3. (The two-temperature effect is beneficial for non-ideal HCSCs)
Two temperature effect allows an increase in efficiency of HCSCs. In best case scenario,

when electrons and holes have identical effective masses and strongly different temperatures and when $T_{\text{eff}} \simeq 2000$ K at open-circuit, the increase of efficiency can be up to 2 percentage points as compared with the case $r = 1$. However, the two-temperature effect does not increase the optimal efficiency of HCSCs, as its contribution becomes negligible when $Q \to 0$.

6.4.2.2 Optimal design of the two-temperature hot-carrier solar cell

To understand why the two-temperature effect is beneficial to the efficiency of HCSCs, we represent the optimal designs mentioned in the previous paragraph. We report in Figure 6.6 the value of the extraction energies for the 1T and 2T designs as a function of the temperature mismatch. For this effective temperature $T_{\text{eff}} = 2000$ K and bandgap $E_g = 1$ eV, the extraction energy of the 1T design is $\Delta E_{\text{ext}} = 1.686$ eV, which corresponds to $E_{\text{ext,e}} = E_{\text{ext,h}} = 0.843$ eV in the symmetrical case, and to $E_{\text{ext,e}} = 1.124$ eV and $E_{\text{ext,h}} = 0.562$ eV when $\xi = 1/11$ (see Equation (6.13)). Since the 1T design does not depend on the value of r, we only report the difference between the 1T and 2T designs.

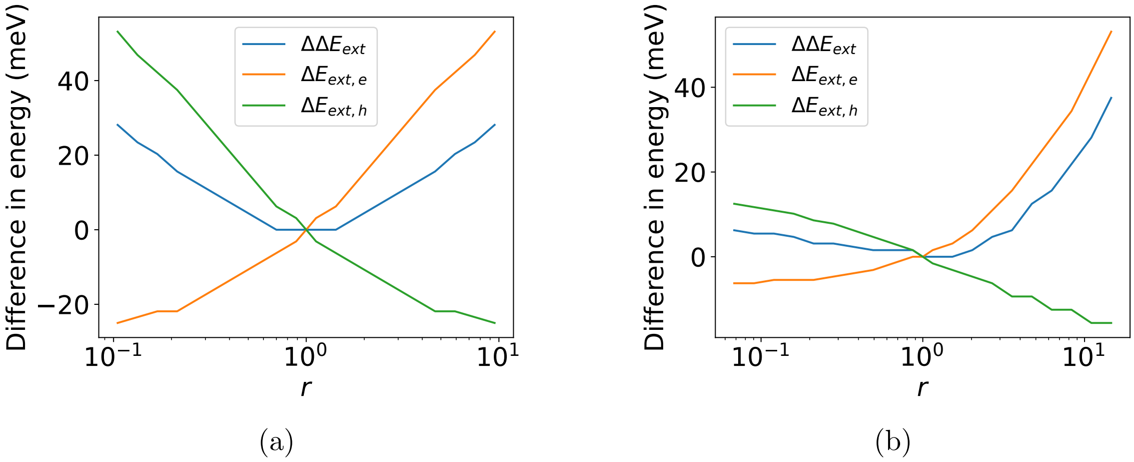

(a) (b)

Figure 6.6: *Difference in extraction energies between the 1T and 2T designs, as a function of the temperature mismatch r and for an effective mass mismatch (a) $\xi = 1/2$ and (b) $\xi = 1/11$. Computations are performed assuming an effective temperature $T_{\text{eff}} = 2000$ K at open-circuit and a bandgap $E_g = 1$ eV.*

When $r = 1$, 1T and 2T designs are the same, as expected. However, both electron and hole optimal extraction energies in the 2T design depend on the observed value of r. This is simply a consequence of the fact that electron and hole temperatures depend on r. The optimal extraction energy of a given carrier is an increasing function of its temperature, which was a well-known fact for one-temperature HCSCs [Le Bris and Guillemoles 2010].

However, the total extraction energy $\Delta E_{\text{ext}} = E_{\text{ext,e}} + E_{\text{ext,h}}$ is minimal when $r = 1$, and increases as r departs from 1 in both directions. This is consistent with the fact that the efficiency of the 2T design is higher when $r \neq 1$. Indeed, if every other parameter was constant, increasing ΔE_{ext} would increase the voltage of the cell and hence the efficiency. This explanation is tentative, because the increase of ΔE_{ext} has the same shape as the one of η^{2T}. However, temperatures in the absorber clearly depend on r, so the explanation cannot be that simple. To obtain more insight into the mechanisms behind this increase in efficiency, we computed the electrical figures of merit of two-temperature HCSC, which are presented in the following section.

Result 6.4. (Efficiency and optimal design of a two-temperature HCSC)
In all our computations, the optimal efficiency of the 2T design was shown to be slightly larger than the corresponding 1T design. The largest observed difference in efficiency between these two designs is ~ 1 points, and the largest difference in design of the energy-selective contacts is ±50 meV.

6.4.2.3 Electrical figures of merit

When comparing the efficiency of different solar cells, it is customary to consider three electrical figures of merit:

1. **The open-circuit voltage, V_{oc} (in V),** is the voltage when no charges are extracted ($J_N = 0$).
2. **The short-circuit current, J_{sc} (in A.m^{-2}),** is the current circulating in the cell when no electrical bias is applied.
3. **The fill-factor, FF (dimensionless),** is the ratio between the output power of the solar cell and the product $J_{\text{sc}}V_{\text{oc}}$.

By definition, the output power of the solar cell writes $P_{\text{elec}} = J_{\text{sc}} \times V_{\text{oc}} \times FF$. Therefore, the variations of these figures of merit at constant absorbed power are directly linked to variations of the efficiency.

We represent the variations of these three figures of merit, first for the 1T design in Figure 6.7a, then for the 2T design in Figure 6.7b. As we considered the case $\xi = 1/2$, we only report the case $r \geq 1$, which is symmetrical of the case $r \leq 1$.

For the 1T design, only the fill factor changes with r. Therefore the effect of the two-temperature effect alone is to increase the fill factor. The maximum increase of the fill factor is about 2 %, which corresponds to an increase of 1 percentage point of the efficiency.

When we further optimize the design of energy-selective contacts by going to the 2T design, we can almost maintain the increase in fill factor, while increasing also the open-circuit voltage by about 2 % (see Figure 6.7b). This results in another increase of 1 point of the total efficiency. These results are perfectly consistent with the increase in efficiency for the 1T and 2T designs, shown in Figure 6.5a.

Note that the short circuit current never depends on r. This is simply because we assumed a perfect absorptivity, such that in most configurations, $J_{\text{sc}} = J_{\text{abs}} = e\Phi_{\text{abs}}$. The only exceptions are cases where one of the extraction energies is above its critical value (see Equation (6.17)), but that should not happen for designs close to the optimum.

More surprising is the fact that the open-circuit voltage does not depend on r for the 1T design. Indeed, all thermodynamical variables controlling the voltage (see Equation (6.11)) change with r. However, for some reason, their changes compensate one

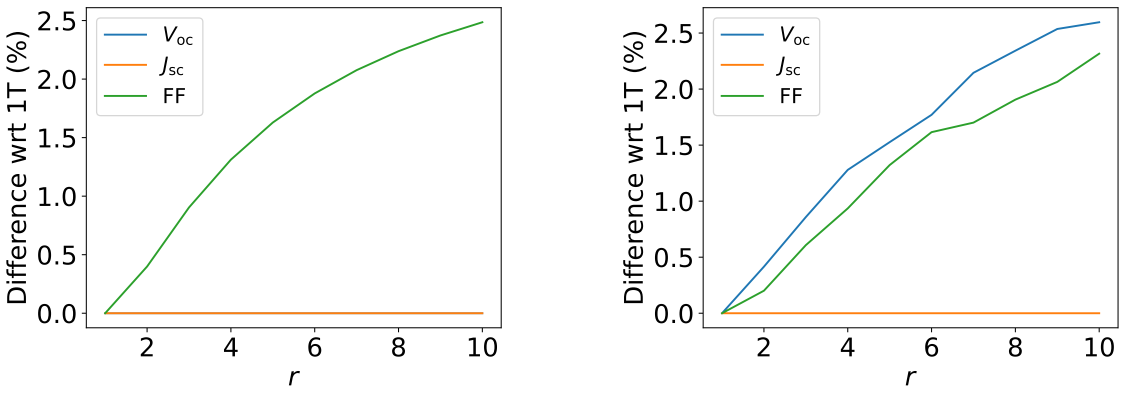

(a) (b)

Figure 6.7: *Variation of the electrical figures of merit of (a) 1T design and (b) 2T design, shown as a percentage with respect to their value at* $r = 1$. *Computations are done assuming* $\xi = 1/2$. *In panel (a), lines for* V_{oc} *and* J_{sc} *are indistinguishable.*

another. This could certainly be linked to more fundamental aspects of two-temperature HCSCs in future research.

Result 6.5. (Effect of the temperature mismatch on HCSCs)
For a fixed design of HCSC, temperature mismatch results in an increase of the fill-factor.

6.4.3 Resilience of two-temperature hot-carrier solar cells

6.4.3.1 Sensitivity to extraction energies

When designing a one-temperature HCSC according to Ross-Nozik model, the specific position of each energy-selective contact has no impact. Only their difference does. However, for two-temperature HCSCs, the efficiency depends strongly on the position of each contact, and it becomes important to select the right position. To illustrate this idea, we represent the efficiency of a two-temperature HCSC at a fixed value of $\Delta E_{\text{ext}} = E_{\text{ext,e}} + E_{\text{ext,h}}$, but depending on the position of $E_{\text{ext,e}}$ in Figure 6.8.

It confirms that the efficiency depends on the position of the contacts. However, the sensitivity depends strongly on the effective mass mismatch and the effective temperature in the absorber. The symmetrical cell is only weakly sensitive to the position of the contacts, and a variation of ±100 meV around the maximum translates into a change in efficiency of ~ 5 percentage points. In comparison, the asymmetrical cell is much more sensitive to the position of the contact, especially for cells close to ideality with large effective temperatures. In such cases, a change in 100 meV of the position of the contacts can entail a change in efficiency larger than 20 percentage points. This effect is attributed to the sensitivity to the position of the hole extraction energy $E_{\text{ext,h}} = \Delta E_{\text{ext}} - E_{\text{ext,e}}$ rather than of the electron extraction energy. Indeed, for such an asymmetrical cell, holes

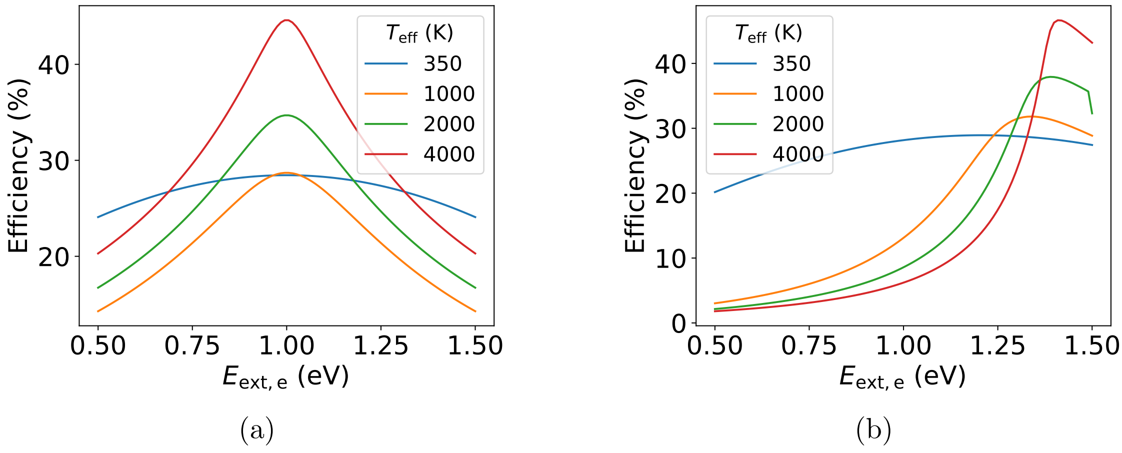

Figure 6.8: *Efficiency of a two-temperature HCSC as a function of the position of the electron extraction level* $E_{\mathrm{ext,e}}$ *for an effective mass mismatch (a)* $\xi = 1/2$ *and (b)* $\xi = 1/11$. *Computations are performed under one sun illumination, assuming* $E_g = 1$ eV, $\Delta E_{\mathrm{ext}} = 2$ eV, $Q_e = Q_h$ *and for different effective temperatures at open circuit.*

are much colder than electrons, and therefore they must be extracted close to the bottom of the valence band.

Generally speaking, the sensitivity to the position of the contacts decreases when the thermalization coefficient increases. In the limit of very large thermalization coefficient ($T_{\mathrm{eff}} \to 300$ K), we recover the result of Shockley-Queisser that the efficiency of the cell no longer depends on the position of the contacts.

Note also how the optimal position of the energy-selective contacts depends on the thermalization coefficient Q in the asymmetrical case. This is again an illustration of the fact that the optimal extraction energy of carriers depend on their temperature.

Result 6.6. (Sensitivity of the two-temperature HCSC to its design)
Two-temperature HCSCs are sensitive to the position of their extraction energies. This is particularly the case of almost ideal HCSCs with vanishing thermalization coefficient. In this case, a change of 100 meV of the extraction energy can lead to a change in efficiency larger than 20 points. This result emphasizes on the importance of carefully designing energy-selective contacts for highly efficient two-temperature HCSCs.

6.4.3.2 Resilience to incorrect determination of the temperature mismatch

Our final investigation on the two-temperature effect is towards the determination of the temperature mismatch r. We understand how to design the two-temperature HCSC for a given value of r, but how well will this cell operate if our estimate of r was wrong in the first place? In other words: is it crucial to measure precisely the temperature of electrons and holes?

Figure 6.9 presents the efficiency of a cell that was designed assuming an incorrect value of $r = r_0$ at open circuit, but that operates at a different value of r. The difference in efficiency is only of 2 percentage points at worse, which means that estimating precisely the value of the temperature mismatch is not crucial to design a two-temperature HCSC with high efficiency. In particular, as shown in Figure 6.9a, the 1T design is suitable for any temperature mismatch.

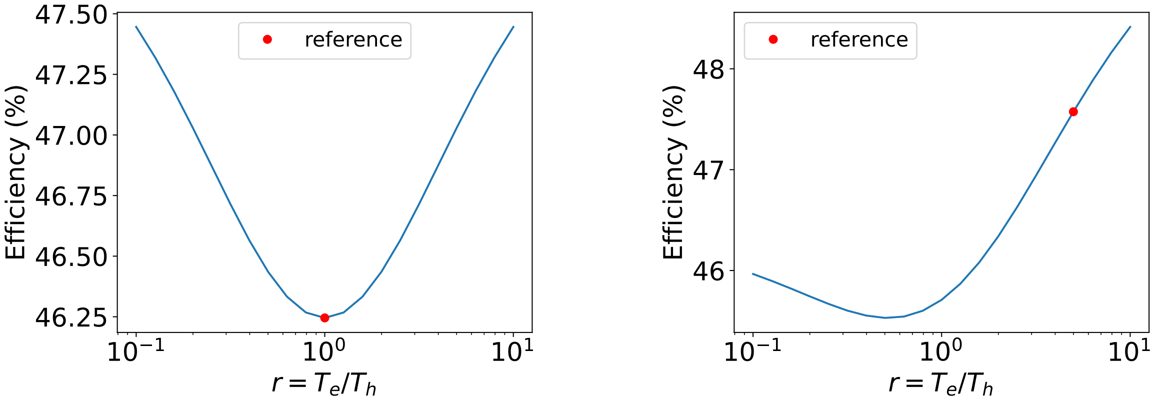

(a) (b)

Figure 6.9: *Efficiency of a two-temperature HCSC designed assuming (a)* $r = 1$*, (b)* $r = 5$*, as a function of the* real *temperature mismatch* r*. Computations are performed under one sun illumination and assuming* $E_g = 1$ eV*,* $T_{\text{eff}} = 2000$ K *and* $\xi = 1/2$*.*

Result 6.7. (Resilience of two-temperature HCSCs to incorrect determination of the temperature mismatch)
When designing a two-temperature HCSC, it is not necessary to assess very precisely electron and hole temperatures. Assuming $T_e = T_h$ would only result in an efficiency drop of about 2 percentage points at worse. In conclusion, HCSCs are resilient to incorrect determination of the temperature mismatch.

6.5 Conclusion

In this chapter, we showed that it was possible to extend the usual HCSC model to include different temperatures for electrons and holes. Our findings indicate that the two-temperature effect increases HCSCs performances, and can amount to an increase in efficiency of up to 2 percentage points. However, this effect becomes negligible for ideal HCSCs with vanishing thermalization coefficients such that two-temperature HCSCs have the same optimal efficiency than one-temperature ones.

We studied the resilience of two-temperature HCSCs and showed that, contrary to one-temperature HCSCs, they are sensitive to the position of each energy-selective contact, and not only on their spacing. However, the optimal design of two-temperature HCSCs as well as its efficiency do not depend much on the temperature mismatch in the absorber.

Therefore a proper determination of this temperature mismatch is not required when designing HCSCs.

Perspectives: In this chapter, we introduced a methodology for deriving model parameters from PL measurements, thus providing a tool for evaluating the potential of hot-carrier absorbers. However, our model so far is incompatible with real-world absorbers, who may have non-ideal absorptivity and non-ideal radiative efficiency. In addition, hot-carrier absorbers such as sample 5006 may be subject to band filling, and therefore they cannot be described in the Boltzmann approximation. As a consequence, we would like to improve our model to account for more realistic absorbers by including effects such as

1. Non-ideal absorptivity. In particular, assessing the performances of absorbers with $\mathcal{A} < 1$ and including Band Filling (BF) would be interesting.
2. Degeneracy. The model could easily be rephrased in terms of generic Fermi-Dirac distributions for electrons and holes. However, solving it numerically would prove much more intensive in terms of computations, unless we tabulate the values of the integrals necessary to compute the state of the system.
3. Non radiative recombinations.
4. Electron-hole interactions. There exist two types of electron-hole interactions. Elastic interactions such as Coulomb interaction simply redistribute the kinetic energy between carriers, and change T_e and T_h but not T_{eff}. On the contrary, non-elastic interactions such as Auger recombinations and impact ionization will change both the effective temperature and the effective QFLS.

Another interesting development would be to study the impact of Seebeck coefficient on the operation of a HCSC subject to a temperature gradient. To address this question, we would like to simulate the operation of a cell as depicted in Figure 6.1b. Formally speaking, the voltage of this cell would write as for a two-temperature cell with homogeneous temperatures (Equation (6.11)). However, the internal state of the absorber is completely different and necessitates that the balance equations are expressed as integrals over the thickness of the absorber.

Chapter 7

From hot to cold: thermionic and extractive cooling

In this manuscript, we have extensively discussed the question of *hot* carrier characterization. However, all the Photoluminescence (PL) analysis tools introduced so far are also adapted to the study of *cold* carriers (*i.e.* colder than the lattice).

Such cold carriers arise when high-energy carriers are selectively removed through a high-energy contact, or above a high thermionic barrier. This interesting case is reminiscent of *evaporative cooling* in cold atoms physics [Ketterle and Druten 1996] and *thermionic cooling* in semiconductors physics [Mahan 1994]. The fact that carrier extraction by energy-selective contacts reduces the temperature in the absorber is a well-know detrimental effect for Hot-Carrier Solar Cells (HCSCs), as was shown in chapter 3, chapter 6. However, it offers a signature of hot-carrier selective extraction, as was proposed by [Suchet *et al.* 2017]. Note however that carriers are not expected to drop below lattice temperature in standard HCSC operation regimes.

To study the extreme case of cold carriers, our usual characterization techniques must be adapted, as shown in Figure 7.1. In the cold carrier configuration, light is no longer the primary excitation of the system. Instead, carriers are put out of equilibrium by forcing them to flow through the system, *i.e.* by electrical excitation. Light is only used as a perturbation allowing to probe carrier temperature, and therefore must be kept at a low power.

When carriers are cold, they drain heat from the lattice and hence the system works as a cooler. This idea was investigated in GELATO project (ANR-21-CE50-0017), which is a collaboration between LIMMS in Tokyo, LPENS in Paris, IPVF in Palaiseau and IM2NP in Marseille. GELATO aims at designing thermionic cooling nano-devices. It was shown, both theoretically [Bescond *et al.* 2018] and experimentally [Yangui *et al.* 2019], that the effect of thermionic extraction could result in a drop of carrier temperature of several tens of kelvins in the absorber. However, the change in lattice temperature had never been measured experimentally.

In this chapter, we first present one on the architectures that were investigated in the GELATO project, the so-called *asymmetric double barrier heterostructures* (section 7.2). We then make use of the experimental tools developed for *hot* carrier characterization to measure simultaneously the temperature of *cold* carriers and that of the the lattice (section 7.3). We prove that carriers are indeed cooled by thermionic cooling, while the lattice stays at ambient temperature. Finally, we show in section 7.4 that the system

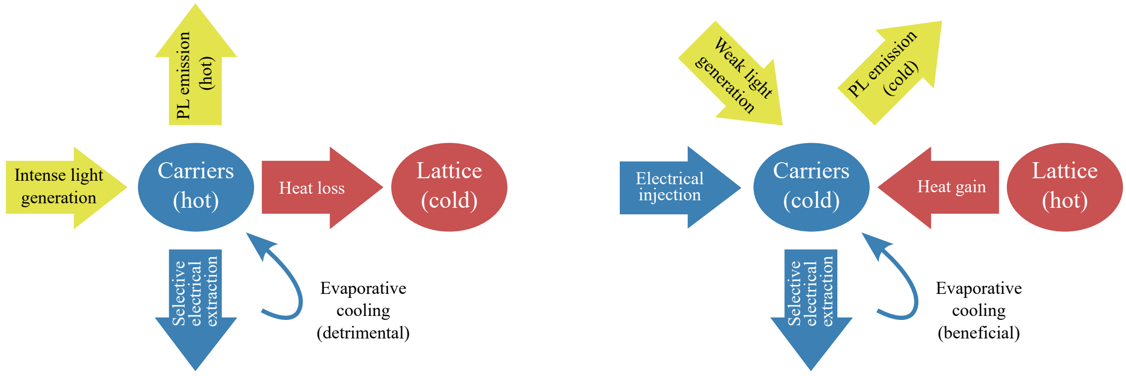

(a) (b)

Figure 7.1: *Comparison between the experimental PL configurations for the characterization of (a) hot and (b) cold carriers. Pear color indicates photons, blue indicates carriers and red indicates heat/phonons.*

under consideration is actually close to a HCSC. Therefore we test whether it supports hot-carrier effect, and show that it does not.

Table of contents

7.1 Highlights

Experimental Highlight 7.1. (Simultaneous determination of carrier and lattice temperature)
We show that lattice and carrier temperature can be measured simultaneously from PL measurements. In this example, carrier temperature is measured with Photoluminescence Ratio (PLR) method, while lattice temperature is assessed based on the PL peak shift.

Experimental Highlight 7.2. (Cooling efficiency of GELATO nanocoolers)
While carriers are cooled by several tens of kelvins, the lattice stays at ambient temperature. This comes from the weak carrier-phonon coupling and weak carrier density in the Quantum Well (QW), as well as from the high thermal conductivity of the thermionic barrier.

7.2 Asymmetric double barrier heterostructure

GELATO project studies structures called *asymmetric double barrier heterostructures*, which where historically proposed by [Chao *et al.* 2005]. In section 7.2.1, we present the design of these samples with GaAs/AlGaAs heterostructure. We then present an experiment designed to test whether this system can cool the lattice significantly in section 7.2.2.

7.2.1 Sample design

An asymmetric double barrier heterostructure is represented in Figure 7.2. It is composed of a GaAs QW in contact with an AlGaAs thermionic barrier. Doped GaAs layers serve as emitter and collector of electrons and ensure good electrical contact with gold contacts. Holes are not represented here but they have a similar band structure. These samples are grown (by molecular beam epitaxy) and processed in the team of Prof. Hirakawa, in Tokyo.

When a current flows through the device, carriers are first injected in the QW by resonant tunneling. This energy-selective injection is key to the operation of the device, as it allows to inject *low-energy* electrons in the QW [Zhu *et al.* 2021]. Carriers in the QW are then extracted by thermionic emission over the barrier. Only high-energy carriers of the QW can be extracted. Consequently, the average carrier energy in the QW, and hence its temperature is reduced. Cold carriers thus generated will drain heat from the lattice.

7.2.2 Description of the experiment

To assess whether cold carriers can significantly cool down the lattice, we perform a bias-dependent PL experiment.

Data reported below are collected from a cell of size 180×180 µm, with an opening of size 70×70 µm. We connect the cell to a Keithley Sourcemeter (model 2400) and impose an electrical bias from -2 V (reverse bias) to $+2$ V (forward bias). For each bias, we record the value of the current flowing through a device, as well as a PL spectrum.

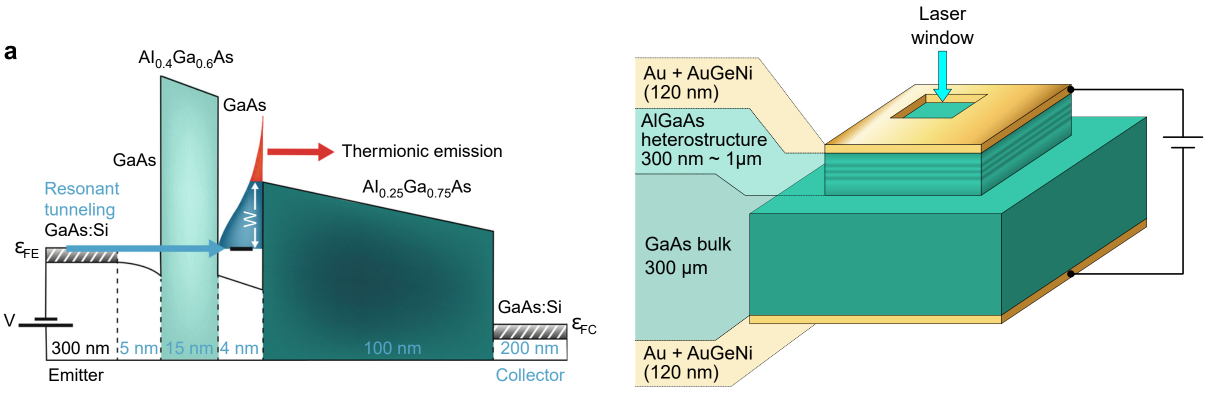

(a) (b)

Figure 7.2: *Schematic representation of the asymmetric double barrier heterostructure. (a) Band structure of the conduction band, reproduced from [Yangui et al. 2019]. (b) 3D vue of the sample with its contacts. A square window is left open on each top contact to allow characterization by PL. Courtesy of Hirakawa Lab.*

PL is obtained by exciting the system with a green laser 532 nm and collect the PL with an Acton SP-2760 spectrometer equipped with a Pixis100B CCD camera (both from Princeton Instruments). This spectrometer has a 2 nm spectral resolution. We use a laser intensity $I_{\text{exc}} \simeq 200$ W.cm^{-2}. This is 30 to 600 times less than the intensities used in chapter 4 and chapter 5 to generate hot carriers. In this setup, photogeneration is a "weak" perturbation of the system, and is only used as a probe. PL spectra are calibrated following the procedure explained in section 2.2.3. Note that, in this case, the calibration is only *relative* and therefore PL spectra are expressed in arbitrary units.

7.3 Simultaneous determination of carrier and lattice temperature

In this section, we analyse the influence of carrier extraction on both carrier and lattice temperatures. We first report the bias-dependent PL spectra, along with the methodology to extract carrier and lattice temperature in section 7.3.1. Then we discuss the performances of GELATO nanocoolers in section 7.3.2.

7.3.1 Bias-dependent photoluminescence spectra

Figure 7.3a presents a collection PL spectra acquired on the asymmetric double barrier heterostructure for various electrical biases. These PL spectra are composed of three peaks.

The main peak at 1.43 eV is attributed to the GaAs emitter. The second peak at 1.53 eV is attributed to the QW. Finally, a weak third peak is visible at 1.73 eV, and corresponds to the emission of the thermionic barrier.

The QW peak exhibits a strong bias-dependent behavior. At small positive biases, resonant tunneling between the emitter and the QW occurs and the carrier density in the

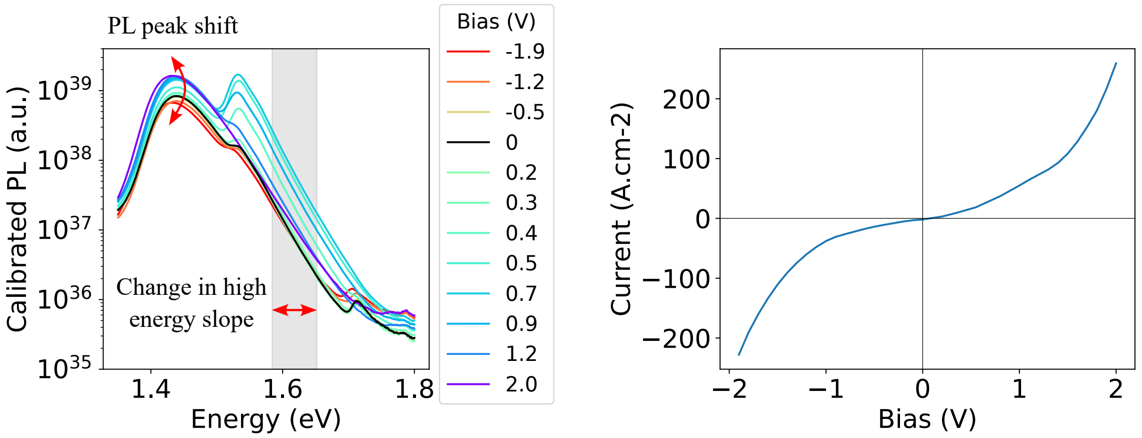

(a)

(b)

Figure 7.3: *Bias-dependent measurement of the asymmetric double barrier heterostructure at room temperature. (a) Selection of a few representative PL spectra. (b) JV characteristic.*

well increases. However, when the bias is too large ($V > 0.6$ V), then thermionic emission over the AlGaAs barrier takes over and the QW is depleted.

Carrier temperature is measured with Photoluminescence Ratio (PLR) method (see section 2.3.2). The reference spectrum is taken as the unbiased spectrum ($V = 0$ V, shown in black). Since PL excitation intensity is relatively weak, this spectrum is assumed to be representative of a carrier distribution at ambient temperature $T = T_L = 293$ K. The boundaries for the temperature determination are represented in pale grey color in Figure 7.3a. The uncertainty on carrier temperature is computed by repeating the fit several times with different energy boundaries. The lower and upper energy boundary are both allowed to vary in a range ±10 meV.

Lattice temperature is measured using the methodology presented in section 2.3.6, and relies on the determination of the PL peak shift. In this case, we measure the variation of the GaAs PL peak, which visibly depends on bias. Given the spectral resolution of our spectrometer, the uncertainty on lattice temperature determination is ±2 K.

7.3.2 Temperatures determination and discussion

Both carrier and lattice temperature variations with bias are represented in Figure 7.4.

A significant decrease in carrier temperature at small forward biases ($0.5 - 1$ V) is observed. This confirms that selective extraction changes the carrier temperature in the QW. The minimum temperature reached in the QW is about 30 K below ambient. The extent of carrier cooling is consistent with theoretical predictions as well as with previous measurements on similar sample [Bescond *et al.* 2018, Yangui *et al.* 2019].

However, the lattice temperature does not change significantly in this range of biases. This is to be expected, for several reasons. First, QWs exhibit weak carrier-phonon interaction [Ryan *et al.* 1984, Pelouch *et al.* 1992, Rosenwaks *et al.* 1993] such that carrier and lattice temperature can be effectively decoupled. Second, GaAs and AlGaAs have a high thermal conductivity ($\sim$ 46 W.m^{-1}.K^{-1}), which prevents large lattice temperature variations [Bescond *et al.* 2018]. Third, heat capacity of electrons in the QW is orders of

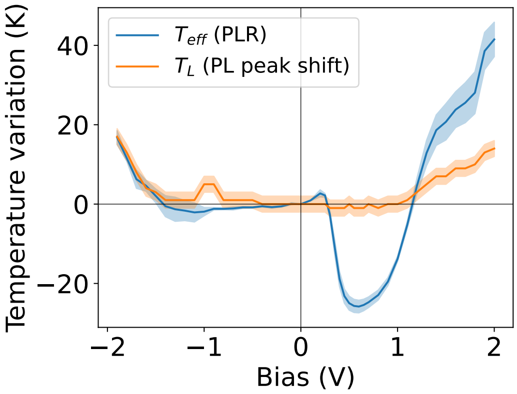

Figure 7.4: *Variation of carrier temperature* T_{eff} *and lattice temperature* T_L*, both measured from PL measurements, as a function of electrical bias. The unbiased spectrum (*$V = 0$ V*) serves as a reference.*

magnitude lower than that of the lattice, and therefore it is unlikely that electrons can induce a significant change of lattice temperature.

At large bias (both negative and positive), an increase of both carrier and lattice temperature is visible. This can be linked to Joule effect, as the lattice temperature increase is proportional to the electrical power provided to the system (see Figure 7.5).

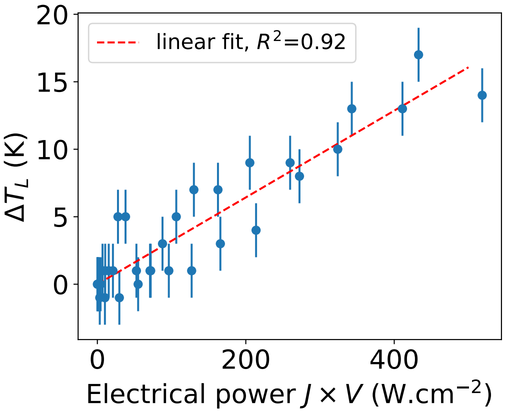

Figure 7.5: *Increase in lattice temperature as a function of the electrical power provided to the system. The red line indicates a linear fit compatible with Joule effect.*

At large negative biases, carrier and lattice temperatures are the same, which is expected as there should be no thermionic extraction in this case. However, at large positive bias, carrier temperature appears to increase faster than lattice temperature. This is due to the fact that Photoluminescence Ratio (PLR) method is no longer valid in this range. Indeed, the QW emission becomes negligible (see Figure 7.3a), and therefore the spectrum is representative of the emission from the GaAs emitter, which does not have the same absorptivity as the QW.

Result 7.1. (Thermionic vs lattice cooling)
The asymmetric double barrier heterostructure allows to cool carriers in the GaAs QW by up to 30 K. However, the lattice temperature variation is negligible (< 1 K). Therefore, this sample is not an efficient cooler for the lattice.

7.4 Hot-carrier characterization

The asymmetric double barrier heterostructure actually resembles a HCSC. Indeed, we have just seen that carrier-phonon interactions in the QW were weak enough to allow carriers to cool down below lattice temperature. In addition, the thermionic AlGaAs barrier is a semi-selective contact. Therefore we could potentially be able to generate hot carriers in this structure and study it as a HCSC.

To this extent, we conducted a power-dependent PL study, much like the one presented in chapter 5, but this time using the same green laser introduced before. The result can be found in Figure 7.6.

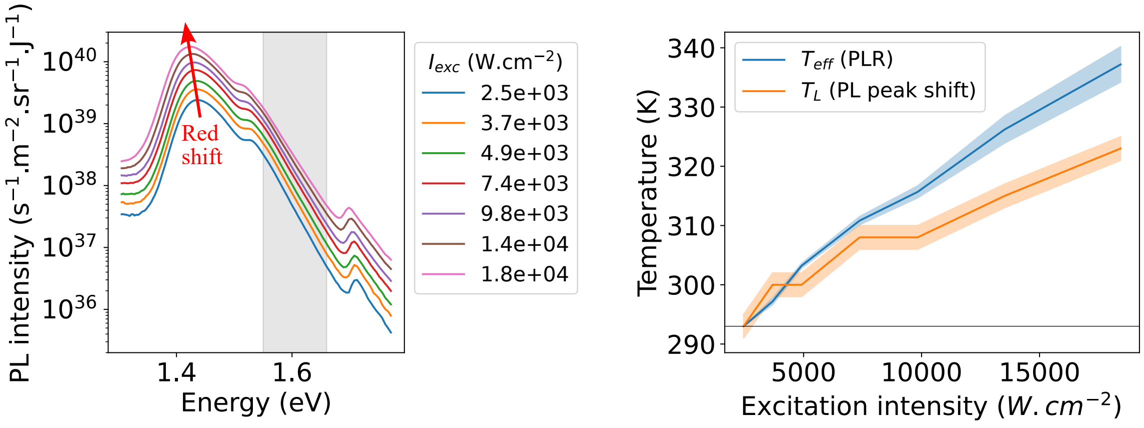

(a) (b)

Figure 7.6: *Characterization of the hot-carrier effect in the asymmetric double barrier heterostructure from continuous-wave PL measurements. (a) Power-dependent PL spectra. (b) Carrier and lattice temperature determined from the spectra. Errorbars are computed based on the same methodology as in section 7.3.2.*

Figure 7.6 shows the power-dependent PL spectra measured with an excitation intensity ranging from 2.5×10^3 to 1.8×10^4 W.cm^{-2}. The high-energy slope of the QW emission seems to depend on the excitation power, which could be attributed to hot carriers. However, a clear red shift can be seen. The latter is indicative of lattice heating, an effect that will also affect the high-energy slope of the spectrum.

Therefore we need to study precisely the magnitude of each effect to see whether some hot-carrier effect can be seen in addition of the lattice heating. As in section 7.3.1, we estimate carrier temperature with PLR method and lattice temperature with PL peak shift method. The reference spectrum in this case is the one with lowest intensity, which is assumed to be representative of PL emission at room temperature $T_{\text{eff}} = T_L = 293$ K. The result of this analysis is presented in Figure 7.6b.

As expected from the apparent red-shift of the PL spectra, the lattice temperature increases by almost 30 K at largest excitation intensity. As for carrier temperature, it first increases at the same rate than lattice temperature. Then, for $I_{\text{exc}} > 7.5 \times 10^3$ W.cm^{-2}, carrier temperature starts to increase faster than lattice temperature. However, the difference between carrier and lattice temperature at largest excitation intensity is at best $15 - 20$ K, which is not large enough to characterize a hot-carrier effect.

Result 7.2. (The asymmetric double barrier heterostructure is not a good HCSC)
The asymmetric double barrier heterostructure does not host hot carriers and therefore is not a good HCSC. This is probably due to the presence of a 300 nm GaAs emitter layer on top of the sample. This thick layer absorbs most of the incident laser power, as the 532 nm laser penetration depth in GaAs is around 50 nm. As it is a bulk layer, it has fast carrier thermalization rates and therefore it thermalizes most of the incident laser power. Consequently, lattice is heated rather than carriers.

7.5 Conclusion

In this chapter, we demonstrated that it was possible to measure simultaneously the temperature of the carriers and of the lattice.

We applied this technique to bias-dependent PL measurements of the asymmetric double barrier heterostructures investigated in GELATO project. We report a significant thermionic cooling of the carriers, which can become as cold as 30 K below ambient temperature. However, this does not translate in a visible cooling of the GaAs emitter, which stays at ambient temperature up to our experimental precision (~ 2 K). Therefore the coolers designed in this project are efficient at cooling the carriers but not the lattice.

We also applied this technique to the determination of hot-carrier effect in the same sample. This showed that the system was subject to lattice heating at elevated excitation intensities rather than a real hot-carrier effect. Therefore this sample is not a good HCSC candidate.

Perspectives:

1. It may be possible to study the variation of QW peak emission to obtain lattice temperature in the QW. Pby via a full fit of some sort. One of the difficulties here is that there are two excitonic peaks, which can be attributed to heavy and light hole bands.

2. For more efficient HCSC: remove the GaAs emitter so that photogeneration occurs directly in the QW.

Chapter 8

Conclusion and perspectives

8.1 Conclusion

This PhD manuscript focused on the advanced characterization and modeling of Hot-Carrier Solar Cells (HCSCs). So far HCSC realizations have underwhelming efficiencies. This motivates us to investigate how real life systems depart from ideal assumptions commonly used in HCSCs modelling. In particular, we explored the notion of *uneven temperatures*, examining systems where carrier temperature was inhomogeneous or differed between electrons and holes.

This work reports two major contributions. In the first one (chapter 4), we investigated the joined transport of heat and charges in the absorber. Doing so, we epitomize the connection between hot-carrier photovoltaics and thermoelectricity. We developed a new framework to describe this transport, which is particularly suitable for large photogenerated carrier densities. Indeed it is valid in the degenerate case and assumes ambipolar transport. We proposed hyperspectral Photoluminescence (PL) measurements using point illumination to test this model. This experiment demonstrated that it was possible to measure transport coefficients, and in particular the ambipolar Seebeck coefficient, from purely optical measurements. The measured values were shown to be consistent with Boltzmann transport equation in the relaxation time approximation.

In a second study (chapter 5), we devised a contactless, purely optical method, to determine electron and hole temperatures separately. This method relies on the precise measurement of the band filling contribution to continuous-wave PL spectra. It is therefore limited to regimes of large carrier density, where the Quasi-Fermi-Level Splitting (QFLS) is typically only a few k_BT below the bandgap. While this regime is restrictive for conventional devices, it corresponds to the expected operation range of HCSCs. Testing this method on an InGaAsP / InGaAsP quantum well with a large mass mismatch ($m_h \simeq 10\, m_e$), we reported hot electron temperatures up to 1000 K, while holes remained below 500 K. The small increase in hole temperature is too large to be explained purely by photon absorption, and is thought to be a signature of electron hole interactions.

Building on the ability to distinguish between electron and hole temperatures, we developed a model in chapter 6 to compute the efficiency of a HCSC with distinct electron and hole temperatures. In such a two-temperature system, the voltage depends on the individual positions of electron and hole extraction levels, not just on their difference. However, we found that HCSCs are resilient to two-temperature effects. Specifically, designing a suboptimal system based on erroneous measurement of electron and hole temperatures would result in an efficiency drop of only 2 percentage points at worse. In addition, we showed that two-temperature effects are actually beneficial for the operation of HCSCs, and could lead to an enhancement of the cell efficiency of about 2 percentage points.

Finally, in chapter 7, we demonstrated that hot-carrier spectroscopy tools could be used to study the influence of electrical extraction over a thermionic barrier. This method, although applied here to cold carriers in the context of thermionic cooling, can also be used to investigate the influence of hot-carrier extraction on the remaining carrier distributions in the absorber.

8.2 Further improvements

The results presented here have several limitations, and we suggest three potential improvements:

1. Throughout this manuscript, the analyses of PL spectra from sample 5006 assumed an idealized band structure with symmetrical energy bands for electrons and holes. Implementing a more realistic band structure with multiple bands for holes (heavy, light, split-off) and a single electron band could enhance the accuracy of the determination of carrier temperatures and chemical potentials.

2. The determination of Seebeck coefficient assumes constant electrical mobility, which is not accurate for degenerate systems. Accounting for mobility variations with temperature and QFLS could help reduce noise in the Seebeck coefficient measurements.

3. To investigate the potential efficiency of more realistic absorbers, the two-temperature cell model presented in chapter 6 needs to be refined. Incorporating factors such as non-ideal radiative efficiency and absorptivity could be achieved without additional computational cost. Additionally, a more accurate treatment of carrier distributions using Fermi-Dirac statistics could be beneficial. The computational burden of this approach could be significantly reduced by computing temperature and QFLS tables prior to running cell simulations.

In addition, it would be interesting to test the experimental methods proposed in chapter 4 and chapter 5 on additional samples. However, both methods require to generate a temperature increase of at least several hundred kelvins, which is not that common even in III-V quantum wells. Therefore finding other suitable candidate materials is a challenge in itself.

8.3 Perspectives

In this manuscript, we exposed several effects that could be included in HCSC modeling to understand their non ideal behavior. This research has also led to the formulation of new questions that we believe are worthy of future investigation.

1. **Simulation of HCSCs with temperature gradients.** Because of internal reflections and interferences, we expect that many nanostructured hot-carrier absorber

may host temperature gradients [Limpert *et al.* 2017]. In such systems, carrier transport will be affected by the presence of temperature gradients, as described in chapter 4. We would like to examine the influence of Seebeck coefficient on the performances of such a device: does thermoelectric transport increase or reduce the energy-conversion efficiency of inhomogeneous devices? To address this question, significant changes of the HCSC model presented in chapter 6 are necessary (see section 6.5).

2. **Impact of hot-carrier transport on thermalization coefficients.** When the laser excitation profile is smaller than the diffusion length of hot carriers, some power is carried away from the generation region. This could lead to an overestimation of thermalization coefficients in point illumination. Note that a similar effect has been investigated in the context of carrier lifetime measurement. When the laser spot size is smaller than carrier diffusion length, diffusion lowers the steady-state carrier density at the laser spot, leading to an underestimation of the carrier lifetime [Vidon 2022, Chapter 3].

3. **Thermalization properties of two-temperature distributions.** Although two-temperature effects are not critical to HCSC performances, understanding the mechanisms of two-temperature thermalization could offer fundamental insights into carrier relaxation processes. As predicted in chapter 5, it would be interesting to experimentally demonstrate and characterize the electron-hole interaction mediated by LO phonons.

Appendix A

Publications, conferences and valorization

A.1 Scientific publications

1	T. Vezin, M. Amara, D. Suchet, “Concepts avancées pour une conversion photovoltaïque à très haut rendement”, in *L'énergie solaire photovoltaique*, ISTE Science, (submitted, 2023).
2	T. Vezin, H. Esmaielpour, L. Lombez, JF Guillemoles, D. Suchet, ”Optical determination of thermoelectric transport coefficients in an InGaAsP quantum well hot carrier absorber”, *Physical Review Applied*, Sept. 2024.
3	T. Vezin, N. Roubinowitz, L. Lombez, JF Guillemoles, D. Suchet, ”Simultaneous determination of electron and hole distributions from continuous-wave photoluminescence measurement”, *Physical Review B*, Sept. 2024.
4	T. Vezin, D. Suchet, ”Hot electrons and cold holes: operation, efficiency and design of a two-temperature hot-carrier solar cell model”, *European Physical Journal Photovoltaics* (submitted Sept. 2024).

Table A.1: *Publications in scientific journals.*

A.2 Participation to conferences

1 T. Vezin, H. Esmaielpour, M. Legrand, D. Suchet, JF. Guillemoles, “Advanced characterization of hot carrier properties of InGaAs multi-quantum well structure using hyperspectral and time-resolved luminescence spectroscopy”, *JNPV* in Dourdan, Dec. 2021 **(oral)**.

2 T. Vezin, H. Esmaielpour, L. Lombez, D. Suchet, JF. Guillemoles, “Advanced characterization of hot carrier solar cells using hyperspectral photoluminescence imager: a roadmap towards Seebeck coefficient”, *Les Houches PVSchool* in Les Houches, Apr. 2022, **(poster)**.

3 T. Vezin, H. Esmaielpour, L. Lombez, D. Suchet, JF. Guillemoles, “Measurement of photo-induced Seebeck effect from photoluminescence of hot carrier solar cells”, *WCPEC-8* in Milan, Oct. 2022 **(poster)**.

4 T. Vezin, H. Esmaielpour, L. Lombez, D. Suchet, JF. Guillemoles, “Measurement of photo-induced Seebeck effect from photoluminescence of hot carrier solar cells”, *JNPV* in Dourdan, Dec. 2022 **(poster)**.

5 T. Vezin, S. Rani, H. Esmaielpour, L. Lombez, D. Suchet, JF. Guillemoles, “Optical determination of photo-induced Seebeck coefficient in InGaAsP quantum well”, *E-MRS* in Strasbourg, May 2023 **(oral)**.

6 T. Vezin, H. Esmaielpour, S. Rani, L. Lombez, D. Suchet, JF. Guillemoles, ”Optical determination of photo-induced Seebeck coefficient in InGaAsP hot carrier solar cell”, *EDISON 22* in Münster, Aug. 2023 **(oral)**.

7 T. Vezin, H. Esmaielpour, S. Rani, L. Lombez, D. Suchet, JF. Guillemoles, ”Optical Determination of Thermoelectric Properties of a Hot Carrier Absorber”, *NEXTPV Workshop 2023* in Tokyo, Nov. 2023 **(oral)**

8 T. Vezin, H. Esmaielpour, S. Rani, L. Lombez, D. Suchet, JF. Guillemoles, ”Optical Determination of Thermoelectric Properties of a Hot Carrier Absorber”, *JNPV* in Dourdan, Dec. 2023 **(oral)**.

Table A.2: *Participation to conferences, workshops and summer schools.*

A.3 Auto-publication and internal reports

1	S. Collin *et al.*, “Solar photovoltaic in France: reality, potential and challenges. Some questions and some answers.”, Mar. 2022, **(Public report)**
2	T. Vezin, ”Hyperspectral User Guide”, V1.0, Sept. 2023, **(internal report)**
3	T. Vezin, ”Hyperspectral calibration code”, V1.3.1, , *hosted on IPVF Github*, Oct. 2023, **(for internal use)**

Table A.3: *Auto-publications and productions for internal use.*

A.4 Teaching and scientific outreach

1	Optics labs for Ecole polytechnique Bachelor (Bachelor 2), 64h/year for 3 years, under the supervision of Y. Laplace.
2	Tutoring for Ecole polytechnique students in ”Energy and Environment” (Masters 2), 10h in 2021, under the supervision of D. Suchet.
3	Participation to IPVF stand at ”Fete de la Science” in Ecole polytechnique, in 2021, 2022 and 2023.

Table A.4: *Teaching and scientific outreach.*

Appendix B

Details on electroneutrality

In this manuscript, we often use electroneutrality as an additional constraint on the carrier distributions, to reduce the number of variables required to describe carrier distributions. In this appendix, we derive electroneutrality relations used in this manuscript, and discuss why electroneutrality holds in sample 5006.

B.1 Electroneutrality relations

B.1.1 Single layers

By definition, electroneutrality states that there are as many electrons as there are holes in the system. If electrons and holes follow thermal distributions, this writes

$$n_e(T_e, \mu_e) = \int_0^\infty d\epsilon D_e(\epsilon) f(\epsilon, T_e, \mu_e) = \int_0^\infty d\epsilon D_h(\epsilon) = n_h(T_h, \mu_h) \tag{B.1}$$

where

D_i = The density of states of carrier i. In the parabolic band approximation, $D_{i,2D}(\epsilon) = m_i/(2\pi\hbar^2)$ (in the QW) and $D_{i,3D}(\epsilon) = \sqrt{2\epsilon(m/\hbar^2))^3}/(2\pi^2)$ (in the barrier).

T_i = The temperature of carrier i.

μ_i = The chemical potential of carrier i, which is equal to the electrochemical potential as there is no electrical potential in the case considered here.

f = $\left[\exp\left(\frac{\epsilon - \mu}{k_B T}\right) - 1\right]^{-1}$ is the Fermi-Dirac distribution.

In the most general case, this electroneutrality relation cannot be solved explicitly, but it can be put in the following dimensionless form:

$$(m_e T_e)^{D/2} \int_0^\infty \frac{x^{D/2-1} dx}{1 + \exp\left(x + \frac{E_g/2 - \mu_e}{k_B T_e}\right)} = (m_h T_h)^{D/2} \int_0^\infty \frac{x^{D/2-1} dx}{1 + \exp\left(x + \frac{E_g/2 - \mu_h}{k_B T_h}\right)} \tag{B.2}$$

where D is the dimension of the system, and we used the fact that $D_i(\epsilon) \propto m^{D/2} \epsilon^{D/2-1}$.

This integral can be further simplified in two cases.

1. **Boltzmann approximation.** When the system is not degenerate and $\mu_i \ll E_g/2$, we can neglect the "+1" in the denominator and perform the integration explicitly. We obtain

$$(m_e T_e)^{D/2} \exp\left(\frac{\mu_e - E_g/2}{k_B T}\right) = (m_h T_h)^{D/2} \exp\left(\frac{\mu_h - E_g/2}{k_B T}\right) \tag{B.3}$$

$$\text{i.e.} \quad \frac{\mu_e}{T_e} = \frac{\mu_h}{T_h} + \frac{D}{2} k_B \ln\left(\frac{m_h T_h}{m_e T_e}\right) + \frac{E_g}{2}\left(\frac{1}{T_e} - \frac{1}{T_h}\right) \tag{B.4}$$

2. **For a two-dimensional system.** In this case, even if Boltzmann approximation is not valid, we can integrate explicitly the electroneutrality relation. We obtain

$$m_e T_e \ln\left[1 + \exp\left(-\frac{E_g/2 - \mu_e}{k_B T}\right)\right] = m_h T_h \ln\left[1 + \exp\left(-\frac{E_g/2 - \mu_h}{k_B T}\right)\right] \tag{B.5}$$

   Note that in QWs, it is usual to have several conduction and/or valence bands corresponding to successive bound states of the QW. If we denote by $\{E_i\}_{i=1,\dots,n}$ the energies of the conduction bands and by $\{E_j\}_{j=1,\dots,m}$ the energies of the valence bands, the previous formula can be generalized

$$m_e T_e \sum_{i=1}^{n} \ln\left[1 + \exp\left(-\frac{E_i - \mu_e}{k_B T_e}\right)\right] = m_h T_h \sum_{j=1}^{m} \ln\left[1 + \exp\left(-\frac{E_j - \mu_h}{k_B T_h}\right)\right] \tag{B.6}$$

B.1.2 Multilayers

If there are several layers, and if those layers can exchange carriers, then electroneutrality cannot be written over a single layer anymore, and must be replaced by a balance across all layers:

$$\sum_j n_{e,j}(T_{e,j}, \mu_{e,j}) = \sum_j n_{h,j}(T_{h,j}, \mu_{h,j}) \tag{B.7}$$

where j indexes layers.

B.2 Electroneutrality in sample 5006

Sample 5006 is an intrinsic III-V heterostructure (see section 2.4). Therefore, it must have as many electrons as holes in order to be electrically neutral. In addition, we characterize it with PL in strong excitation regime. Therefore, even if there was some unintentional doping, the impurity concentration would be negligible as compared with photogenerated populations ($n \gtrsim 10^{17}$ cm^{-3}, see section 4.3.2).

Sample 5006 is not a single layer, as it is composed of a QW and two barriers. However, the band-edge mismatch between the QW and the barrier is approximately the same for electrons and holes (see Figure 2.11). Therefore, carriers exchange between the QW and the barrier should be symmetrical for electrons and holes. We thus expect that *electroneutrality holds in the QW and in the barrier individually.*

Finally, even when we investigate the properties of this sample with strongly inhomogeneous illumination (in chapter 4), carrier densities are sufficiently high so that carrier diffusion is ambipolar, and hence electroneutrality holds *locally.*

As seen from its PL spectra, sample 5006 is a QW with two optical transitions $E_1 \simeq 0.82$ eV and $E_2 \simeq 0.89$ eV. Therefore, we assume that there are two bands for electrons and two bands for holes, placed symmetrically with band-edges $E_1/2$ and $E_2/2$ each. It is likely that this assumption is too simplistic, and that electrons actually have only one confined state while holes have several (at least 3: light, heavy and split-off band). It would be interesting to see if the proper inclusion of this QW band structure would change our conclusions regarding the analysis of PL spectra.

Appendix C

Effects limiting the accuracy of hyperspectral acquisitions

In this appendix, we describe briefly two effects that limit the accuracy of Hyperspectral Imager (HI) acquisitions: chromatic aberrations (Appendix C.1) and the so-called PL glow effect (Appendix C.2). For each effect, we describe solutions that were implemented during this PhD.

C.1 Chromatic aberration

Chromatic aberration is the fact the focal plane of an optical system depends on the wavelength. When collimated laser beams of different wavelengths go through a *chromatic* objective lens, they are focused in two different planes, as illustrated in Figure C.1 (panel (a)). On the contrary, if the system is *achromatic*, the two laser beams will be focused in the same focal plane, as can be seen in panel (b).

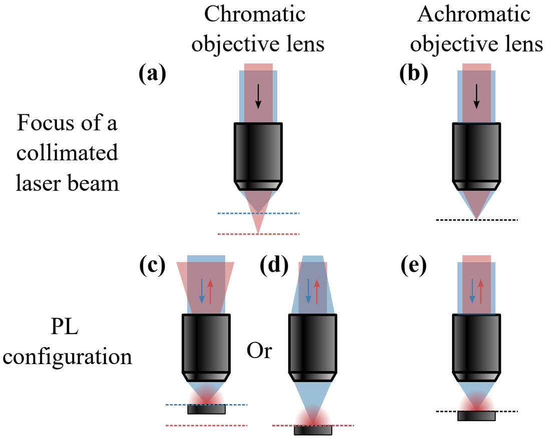

Figure C.1: *Chromatic aberration and ways to mitigate it.*

Chromatic aberration is an issue for PL experiments because, in general, the excitation light has a much shorter wavelength than the emitted PL. Therefore, with a chromatic objective lens, it is not possible to focus properly the laser and the PL signal simultaneously, as shown in panel (c). This is particularly problematic for HIs when high spatial resolution is required. In configuration (c), PL is out of focus and appears blurry, because the light collected by the objective lens is not properly collimated. This blur can be mistaken for a diffusion effect, and therefore is detrimental for optical measurements of carrier transport, as was proposed in chapter 4 for instance.

There exists two solutions to this problem.

1. Control the laser beam divergence at the entrance of the objective to displace the point of convergence of the laser excitation in the focal plane of the PL signal. This is represented in panel (d).
2. Use an achromatic objective lens, as represented in panel (e). This solution is much easier than the first one, but achromatic objective lenses are expensive.

In our study of hot-carrier transport in chapter 4, we used both techniques to ensure that laser spot and PL where simultaneously at focus: the divergence of the laser beam was controlled via a beam expander, while the objective used was apochromatic over the range $400 - 1800$ nm.

C.2 Photoluminescence glow

C.2.1 Characterization

PL glow effect was observed when measuring PL signal close to the edge of a GaAs sample. We noticed that our HI would measure a sizeable PL signal from spatial regions where there was no sample. This is illustrated in Figure C.2.

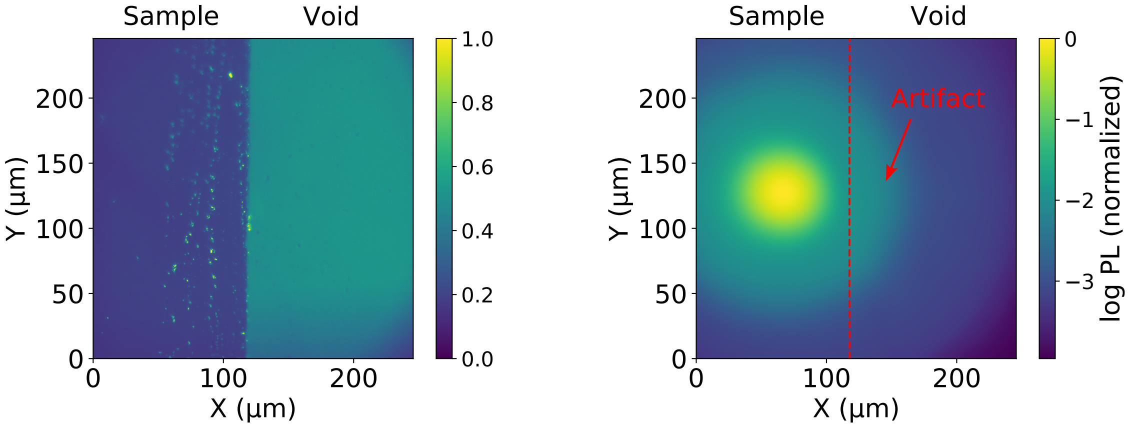

(a)

(b)

Figure C.2: *PL glow observed on HIs. (a) Reflection map of the edge of a GaAs sample. (b) Normalized PL signal observed at the edge of the sample. Note how this signal extends in the region with no sample.*

This glow signal can be as large as 1 % of the signal at the center of the laser spot, and decays slowly (typically one order of magnitude over ~ 70 µm). As there are no charge carriers in the region $x > 110$ µm, this PL signal coming from the void is necessarily an artifact. In fact, it is as if the PL signal measured at a certain position (x_0, y_0),

$I_{\mathrm{PL}}^{\mathrm{meas}}(x_0, y_0)$, depends on the "real" signal $I_{\mathrm{PL}}^{\mathrm{true}}(x_0, y_0)$ plus a "leaking" term that depends on the signal at every other position.

$$I_{\mathrm{PL}}^{\mathrm{meas}}(x_0, y_0) = I_{\mathrm{PL}}^{\mathrm{true}}(x_0, y_0) + \int_{x,y} I_{\mathrm{PL}}^{\mathrm{true}}(x, y) \times g(x - x_0, y - y_0)\, dx\, dy \qquad \text{(C.1)}$$

where g is a convolution function to be characterized.

This artifact (magnitude, scaling with distance) was not characterized precisely, but a similar effect was identified with four different objective lenses and two different samples. Hence we think that it comes from the HI itself, and not from the rest of the setup. Possible causes are (i) chromaticity of HI collection path, which is composed of several lenses and mirrors, (ii) internal reflections in the collection path, (iii) systematic issues in focusing the PL (unlikely).

C.2.2 Possible correction

PL glow can be mistaken for a PL signal coming from carriers that have travelled far from the center. Therefore, it is an issue when measuring carrier diffusion in punctual illumination configuration, as was done in chapter 4. In this section, we will present the manifestation of the PL glow effect in our data, and propose a solution to remove it.

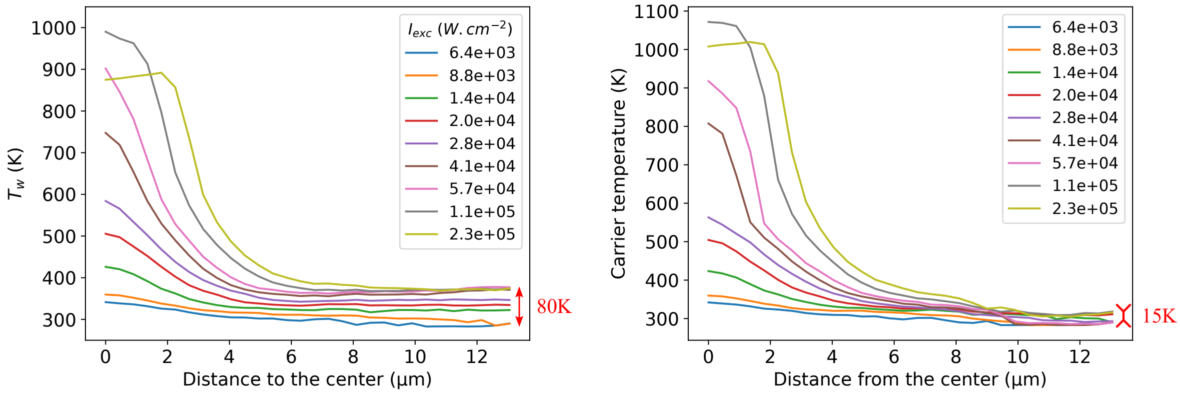

(a) (b)

Figure C.3: *PL glow correction used in chapter 4. (a) Temperature profiles obtained before the correction. (b) Temperature profiles obtained after the correction.*

Manifestation of the PL glow When we fitted PL spectra at increasing distance to the center, we noticed that the temperature at large distance did not go back to lattice temperature, in particular for high intensity acquisitions. Such uncorrected temperature profiles are presented in Figure C.3a.

This effect is consistent with PL glow. Indeed, if the signal from the center leaks to regions far from the center, temperatures measured far from the center will be artificially high. In addition, PL glow effect depends on the intensity of the spectrum at the center, and on its shape – hence its temperature. Therefore, we expect that the artificial increase in temperature far from the center should be larger for acquisitions at higher excitation intensity I_{exc} and/or higher temperatures at the center.

Temporary solution As stated above, we do not have a precise characterization of the PL glow yet. Therefore, we tried to correct this parasitic signal with a simplistic approach. We first defined a spectrum representative of the acquisition as $I_{\text{ref}} = \int_r I_{\text{PL}}(r)\, 2\pi r dr$. Then, we subtracted a fraction of this representative spectrum from each spectrum measured at radius r, with the correction strength varying linearly with the radius.

$$I_{\text{PL}}^{\text{corr}}(r) = I_{\text{PL}}^{\text{meas}}(r) - (\alpha r + \beta) I_{\text{ref}} \tag{C.2}$$

The parameters α and β were set by hand, and we found $\alpha \simeq -7 \times 10^{-3}$ µm^{-1} and $\beta \simeq 0.12$.

The result of this correction can be seen on Figure C.3b. It allowed to greatly reduce the difference in temperature far from the center. Note that we carefully assessed the sensitivity of the determination of transport parameters to this correction, and found that it was negligible as compared with other error sources.

Appendix D

Absolute calibration of hyperspectral imagers

In chapter 2, we emphasized on how important it was to calibrate properly PL spectra. In this annex, we provide methodological details on the absolute calibration (in Appendix D.1). We also describe the implementation implementation in Python that I wrote during my PhD (in Appendix D.2).

D.1 Absolute calibration of an hyperspectral imager

D.1.1 Wavelength calibration of the spectrometer

The first step to perform when calibrating any spectrometer is to check that the software attributes the correct wavelength for any given angle of the diffraction grating. This step is called *wavelength calibration*. Typically, it requires to measure two or more known wavelengths and make sure that they appear where they should on the wavelength axis. This can be done for instance with a spectral lamp of known spectrum. For the NIR HI used in this manuscript, we use a Xe lamp with distinctive emission rays at $\lambda = 980$ nm and $\lambda = 1263$ nm.

D.1.2 Old absolute calibration procedure

The purpose of absolute calibration is to recover the absolute *PL* intensity, in SI unit, from a measurement on the camera expressed in counts. In most general case, the signal measured by a camera collecting PL during an exposure time t_{exp}, collecting light over a surface S and a solid angle Ω and in an energy window $[E_0 - \delta E/2, E_0 + \delta E/2]$ is

$$\underbrace{N(E_0)}_{\text{counts}} = \int_{t=0}^{t_{\text{exp}}} \int_{x,y\in S} \int_{\Omega} \int_{E_0-\delta E/2}^{E_0+\delta E/2} \underbrace{I_{\text{PL}}(t,x,y,\Omega,E)}_{\text{s}^{-1}.\text{m}^{-2}.\text{sr}^{-1}.\text{J}^{-1}} \underbrace{r(x,y,\Omega,E)}_{\text{counts.ph}^{-1}} \, dt \, dx \, dy \, d\Omega \, dE \tag{D.1}$$

where r is the *response function* of the spectrometer, *i.e.* the number of counts per emitted photon.

Dark substraction First, let us note that N is not directly given by measuring counts on the camera. Indeed, all cameras are subject to *dark noise*, such that $N = N_{\text{acq}} - N_{\text{dark}}$.

Generally, dark noise is composed of an offset and of random fluctuations around this offset (see Figure 2.6). Both depend on the camera setup (exposure time, readout speed, gain mode, etc). Dark substraction corrects the offset but not the random fluctuations. Therefore, the Signal to Noise Ratio (SNR) is controlled by random fluctuations.

Normalization with exposure time In continuous-wave PL, the signal does not depend on time. Therefore the integral with respect to time simply yields a factor t_{exp}. In a regime where the camera signal is linear in the exposure time, $(N_{\mathrm{acq}} - N_{\mathrm{dark}})/t_{\mathrm{exp}}$, expressed in counts.s^{-1} does not depend on the specific value of t_{exp} used.

Normalization with pixel size (spatial calibration) HIs collect PL signal with a spatial resolution of typically few hundred nanometers. Over such a short distance, the PL can be considered constant. Therefore, the integral over the surface simply yields a factor S_{pix}, surface of each pixel. By measuring the length in pixel of an object of known size, for instance a USAF target, we measure the pixel size and hence S_{pix}. This step is called *spatial calibration*.

Normalization with collection angle We have seen in section 2.1 that PL emission is *lambertian*. Therefore, $I_{\mathrm{PL}}(\Omega)\, d\Omega = I_{\mathrm{PL},0} \cos\theta \, d\Omega = I_{\mathrm{PL},0} \cos\theta \sin\theta \, d\theta \, d\phi$. Assuming that the response function r does not depend on photons direction Ω, the integral over $d\Omega$ yields a factor $\pi \sin^2 \theta_{\mathrm{obj}}$, where $0 \leq \theta_{\mathrm{obj}} \leq \pi/2$ is the objective collection half-angle. This can be more conveniently rephrased in terms of objective numerical aperture $\mathrm{NA} = \sin\theta_{\mathrm{obj}}$. Therefore, the integral over $d\Omega$ yields a factor $\pi \mathrm{NA}^2$.

Normalization with energy resolution Assuming that PL intensity is constant over the spectral window, the integral over the energy simply yields a factor δE. This energy resolution is imposed by the grating used. Grating resolutions are more often described in terms of wavelength $\delta\lambda = \lambda^2 \, \delta E/(hc)$. Our HIs have a spectral resolution of $\delta\lambda = 1$ nm.

At this stage, we have shown that, under a few assumptions,

$$\frac{N(x,y,E)}{t_{\mathrm{exp}} \cdot S_{\mathrm{pix}} \cdot \pi \mathrm{NA}^2 \cdot \delta E} = I_{\mathrm{PL}}(x,y,E) r(x,y,E) \tag{D.2}$$

where the right hand side of the equation does not depend on the choice of exposure time, pixel size, collection angle and energy resolution of the spectrometer. The last step is to measure the response function r of the spectrometer.

Transmission calibration Correcting for the spectral response of the setup is particularly important for hot-carrier characterization, which requires to know the *shape* of the spectrum with good accuracy (see section 2.3). The response of the spectrometer depends strongly on the quantum efficiency of the detector used, but also on its configuration in terms of filters, lenses, mirrors, etc. Therefore, it must be measured at every change of configuration.

Practically, we estimate the response of the system by measuring a reference known spectrum I_{ref}. This spectrum can be provided by electroluminescence of a reference cell, or by any lamp with known spectrum. The acquisition of the reference spectrum is called *transmission acquisition*. It allows to estimate the relative response function, r, as

$$r(x, y, E) \propto \frac{N_{\text{ref}}(x, y, E)}{I_{\text{ref}}(x, y, E)} \tag{D.3}$$

With this relative response function, we obtain a *relative calibration*. For the absolute calibration, a final step of *power calibration* is necessary.

Power calibration When the calibration is relative, we know the *shape* of the PL spectrum but not its absolute intensity. To obtain the absolute intensity of the whole spectrum, it is sufficient to determine it *at a given energy*. This can be done by measuring the number of counts obtained with a laser emission of known power P_{las} and energy E_{las} within the spectral range of the reference spectrum. This laser corresponds to an input photon flux $n_{\text{las}} = P_{\text{las}}/E_{\text{las}}$ in s^{-1}. It produces an integrated number of counts $\int_{x,y}\int_E N_{\text{las}}(x, y, E)\, dx\, dy\, dE = t_{\text{exp,las}}\, n_{\text{las}}\, r(E_{\text{las}})$. This gives us the absolute response function at the laser energy and hence over the whole spectral range of interest.

D.1.3 New absolute calibration procedure

As shown in the previous section, absolute calibration requires many steps, and relies on several independent measurements (dark substraction, normalization with pixel size, collection angle and energy resolution, transmission calibration). At every step, the user may make a mistake. This is why a simpler calibration procedure was proposed by Baptiste Bérenguier, our research engineer. I helped him develop this new calibration procedure, in particular by developing a code presented in the next section. Unfortunately, I cannot describe the new calibration procedure in this manuscript, as we just deposited a *Déclaration d'Invention* which has not been validated yet.

D.2 Implementation in Python

At the beginning of my PhD, there was many versions of the calibration code available. Indeed, almost every user developed its own version depending on his/her specific need. Absolute calibration is a crucial step of our research, so we proposed a way to unify all previous codes in a single standard version. This unified calibration code relies on the calibration procedure described in Appendix D.1.3 We put an emphasis on developing a code that would prevent user mistakes and that would not require any prior knowledge on calibration. In this section, we provide details on the implementation of this calibration code, which was done in Python. It is illustrated in Figure D.1.

Class Data The first step was to build an object that would be able to represent all possible PL data types. Four such types exist: cubes (2 spatial dimensions, 1 spectral dimension), images (2 spatial dimensions, no spectral dimension), spectra (1 spectral dimension, no spatial dimension), number (no spatial nor spectral dimensions). This class is called `Data`. We interfaced it with both output formats of our HIs (`.h5` and `.fits`).

Compatibility between acquisitions Calibration depends on many parameters of the HI setup such as the gain mode or the readout speed of the camera. For a proper calibration, these parameters must be the same for all acquisitions (the cube to calibrate, its dark cube, the transmission cube and the transmission dark cube). Therefore, all parameters relevant for calibration are loaded in `Data` class and the compatibility between all `Data` used in the calibration is carefully ensured by a set of methods called `isCompatibleXXX` where `XXX` are keywords to specify different compatibility types. This allows to prevent improper calibrations coming from comparison of HI acquisitions that should not be compared together.

Automatic file assignment For users who may want to calibrate a large number of acquisitions, I implemented an automatic file assignment procedure in the function `assignData`. This function can be used in two distinct cases : (i) to find which dark acquisition is *compatible* with a given acquisition (see `assignDark`) and (ii) to find which transmission acquisition is *compatible* with this acquisition (see `assignTrans`). The proper definition of the term “compatible” is quite complex and is contained in `isCompatibleXXX`.

Interpolation Another very useful feature of this code is that it automatically performs cumbersome interpolation steps. Say that we want to calibrate a HI *cube*, with two spatial dimensions and one spectral dimensions. However, because dark was assumed to be invariant with spectral dimension, we only acquired a dark *image*, with two spatial dimensions and no spectral dimension. In this configuration, we would like to substract the dark image to every image forming the acquired cube. Similarly, we may want to calibrate several cubes acquired with different regions of interest (*i.e.* restricted spatial dimensions). In this case, it may be useful to acquire a single transmission cube on the full sensor, and use this single acquisition to calibrate all acquisition in a row. This requires to extract the relevant regions of interest from the transmission cube. Both situations can be conveniently handled via the method `interpolate`, which is reproduced below.

```python
def interpolate(self,otherData):
    """
    Interpolates the data contained in self such that they match the
    cube otherData [i.e. same ROI, same binning and same wavelengths].

    Note that if self misses some dimensions of otherData, those are
    EXTRApolated and not INTERpolated.

    Parameters
    ----------
    otherData : instance of Data class
        Has to be a cube.
        Represents the dataset that we want to match in terms of
        wavelength, ROI and binning.

    Returns
    -------
    dataOut : instance of Data class
        Is a cube.
        New dataset that is an interpolation of self to match otherData
    """
```

```
    if not self.isConsistent():
        raise TypeError("'self' is not consistent.")
    if not otherData.isConsistent():
        raise TypeError("'otherData' is not consistent.")
    if not self.isCompatibleXYZ(otherData):
        raise TypeError("You are trying to interpolate data that are not
                                                    compatible.")

    dataOut = self.copy()

    if self.dtype == 'constant':
        # first construct the wavelengths
        dataOut = dataOut._extrapolateWvl(otherData)
        # then construct the spatial dimensions
        dataOut = dataOut._extrapolateSpatialDim(otherData)
    if self.dtype == 'spectrum':
        # first match the wavelengths
        dataOut = dataOut._interpolateWvl(otherData)
        # then construct the spatial dimensions
        dataOut = dataOut._extrapolateSpatialDim(otherData)
    elif self.dtype == 'image':
        # first match the pixels
        dataOut = dataOut._interpolateROI(otherData)
        dataOut = dataOut._interpolateBin(otherData)
        # then construct the wavelength dimension
        dataOut = dataOut._extrapolateWvl(otherData)
    elif self.dtype == 'cube':
        dataOut = dataOut._interpolateROI(otherData)
        dataOut = dataOut._interpolateBin(otherData)
        dataOut = dataOut._interpolateWvl(otherData)
    # NB: be careful with the order of the interpolation steps, as they
    #   do not commute (especially _Bin needs to be performed after
    #   _ROI)
    return dataOut
```

We do not report here the technical details of the implementation of `_interpolateXXX` and `_extrapolateYYY` methods. Simply note that `ROI` stands for “Region Of Interest” and `Bin` stands for “Binning”.

Calibration Thanks to the auxiliary functions described above, the calibration function (called `calibrate` in the code) writes very simply.

```
def calibrate(dataRaw,dataTrans,dataRef):
    """
    Calibrates the raw data obtained from an hyperspectral measurements.

    /!\\ dataRaw and dataTrans must be dark-corrected before this
    function.

    Parameters
    ----------
    dataRaw : instance of Data class
        Raw data (dark-substracted, in count.s-1).
    dataTrans : instance of Data class
```

```
        Transmission data, i.e. measurement of the calibration lamp in a
        specific configuration of the setup (dark-substracted, in
        count.s-1).
    dataRef : instance of Data class
        Spectrum of the calibration lamp (output of
        readFunctions.readRefSp).

    Returns
    -------
    dataCalib : instance of Data class
        calibrated cube corresponding to the input raw data.
    """

    # Check that both cubes are consistent
    if (not dataRaw.isConsistent()) or (not dataTrans.isConsistent()):
        raise ValueError("Data or trans is not consistent. Calibration
                                    cannot be performed.")

    # Check that both cubes are rectified
    if dataRaw.rectify and dataTrans.rectify:
        # compute the response cube
        dataResp = getResponseData(dataRaw,dataTrans,dataRef) # in ph.m-
                                    2.sr-1.count-1
        # compute the calibrated cube
        dataCalib = correctResponse(dataRaw,dataResp)
    else:
        raise ValueError("Data file or trans file are not rectified.
                                    Please perform"+\
                         " rectification prior to calibration.")

    return dataCalib
```

where `getResponseData` performs the computation of $r(x,y,E) = t_{\text{exp,ref}}\, I_{\text{ref}}(E)/N_{\text{ref}}(x,y,E)$ (and the necessary interpolations) and `correctResponse` simply multiplies the result by $N_{\text{acq}}(x,y,E)/t_{\text{exp,acq}}$.

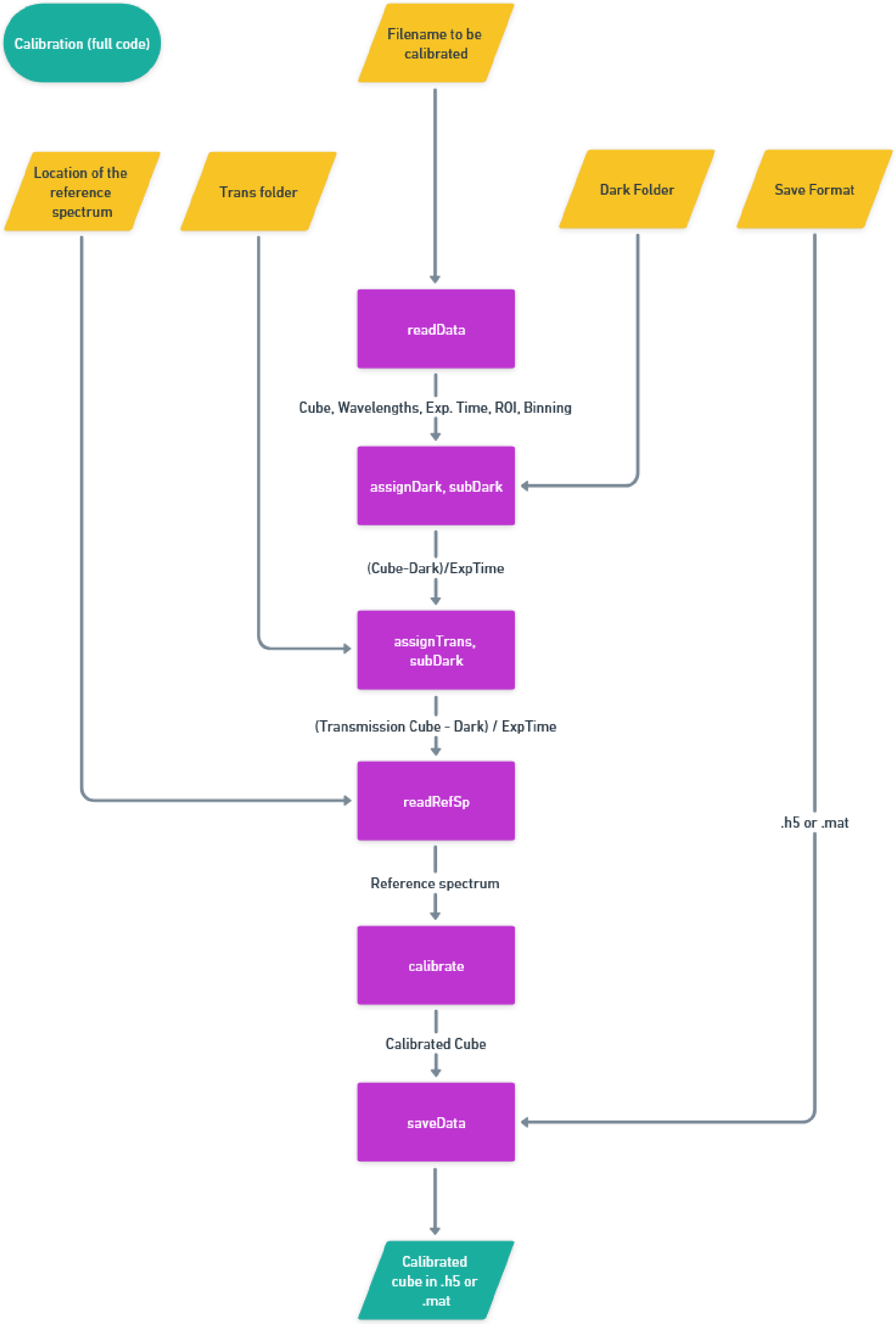

Figure D.1: *Flowchart representation of the calibration code. Inputs are shown in yellow, functions in purple and outputs in green. More details can be found on this Whimsical chart.*

Annexe E

Résumé en français

Les cellules solaires à porteurs chauds sont un concept inventé dans les années 80 pour augmenter l'efficacité de conversion de l'énergie solaire au-delà de 66% [Ross and Nozik 1982, Vezin *et al.* 2024a], là où les cellules solaires « conventionnelles » sont limitées à environ 30% d'efficacité [Shockley and Queisser 1961]. À ce jour, les quelques tentatives de construire des cellules à porteurs chauds ont mené à des rendements décevants, de l'ordre de 10% [Nguyen *et al.* 2018]. Il est donc nécessaire de complexifier notre compréhension des cellules solaires à porteurs chauds, par exemple en étudiant des effets non-idéaux. Dans cette thèse, nous étudions deux effets dits « d'écart de température » : (i) l'existence d'un gradient de température dans l'absorbeur (température inhomogène) et (ii) l'existence de deux températures différentes pour les électrons et les trous. Nous étudions ces deux cas de figure à la fois d'un point de vue expérimental, par des mesures de photoluminescence en régime continu, et d'un point de vue théorique par la modélisation.

Dans le premier cas, nous proposons une description théorique du transport de porteurs chauds dans un gradient de température, en revenant à la théorie du transport linéaire d'Onsager [Vezin *et al.* 2024b]. Nous montrons que le transport de porteurs chauds est ambipolaire, thermoélectrique et photogénéré, mais qu'il s'exprime dans un formalisme proche du transport ambipolaire thermoélectrique classique [Goldsmid 2016], à la condition d'introduire des coefficients de transport adaptés. Ensuite, nous proposons une expérience basée sur une mesure hyperspectrale de photoluminescence en régime continu pour caractériser le transport latéral de porteurs chauds dans un puits quantique de (In,Ga,As)P. Nous montrons que, dans ce matériau, les porteurs chauds sont capables de diffuser sur plusieurs microns, alors que la plupart des caractérisations dans les matériaux 2D ou les nanofils rapportent des longueurs de diffusion de quelque centaines de nanomètres. En outre, nous montrons que nous sommes capables d'estimer le taux de recombinaison et la conductivité électrique à un facteur multiplicatif près, ainsi que de mesurer absolument le coefficient Seebeck ambipolaire de cette structure.

Dans le second cas, nous commençons par prouver que la température des électrons et des trous sont toutes deux accessibles par une simple mesure de photoluminescence en régime continu. En effet, l'absorptivité d'un échantillon dépend de la distribution des porteurs dans chacune des bandes grâce à l'effet de « band filling ». Dans un régime de forte excitation, où les électrons et/ou les trous sont dégénérés, ce terme de « band filling » dépend individuellement de la température des électrons et des trous. En utilisant ce principe sur des spectres de photoluminescence issus du puits quantique de (In,Ga,As)P, nous mesurons des températures électroniques supérieures à 1000 K tandis que les trous restent à des température inférieures à 400 K [Vezin *et al.* 2024c]. En effet, dans les matériaux III-V, les trous sont généralement plus lourds que les électrons, et gagnent donc moins d'énergie lors de l'absorption d'un photon.

Enfin, nous étudions l'impact de ces deux effets d'écart de température sur l'opération des cellules à porteurs chauds. Nous montrons tout d'abord que le voltage d'une cellule sujette à l'un ou l'autre de ces deux effets s'exprime de la même manière, car le voltage ne dépend que de la distribution des porteurs au niveau du contact sélectif. Dans un second temps, nous construisons un modèle de bilan détaillé pour une cellule à porteurs chauds à deux températures – où les électrons et les trous peuvent avoir des températures différentes, bien qu'homogènes. Dans ce cas, nous montrons que la différence de température entre les électrons et les trous (à température effective fixée) conduit à une augmentation de l'efficacité de la cellule, de l'ordre de 1 à 2 points dans le meilleur des cas – et négligeable pour une cellule idéale avec des taux de thermalisation tendant vers 0. Cet effet étant limité, il n'est pas nécessaire de caractériser avec précision la température des électrons et des trous pour construire une cellule à porteurs chauds efficace.

Dans la continuité logique de cette thèse, il serait intéressant de construire un modèle de cellule solaire à porteurs chauds sujette à un gradient de température entre ses bornes, pour comprendre si le transport thermoélectrique pourrait impacter les performances de la cellule. En outre, cette thèse ouvre des perspectives pour mieux comprendre la physique des porteurs chauds, et en particulier :

1. ayant montré que les électrons et les trous pouvaient être maintenus à des températures différentes, nous nous demandons quels sont les mécanismes de relaxations dominants dans une telle situation. En particulier, comment modéliser la redistribution d'énergie entre les électrons chauds et les trous froids ?

2. ayant étudié le transport des porteurs chauds dans le cadre d'une expérience de photoluminescence en illumination ponctuelle, nous aimerions quantifier à quel point ce transport pourrait parasiter les mesures de taux de thermalisation. En effet, il est courant d'utiliser une configuration d'illumination ponctuelle pour augmenter la puissance surfacique de l'illumination et ainsi générer des porteurs plus chauds. Dans la limite où la taille du laser devient plus petite que la longueur de diffusion des porteurs chauds, ces derniers diffusent hors de la zone de génération. Ils emportant avec eux une fraction de l'énergie apportée par le laser, ce qui résulte en une température de porteurs plus faible au point de mesure. Cet effet est bien connu pour les estimations de temps de vie de porteurs dans les semiconducteurs [Vidon 2022], et mériterait d'être mis en évidence dans le cadre des porteurs chauds également.

Bibliography

[Agrawal and Dutta 1993] G. P. Agrawal and N. K. Dutta. *Semiconductor Lasers*. Springer US, Boston, MA (1993). ISBN 978-1-4613-0481-4 (cited pages 97, 98)

[Alexandrou *et al.* 1995] A. Alexandrou, V. Berger and D. Hulin. ‘Direct observation of electron relaxation in intrinsic GaAs using femtosecond pump-probe spectroscopy’. *Physical Review B*, **vol. 52**, no. 7, pp. 4654–4657 (1995) (cited page 104)

[Asche and Sarbei 1984] M. Asche and O. G. Sarbei. ‘The Role of Electron-Hole Interaction in the Cooling Process of Highly Excited Carriers’. *physica status solidi (b)*, **vol. 126**, no. 2, pp. 607–616 (1984) (cited pages 103, 115)

[Bauer 1978] G. Bauer. ‘Experimental aspects of hot electron distribution functions’. *Solid-State Electronics*, **vol. 21**, pp. 17–27 (1978) (cited page 26)

[Behaghel *et al.* 2019] B. Behaghel, R. Tamaki, H.-L. Chen, P. Rale, L. Lombez, Y. Shoji, A. Delamarre, A. Cattoni, S. Collin, Y. Okada and J.-F. Guillemoles. ‘A hot-carrier assisted InAs/AlGaAs quantum-dot intermediate-band solar cell’. *Semiconductor Science and Technology*, **vol. 34**, no. 8, p. 084001 (2019) (cited page 29)

[Bennett *et al.* 1990] B. Bennett, R. Soref and J. Del Alamo. ‘Carrier-induced change in refractive index of InP, GaAs and InGaAsP’. *IEEE Journal of Quantum Electronics*, **vol. 26**, no. 1, pp. 113–122 (1990) (cited pages 41, 45, 52, 61, 107, 114, 117)

[Bescond *et al.* 2018] M. Bescond, D. Logoteta, F. Michelini, N. Cavassilas, T. Yan, A. Yangui, M. Lannoo and K. Hirakawa. ‘Thermionic cooling devices based on resonant-tunneling AlGaAs/GaAs heterostructure’. *Journal of Physics: Condensed Matter*, **vol. 30**, no. 6, p. 064005 (2018) (cited pages 143, 147)

[Bradley *et al.* 1989] C. W. W. Bradley, R. A. Taylor and J. F. Ryan. ‘Femtosecond electron and hole thermalisation in AlGaAs’. *Solid-State Electronics*, **vol. 32**, no. 12, pp. 1173–1177 (1989) (cited pages 104, 115, 118, 119)

[Bremner *et al.* 2009] S. Bremner, N. Faleev, L. Nataraj, S. Cloutier, S. Dahal and C. Honsberq. ‘Passivation of InAs quantum dots for novel photovoltaics’. In ‘Conference Record of the IEEE Photovoltaic Specialists Conference’, pp. 001306–001311 (2009). ISBN 9781424429509 (cited page 29)

[Cavassilas *et al.* 2022] N. Cavassilas, I. Makhfudz, A.-M. Daré, M. Lannoo, G. Dangoisse, M. Bescond and F. Michelini. ‘Theoretical Demonstration of Hot-Carrier Operation in an Ultrathin Solar Cell’. *Physical Review Applied*, **vol. 17**, no. 6, p. 064001 (2022) (cited page 30)

[Chao *et al.* 2005] K. A. Chao, M. Larsson and A. G. Mal'shukov. 'Room-temperature semiconductor heterostructure refrigeration'. *Applied Physics Letters*, **vol. 87**, no. 2, p. 022103 (2005) (cited page 145)

[Chemla 1985] D. S. Chemla. 'Two-dimensional semiconductors: Recent development'. *Journal of Luminescence*, **vol. 30**, no. 1, pp. 502–519 (1985) (cited pages 45, 55, 61, 107, 114, 117)

[Chuang 2012] S. L. Chuang. *Physics of Photonic Devices.* John Wiley & Sons (2012). ISBN 978-1-118-58565-8 (cited page 45)

[Chébira *et al.* 1992] A. Chébira, J. Chesnoy and G. M. Gale. 'Femtosecond relaxation of photoexcited holes in bulk gallium arsenide'. *Physical Review B*, **vol. 46**, no. 8, pp. 4559–4563 (1992) (cited pages 103, 104, 106)

[Collin *et al.* 2023] S. Collin, J.-F. Guillemoles, A. Delamarre, T. Vezin, G. Vidon, C. Tong, B. Frouin, M. Legrand, M. Amara, T. Mathieu, L. Gavotto, D. Suchet, M. Levillayer, M. Thebault, N. Harada and A. Perelman. *Le solaire photovoltaïque en France* (2023) (cited pages 16, 17, 19)

[Conibeer *et al.* 2008] G. J. Conibeer, D. König, M. A. Green and J. F. Guillemoles. 'Slowing of carrier cooling in hot carrier solar cells'. *Thin Solid Films*, **vol. 516**, no. 20, pp. 6948–6953 (2008) (cited pages 29, 30)

[Conibeer *et al.* 2014] G. Conibeer, S. Shrestha, S. Huang, R. Patterson, H. Xia, Y. Feng, P. Zhang, N. Gupta, M. Tayebjee, S. Smyth, Y. Liao, Z. Zhang, S. Chung, S. Lin, P. Wang and X. Dai. 'Hot carrier solar cell absorbers: Materials, mechanisms and nanostructures'. In Sulima OV and Conibeer G, editors, 'Proceedings of SPIE International Society for Optical Engineering', vol. 9178. SPIE (2014). ISBN 9781628412055 (cited page 29)

[Dimmock *et al.* 2014] J. A. R. Dimmock, S. Day, M. Kauer, K. Smith and J. Heffernan. 'Demonstration of a hot-carrier photovoltaic cell'. *Progress in Photovoltaics: Research and Applications*, **vol. 22**, no. 2, pp. 151–160 (2014) (cited pages 29, 30)

[Esmaielpour *et al.* 2017] H. Esmaielpour, V. R. Whiteside, L. C. Hirst, J. G. Tischler, C. T. Ellis, M. P. Lumb, D. V. Forbes, R. J. Walters and I. R. Sellers. 'Effect of occupation of the excited states and phonon broadening on the determination of the hot carrier temperature from continuous wave photoluminescence in InGaAsP quantum well absorbers'. *Progress in Photovoltaics: Research and Applications*, **vol. 25**, no. 9, pp. 782–790 (2017) (cited pages 55, 61)

[Esmaielpour *et al.* 2020] H. Esmaielpour, L. Lombez, M. Giteau, A. Delamarre, D. Ory, A. Cattoni, S. Collin, J.-F. Guillemoles and D. Suchet. 'Investigation of the spatial distribution of hot carriers in quantum-well structures via hyperspectral luminescence imaging'. *Journal of Applied Physics*, **vol. 128**, no. 16, p. 165704 (2020) (cited page 90)

[Esmaielpour *et al.* 2021a] H. Esmaielpour, B. K. Durant, K. R. Dorman, V. R. Whiteside, J. Garg, T. D. Mishima, M. B. Santos, I. R. Sellers, J.-F. Guillemoles and D. Suchet. 'Hot carrier relaxation and inhibited thermalization in superlattice heterostructures: The potential for phonon management'. *Applied Physics Letters*, **vol. 118**, no. 21, p. 213902 (2021) (cited page 29)

[Esmaielpour *et al.* 2021b] H. Esmaielpour, L. Lombez, M. Giteau, A. Delamarre, D. Ory, A. Cattoni, S. Collin, J.-F. Guillemoles and D. Suchet. 'Investigation of hot carrier thermalization mechanisms in quantum well structures'. In Freundlich A, Collin S and Hinzer K, editors, 'Proceedings of SPIE International Society of Optical Engineering', vol. 11681. SPIE (2021). ISBN 9781510641976 (cited page 29)

[Esmaielpour *et al.* 2022] H. Esmaielpour, L. Lombez, M. Giteau, J.-F. Guillemoles and D. Suchet. 'Impact of excitation energy on hot carrier properties in InGaAs multi-quantum well structure'. *Progress in Photovoltaics: Research and Applications*, **vol. 30**, no. 11, pp. 1354–1362 (2022) (cited pages 50, 107, 114, 117)

[Fang *et al.* 2018] H.-H. Fang, S. Adjokatse, S. Shao, J. Even and M. A. Loi. 'Long-lived hot-carrier light emission and large blue shift in formamidinium tin triiodide perovskites'. *Nature Communications*, **vol. 9**, no. 1, p. 243 (2018) (cited page 29)

[Fast *et al.* 2021] J. Fast, U. Aeberhard, S. P. Bremner and H. Linke. 'Hot-carrier optoelectronic devices based on semiconductor nanowires'. *Applied Physics Reviews*, **vol. 8**, no. 2, p. 021309 (2021) (cited page 29)

[Fast *et al.* 2022] J. Fast, Y.-P. Liu, Y. Chen, L. Samuelson, A. M. Burke, H. Linke and A. Mikkelsen. 'Optical-Beam-Induced Current in InAs/InP Nanowires for Hot-Carrier Photovoltaics'. *ACS Applied Energy Materials*, **vol. 5**, no. 6, pp. 7728–7734 (2022) (cited page 94)

[Feng *et al.* 2012] Y. Feng, P. Aliberti, B. P. Veettil, R. Patterson, S. Shrestha, M. A. Green and G. Conibeer. 'Non-ideal energy selective contacts and their effect on the performance of a hot carrier solar cell with an indium nitride absorber'. *Applied Physics Letters*, **vol. 100**, no. 5, p. 053502 (2012) (cited page 29)

[Ferry *et al.* 1988] D. K. Ferry, M. A. Osman, R. Joshi and M. J. Kann. 'Ultrafast relaxation of hot photoexcited carriers in GaAs'. *Solid-State Electronics*, **vol. 31**, no. 3, pp. 401–406 (1988) (cited page 103)

[Ferry *et al.* 2020] D. K. Ferry, S. M. Goodnick, V. R. Whiteside and I. R. Sellers. 'Challenges, myths, and opportunities in hot carrier solar cells'. *Journal of Applied Physics*, **vol. 128**, no. 22, p. 220903 (2020) (cited page 30)

[Fox 2010] M. Fox. *Optical Properties of Solids*. Oxford University Press (2010). ISBN 978-0-19-957336-3 (cited page 45)

[Freitag *et al.* 2004] M. Freitag, V. Perebeinos, J. Chen, A. Stein, J. C. Tsang, J. A. Misewich, R. Martel and P. Avouris. 'Hot Carrier Electroluminescence from a Single Carbon Nanotube'. *Nano Letters*, **vol. 4**, no. 6, pp. 1063–1066 (2004) (cited page 29)

[Fressoz 2024] J.-B. Fressoz. *Sans transition: Une nouvelle histoire de l'énergie*. Seuil (2024). ISBN 978-2-02-153856-4 (cited page 17)

[Frohlich 1947] H. Frohlich. 'New theory of electrical discharge and breakdown in low-mobility condensed insulators'. *Proc. Roy. Soc.*, **vol. 188** (1947) (cited page 27)

[Gabor *et al.* 2011] N. M. Gabor, J. C. W. Song, Q. Ma, N. L. Nair, T. Taychatanapat, K. Watanabe, T. Taniguchi, L. S. Levitov and P. Jarillo-Herrero. 'Hot Carrier–Assisted Intrinsic Photoresponse in Graphene'. *Science*, **vol. 334**, no. 6056, pp. 648–652 (2011) (cited pages 29, 78)

[Gibelli 2016] F. Gibelli. *Photovoltaic & Thermoelectric energy harvesting in hot carrier solar cells*. Ph.D. thesis (2016) (cited page 30)

[Gibelli *et al.* 2016a] F. Gibelli, L. Lombez and J.-F. Guillemoles. 'Accurate radiation temperature and chemical potential from quantitative photoluminescence analysis of hot carrier populations'. *Journal of Physics: Condensed Matter*, **vol. 29**, no. 6, p. 06LT02 (2016) (cited page 37)

[Gibelli *et al.* 2016b] F. Gibelli, L. Lombez and J.-F. Guillemoles. 'Two carrier temperatures non-equilibrium generalized Planck law for semiconductors'. *Physica B: Condensed Matter*, **vol. 498**, pp. 7–14 (2016) (cited pages 37, 104, 106, 117)

[Gibelli *et al.* 2016c] F. Gibelli, L. Lombez, J. Rodiere and J.-F. Guillemoles. 'Optical Imaging of Light-Induced Thermopower in Semiconductors'. *Physical Review Applied*, **vol. 5**, no. 2, p. 024005 (2016) (cited pages 78, 90)

[Gibelli *et al.* 2019] F. Gibelli, L. Lombez and J.-F. Guillemoles. 'Hot-Carrier Solar Cells: Modeling Carrier Transport'. In D Ginley and T Fix, editors, 'Advanced Micro- and Nanomaterials for Photovoltaics', Micro and Nano Technologies, pp. 53–92. Elsevier (2019). ISBN 978-0-12-814501-2 (cited page 124)

[Giteau *et al.* 2019] M. Giteau, D. Suchet, S. Collin, J.-F. Guillemoles and Y. Okada. 'Detailed balance calculations for hot-carrier solar cells: coupling high absorptivity with low thermalization through light trapping'. *EPJ Photovoltaics*, **vol. 10**, p. 1 (2019) (cited page 76)

[Giteau *et al.* 2020] M. Giteau, E. de Moustier, D. Suchet, H. Esmaielpour, H. Sodabanlu, K. Watanabe, S. Collin, J.-F. Guillemoles and Y. Okada. 'Identification of surface and volume hot-carrier thermalization mechanisms in ultrathin GaAs layers'. *Journal of Applied Physics*, **vol. 128**, no. 19, p. 193102 (2020) (cited pages 26, 66, 119)

[Goebel and Hildebrand 1978] E. O. Goebel and O. Hildebrand. 'Thermalization of the Electron—Hole Plasma in GaAs.' *physica status solidi (b)*, **vol. 88**, no. 2, pp. 645–652 (1978) (cited page 24)

[Goldsmid 2016] H. J. Goldsmid. *Introduction to Thermoelectricity*, vol. 121 of *Springer Series in Materials Science*. Springer Berlin Heidelberg, Berlin, Heidelberg (2016). ISBN 978-3-662-49256-7 (cited pages 78, 81, 84, 85, 86, 100, 175)

[Gong *et al.* 1993] T. Gong, P. M. Fauchet, J. F. Young and P. J. Kelly. 'Subpicosecond hot hole dynamics in highly excited GaAs'. *Applied Physics Letters*, **vol. 62**, no. 5, pp. 522–524 (1993) (cited page 103)

[Gong *et al.* 2024] S. Gong, G. Qu, Y. Qiao, Y. Wen, Y. Huang, S. Cai, L. Zhang, K. Jiang, S. Liu, M. Lin, M. C. Beard, Z.-X. Xu and X. Chen. 'A hot carrier perovskite solar cell with efficiency exceeding 27% enabled by ultrafast hot hole transfer with phthalocyanine derivatives'. *Energy & Environmental Science* (2024) (cited page 31)

[Green 2003] M. A. Green. 'Hot Carrier Cells'. In 'Third Generation Photovoltaics: Advanced Solar Energy Conversion', Springer series in photonics, pp. 69–80. Springer, Berlin, Heidelberg (2003). ISBN 978-3-540-26563-4 (cited pages 23, 24, 29)

[Green 2006] M. A. Green. *Third generation photovoltaics: advanced solar energy conversion*. No. 12 in Springer series in photonics. Springer, Berlin ; New York (2006). ISBN 978-3-540-40137-7 (cited page 21)

[Green *et al.* 2010] M. A. Green, G. Conibeer, D. König, S. Shrestha, S. Huang, P. Aliberti, L. Treiber, R. Patterson, B. P. Veettil, A. Hsieh, Y. Feng, A. Luque, A. Marti, P. Linares, E. Cánovas, E. Antolín, D. Fuertes Marrón, C. Tablero, E. Hernández, J.-F. Guillemoles, L. Huang, A. Le Bris, T. Schmidt, R. Clady and M. Tayebjee. 'Hot carrier solar cells: Challenges and recent progress'. In '2010 35th IEEE Photovoltaic Specialists Conference', pp. 000057–000060 (2010). ISSN: 0160-8371 (cited page 29)

[Green *et al.* 2022] M. A. Green, E. D. Dunlop, J. Hohl-Ebinger, M. Yoshita, N. Kopidakis, K. Bothe, D. Hinken, M. Rauer and X. Hao. 'Solar cell efficiency tables (Version 60)'. *Progress in Photovoltaics: Research and Applications*, **vol. 30**, no. 7, pp. 687–701 (2022) (cited page 19)

[Guillemoles *et al.* 2005] J.-F. Guillemoles, G. Conibeer and M. Green. 'Phononic engineering with nanostructures for hot carrier solar cells'. *PVSEC (Shanghai)*, **vol. 15th edition**, p. 3 (2005) (cited pages 26, 29)

[Guillemoles *et al.* 2019] J.-F. Guillemoles, T. Kirchartz, D. Cahen and U. Rau. 'Guide for the perplexed to the Shockley–Queisser model for solar cells'. *Nature Photonics*, **vol. 13**, no. 8, pp. 501–505 (2019) (cited page 20)

[Gunn 1963] J. B. Gunn. 'Microwave oscillations of current in III–V semiconductors'. *Solid State Communications*, **vol. 1**, no. 4, pp. 88–91 (1963) (cited page 28)

[Guo *et al.* 2017] Z. Guo, Y. Wan, M. Yang, J. Snaider, K. Zhu and L. Huang. 'Long-range hot-carrier transport in hybrid perovskites visualized by ultrafast microscopy'. *Science*, **vol. 356**, no. 6333, pp. 59–62 (2017) (cited page 94)

[Gurevich *et al.* 1995] Y. G. Gurevich, O. Y. Titov, G. N. Logvinov and O. I. Lyubimov. 'Nature of the thermopower in bipolar semiconductors'. *Physical Review B*, **vol. 51**, no. 11, pp. 6999–7004 (1995) (cited pages 78, 81, 82)

[Hanna and Nozik 2006] M. C. Hanna and A. J. Nozik. 'Solar conversion efficiency of photovoltaic and photoelectrolysis cells with carrier multiplication absorbers'. *Journal of Applied Physics*, **vol. 100**, no. 7, p. 074510 (2006) (cited page 22)

[Harada *et al.* 2016] Y. Harada, N. Kasamatsu, D. Watanabe and T. Kita. 'Nanosecond-scale hot-carrier cooling dynamics in one-dimensional quantum dot superlattices'. *Physical Review B*, **vol. 93**, no. 11, p. 115303 (2016) (cited page 29)

[Hayes and Phillips 1994] G. R. Hayes and R. T. Phillips. 'The effects of intervalley scattering on the cooling of hot carriers in In0.53Ga0.47As'. *Journal of Physics: Condensed Matter*, **vol. 6**, no. 37, p. 7589 (1994) (cited page 103)

[Heavens 1960] O. S. Heavens. 'Optical properties of thin films'. *Reports on Progress in Physics*, **vol. 23**, no. 1, p. 1 (1960) (cited page 53)

[Hicks *et al.* 1996] L. D. Hicks, T. C. Harman, X. Sun and M. S. Dresselhaus. 'Experimental study of the effect of quantum-well structures on the thermoelectric figure of merit'. *Physical Review B*, **vol. 53**, no. 16, pp. R10493–R10496 (1996) (cited page 100)

[Hirst *et al.* 2014] L. Hirst, M. Yakes, C. Bailey, J. Tischler, M. Lumb, M. Gonzalez, M. Fuhrer, N. Ekins-Daukes and R. Walters. 'Enhanced hot-carrier effects in InAlAs/InGaAs quantum wells'. *IEEE Journal of Photovoltaics*, **vol. 4**, no. 6, pp. 1526–1531 (2014). Publisher: IEEE Electron Devices Society (cited page 29)

[Holonyak 1997] N. Holonyak. 'The semiconductor laser: a thirty-five-year perspective'. *Proceedings of the IEEE*, **vol. 85**, no. 11, pp. 1678–1693 (1997) (cited page 28)

[Höpfel *et al.* 1986] R. A. Höpfel, J. Shah and A. C. Gossard. 'Nonequilibrium electron-hole plasma in GaAs quantum wells'. *Physical Review Letters*, **vol. 56**, no. 7, pp. 765–768 (1986) (cited pages 101, 103, 106)

[IEA 2024] IEA. 'IEA World Energy Balances' (2024) (cited page 17)

[IPCC 2023] IPCC. *Climate Change 2021 – The Physical Science Basis: Working Group I Contribution to the Sixth Assessment Report of the Intergovernmental Panel on Climate Change*. Cambridge University Press, 1 ed. (2023). ISBN 978-1-00-915789-6 (cited page 15)

[Kane 1963] E. O. Kane. 'Thomas-Fermi Approach to Impure Semiconductor Band Structure'. *Physical Review*, **vol. 131**, no. 1, pp. 79–88 (1963) (cited page 44)

[Katahara and Hillhouse 2014] J. K. Katahara and H. W. Hillhouse. 'Quasi-Fermi level splitting and sub-bandgap absorptivity from semiconductor photoluminescence'. *Journal of Applied Physics*, **vol. 116**, no. 17, p. 173504 (2014) (cited pages 45, 56)

[Ketterle and Druten 1996] W. Ketterle and N. J. V. Druten. 'Evaporative Cooling of Trapped Atoms'. In B Bederson and H Walther, editors, 'Advances In Atomic, Molecular, and Optical Physics', vol. 37, pp. 181–236. Academic Press (1996) (cited page 143)

[Kirk and Fischetti 2012] A. P. Kirk and M. V. Fischetti. 'Fundamental limitations of hot-carrier solar cells'. *Physical Review B*, **vol. 86**, no. 16, p. 165206 (2012) (cited page 30)

[Koenig 1959] S. Koenig. 'Hot and warm electrons — A review'. *Journal of Physics and Chemistry of Solids*, **vol. 8**, pp. 227–234 (1959) (cited page 27)

[Konovalov and Emelianov 2017] I. Konovalov and V. Emelianov. 'Hot carrier solar cell as thermoelectric device'. *Energy Science & Engineering*, **vol. 5**, no. 3, pp. 113–122 (2017) (cited pages 23, 31, 77)

[Kumekov and Perel 1988] S. E. Kumekov and V. I. Perel. ‘Static and Dynamic Cooling Rate of Photocreated Plasmas in Semiconductors’. In JL Birman, HZ Cummins and AA Kaplyanskii, editors, ‘Laser Optics of Condensed Matter’, pp. 25–29. Springer US, Boston, MA (1988). ISBN 978-1-4615-7341-8 (cited pages 27, 119)

[König *et al.* 2010] D. König, K. Casalenuovo, Y. Takeda, G. Conibeer, J. Guillemoles, R. Patterson, L. Huang and M. Green. ‘Hot carrier solar cells: Principles, materials and design’. *Physica E: Low-dimensional Systems and Nanostructures*, **vol. 42**, no. 10, pp. 2862–2866 (2010) (cited page 29)

[König *et al.* 2012] D. König, Y. Takeda and B. Puthen-Veettil. ‘Technology-compatible hot carrier solar cell with energy selective hot carrier absorber and carrier-selective contacts’. *Applied Physics Letters*, **vol. 101**, no. 15, p. 153901 (2012) (cited page 29)

[Landsberg and Tonge 1979] P. T. Landsberg and G. Tonge. ‘Thermodynamics of the conversion of diluted radiation’. *Journal of Physics A: Mathematical and General*, **vol. 12**, no. 4, p. 551 (1979) (cited page 20)

[Langot *et al.* 1996] P. Langot, R. Tommasi and F. Vallée. ‘Nonequilibrium hole relaxation dynamics in an intrinsic semiconductor’. *Physical Review B*, **vol. 54**, no. 3, pp. 1775–1784 (1996) (cited page 104)

[Lasher and Stern 1964] G. Lasher and F. Stern. ‘Spontaneous and Stimulated Recombination Radiation in Semiconductors’. *Physical Review*, **vol. 133**, no. 2A, pp. A553–A563 (1964) (cited pages 40, 41)

[Le Bris 2011] A. Le Bris. *Étude de faisabilité de dispositifs photovoltaïques à porteurs chauds : conception, modélisation, caractérisation*. Ph.D. thesis (2011) (cited page 65)

[Le Bris and Guillemoles 2010] A. Le Bris and J.-F. Guillemoles. ‘Hot carrier solar cells: Achievable efficiency accounting for heat losses in the absorber and through contacts’. *Applied Physics Letters*, **vol. 97**, no. 11, p. 113506 (2010) (cited pages 30, 31, 64, 73, 124, 136)

[Le Bris *et al.* 2012] A. Le Bris, L. Lombez, S. Laribi, G. Boissier, P. Christol and J.-F. Guillemoles. ‘Thermalisation rate study of GaSb-based heterostructures by continuous wave photoluminescence and their potential as hot carrier solar cell absorbers’. *Energy and Environmental Science*, **vol. 5**, no. 3, pp. 6225–6232 (2012) (cited pages 26, 29, 30, 32, 76)

[Legifrance 2021] Legifrance. ‘Loi n° 2021-1104 du 22 août 2021 portant lutte contre le dérèglement climatique et renforcement de la résilience face à ses effets’ (2021) (cited page 19)

[Leo and Collet 1991] K. Leo and J. H. Collet. ‘Influence of electron-hole scattering on the plasma thermalization in doped GaAs’. *Physical Review B*, **vol. 44**, no. 11, pp. 5535–5539 (1991) (cited pages 103, 118, 119)

[Lim *et al.* 2022] J. W. M. Lim, Y. Wang, J. Fu, Q. Zhang and T. C. Sum. ‘Spotlight on Hot Carriers in Halide Perovskite Luminescence’. *ACS Energy Letters*, pp. 749–756 (2022) (cited page 29)

[Limpert and Bremner 2015] S. C. Limpert and S. P. Bremner. ‘Hot carrier extraction using energy selective contacts and its impact on the limiting efficiency of a hot carrier solar cell’. *Applied Physics Letters*, **vol. 107**, no. 7, p. 073902 (2015) (cited pages 32, 68)

[Limpert *et al.* 2015] S. Limpert, S. Bremner and H. Linke. ‘Reversible electron–hole separation in a hot carrier solar cell’. *New Journal of Physics*, **vol. 17**, no. 9, p. 095004 (2015) (cited pages 77, 124)

[Limpert *et al.* 2017] S. Limpert, A. Burke, I.-J. Chen, N. Anttu, S. Lehmann, S. Fahlvik, S. Bremner, G. Conibeer, C. Thelander, M.-E. Pistol and H. Linke. ‘Bipolar Photothermoelectric Effect Across Energy Filters in Single Nanowires’. *Nano Letters*, **vol. 17**, no. 7, pp. 4055–4060 (2017) (cited pages 29, 32, 46, 77, 78, 89, 153)

[Luque and Martí 1997] A. Luque and A. Martí. ‘Increasing the Efficiency of Ideal Solar Cells by Photon Induced Transitions at Intermediate Levels’. *Physical Review Letters*, **vol. 78**, no. 26, pp. 5014–5017 (1997) (cited page 21)

[Luque and Martí 2010] A. Luque and A. Martí. ‘Electron–phonon energy transfer in hot-carrier solar cells’. *Solar Energy Materials and Solar Cells*, **vol. 94**, no. 2, pp. 287–296 (2010) (cited page 29)

[Lyon 1986] S. A. Lyon. ‘Spectroscopy of hot carriers in semiconductors’. *Journal of Luminescence*, **vol. 35**, no. 3, pp. 121–154 (1986) (cited page 26)

[Mahan 1994] G. D. Mahan. ‘Thermionic refrigeration’. *Journal of Applied Physics*, **vol. 76**, no. 7, pp. 4362–4366 (1994) (cited pages 69, 143)

[Makhfudz *et al.* 2022] I. Makhfudz, N. Cavassilas, M. Giteau, H. Esmaielpour, D. Suchet, A.-M. Daré and F. Michelini. ‘Enhancement of hot carrier effect and signatures of confinement in terms of thermalization power in quantum well solar cell’. *Journal of Physics D: Applied Physics*, **vol. 55**, no. 47, p. 475102 (2022) (cited pages 29, 30)

[Marti *et al.* 2022] A. Marti, E. Antolin and I. Ramiro. ‘Thermodynamics of the Monoenergetic Energy-Selective Contacts of a Hot-Carrier Solar Cell’. *Physical Review Applied*, **vol. 18**, no. 6, p. 064048 (2022) (cited pages 31, 77)

[Nguyen *et al.* 2018] D.-T. Nguyen, L. Lombez, F. Gibelli, S. Boyer-Richard, A. Le Corre, O. Durand and J.-F. Guillemoles. ‘Quantitative experimental assessment of hot carrier-enhanced solar cells at room temperature’. *Nature Energy*, **vol. 3**, no. 3, pp. 236–242 (2018) (cited pages 29, 31, 46, 58, 60, 92, 175)

[Nie *et al.* 2014] Z. Nie, R. Long, L. Sun, C.-C. Huang, J. Zhang, Q. Xiong, D. W. Hewak, Z. Shen, O. V. Prezhdo and Z.-H. Loh. ‘Ultrafast Carrier Thermalization and Cooling Dynamics in Few-Layer MoS2’. *ACS Nano*, **vol. 8**, no. 10, pp. 10931–10940 (2014) (cited page 29)

[NREL 2024] NREL. ‘Best Research-Cell Efficiency Chart’ (2024) (cited page 21)

[Okazaki *et al.* 2012] R. Okazaki, A. Horikawa, Y. Yasui and I. Terasaki. 'Photo-Seebeck Effect in ZnO'. *Journal of the Physical Society of Japan*, **vol. 81**, no. 11, p. 114722 (2012) (cited pages 78, 87, 100)

[Osman and Ferry 1987] M. A. Osman and D. K. Ferry. 'Monte Carlo investigation of the electron-hole-interaction effects on the ultrafast relaxation of hot photoexcited carriers in GaAs'. *Physical Review B*, **vol. 36**, no. 11, pp. 6018–6032 (1987) (cited page 103)

[Othonos 1998] A. Othonos. 'Probing ultrafast carrier and phonon dynamics in semiconductors'. *Journal of Applied Physics*, **vol. 83**, no. 4, pp. 1789–1830 (1998) (cited pages 25, 28)

[Paget *et al.* 2012] D. Paget, F. Cadiz, A. C. H. Rowe, F. Moreau, S. Arscott and E. Peytavit. 'Imaging ambipolar diffusion of photocarriers in GaAs thin films'. *Journal of Applied Physics*, **vol. 111**, no. 12, p. 123720 (2012) (cited page 90)

[Pan *et al.* 1986] J. L. Pan, R. A. Höpfel and J. Shah. 'Photoluminescence from GaAs quantum wells under high electric fields'. *Journal of Applied Physics*, **vol. 59**, no. 11, pp. 3925–3927 (1986) (cited pages 103, 106, 115)

[Papagiorgis *et al.* 2019] P. Papagiorgis, A. Manoli, S. Michael, C. Bernasconi, M. I. Bodnarchuk, M. V. Kovalenko, A. Othonos and G. Itskos. 'Unraveling the Radiative Pathways of Hot Carriers upon Intense Photoexcitation of Lead Halide Perovskite Nanocrystals'. *ACS Nano*, **vol. 13**, no. 5, pp. 5799–5809 (2019) (cited page 29)

[Park *et al.* 2021] S. Park, B. Han, C. Boule, D. Paget, A. Rowe, F. Sirotti, T. Taniguchi, K. Watanabe, C. Robert, L. Lombez, B. Urbaszek, X. Marie and F. Cadiz. 'Imaging Seebeck drift of excitons and trions in MoSe2 monolayers'. *2D Materials*, **vol. 8**, no. 4, p. 045014 (2021) (cited pages 78, 94)

[Pelouch *et al.* 1992] W. S. Pelouch, R. J. Ellingson, P. E. Powers, C. L. Tang, D. M. Szmyd and A. J. Nozik. 'Comparison of hot-carrier relaxation in quantum wells and bulk GaAs at high carrier densities'. *Physical Review B*, **vol. 45**, no. 3, pp. 1450–1453 (1992) (cited pages 28, 147)

[Polland *et al.* 1987] H. J. Polland, W. W. Rühle, J. Kuhl, K. Ploog, K. Fujiwara and T. Nakayama. 'Nonequilibrium cooling of thermalized electrons and holes in GaAs/AlGaAs quantum wells'. *Physical Review B*, **vol. 35**, no. 15, pp. 8273–8276 (1987) (cited page 103)

[Pottier 2007] N. Pottier. *Physique statistique hors d'équilibre.* Savoirs Actuels. EDP Sciences / CNRS Editions (2007). ISBN 978-2-271-06548-3 (cited pages 80, 81, 82, 83, 84, 85)

[Price 1955] P. Price. 'Ambipolar thermodiffusion of electrons and holes in semiconductors'. *The London, Edinburgh, and Dublin Philosophical Magazine and Journal of Science*, **vol. 46**, no. 382, pp. 1252–1260 (1955) (cited pages 78, 88)

[Project 2023] F. P. Project. 'The Forever Pollution Project – Journalists tracking PFAS across Europe' (2023) (cited page 15)

[Pérez-Lopez *et al.* 2020] P. Pérez-Lopez, R. Jolivet, I. Blanc, R. Besseau, M. Douziech, B. Gshwind, S. Tannous, J. Schlesinger, R. Brière, A. Prieur-Vernat and J. Clavreul. 'INCER-ACV : Incertitudes dans les méthodes d'évaluation des impacts environnementaux des filières de production énergétique par ACV'. Tech. rep. (2020) (cited page 16)

[Riddoch and Ridley 1985] F. A. Riddoch and B. K. Ridley. 'Electron scattering rates associated with the polar optical phonon interaction in a thin ionic slab'. *Physica B+C*, **vol. 134**, no. 1-3, pp. 342–346 (1985) (cited page 30)

[Rodiere *et al.* 2015] J. Rodiere, L. Lombez, A. Le Corre, O. Durand and J.-F. Guillemoles. 'Experimental evidence of hot carriers solar cell operation in multi-quantum wells heterostructures'. *Applied Physics Letters*, **vol. 106**, no. 18 (2015) (cited pages 23, 29, 77)

[Rodière 2014] J. Rodière. *Optoelectronic characterization of hot carriers solar cells absorbers*. Ph.D. thesis, Université Pierre et Marie Curie - Paris VI (2014) (cited pages 79, 90)

[Rosenwaks *et al.* 1993] Y. Rosenwaks, M. C. Hanna, D. H. Levi, D. M. Szmyd, R. K. Ahrenkiel and A. J. Nozik. 'Hot-carrier cooling in GaAs: Quantum wells versus bulk'. *Physical Review B*, **vol. 48**, no. 19, pp. 14675–14678 (1993) (cited pages 28, 147)

[Ross and Nozik 1982] R. T. Ross and A. J. Nozik. 'Efficiency of hot-carrier solar energy converters'. *Journal of Applied Physics*, **vol. 53**, no. 5, pp. 3813–3818 (1982) (cited pages 22, 23, 28, 32, 63, 66, 68, 73, 124, 175)

[Ruzicka *et al.* 2010a] B. A. Ruzicka, S. Wang, L. K. Werake, B. Weintrub, K. P. Loh and H. Zhao. 'Hot carrier diffusion in graphene'. *Physical Review B*, **vol. 82**, no. 19, p. 195414 (2010) (cited page 94)

[Ruzicka *et al.* 2010b] B. A. Ruzicka, L. K. Werake, H. Samassekou and H. Zhao. 'Ambipolar diffusion of photoexcited carriers in bulk GaAs'. *Applied Physics Letters*, **vol. 97**, no. 26, p. 262119 (2010) (cited page 78)

[Ryan *et al.* 1984] J. F. Ryan, R. A. Taylor, A. J. Turberfield, A. Maciel, J. M. Worlock, A. C. Gossard and W. Wiegmann. 'Time-Resolved Photoluminescence of Two-Dimensional Hot Carriers in GaAs-AlGaAs Heterostructures'. *Physical Review Letters*, **vol. 53**, no. 19, pp. 1841–1844 (1984) (cited page 147)

[Sandner *et al.* 2023] D. Sandner, H. Esmaielpour, F. d. Giudice, S. Meder, M. Nuber, R. Kienberger, G. Koblmüller and H. Iglev. 'Hot Electron Dynamics in InAs–AlAsSb Core–Shell Nanowires'. *ACS Applied Energy Materials* (2023) (cited page 29)

[Sawaki 1986] N. Sawaki. 'On the reduction of the electron-LO phonon scattering in a semiconductor superlattice'. *Journal of Physics C: Solid State Physics*, **vol. 19**, no. 25, pp. 4965–4975 (1986) (cited page 30)

[Shah 1981] J. Shah. 'Investigation of hot carrier relaxation with picosecond laser pulses'. *Le Journal de Physique Colloques*, **vol. 42**, no. C7, pp. C7–445–C7–462 (1981) (cited page 24)

[Shah and Leite 1969] J. Shah and R. C. C. Leite. 'Radiative Recombination from Photoexcited Hot Carriers in GaAs'. *Physical Review Letters*, **vol. 22**, no. 24, pp. 1304–1307 (1969) (cited pages 26, 29, 50)

[Shah *et al.* 1985] J. Shah, A. Pinczuk, A. C. Gossard and W. Wiegmann. 'Energy-Loss Rates for Hot Electrons and Holes in GaAs Quantum Wells'. *Physical Review Letters*, **vol. 54**, no. 18, pp. 2045–2048 (1985) (cited page 103)

[Sharma 2023] A. Sharma. *The role of remote valleys in photovoltaic devices*. Ph.D. thesis, UNSW Sydney (2023) (cited page 32)

[Sharma *et al.* 2023] A. S. Sharma, M. Hanif, S. P. Bremner, M. P. Nielsen, M. J. Y. Tayebjee, F. E. Rougieux, N. J. Ekins-Daukes and A. Pusch. 'Heat Flow through Nonideal Contacts in Hot-Carrier Solar Cells'. *Physical Review Applied*, **vol. 20**, no. 3, p. 034001 (2023) (cited page 31)

[Shockley 1951] W. Shockley. 'Hot electrons in germanium and Ohm's law'. *The Bell System Technical Journal*, **vol. 30**, no. 4, pp. 990–1034 (1951) (cited pages 26, 27)

[Shockley and Queisser 1961] W. Shockley and H. J. Queisser. 'Detailed Balance Limit of Efficiency of p-n Junction Solar Cells'. *Journal of Applied Physics*, **vol. 32**, no. 510, p. 11 (1961) (cited pages 19, 20, 71, 175)

[Shockley and Read 1952] W. Shockley and W. T. Read. 'Statistics of the Recombinations of Holes and Electrons'. *Physical Review*, **vol. 87**, no. 5, pp. 835–842 (1952). Publisher: American Physical Society (cited page 96)

[Smith *et al.* 1985] C. Smith, R. A. Abram and M. G. Burt. 'Theory of Auger recombination in a quantum well heterostructure'. *Superlattices and Microstructures*, **vol. 1**, no. 2, pp. 119–123 (1985) (cited page 98)

[Snoke *et al.* 1992] D. W. Snoke, W. W. Rühle, Y.-C. Lu and E. Bauser. 'Nonthermalized distribution of electrons on picosecond time scale in GaAs'. *Physical Review Letters*, **vol. 68**, no. 7, pp. 990–993 (1992) (cited pages 103, 104)

[Sourabh *et al.* 2024] S. Sourabh, H. Afshari, V. R. Whiteside, G. E. Eperon, R. A. Scheidt, T. D. Creason, M. Furis, A. R. Kirmani, B. Saparov, J. M. Luther, M. C. Beard and I. R. Sellers. 'Evidence of hot carrier extraction in metal halide perovskite solar cells'. *Progress in Photovoltaics: Research and Applications*, **vol. 32**, no. 8 (2024) (cited page 29)

[Sritrakool *et al.* 1986] W. Sritrakool, V. Sa-yakanit and H. R. Glyde. 'Band tails in disordered systems'. *Physical Review B*, **vol. 33**, no. 2, pp. 1199–1202 (1986) (cited page 44)

[Storn 1997] R. Storn. 'Differential Evolution – A Simple and Efficient Heuristic for Global Optimization over Continuous Spaces'. *Journal of Global Optimization*, , no. 11, pp. 341–359 (1997) (cited pages 53, 54)

[Suchet and Johnson 2023] D. Suchet and E. Johnson. *L'énergie solaire photovoltaïque. Une introduction à*. EDP sciences, Les Ulis (2023). ISBN 978-2-7598-2923-1 (cited pages 18, 19)

[Suchet *et al.* 2017] D. Suchet, Z. Jehl, Y. Okada and J.-F. Guillemoles. 'Influence of Hot-Carrier Extraction from a Photovoltaic Absorber: An Evaporative Approach'. *Physical Review Applied*, **vol. 8**, no. 3, p. 034030 (2017) (cited pages 69, 143)

[Takeda *et al.* 2010] Y. Takeda, T. Motohiro, D. König, P. Aliberti, Y. Feng, S. Shrestha and G. Conibeer. 'Practical Factors Lowering Conversion Efficiency of Hot Carrier Solar Cells'. *Applied Physics Express*, **vol. 3**, no. 10, p. 104301 (2010) (cited page 29)

[Taylor *et al.* 1992] R. A. Taylor, C. W. W. Bradley, N. Mayhew, T. N. Thomas and J. F. Ryan. 'Femtosecond hole burning measurements in semiconductors'. *Journal of Luminescence*, **vol. 53**, no. 1, pp. 321–326 (1992) (cited page 103)

[Tedeschi *et al.* 2016] D. Tedeschi, M. De Luca, H. A. Fonseka, Q. Gao, F. Mura, H. H. Tan, S. Rubini, F. Martelli, C. Jagadish, M. Capizzi and A. Polimeni. 'Long-Lived Hot Carriers in III–V Nanowires'. *Nano Letters*, **vol. 16**, no. 5, pp. 3085–3093 (2016) (cited page 29)

[Tomic *et al.* 2003] S. Tomic, E. O'Reilly, R. Fehse, S. Sweeney, A. Adams, A. Andreev, S. Choulis, T. Hosea and H. Riechert. 'Theoretical and experimental analysis of 1.3-µm InGaAsN/GaAs lasers'. *IEEE Journal of Selected Topics in Quantum Electronics*, **vol. 9**, no. 5, pp. 1228–1238 (2003) (cited page 53)

[Trupke *et al.* 2002] T. Trupke, M. A. Green and P. Würfel. 'Improving solar cell efficiencies by up-conversion of sub-band-gap light'. *Journal of Applied Physics*, **vol. 92**, no. 7, pp. 4117–4122 (2002) (cited pages 21, 22)

[Tsai 2018] C.-Y. Tsai. 'Theoretical model and simulation of carrier heating with effects of nonequilibrium hot phonons in semiconductor photovoltaic devices'. *Progress in Photovoltaics: Research and Applications*, **vol. 26**, no. 10, pp. 808–824 (2018) (cited pages 27, 32, 119)

[Tsai 2019] C.-Y. Tsai. 'The effects of intraband and interband carrier-carrier scattering on hot-carrier solar cells: A theoretical study of spectral hole burning, electron-hole energy transfer, Auger recombination, and impact ionization generation'. *Progress in Photovoltaics: Research and Applications*, **vol. 27**, no. 5, pp. 433–452 (2019) (cited page 32)

[van Roosbroeck and Shockley 1954] W. van Roosbroeck and W. Shockley. 'Photon-Radiative Recombination of Electrons and Holes in Germanium'. *Physical Review*, **vol. 94**, no. 6, pp. 1558–1560 (1954) (cited pages 40, 41)

[Varshni 1967] Y. P. Varshni. 'Temperature dependence of the energy gap in semiconductors'. *Physica*, **vol. 34**, no. 1, pp. 149–154 (1967) (cited pages 45, 56)

[Vezin *et al.* 2024a] T. Vezin, H. Esmaielpour, M. Amara and D. Suchet. 'Concepts avancées pour une conversion photovoltaïque à très haut rendement'. In 'L'énergie solaire photovoltaique', Iste science ed. (2024) (cited pages 20, 21, 22, 175)

[Vezin *et al.* 2024b] T. Vezin, H. Esmaielpour, L. Lombez, J.-F. Guillemoles and D. Suchet. 'Optical determination of thermoelectric transport coefficients in a hot-carrier absorber'. *Physical Review Applied*, **vol. 22**, no. 3, p. 034018 (2024) (cited pages 78, 89, 94, 100, 175)

[Vezin *et al.* 2024c] T. Vezin, N. Roubinowitz, L. Lombez, J.-F. Guillemoles and D. Suchet. 'Direct determination of electron and hole temperatures from continuous-wave photoluminescence measurements'. *Physical Review B*, **vol. 110**, no. 12, p. 125207 (2024) (cited pages 104, 108, 115, 119, 176)

[Vidon 2022] G. Vidon. *Why do decays decay? Transport and recombination dynamics of solar cells revealed via time resolved photoluminescence imaging: application to hybrid perovskites*. Ph.D. thesis (2022) (cited pages 101, 153, 176)

[Vurgaftman *et al.* 2001] I. Vurgaftman, J. R. Meyer and L. R. Ram-Mohan. 'Band parameters for III–V compound semiconductors and their alloys'. *Journal of Applied Physics*, **vol. 89**, no. 11, pp. 5815–5875 (2001) (cited page 56)

[Wachutka 1990] G. Wachutka. 'Rigorous thermodynamic treatment of heat generation and conduction in semiconductor device modeling'. *IEEE Transactions on Computer-Aided Design of Integrated Circuits and Systems*, **vol. 9**, no. 11, pp. 1141–1149 (1990) (cited pages 82, 101)

[Wang *et al.* 2021] H. Wang, F. Wang, T. Xu, H. Xia, R. Xie, X. Zhou, X. Ge, W. Liu, Y. Zhu, L. Sun, J. Guo, J. Ye, M. Zubair, M. Luo, C. Yu, D. Sun, T. Li, Q. Zhuang, L. Fu, W. Hu and W. Lu. 'Slowing Hot-Electron Relaxation in Mix-Phase Nanowires for Hot-Carrier Photovoltaics'. *Nano Letters*, **vol. 21**, no. 18, p. 7761–7768 (2021) (cited page 29)

[Werner *et al.* 1994] J. H. Werner, S. Kolodinski and H. J. Queisser. 'Novel optimization principles and efficiency limits for semiconductor solar cells'. *Physical Review Letters*, **vol. 72**, no. 24, pp. 3851–3854 (1994) (cited page 22)

[Whiteside *et al.* 2016] V. Whiteside, H. Esmaielpour, J. Tang, S. Vijeyaragunathan, T. Mishima, M. Santos, B. Wang, R. Yang and I. Sellers. 'Evidence of suppressed hot carrier relaxation in type-II InAs/AlAsSb quantum wells'. In Conibeer G and Sulima OV, editors, 'Proceedings of SPIE International Society of Optical Engineering', vol. 9937. SPIE (2016). ISBN 9781510602656 (cited page 29)

[Whiteside *et al.* 2019] V. R. Whiteside, B. A. Magill, M. P. Lumb, H. Esmaielpour, M. A. Meeker, R. R. H. H. Mudiyanselage, A. Messager, S. Vijeyaragunathan, T. D. Mishima, M. B. Santos, I. Vurgaftman, G. A. Khodaparast and I. R. Sellers. 'Valence band states in an InAs/AlAsSb multi-quantum well hot carrier absorber'. *Semiconductor Science and Technology*, **vol. 34**, no. 2, p. 025005 (2019) (cited page 115)

[Wolf 1960] M. Wolf. 'Limitations and Possibilities for Improvement of Photovoltaic Solar Energy Converters: Part I: Considerations for Earth's Surface Operation'. *Proceedings of the IRE*, **vol. 48**, no. 7, pp. 1246–1263 (1960) (cited page 21)

[Wurfel 1982] P. Wurfel. 'The chemical potential of radiation'. *Journal of Physics C: Solid State Physics*, **vol. 15**, no. 18, pp. 3967–3985 (1982) (cited pages 37, 40, 43, 106)

[Wurfel 1997] P. Wurfel. 'Solar energy conversion with hot electrons from impact ionisation'. *Solar Energy Materials and Solar Cells*, **vol. 46**, no. 1, pp. 43–52 (1997) (cited pages 29, 30, 32, 66, 68, 124)

[Wurfel and Wurfel 2016] P. Wurfel and U. Wurfel. *Physics of solar cells: from basic principles to advanced concepts.* Wiley-VCH Verlag GmbH & Co. KGaA, Weinheim, 3rd edition ed. (2016). ISBN 978-3-527-41312-6 (cited pages 21, 88)

[Wurfel *et al.* 2005] P. Wurfel, A. S. Brown, T. E. Humphrey and M. A. Green. 'Particle conservation in the hot-carrier solar cell'. *Progress in Photovoltaics: Research and Applications*, **vol. 13**, no. 4, pp. 277–285 (2005) (cited page 71)

[Yang *et al.* 2016] Y. Yang, D. P. Ostrowski, R. M. France, K. Zhu, J. van de Lagemaat, J. M. Luther and M. C. Beard. 'Observation of a hot-phonon bottleneck in lead-iodide perovskites'. *Nature Photonics*, **vol. 10**, no. 1, pp. 53–59 (2016) (cited page 29)

[Yangui *et al.* 2019] A. Yangui, M. Bescond, T. Yan, N. Nagai and K. Hirakawa. 'Evaporative electron cooling in asymmetric double barrier semiconductor heterostructures'. *Nature Communications*, **vol. 10**, no. 1, p. 4504 (2019) (cited pages 143, 146, 147)

[Yuan *et al.* 2017] P. Yuan, J. Liu, R. Wang and X. Wang. 'The hot carrier diffusion coefficient of sub-10 nm virgin MoS2: uncovered by non-contact optical probing'. *Nanoscale*, **vol. 9**, no. 20, pp. 6808–6820 (2017) (cited page 94)

[Zhang *et al.* 2016] P. Zhang, Y. Feng, X. Wen, W. Cao, R. Anthony, U. Kortshagen, G. Conibeer and S. Huang. 'Generation of hot carrier population in colloidal silicon quantum dots for high-efficiency photovoltaics'. *Solar Energy Materials and Solar Cells*, **vol. 145**, pp. 391–396 (2016) (cited page 29)

[Zhang *et al.* 2021] Y. Zhang, X. Jia, S. Liu, B. Zhang, K. Lin, J. Zhang and G. Conibeer. 'A review on thermalization mechanisms and prospect absorber materials for the hot carrier solar cells'. *Solar Energy Materials and Solar Cells*, **vol. 225**, p. 111073 (2021) (cited page 29)

[Zhou *et al.* 1992] X. Q. Zhou, K. Leo and H. Kurz. 'Ultrafast relaxation of photoexcited holes in n-doped III-V compounds studied by femtosecond luminescence'. *Physical Review B*, **vol. 45**, no. 7, pp. 3886–3889 (1992) (cited pages 103, 104)

[Zhu *et al.* 2021] X. Zhu, M. Bescond, T. Onoue, G. Bastard, F. Carosella, R. Ferreira, N. Nagai and K. Hirakawa. 'Electron Transport in Double-Barrier Semiconductor Heterostructures for Thermionic Cooling'. *Physical Review Applied*, **vol. 16**, no. 6, p. 064017 (2021) (cited page 145)

ECOLE DOCTORALE

Titre : Mesure des écarts de température par photoluminsecence dans les cellules solaires à porteurs chauds : vers une étude des dispositifs non idéaux.

Mots clés : Photovoltaïque, Porteurs chauds, Photoluminescence, Modélisation, Transport

Résumé : Les cellules solaires à porteurs chauds promettent des rendements théoriques supérieurs à 66%. Néanmoins, les dispositifs réels ont des rendements nettement inférieurs, de l'ordre de 10%. Pour comprendre cette différence, il est nécessaire de complexifier notre compréhension des cellules solaires à porteurs chauds en introduisant des effets non-idéaux. Dans cette thèse, nous étudions deux effets ≪ d'écart de température ≫: (i) l'existence d'un gradient de température dans l'absorbeur (température inhomogène) et (ii) l'existence de deux températures différentes pour les électrons et les trous.

Dans le premier cas, nous proposons une description théorique du transport adaptée à cette situation particulière. Nous montrons que le transport est ambipolaire et thermoélectrique, et proposons une expression théorique pour les coefficients de transport. Ensuite, nous proposons une expérience basée sur une mesure hyperspectrale de photoluminescence en régime continu pour caractériser les coefficients de transport. Nous mesurons en particulier le coefficient Seebeck ambipolaire d'un puits quantique de (In,Ga,As)P.

Dans le second cas, nous commençons par prouver que la température des électrons et des trous sont toutes deux accessibles par une simple mesure de photoluminescence en régime continu. En effet, l'absorptivité d'un échantillon dépend des distributions des électrons et des trous grâce au terme de ≪ band filling ≫. Cette technique nécessite que l'échantillon soit soumis à une excitation intense, de sorte que les électrons et les trous soient dans un régime dégénéré.

Enfin, nous avons étudié l'impact de ces deux effets sur l'opération des cellules à porteurs chauds. Nous avons d'abord calculé le voltage d'une cellule sujette à l'un ou l'autre de ces deux effets d'écart de température, et montré qu'ils sont identiques. Ensuite, nous avons montré que la différence de température entre les électrons et les trous (à température effective fixée) conduit à une augmentation de l'efficacité de la cellule, de l'ordre de 1 à 2 points maximum. Cet effet étant limité, il n'est pas nécessaire de caractériser avec précision la température des électrons et des trous, la connaissance de la température effective semble suffisante.

Title : Uneven temperatures in hot-carrier solar cells: optical characterization and device modelling.

Keywords : Photovoltaics, Hot-carrier solar cells, Photoluminescence, Modelling, Transport

Abstract : Hot-carrier solar cells promise theoretical efficiencies exceeding 66%. However, actual devices exhibit significantly lower efficiencies, around 10%. To understand this discrepancy, it is necessary to complicate our understanding of hot-carrier solar cells by introducing non-ideal effects. In this thesis, we study two “uneven temperature” effects: (i) the existence of a temperature gradient within the absorber (inhomogeneous temperature) and (ii) the existence of two different temperatures for electrons and holes.

In the first case, we propose a theoretical description of transport adapted to this specific situation. We show that the transport is ambipolar and thermoelectric, and we propose a theoretical expression for the transport coefficients. Next, we suggest an experiment based on hyperspectral photoluminescence imaging in steady-state to characterize transport coefficients. In particular, we measure the ambipolar Seebeck coefficient of an (In,Ga,As)P quantum well.

In the second case, we begin by proving that electron and hole temperatures s are both accessible through steady-state photoluminescence spectroscopy. Indeed, the absorptivity of a sample depends on the distributions of electrons and holes due to the ”band filling” effect. This technique requires that the sample be subjected to intense excitation, ensuring that the electrons and holes are in a degenerate regime.

Finally, we studied the impact of these two uneven temperature effects on the operation of hot-carrier solar cells. We first calculated the voltage of a cell subject to either of these effects and showed that they result in identical cell voltage. We then demonstrated that the temperature difference between electrons and holes (at a fixed effective temperature) leads to an increase in cell efficiency, by about 1 to 2 points maximum. This effect being limited, precise characterization of electron and hole temperatures is unnecessary to design hot-carrier solar cells.

Institut Polytechnique de Paris
91120 Palaiseau, France